

UNIVERSITÉ PARIS DIDEROT - SORBONNE PARIS CITÉ

ÉCOLE DOCTORALE 518
CONDENSED MATTER
AND INTERFACES

T H È S E

pour obtenir le grade de

Docteur en Sciences

de l'Université PARIS DIDEROT (Paris 7)

Présentée et soutenue par

Matthias BUSSONNIER

Actin Gel mechanics Mécanique des Gels D'actine

Thèse dirigée par Timo BETZ et Cécile SYKES

préparée à l'Institut Curie

Soutenance le 16 Septembre 2014, devant le jury composé de :

<i>Président :</i>	Prof. Atef ASNACIOS	- Université Paris Diderot
<i>Rapporteurs :</i>	Prof. Dr. Dr. Karsten KRUSE	- Universität des Saarlandes
	Dr. Guillaume ROMET-LEMONNE	- LEBS - CNRS
<i>Examinateurs :</i>	Dr. Laurent BLANCHOIN	- CEA Grenoble
<i>Directeurs :</i>	Dr. Timo BETZ	- Institut Curie
	Prof. Cécile SYKES	- Institut Curie

CONTENTS

1	Background	3
1.1	Introduction	3
1.2	Living Cells	4
1.3	Oocyte	4
1.3.1	Cell Organelles	5
1.3.2	The Cytoskeleton	7
1.4	The Role And Composition Of The Cytoskeleton	7
1.4.1	Composition of the cell cytoskeleton	8
1.4.2	The actin cortex	17
1.4.3	Cell Motility	18
1.4.4	Organelle Positioning	21
1.5	In vitro reconstituted actin networks	22
1.5.1	Bead motility assay	23
1.5.2	Liposomes	24
1.6	Membrane Physics	25
1.7	Actin networks as viscoelastic material	27
1.7.1	Elastics Modulus	28
1.7.2	Poisson Ratio	29
1.7.3	Viscosity	30
1.7.4	Viscoelasticity	30
1.8	Optical tweezer	32
1.8.1	Determination of trapping forces and bead displacement	33
2	Materials and Methods	37
2.1	Buffers	37
2.1.1	G-Buffer	37
2.1.2	Polymerisation Buffer	37
2.1.3	X-Buffer with BSA	38
2.1.4	ATP-Mix Buffer	38
2.2	Protein preparation	38
2.2.1	pWA (also called pVCA)	38
2.2.2	Actin	38
2.2.3	Profilin	38
2.2.4	Arp2/3	39
2.2.5	Capping protein	39

2.2.6	Myosin II	39
2.3	Lipids, reagent and proteins	39
2.4	Doublet preparation	40
2.5	Bead Preparation	40
2.5.1	Actin-Bead Preparation	40
2.5.2	Probe Bead Preparation	41
2.6	Force indentation experiments	41
2.6.1	Preparation of sample	41
2.6.2	QPD positioning and calibration of microscope	41
2.6.3	Initial bead trapping	42
2.6.4	Indentations	43
2.7	Time Shared Optical Traps	43
2.8	Oocyte	45
2.8.1	Oocyte obtention	45
3	Mechanical properties of a far reaching actin cloud	47
3.1	Introduction	47
3.2	Actin-Bead System	48
3.3	Probe Bead System	50
3.4	Experimental description	50
3.4.1	Approach Phase	50
3.4.2	Relaxation Phase	51
3.4.3	Retraction part	51
3.4.4	Reconstitution of Force-distance-curve	51
3.4.5	Repetitive indent	52
3.4.6	Effect of approach speed	52
3.5	Experimental observations	54
3.5.1	Approach phase modeling	54
3.5.2	Variation of parameters with Capping Protein	58
3.5.3	Determination of Young's Modulus	61
3.5.4	Mechanical properties	62
3.5.5	Interpretation	67
3.6	Relaxation phase	69
3.6.1	Retraction Phase	71
3.7	Discussion	73
4	Cortical tension measured on liposome doublets	75
4.1	Introduction	75
4.2	Experimental description	75
4.2.1	Formation of liposomes doublets	75
4.2.2	Formation of actin cortex on doublets	76
4.2.3	Visualisation of the interface	76
4.2.4	Geometrical parameters	78
4.3	Experimental Observations	78
4.3.1	Effect of myosin-II injection	78
4.3.2	Relation between the angles and tension	79
4.3.3	Contact angle dispersion	81
4.3.4	Tension of actin-shell	81

4.4	3D observation	81
4.5	Discussion	86
4.5.1	Cortical tension is homogeneous for single doublet	86
4.5.2	Relative increase in cortical tension	86
4.5.3	Cortical tension increase in doublets and in cells	86
4.5.4	Different contributions for cortical tension	87
4.5.5	Conclusion	87
4.6	3D fitting	87
4.6.1	First step: Fitting a single liposome	88
4.6.2	Fitting a doublet	89
4.6.3	Discussion	96
4.6.4	Conclusion	96
5	Active cytoplasm movement in mouse oocytes	99
5.1	Introduction	99
5.2	Oocytes	99
5.3	Measure of activity	99
5.4	Conclusion	101
6	Conclusion	105
7	Appendix	107
7.1	Mechanical detection of a long range actin network emanating from a biomimetic cortex Preprint	107
7.2	Cell-sized liposome doublets reveal active cortical tension build up Draft	127
Bibliography		149

PREAMBLE

During my PhD I decided to investigate the effect of the actin network on the mechanical properties of cells. Indeed, cell mechanics are a key parameter that has crucial impact on cellular and organisms functions. Being able to detect changes in the mechanical properties, and to understand the mechanism that govern these changes is an important step in the study of cellular behavior as well as in differentiating healthy from cancerous cells and tissue. Understanding the mechanisms that are at the origin of cell motion and shape changes is also a decisive step in controlling cell behavior, with the ultimate goal to prevent cancer cell invasion and division without impairing healthy cells.

During the last three years, I decided to focus on biomimetic system and to determine the characteristics of actin networks. Actin is a highly conserved component across the living domain, and it plays a major role in cell mechanics. By interacting with a number of other components of the cell, actin is able to form various different types of networks. I decided to focus my research on such networks that were created under controlled conditions.

Along this dissertation we will mainly focus on three systems.

First, we reconstitute an already observed actin network — the actin cortex — on a biomimetic system, then show that a second sparse actin network that was previously unseen emanates from it, and finally characterize its mechanical properties. We developed the idea that the effect of this second network cannot be neglected in cells and investigate a few of the phenomenon it may be involved in.

As the effect of such a sparse actin has not been demonstrated in living cells, we decided to investigate the effect of another sparse actin network found in a living cells. In collaboration with the group of Marie Hélène Verlhac at College de France, we studied the mechanical properties in the cytosol of mouse oocytes. We see in this system that actin related proteins have hi-impact on the structure and the mechanics of both the cell and the actin network.

Characterizing the dynamics of a network in a living cell by controlling the conditions remains complex. In a third research stream we characterized the dynamical changes of tension created by reconstituted actin cortices that are linked to a lipid membrane. By studying liposome “doublets” we are able to measure the variation of tension generated by the acto-myosin cortex over time. This system is composed by a liposome doublet covered with an actin network. Imaging with Spinning disk microscopy, we are able to reconstruct changes in the acto-myosin network and deduce the changes in its properties from the geometrical variation during network contraction.

CHAPTER

ONE

BACKGROUND

1.1 Introduction

Cells are the basic components of living organisms. Understanding their individual behavior and the way they function is a key step to understand how they interact with their environment. One of the key components within most cells is the actin cytoskeleton, which is made up of actin monomers, a protein that is highly conserved across species and which plays an important role for cell mechanics, ranging from cell migration to cell differentiation and division. It plays hence a crucial role for the mechanical properties of the cell and its mechanical interaction with the environment. Under the cell membrane lies a thin actin network which controls the mechanical properties of the cell: the actin cortex. The mechanical behavior of this actin cortex is itself driven by the dynamics and interaction within the actin network it is made off. Understanding this actin network is hence a key to learn how the actin cortex behaves, leading to a better understanding of cells and tissue.

The properties of an actin network highly depend on its structure. The structure itself depends on many parameters that influence how the network is formed. The network structure and formation is influenced by physical and chemical conditions and the spatial and temporal variation of these parameters like mechanical stress or ion-concentration can determine the fate of the network. Hence it is important to study these networks and their dynamic behaviour in order to grasp the changing structure of the cell.

Cells are complex systems that adapt their shape, mechanical properties and biochemical conditions permanently. The spatial repartition of theses properties is also variable as the cell regulates the concentration of proteins all across its cytoplasm. To well study the effect of each component independently, it is crucial to study actin networks in a controlled environment.

Biomimetic systems allow to respond to most of these concerns, they provide a controlled environment that mimic *in-vivo* phenomena. Biochemical conditions can be well controlled, both in space and time hence allowing to precisely fine tune experimental conditions. Biomimetic systems are also particularly adapted to be combined with optical traps which allow us to study local mechanical properties of actin networks with high temporal resolution. The combination of both allows us to get insight into the variation of theses mechanical properties as a function of time and space with high precision.

During my PhD, I have focused on the mechanical properties of branched actin networks polymerizing on optically trapped polystyrene beads. Such networks where studied before [Kawska, Carvalho, Manzi, et al. 2012] but have been suspected to be highly inhomogeneous. Optical traps allows to probe the mechanics of yet unaccessible parts of the network. I further studied actin networks on other biomimetic systems constituted of liposomes, in order to better understand the effect of actin cortex polymerisation on membrane

tension and to characterize network dynamics over time. Finally, I participated in a collaboration in order to understand the implication such actin networks in living mouse oocytes.

1.2 Living Cells

Cells are the basic building blocks of life, and all living beings are composed of cells, from unicellular up to multicellular organisms like us. Unicellular organisms must accomplish all their functions within a single cell. At the other end, in multicellular organisms cells differentiate in order to accomplish specialised tasks often by regrouping into organs. Despite sharing the same genetic material, for each cell to accomplish a different task often requires different mechanical properties. The variation of elasticity and other mechanical properties of cells derive from the structure they are composed of.

Cells are hence able to adapt to their environment and develop functions and behavior that may change over time. A small change of timing and/or biochemical conditions can highly injure the development of an organism: for example modification of the actin network at a given time during the cell cycle prevents symmetric division [Lenart, Bacher, Daigle, et al. 2005], [Vasilev, Chun, Gragnaniello, et al. 2012]. Furthermore, the mechanical properties of the substrate can govern the differentiation of cells: Soft substrate will favor brain-tissue cell, where stiff substrates increase the appearance of muscle cells [Engler, Sen, Sweeney, Discher, 2006].

Nonetheless, even with all these different behavior and phenotypes, cells have a common structure. The exterior of the cell is separated from the inside by a plasma membrane. The interior of the cell is filled with the cytoplasm which contains diverse structures such as organelles, genetic material, and a large number of proteins that the cell uses to accomplish its functions. To communicate with the outside, cells have a series of mechanisms that allow signals and cargo to pass the membrane. This communication can be chemical, but mechanics is also known to participate in the process. To sense their mechanical environment, cells often use adhesion complexes to attach to the substrate, and integrins as trans-membrane protein to transfer the force to the cell cytoskeleton situated inside the cell. Chemical signals can either cross the membrane through trans-membrane proteins, while endocytosis and exocytosis are ways for the cell to import and export proteins and chemicals through its membrane.

1.3 Oocyte

A particular cell type I was interested in during my PhD are mouse oocytes. Oocytes are female germinal cells in the process of gametogenesis. Unlike somatic cells that undergoes symmetric division via mitosis which leads to two identical cells sharing the same genetic material, oocytes undergo a different process called meiosis. Meiosis in oocytes is a highly asymmetric process necessary for the specificity of being large haploid cells, containing at the end of meiosis only one chromosome of each pair that constitutes the genetic material of a mouse. The second chromosome of each pair will be provided during fertilisation of the oocyte by the male sperm.

The exact process of oocyte formation can vary among species, and in the following we will describe the main mechanisms.

The complete process of egg maturation starts with primordial germ cells that undergo mitosis to replicate until they enter the first meiosis (Meiosis I) at which state they are called primary oocytes and are still diploid, that is to say still contains two chromosomes of each pair.

The primary oocyte will start maturation and growth and then undergo a first asymmetric division just after prophase I. This first division is asymmetric both in the genetic material separation and in the unequal size of the formed daughter cell. Indeed, the primary oocyte will divide into a secondary oocyte and a polar body. Both, the secondary oocyte and the polar body are haploid and contain only half of the genetic material of the primary oocyte. The secondary oocyte can go through Meiosis II in which it undergoes a second asymmetric division and expulsion of a second polar body. These polar bodies will eventually degenerate (Fig 1.1).

During meiosis, the process of cell division also differ from mitosis. Instead of separating into two identically sized cells through the formation of a cytokinetic ring, the primary oocyte will become the secondary oocyte by expulsion a polar body. The formation expulsion of the polar body require precise positioning of the cell organelles. During prophase I the nucleus of the oocyte is carefully centered, undergoes a nuclear breakdown and spindle formation. The first meiotic spindle will migrate toward the oocyte cortex along its major axis. Once at the cortex, half of the genetic material of the spindle will be expelled through the membrane forming the first polar body of much smaller size than second oocyte.

Mouse oocyte are good model systems to study the mechanical properties inside cells. They form big spherical cells with a diameter of around 80 μm which allow to study the mechanical properties at different locations in the cytoplasm.

In the third part of my PhD I participated in a collaboration with Marie-Hélène Verlhac and Maria Almonacid at Collège de France who are interested in the effect of actin dynamics in oocyte cytoplasm during the different parts of oocyte gametogenesis.

1.3.1 Cell Organelles

Inside the cytoplasm, cells have a number of structures with different and specialised functions which are called organelles. The position and state of organelles is of great importance for the cell to achieve its functions. Probably the most known organelle is the cell nucleus of eukaryotic cells that contains the genetic material. Attached to the nucleus is the endoplasmic reticulum which is the organelle responsible for translating RNA coming from the nucleus to functional proteins that will be delivered across the cell after maturation in vesicles. These vesicles are transported across the cell both by dyneins and kinesins — molecular motors — that walk along microtubules originating from the centriole part of the centrosome but also by myosins walking along actin filaments. All of those processes consume energy in the form of ATP, generated within the mitochondria spread across the cytoplasm. A schematic of the cell with some organelles can be seen on figure 1.2

The positioning of organelles is crucial for the life of the cell. During meiotic division of cells, for example, it has been seen that the positioning of the nucleus at the center of mouse oocytes happens before its migration closer to the cortex to expel the first polar body. Failure to do so results in an incorrect amount of DNA in germinal cell that can lead to infertility.

It is already known that microtubules play a key role in organelle positioning. Microtubules emanating from centrosome position at the two ends of the cell during its division are used to fetch the correct chromosomes. Each chromosome is pulled towards the centrosome which leads to each daughter cell having the same amount of DNA.

Actin plays also an determinant role in organelle positioning process, like in drosophila oocyte maturation where it positions the nurses cell away from the dumping canal [Huelsmann, Ylanne, Brown, 2013]. In a

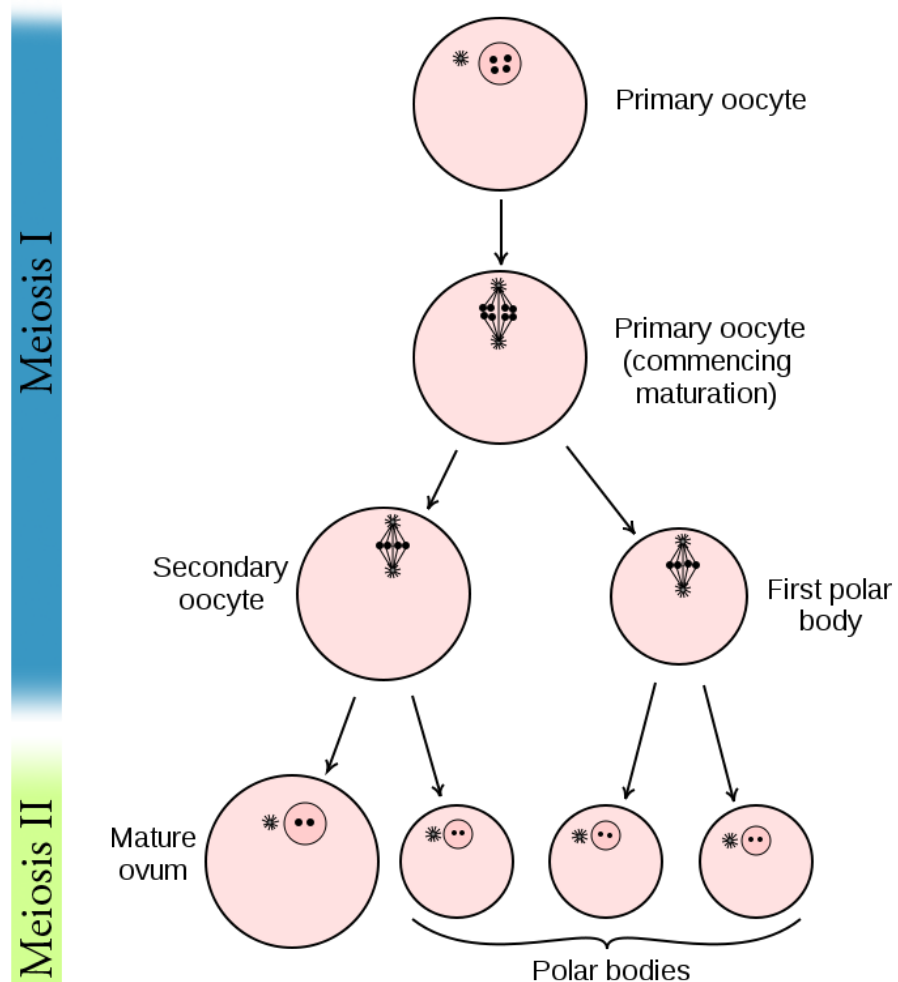


Figure 1.1: Asymmetric division of oocytes into polar bodies. The primary oocyte asymmetrically divides into a secondary oocyte and a smaller polar body each containing half the DNA of the mother cell. The secondary oocyte will divide asymmetrically a second time to become the mature ovum while expelling a polar body. This asymmetric division process allows the formation of a large haploid cell. Adapted from Wikipedia – Gray's Anatomy – and [Alberts, Johnson, Lewis, et al. 2008].

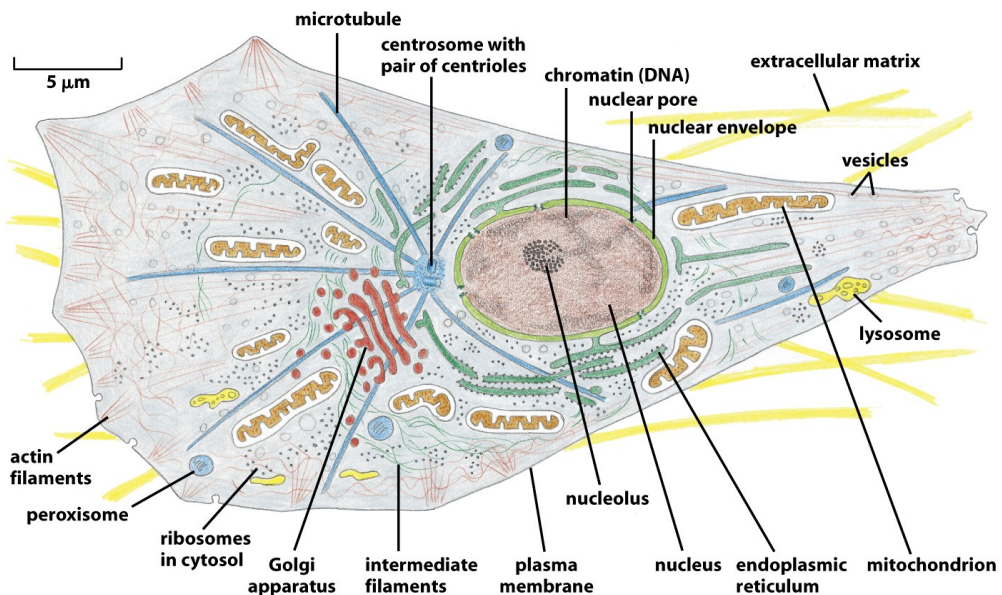


Figure 1-30 Molecular Biology of the Cell 5/e (© Garland Science 2008)

Figure 1.2: Schematic of an eukaryotic cell, adapted from [Alberts, Johnson, Lewis, et al. 2008]. Visualized are the many components that constitute the majority of cells. Cell shape and size can highly vary, from quasi spherical with a typical size of ten micrometers to elongated neurones that can be tens of centimeters long.

later chapter (*Organelle Positioning* (page 21)) we will develop a few keys points where actin is indispensable in organelle positioning and how this relate to the biomimetic actin networks we reconstitute.

1.3.2 The Cytoskeleton

The cytoskeleton, literally skeleton of the cell, is the structure which gives the shape to a cell. As for other multicellular animals that posses skeleton, its shape is often a hint on how an organism moves. As feet, fins and wings are characteristics that will tell you whether a animal prefer land, sea or air, the cytoskeleton will tell you many things about a cell.

Unlike the (exo)-skeleton of animals which is rigid and static, the cytoskeleton of cell is a highly dynamic structure that keeps remodeling itself on a short time scale compared to the speed at which a cells move. Thanks to these dynamics, the cytoskeleton can achieve its functions. As vertebrates skeletons are necessary to transmit force from one part of the body to another, the cytoskeleton is responsible not only to transmit the forces the cell is exerting, but also to generate these forces. The cytoskeleton connect a cell to its environment, both mechanically and biochemically.

We will consecrate a longer part of this work to describe the cytoskeleton.

1.4 The Role And Composition Of The Cytoskeleton

We have already introduced the cell cytoskeleton in the previous part, and we will now describe its components and functionality more in detail here. The cytoskeleton has three main functions, it connects the

cell both physically and biochemically to the external environment, generate and coordinate the forces that give the cell its shape and allows it to move. It is also responsible for organising spatially the cell content [Fletcher, Mullins, 2010]. The cytoskeleton is also in particular sensitive to spatial and temporal information that can affect cell fate and the assembly of the cytoskeletal structure. This can be seen for example with the bud scar of budding yeast that persists after division.

1.4.1 Composition of the cell cytoskeleton

The cytoskeleton is mainly composed of three types of filaments. Microtubules, intermediate filament and actin filament, also known as microfilaments.

Microtubules are the widest structure with a diameter of 20nm (Fig 1.3) and the stiffest of the three kinds of filaments with a *persistence length* (page 27) in the order of millimeters, much longer than the size of the usual cell. Microtubules are extensively studied [Valiron, Caudron, Job, 2001]. Microtubules are formed by the polymerisation of a heterodimer of tubulin that leads to the formation of polar (oriented) filaments that can be walked on by molecular motors. These molecular motors can be decomposed in two families – kinesins and dyneins – depending on the end towards which the motor preferably walk. Microtubules are mostly known for their action during mitosis where they will form the majority of the mitotic spindle that drive the segregation of the chromosomes in two groups, each group ending in one of the daughter cells.

Microtubules have the characteristic of being highly dynamic by alternating between two states of rapid growth and a rapid shrinkage. The transition from microtubule growth to shrinkage is called a *catastrophe*, the transition from shrinkage to growth is called a *rescue*.

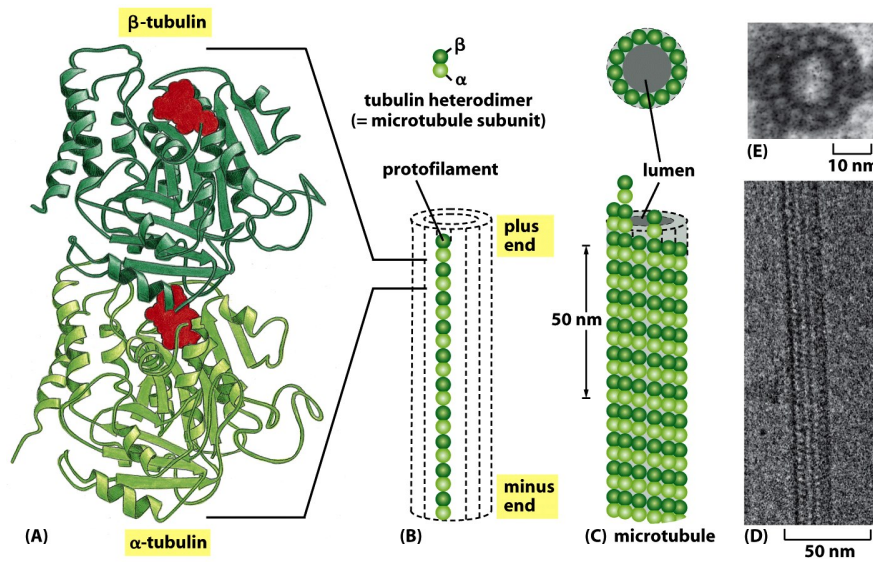


Figure 16-11 Molecular Biology of the Cell 5/e (© Garland Science 2008)

Figure 1.3: Structure of an heterodimer of tubulin and assembly into a microtubule. Electron microscopy of a single microtubule filament. From [Alberts, Johnson, Lewis, et al. 2008]. A) Structure of heterodimer of tubulin B) Heterodimers can assemble forming polar filaments. C) Filaments can assemble into microtubules. D,E) Electron microscopy image of microtubules.

Intermediate filaments are of medium diameter in the order of around 10nm, in between actin and microtubules filaments, hence their name. Unlike microtubules and actin filaments, intermediate filaments are

composed by several sub-families of proteins and are non-polar.

Intermediate filament have an important role in the mechanical properties of cells due to the fact that they are particularly resistant to stretching.

Unlike actin and microtubules, they are thought to be passive, with mechanical properties mainly deriving from how multiple filaments are linked together laterally.

Actin, is the third component of the cytoskeleton, the one on which we will focus on most of our efforts. Actin monomers, also called *G-Actin* for globular actin can polymerise. By polymerizing actin monomers (*G-actin*) into actin filaments (*F-actin*), the thinnest of the three cytoskeletal components forms. Actin is produced in the cell as a globular protein of ~40 kDa (Fig 1.4) that once associated with ATP or ADP polymerises into helicoidal filament with a diameter between 7 and 9nm. The formed actin filaments are polar, where both extremities are respectively called the plus (+) or barbed end, and the minus (-) or pointed end. The polarity of the actin filament is of importance as this gives rise to a preferred direction for most processes that can happen on the filaments.

The actin protein is highly conserved across species, and is known to directly interact with hundreds of proteins [DosRemedios, Chhabra, Kekic, et al. 2003].

Single undecorated filaments will behave as semi-flexible polymers at the scale of the cell with a persistence length in the order of 10 μm [Isambert, Venier, Maggs, et al. 1995]. When they assemble into different structures and networks, or associate with other proteins and molecules the resulting mechanical and dynamic properties can be highly variable.

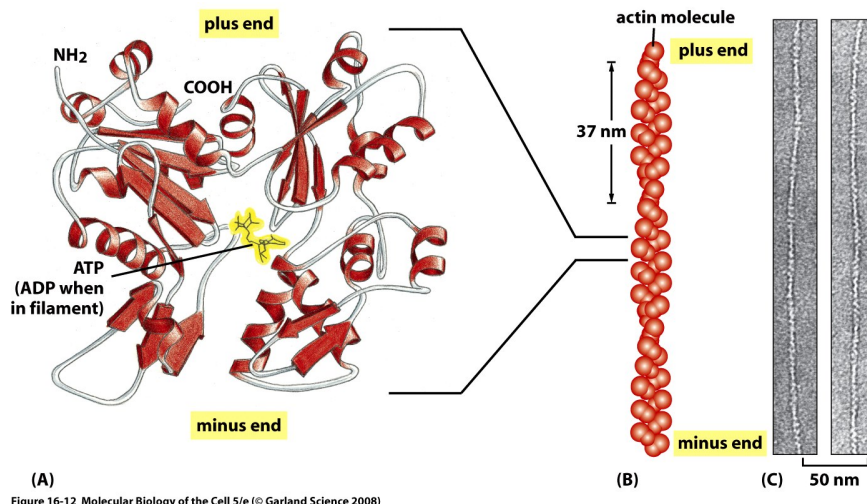


Figure 1.4: A) Structure of a single monomer of actin, and electron microscopy snapshot. — from [Alberts, Johnson, Lewis, et al. 2008].

Dynamics of actin polymerisation

The assembly mechanisms that allow to go from single monomers of actin (also refer to as *G-actin* for globular actin) to actin filament (also refer as *F-actin*) need to be well understood to explain the different network structures created by actin filaments in the presence of other proteins.

Actin Gels dynamics,

The polymerisation of ATP/ADP actin monomers to form an actin filament need to go through the step of forming an actin proto-filament which is constituted of at least 3 actin monomers. This will most of the time be the kinetically limiting step. Once proto-filaments are present in solution, single monomers can be freely added or removed on both ends of the filament. The process of forming these proto-filaments is called nucleation and it is the rate limiting factor to form actin filaments. To circumvent this limitation experimentally one can use preformed actin filament seeds, or actin nucleators to direct the polymerisation on the cell.

We need to distinguish between the dynamics of polymerisation and depolymerisation on both ends of the filament. Indeed, it has been shown that the association and dissociation rates differ between the pointed (-) and barbed (+) end. The barbed end has higher dynamics than its pointed counterpart which is the reason for its (+) name. The dynamics of polymerisation is higher both in the case of ATP and ADP, though the rate constant of association and dissociation differ for both kind of filaments (Figure 1.5)

Elongation rate constants



Figure 1.5: Association and dissociation rate of both ATP and ADP actin on pointed and barbed end as measured in [Pollard, Borisy, 2003]. The difference of equilibrium constant between the barbed end (bottom) and pointed end (top) in the presence of ATP allow filament treadmilling.

The equations that drive the polymerisation can be written as follow

$$\begin{aligned} \frac{dC_{barbed}}{dt} &= k_{+,barbed} \cdot [GActin] - k_{-,barbed} \\ \frac{dC_{pointed}}{dt} &= k_{+,pointed} \cdot [GActin] - k_{-,pointed} \end{aligned} \quad (1.1)$$

Where *barbed* and *pointed* designate respectively the barbed and pointed end, and k_+ and k_- are the polymerisation and de-polymerisation rate. The concentration in barbed and pointed-end denoted by $C_{barbed/pointed}$. By assuming that the number of pointed ends is equal to the number of barbed ends, one can

derive the steady state which give rise to the critical monomer concentration below which an actin filament cannot grow: $[GActin]_c$.

The rate constants of elongation of actin have been determined and depend on whether the monomer is bound to ADP or ATP [Pollard, 1986]. We should consider the fact that the ATP bound to actin will hydrolyse to ADP-Pi before releasing the inorganic phosphate. The hydrolysis and phosphate release rates also depend on whether the monomer is part of a filament or in solution. The hydrolysis of ATP-bound actin into ADP bound actin in the filament leads to an imbalance of actin (de)-polymerisation on both ends. The actin filaments preferably grow from the barbed end and shrink preferably from the pointed end.

This will lead to a phenomenon known as treadmilling where a single actin monomer bound to an ATP molecule, will be incorporated at the + end of the filament and progressively migrate toward the - end, eventually hydrolysing its ATP into ADP before detaching from the filament on the pointed end. During this process the filament will grow / shrink until it reaches the stationary state where its length would stay constant but the treadmilling continues.

Treadmilling requires an imbalance in the global rate constant on the barbed and pointed end and an energy source, in the case of actin this is provided by the hydrolysis of ATP into ADP+Pi before releasing the inorganic phosphate, without which treadmilling would not occur.

Practically, this can be approximated by having only ATP monomers at the barbed end of actin filaments while the pointed end is typically constituted only of ADP monomers, thus the critical concentration is lower at the pointed end compared to the barbed end. The growth speed of the filament on both ends depends on the monomer concentration in solution. In between the critical concentration of both ends, there exists a concentration at which the polymerisation on (+) exactly compensates the depolymerisation on (-).

Actin network can be controlled by a host of actin binding proteins

Despite the already complex process of actin polymerisation and the number of parameters that we have already introduced, the formation of an actin network is an even more complex process that involves many other components. Especially, actin monomers and filaments can interact with a high number of proteins that will affect the previously introduced dynamics. We will present some categories of such proteins in the following.

Formins

Formins are polymerase proteins that will increase the polymerisation rate of actin filaments by dimerizing and binding to the barbed end. It has the particularity of being processive, meaning that it will stay bound to the barbed end while catalysing the addition of new monomers. The processivity of formins also permits the control of the localization of actin polymerisation where formin proteins are present, like the tip of filopodia [Faix, Rottner, 2006] [Bornschlogl, 2013]. *Formins* posses domains rich in proline, capable of binding to profilin (*FH1*) which allows formin to elongate F-Actin using actin monomers bounds to profilin [Pruyne, Evangelista, Yang, et al. 2002] [Pring, Evangelista, Boone, et al. 2003].

Actin Gels dynamics,

Actin depolymerization and severing

Like polymerisation that can be enhanced by formins, depolymerization can also be speed up. ADF/Cofilin is a protein which is able to increase the rate of actin depolymerization. ADF/Cofilin can do so by increasing the off rate at the pointed end [Carlier, Laurent, Santolini, et al. 1997], or by actively severing the filament in different points, thus disassembling the formed network [McCullough, Grintsevich, Chen, et al. 2011].

It should be noted that depolymerization can not only be enhanced at the pointed end, indeed formin that accelerate the polymerisation is also able to speed-up the detachment of actin monomers from the barbed end.

Capping Protein

To regulate polymerisation, cells also have the possibility to reduce or stop the polymerisation. To achieve this, some proteins will bind to the growing end of actin filaments and prevent the addition of new monomers. *Capping Protein* (CP) being one particular example that will specifically bind to the barbed end of a growing filament and prevent it from growing. Capping proteins are necessary to prevent polymerisation of actin in undesired area and are essential for the structure and mechanical properties of actin gel [Kawska, Carvalho, Manzi, et al. 2012]. *Gelsoline* is another example of Capping Protein, that unlike CP can only attach to the barbed end of an actin filament after severing it. Gelsoline is hence both a severing and a Capping Protein.

Cross-linkers

We have seen that some proteins were able to attach to actin filaments. When such a protein is able to attach to many filament at once, it can act as an attachment point between the two filament, preventing them to move with respect one to each other. Such proteins, are referred to as cross-linkers.

The amount of freedom in movement between the two filaments depends on the cross-linker used. For example , α -actinin will allow rotation of the two filament at their anchoring point whereas cross-linkers like fascine will prefer a parallel conformation of the filament and favor the formation of actin bundles.

Cross-linkers are essential for the formation of elastic network as they allow forces to be carried from one actin filament to the other. The quantity of cross link of a network will often be a key parameter for the elastic properties. The distance between the link points in the network (both cross links and entanglement points) will give the typical network mesh-size which is used to calculate the viscoelastic response of networks : [Morse, 1998a].

Stabilizing actin filaments

As actin networks are dynamic constructs that are changing shape and properties over time, it is convenient to be able to stabilize those networks. Tropomyosins are proteins capable to bind on the side of actin filament to stabilize them.

The use of phalloidin, a toxin extracted from fungus (*Amanita phalloides*), binds between F-actin subunits on the filament, and hence prevents it from de-polymerising. Though, it is known that stabilizing actin

filaments with phalloidin will increase their stiffness as measure by the persistence length which can change the mechanical properties of the formed actin network.

Profilin

Profilin is a protein that will bind to the barbed end of single monomers of actin in solution. By doing so it will first prevent the association of monomers into dimers and trimmers, thus preventing the nucleation of actin filament. It thus allows a better control of localisation of actin filament both *in vivo* and *in vitro* in the presence of actin seeds of actin nucleator.

Profilin was for a long time believed to be only a sequestering protein that inhibit polymerisation [Yarmola, Bubb, 2009], though it has a more complex behavior, and if it prevent polymerisation of actin filaments by the pointed end, it can facilitate polymerisation. One of the cause of increase in polymerisation speed by profilin is the fact it binds preferably to ADP-Actin and increase the exchange rate of ADP into ATP.

Branching Agent

A type of network found of the leading edge of cells lamellipodia is dendritic network. It is characterised by tree-like structure of actin filaments in which thanks to the Arp2/3 complex branching agent a mother actin filament will form a daughter filament on its side.

We have seen previously that crosslinkers are proteins capable of linking two or more actin filaments together by binding on their side. Another mechanism involving binding on the side on actin filament is responsible for a closely related network, the branching mechanism.

The Arp2/3 complex is composed of seven subunits, two of which are highly similar to actin, forming the Arp2 and Arp3 family for Actin Related Proteins, giving the complex its name. Typically Arp2/3 will bind on the side of a pre-existing actin filament, hence initiating the growth of a daughter filament with an angle of 70° to the mother filament. The newly created daughter filament pointed end is terminated by the Arp2/3 complex that will stay attached to the mother filament, thus increasing the number of available barbed end, without changing the number of available pointed end. See Nature Review by Erin D. Goley and Matthew D. Welch [Goley, Welch, 2006] for a longer review about the Arp2/3 complex.

In cells, the Arp2/3 complex needs to be activated by a Nucleation Promoting Factor (NPF). Among them is the WASp protein (Wiskott-Aldrich Syndrome protein) and its neural homologue N-WASP which are from the same family as SCAR/WAVE [Machesky, Mullins, Higgs, et al. 1999]. All these activators of Arp2/3 have in common a WCA motif. The wild type protein need to be activated in order to activate Arp2/3. The activation is done by a change in conformation that exposes the active region and provides the first actin monomer necessary for nucleation of the daughter filament (Figure 1.6). To circumvent the activation process of these proteins, we use a reconstructed version of the protein that cut all region before the poly-proline. This confer to pVCA the ability to be permanently active. This region can also be replaced by streptavidin in order to selectively bind pVCA to selected regions. Characterisation and more detailed description of pVCA can be found in [Noguera, 2012].

Unlike Cells that are able to control the localisation of actin nucleation processes thanks to activation of WASp and its homologue, the ‘*in vitro*’ control of localisation of actin polymerisation is directly done by the localisation of pVCA.

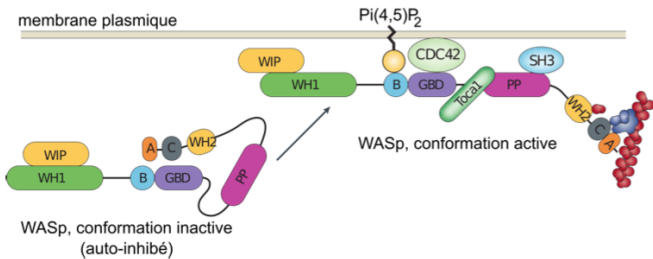


Figure 1.6: Organisation of Wasp domains. A change in conformation make the protein active, which allow the activation of the Arp2/3 complex and the nucleation of a daughter filament. Adapted from [Goley, Welch, 2006]

The network formed by Arp2/3 is called a dendritic network, and is in particular found at the leading edge of the cell in the lamellipodia. It is such a network that is present in the bead system we will study hereafter.

As for crosslinkers, dendritic networks are able to carry forces across single actin filaments by the intermediary of Arp2/3. Two dendritic network of Arp2/3 can also entangle and allow forces to be carried across them [Kawska, Carvalho, Manzi, et al. 2012].

A schematic that recapitulate the interaction of actin with other protein and the formation of a dendritic network at the leading edge of the cell is presented on figure 1.7.

Molecular Motor

A particular kind of protein that can bind to the cytoskeletal filaments are molecular motors. Molecular motors are proteins that will consume energy in the form of ATP, hydrolyse it to change conformation and produce forces.

The motors that move along actin filaments are part of the myosin superfamily, they are both responsible for the transport of cargo along filaments, cell motility, division, and muscle contraction. They acquire their name from their discovery in 1864 by Willy Kühne who extracted the first myosin II extract from muscle cell [Hartman, Spudich, 2012].

The myosin super family is divided into subfamilies numbered with roman literals. As of today we count more than 30 families of myosin [Berridge, 2012]. Muscle myosin is part of the myosin II family and is often referred to as conventional myosin for historical reason as being the first discovered. Non-muscle myosin are also referred to as unconventional myosin.

Myosin motors seem to be shared among the living domain, hinting for an early emerging of myosin in the evolution. All the myosin motors move on actin filaments toward the barbed end, with the exception of myosin VI which moves towards the pointed end [Buss, KendrickJones, 2008].

Different subfamily of myosin are used for different function in cells. Even in subfamilies each type of myosin can have specific functions. For example, conventional myosin found in muscle cells are use for large scale cell contraction. In contrast, myosin V is known to transport cargo and is found to be responsible for actin network dynamics and vesicle positioning [Holubcova, Howard, Schuh, 2013].

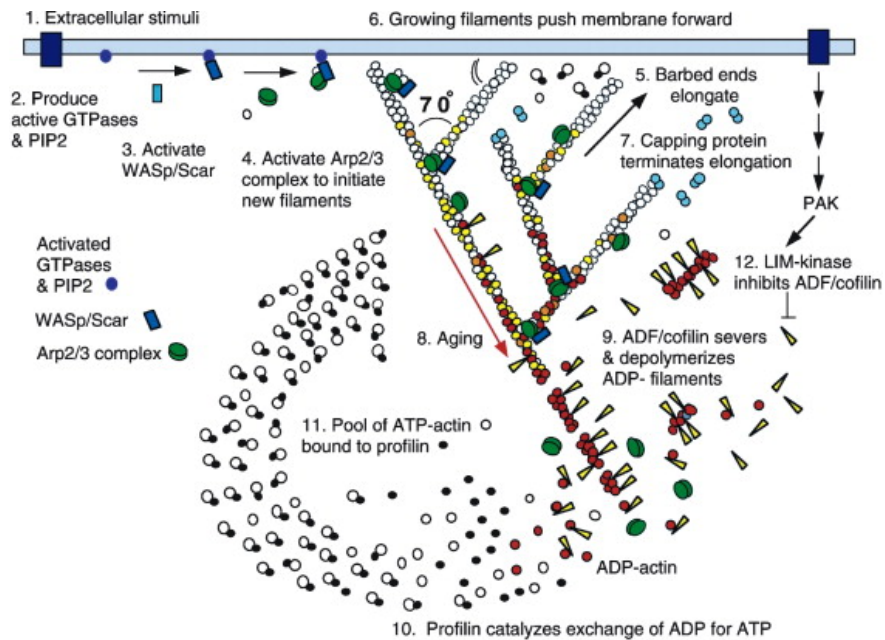


Figure 1.7: Schematic recapitulating the formation of a dendritic network at the leading edge of a cell where several of the function of proteins can be seen. An actin nucleation promoting factor (Active WASp, blue rectangle at the membrane) will activate Arp2/3 (green blob) which will act both as nucleation factor and a branching agent. From an activated Arp2/3 will grow an actin filament pointing towards the membrane. Newly growing barbed ends, rich in ATP-actin (white circle) can eventually be capped by Capping Protein (light-blue pairs of circles) which will terminate their growth. Aging monomers in actin filament will slowly hydrolyse their ATP (yellow and red circle), eventually releasing the inorganic phosphate before detaching from the pointed end. Depolymerisation is helped by severing protein (sharp triangle) and Actin Depolymerisation Factor (ADF). ADP-actin monomer will bind to profilin (Black dots) increasing the turn over rate to ATP-actin which will be reused by the leading edge of the cell. Adapted from [Pollard, Blanchard, Mullins, 2000].

Myosin II As stated before, the myosin II family both encompass conventional myosin as well as Non-muscle myosin II (NMII). Both have a similar structure (Fig 1.8).

All myosin IIs are dimers constituted of two heavy chains and light chains. The heavy chains are held together by a coil-coiled alpha helix referred to as the tail. On the other side of the protein sequence is a globular head, which is responsible for ATP hydrolysis and is able to convert the energy from the hydrolysis into mechanical force. It is also the part that will bind to the actin filaments. In between the tail and head is the neck domain that acts as a lever to transmit the force generated by the head to the tail. The length of the neck influences the length of the movement done by the cargo at each step of the myosin as well as the size of the step the myosin can effect. The two light chains are situated in the neck region and are responsible for the myosin activity regulation.

Myosin II dimers can align and assemble by the tail region, forming myosin minifilaments. These minifilaments are bipolar, having numbers of myosin head with the same orientation at each extremity.

In the myosin II family, conventional myosin and NMII differentiate by the size of the minifilaments they form. Muscle myosin will form minifilaments aggregating around 200 dimers, where NMII minifilaments will be composed only of 10 to 20 minifilaments. The other characteristic of unconventional myosin with muscle myosin is the mode of activation. Conventional myosin activity is regulated by the amount of Ca^{2+} available, which frees the actin filaments to let the myosin motor bind. However, its counterparts are typically activated by the phosphorylation of the Myosin Light Chain (MLC).

Another parameter that discriminates muscle from non-cell myosin is their duty ratio. The duty ratio is define as the ratio of the time the myosin stays attached to an actin filament over the typical time of a contraction cycle. By noting τ_{on} and τ_{off} the time the myosin head spent attached/detached from the filament, the duty-ratio or duty-cycle can be noted :

$$r = \frac{\tau_{on}}{\tau_{on} + \tau_{off}} \quad (1.2)$$

We will see in the following that the duty-ratio might have an important effect on the processivity of the myosin.

It should be noted that as minifilaments can attach to actin filaments on both ends, they can also act as a bridge that holds two points close to each other, though having the properties of crosslinkers.

Myosin V Myosin V is an unconventional myosin. Unlike myosin II it does not aggregate into minifilaments. Though, myosin V has a similar structure to myosin II but with a longer neck, this confers to myosin V the ability to realize longer steps on actin filaments. Indeed, the myosin V step size is of 36nm, which is close to the twisting length of actin filaments. This allows myosin V motors to walk along actin filament without having to rotate around it with the helix they form. At the end the tail domain myosin V posses another globular domain capable of binding to its cargo, and the variability of this region is what mostly define the difference between the different type of myosin V.

Myosin V also has a high duty-ratio, this leads to dimers having almost always one of the two head of the myosin to be bound to actin. It grants to the myosin V the ability to walk in a processive manner toward the barbed end of the actin filaments, both head successively binding 36 nm in front of the other head.

Myosin cycle We saw earlier that the duty ratio of myosin was the ratio of time the head of the myosin spent attached to the actin filament. Indeed, myosin can generate displacement through a cycle of ATP hydrolysis and attachment/detachment described below for a Myosin II motor:

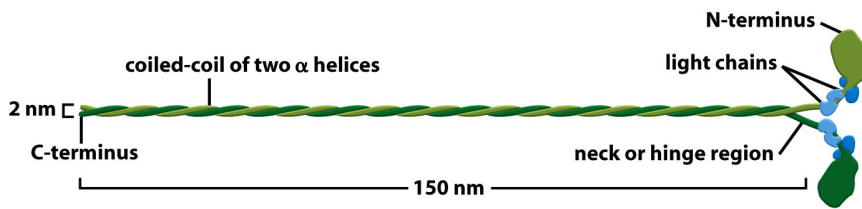


Figure 16-54a Molecular Biology of the Cell 5/e (© Garland Science 2008)

Figure 1.8: Schematic of a dimer of myosin motors with the example of Myosin II. Each of the myosin monomer is colored in a different shade of green. From Right to Left, the myosin head, with the N terminal, is the part of the myosin that binds to the actin filaments. The neck region with the light chain act as a lever arm. Finally the tail, constituted with coiled-coil alpha-helix that aggregate to form minifilaments. Adapted from [Alberts, Johnson, Lewis, et al. 2008].

The cycle can be decomposed in 5 steps, last of which will be responsible for the forced exerted on the myosin cargo.

- The myosin start in the ‘rigor’ conformation where it is lightly bound to the actin filament.
- An ATP molecule binds to the myosin head inducing the detachment of the myosin from the actin filament.
- ATP molecule is hydrolysed into ADP+Pi, providing energy which is stored into a conformational change of the myosin which effects a recovery stroke.
- Inorganic phosphate is released as the myosin head attaches to the actin filament.
- The actin-bound myosin change conformation, applying forces on it’s cargo. This step is known as the power-stroke and is responsible for most of the applied forces or displacements of the myosin. During the power-stroke the ADP bound to the myosin head is released, leading back to first step of the cycle.

This principle is the same for all kinds of myosins. In the case of Myosin II the duty-ratio is only of about 5%, which leave Myosin II detached from the actin filament most of the time. A single dimer cannot achieve processivity. The tail of myosin II can bundle itself with the tail of other myosin II motors. They form large bipolar thick filaments of hundreds of dimers. As each myosin dimer attaches and detaches independently from the actin network the effective attachment of the filament increases with the number of motors in the minifilaments. Indeed the probability of having at least one motor attached increases with the number of motors. The constant attachment of at least one myosin II head in minifilaments insure that the filament does not displace with respect to the actin network when others myosin heads recover from their power stroke and reattach, thus conferring processivity to myosin II minifilaments.

The bipolar nature of myosin II minifilaments also allow them to act as force dipoles, each of the extremity pulling the surrounding actin network or filament towards the center of the minifilaments. This is the mechanism at the origin of muscle contraction and can allow to build-up tension in actin network.

1.4.2 The actin cortex

The actin cortex is a thin layer of between 200 to 500 nm that can be found just underneath the plasma membrane of a cell (Fig 1.9) . The properties of the actin cortex makes it a key component to diverse processes. Its capacity to resist to, and transmit forces is indispensable for locomotion of many cells by

allowing the retraction of the rear of the migrating cell and will be described in more detail in the next section. Its structure is also essential for the cellular division as contractility is necessary to generate cortical tension and achieve the separation of the two daughter cells.

The actin cortex is constituted of actin filaments that can be parallel or orthogonal to the membrane as one can see using electron microscopy on cells [Morone, Fujiwara, Murase, et al. 2006].

We saw through the bud scar of budding yeast that the full cytoskeleton could retain memory of past events. It is also the case for simple actin networks as shown in [Parekh, Chaudhuri, Theriot, Fletcher, 2005] who describe how actin-network growth can be determined by network history, showing actin cortex could also act as a memory for cell.

1.4.3 Cell Motility

The way cells move highly depends on their environment and the cell type. We can distinguish several strategies of movement, mainly categorised into amoeboid and mesenchymal movement. The type of motility for certain cells can be characteristic for malignant tissue, and plays a significant role in the ability of the cells to invade nearby tissues.

Lamellipodium based Motility

We can have a first look into the mesenchymal mode of locomotion of cells, which is also often referred to as crawling. To understand how a cell is able to crawl, to move itself, we will in particular take the example of the lamellipodium. The lamellipodium is a characteristic structure found in cells moving on a 2D substrate. By its nature, motion using lamellipodia is one of the easiest to study using microscopy which might explain why it is one of the best known process of cell displacement. None the less, it does not diminish its importance in tissues behavior as all epithelial cell can be considered as moving on a 2D substrate. Beyond lamellipodia, further structures that are responsible for cell motion are filopodia and pseudopodia. They mainly differ from lamellipodia by their shape and the organisation of the actin structure inside (Fig 1.10). Lamellipodia-based motion can move a cell up to a few micrometers per minute.

The action necessary to move in a mesenchymal way can be decomposed into three steps. First the cell needs to grow a protrusion. Growing this protrusion is typically governed by actin polymerisation just underneath the plasma membrane. The lamellipodium is such a protrusion which is constituted by a 2D dendritic actin network that polymerize at the leading edge. Second the cell's protrusion need to attach to the surface. This is done through trans membrane proteins that are bound to the actin cortex on the inside of the cell. The actin cortex will act as a scaffold to transmit the force across the cellular to these anchor points. The last part is the generation of traction in which the rest of the cell is pulled toward the attached protrusion. The traction force is mediated through the cytoskeleton and actin cortex while the contraction force themselves can originate from actin network contraction and reorganisation due to myosin motors (Fig 1.11).

Blebbing based Motility

The second mode of motility which is known as amoeboid is more characteristic of 3D displacement of cells. In this mode, the cell will also form protrusions but will not rely on adhesion to move its body. This motility relies on blebs, that are blister-like protrusions that appear on the cell surface. A bleb forms on the surface of

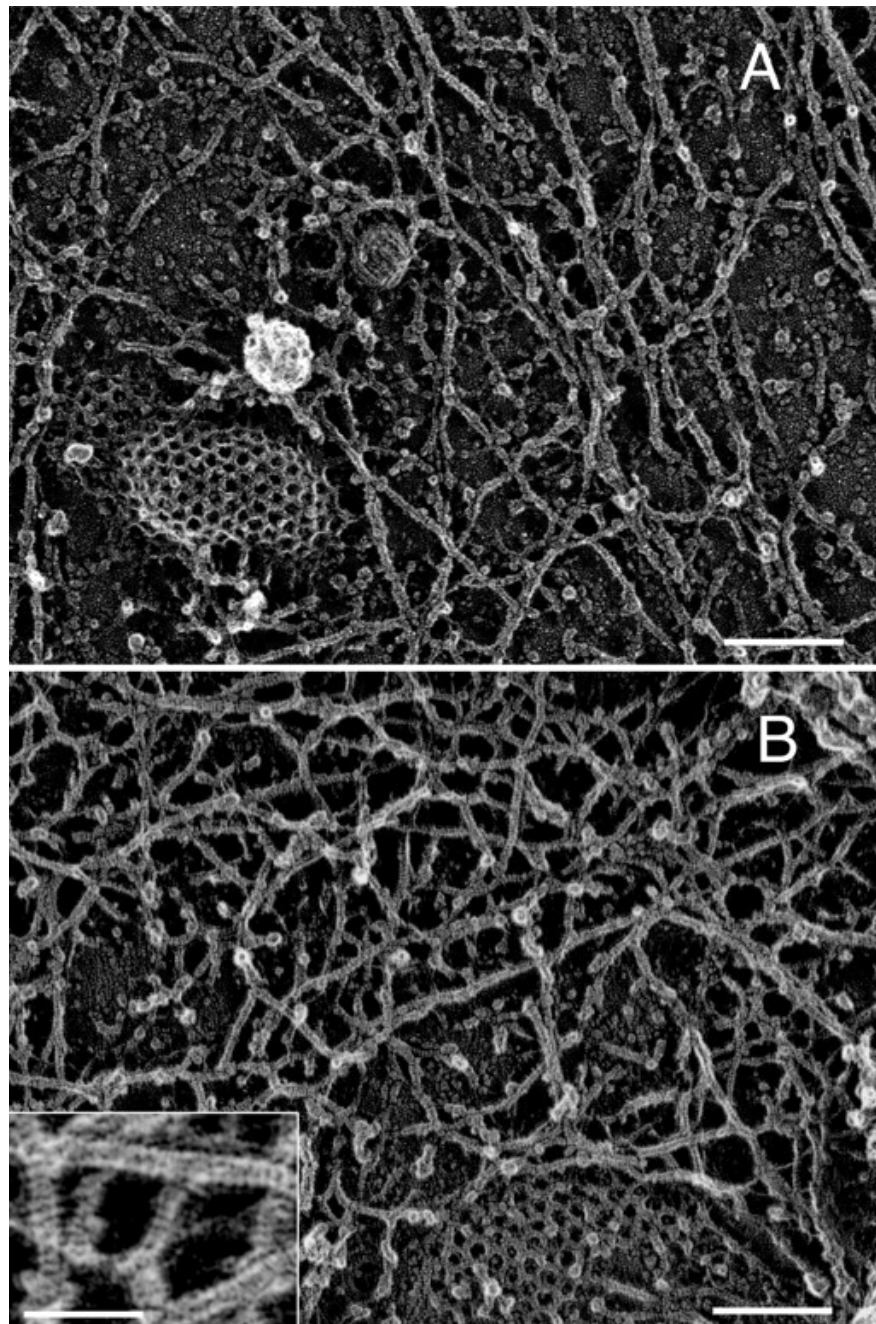


Figure 1.9: Electron microscope view of the actin cortex in rat cell. The inset show a periodicity of ~5nm in filaments characteristic for actin. Scale bars are 100nm, inset 50 nm. Extracted from [Morone, Fujiwara, Murase, et al. 2006].

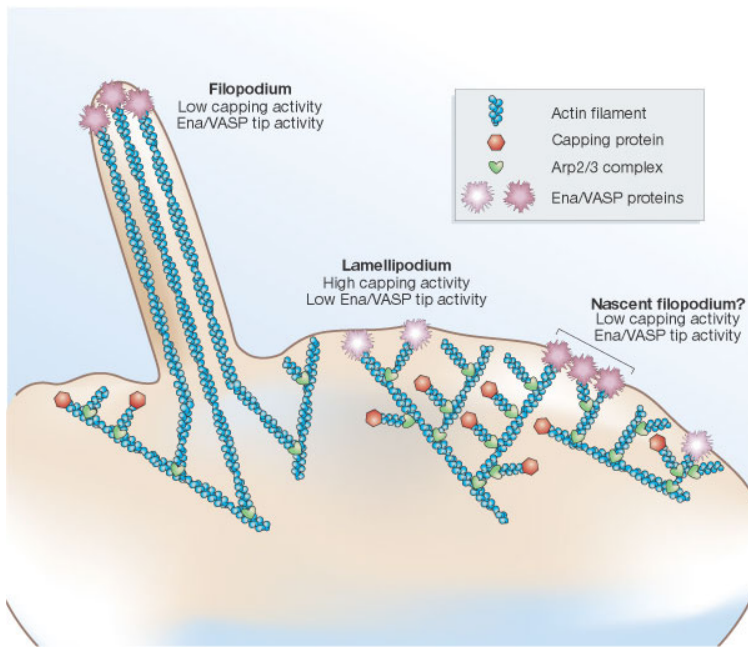


Figure 1.10: Polymerisation at the leading edge of the cell. NPF situated on the membrane of the cell localize the polymerisation. The lamellipodium will be characterized by a dendritic network formed by Arp2/3. Parallel actin structures can form a growing protrusion called filopodium. Adapted from [Schafer, 2004]

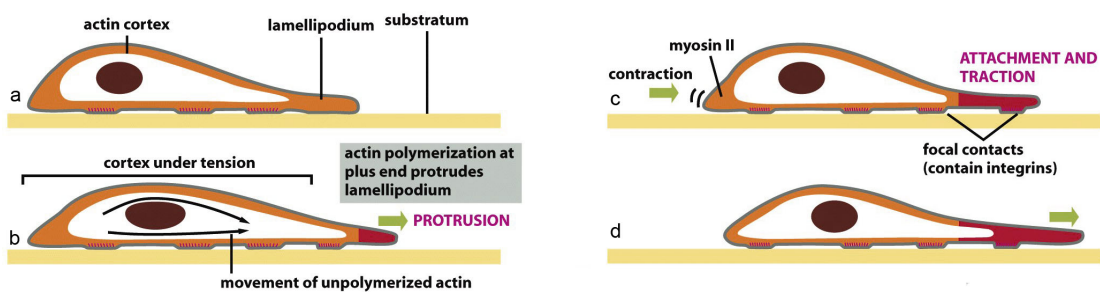


Figure 1.11: Schematic of Lamellipodium base motility. The lamellipodium grows at the leading edge of the cell and attach to a focal point. The actin cortex under tension contract and is capable to pull the rear of the cell. Adapted from [Alberts, Johnson, Lewis, et al. 2008].

cell when the membrane detach from the actin cytoskeleton underneath it, or when the cortex ruptures (Fig 1.12). The small protrusions are formed, quickly grow as they lack the force supporting layer that the actin cortex provides. While growing, the bleb fills with cytosol. The actin cortex can rapidly reform on the bleb slowing down its growth. In some cases, the reformation of the actin cortex in the bleb and the rebuilding of the tension inside the bleb by myosins mediated contraction is enough to reverse the bleb. Though, the content of the cell can also drain itself into the bleb as it grows and while the main body of the cell contract and empties, thus moving the cell from its old position to a new one in the direction of the initial growth of the bleb.

At their initial state, blebs are simple membrane protrusions filled with cytosol and empty of organelles. The stop of their growth is due to the spontaneous formation of an actin cortex on the inner side of the bare membrane.

By their relative simplicity to the rest of the cells, blebs are the perfect system to be reconstituted *in vitro* in liposomes.

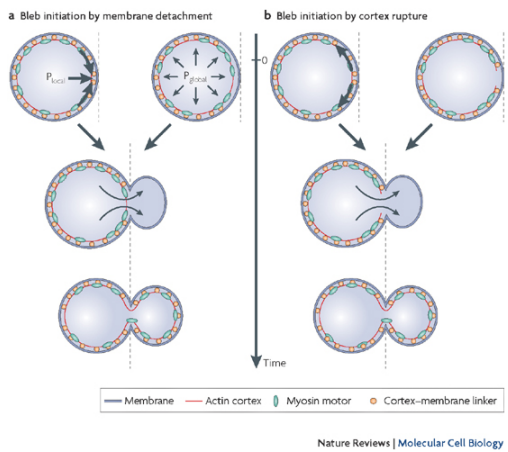


Figure 1.12: Formation of bleb can be done either by a) detachment of the membrane from the cytoskeleton, or b) by a rupture of the cytoskeleton. In both cases the inner pressure of the cell leads to the inflation of the membrane at the point of rupture/detachment. The acto-myosin cortex will rapidly re-polymerize on the inside of the bleb slowing down its growth until the expansion stops. Extracted from [Charras, Paluch, 2008]

1.4.4 Organelle Positioning

We have seen previously that organelle positioning plays an important role in cell function. Several mechanisms involving actin are at the origin of structure positioning in cells. The positioning of organelles by actin can have a wide impact from being necessary for the correct cell division, to allowing locust eyes to adapt in the dark by repositioning mitocondrion [Sturmer, Baumann, Walz, 1995].

We already know that the actin cortex is a necessary element in cell motility. It also plays a determinant role in organelle positioning. It has been shown [Chaigne, Campillo, Gov, et al. 2013] that the correct range of elasticity of the actin cortex during oocyte division is needed for proper spindle positioning. The correct spatial position of this spindle is necessary to perform a viable division of the cell.

The actin cortex is not the only actin structure in the cell, beyond the thin and dense layer just below the membrane lies a softer and sparser actin structure that has a crucial role in organelle positioning.

During cell division, there are several stages that require actin structures. As shown previously [Azoury, Lee, Georget, et al. 2011] the expulsion of polar body during oocyte asymmetric division is strongly dependent on the time evolution of a sparse actin network that can be found in the cell. Actin structures are also required at a later stage to permit the correct capture of chromosomes by microtubules and achieve correct haploid division. [Schuh, Ellenberg, 2008] also shows that a similar sparse actin network contracted by myosins is necessary for spindle migration.

Especially in oocyte that are typically large, the effect of gravity is not negligible. The presence of a sparse “actin scaffold” is discussed in [Feric, Brangwynne, 2013], where it is found that an actin network is present to balance the gravitational force.

In drosophila, nurses cell need to expel their content into oocytes. It has been observed [Huelsmann, Ylanne, Brown, 2013] that during this phase, the nurse cells’ nucleus is pushed away from the dumping canal by single actin filaments polymerising from the membrane and forming a soft and sparse actin network.

1.5 In vitro reconstituted actin networks

Living cells are complex organisms, for which each function requires a number of interacting proteins and components. To understand the action of each individual component it is necessary to isolate or modify their actions independently.

In order to achieve the precise tuning of each component independently, two approaches are envisageable. An approach referred to as “Top-Down” where starting from the full system — in our case the cell — we will modify or remove single or multiple components and study the global change of behavior. This is a complex process that might be difficult to interpret as biological systems have often multiple pathways and feedback loops to regulate each of their processes. With the large number of components that constitute a living cell, it is also difficult to come up with a minimal system necessary to replicate certain behavior.

The other approach, also referred to as the bottom-up approach, requires to reconstitute the system part by part until it replicates the expected behavior. This is also a complex process, as there is a large number of potential component that may be added to the reconstituted system. Often this vast complexity leads to a wide range of testable parameters. These controlled systems allow in principle for a deeper understanding of the governing working mechanisms, and often permit access to a wider range of accessible conditions and individual tweaking of components.

In our lab we are mainly interested in the bottom-up approach and the use of biomimetic systems. We try to reconstitute biologically relevant behavior within minimal systems, constituted from pure protein components.

In particular in this manuscript we are interested in mimicking the motility process by which the *listeria* pathogen is able to hijack cellular mechanisms by recruiting proteins responsible for actin polymerisation at the leading edge of the cell, and use these to polymerize actin on the pathogen surface. This is what allows ‘*listeria*’ to propel itself fast enough (1.5 to 2 μm /min) [Dabiri, Sanger, Portnoy, Southwick, 1990] to be able to penetrate the cell membrane to move from one cell to the other.

The bead motility system is a minimal *in-vitro* system capable of replicating the *listeria* motility.

1.5.1 Bead motility assay

The *Listeria* pathogen is a 1.5 to 5 micrometer cylindrical bacteria that enter cells, hijacks its actin polymerisation machinery to propel itself and infect neighbour cells. It does so by the recruitment of a single protein on its surface : ActA, that activates the Arp2/3 complex. By the recruitment of Arp2/3 a dense branched and entangle actin network grows that will eventually form a comet behind the bacteria propelling it at the speed of actin comet polymerisation. Listeria comets are composed of a wide range of protein, it has been shown [Loisel, Boujemaa, Pantaloni, Carlier, 1999] that the number of required components can be highly reduced, still maintaining the motility features.

A simpler system replicating the listeria motility is the bead motility assay, which consists of a micrometer-sized bead covered with a nucleation promoting factor (NPF) that will activate Arp2/3 that is present in solution. This NPF can be ActA as in the case of listeria, but one can use other NPF like N-WASp or pVCA. In the experiments presented in this work we use pVCA. The NPF covered bead is mixed with a G-Actin solution. Capping Protein is added to prevent polymerisation from happening away from the bead surface as well as the components necessary for actin polymerisation (ATP, Salt..., see *Material and methods* (page 37))

Due to the presence of Capping Protein in solution and NPF on the surface of the bead, the polymerisation of actin will happen only on the surface on the bead forming a thin and dense actin gel capable of sustaining stress depending on the different protein concentrations. Unlike in the case of listeria which seem to control on which of its sides the nucleation process happens, this is not controlled in bead motility assays. Though, in the right condition [Kawska, Carvalho, Manzi, et al. 2012] the dense actin gel formed on the bead surface can accumulate stress induce by polymerisation of inner layer until symmetry breaking occurs. The gels ruptures on one of the side of the bead, leading to the formation of a comet on the opposite side (Fig 1.13).

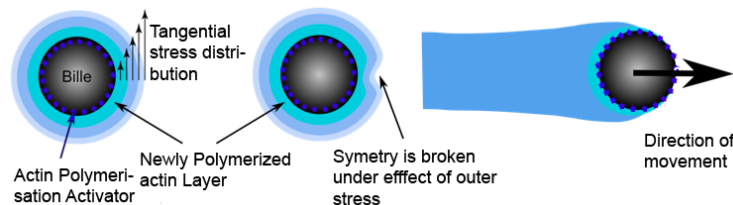


Figure 1.13: Scheme of bead motility assay. The NPF (yellow stars) will localize the actin polymerisation on the surface of the bead thus increasing stress on the outer actin layer. At a sufficient level of stress, the outer layer ruptures, leading to symmetry breaking, formation of a comet, and propulsion of the bead. Adapted from [Plastino, Sykes, 2005]

The further polymerisation of the actin network on the surface of the bead will make the comet grow, propelling the bead forward. This is what makes the bead system a biomimetic system replicating the listeria motion.

It should be noted that during the movement of this system, two phases can be distinguished. In the first phase, the system present a spherical symmetry with an homogeneous actin network around the bead. The gel is growing from the surface and is accumulating stress due to the polymerisation of inner layers.

If the gel had accumulated sufficient stress by polymerisation the symmetry breaking event happens, and the system enters in a second phase with the formation of a comet.

The condition that lead to symmetry breaking have been investigated in detail [Kawska, Carvalho, Manzi, et al. 2012]. In the absence of Capping Protein, the actin polymerisation seems not to be restricted enough near the surface of the bead, and the formed network is not able to generate or sustain enough stress to achieve symmetry breaking. At high Capping Protein concentration, the growth of the gel is heavily impaired, thus preventing symmetry breaking. The concentration of Arp2/3 is also critical as Arp2/3 forms branched networks, and these branched networks are primordial for the ability to sustain stress.

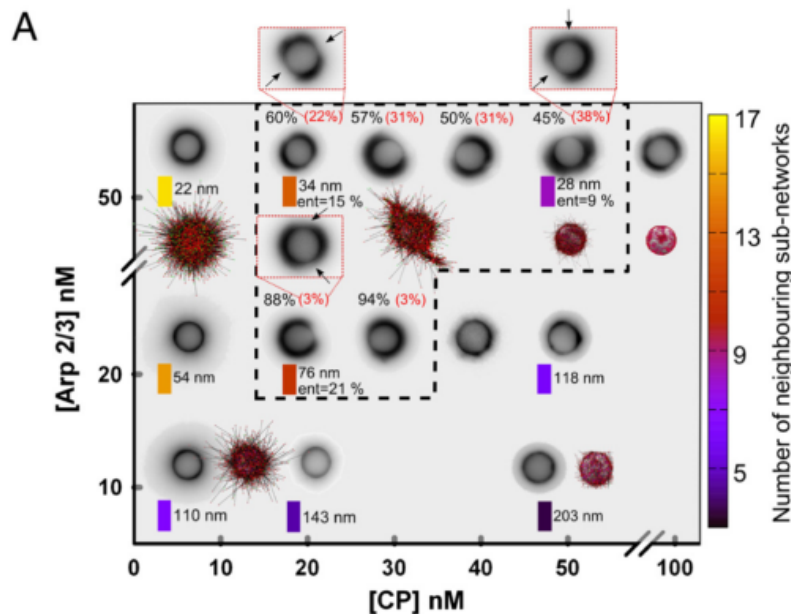


Figure 1.14: Phase diagram showing symmetry breaking in bead motility assay as a function of concentration of Arp2/3 and Capping Protein. Symmetry breaking only occurs inside the area delimited by the dashed line on 4.5 μm beads both *in vitro* and *in silico*. Experiments are displayed as inverted fluorescence image. Adapted from [Kawska, Carvalho, Manzi, et al. 2012]

In the rest of this chapter we use the bead motility system, but only consider it during the first phase, where the symmetry breaking has not yet occurred, or in condition where it should not occur. In particular we will investigate condition at 25 nM Arp2/3 and concentration of Capping Protein varying from 0 to 50 nM. As shown in fig 1.14 this range corresponds to conditions where no symmetry breaking occurs, but also to conditions in which symmetry breaking is expected. It should be noted that unlike other study that also characterize actin network growing on bead [Pujol, dRoure, Fermigier, Heuvingh, 2012], our system is still dynamically polymerising and thus changing with time.

1.5.2 Liposomes

Beads are used as model biomimetic system that replicates the polymerisation mechanism happening on the leading edge of cells. Because of their composition and rigidity, phenomenon observed on beads cannot necessarily reproduce all the interactions and processes that take place on the cell membrane. Cells are finite compartments with a limited amount of actin that act on the dynamics of polymerisation. The fact that cell size is in the order of the persistence length of actin filaments also plays a role on the structure of actin

networks. Indeed at these scales a single filament can never reach the length at which it can be considered fully flexible.

Liposomes are one of the biomimetic systems that are capable of capturing some interactions between cell membranes. Liposomes are lipid bilayers that imprison an aqueous compartment and exhibit many characteristics similar to cells. The inside of liposomes can act as a biochemical reactor of limited size with the lipid bilayer acting as a separation to the outside, like the cell membrane. The composition of the lipid layer can be varied in order to reflect the composition of cell membrane. In particular it is possible to attach proteins to the liposome membrane. Finally, the size of the liposomes can be varied, leading to actin networks of size and shape similar to those found in cells.

It is possible to mimic the cellular actin cortex using liposomes, and especially its contractility. A crosslinked actin network, can be formed and attached to the outer leaflet of liposomes, and contractility can be triggered by injecting molecular motors. The behavior of the system will depend on the attachment between the reconstituted actin cortex and liposome membrane. Weak attachment lead to a favorable rupture of the actin cortex during the increase of tension, implying a symmetry breaking as in the bead motility system. In the case of strong attachment, the liposome actin-cortex will accumulate tension until it has enough force to crush the supporting lipid layer, thus collapsing the liposome [Carvalho, Tsai, Lees, et al. 2013],(Fig 1.15). This system also allows the observation over time giving extra insight into the dynamics of the actin network (Fig 1.16).

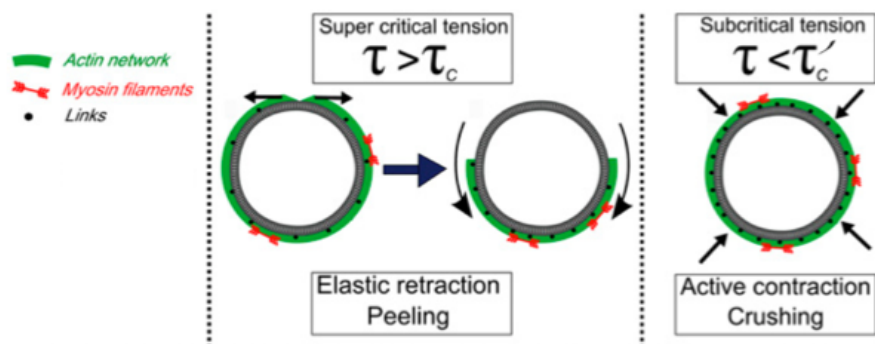


Figure 1.15: Effect of reconstituted rigid actin cortex attachment to a liposome membrane under constraints generated by myosin filaments. Under weak attachment the actin network ruptures thus leading to a “peeling” of the actin cortex. With stronger attachment the actin cortex can sustain higher stresses, until the underlying liposome ruptures (“Crushing”). Adapted from [Carvalho, Tsai, Lees, et al. 2013]

1.6 Membrane Physics

The cell’s plasma membrane is a biological membrane that separates the cell from its outside environment. It consists of a lipid bilayer containing a high numbers of proteins. A lipid bilayer is formed by two layers of lipids and have a thickness of a few nm. The classical theoretical description of these bilayers had been done by W. Helfrich [Helfrich, 1973] in 1973 in a model based on the elasticity and fluidity of lipid bilayers as well as the self assembly properties of lipids.

In the case of close lipid bilayer, the potential energy stored by the deformation of a lipid bilayer by unit

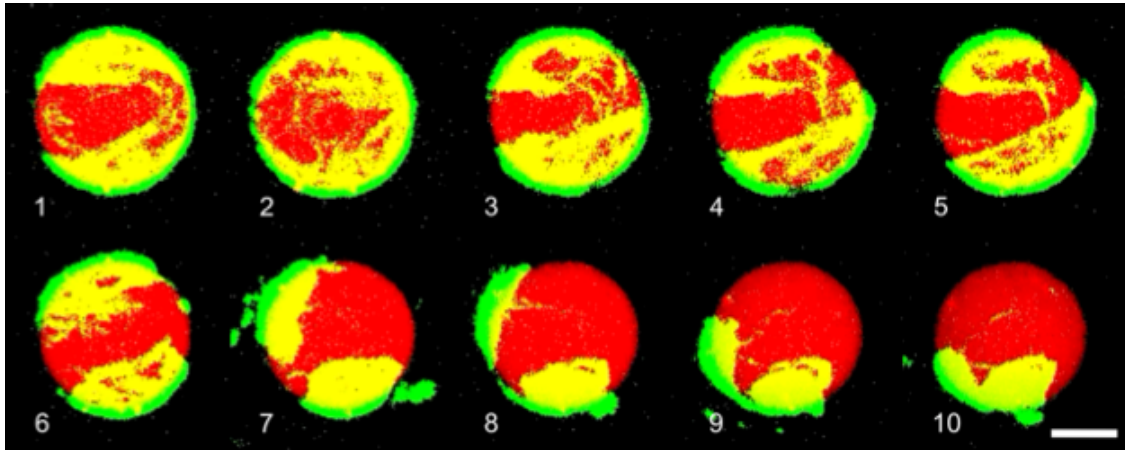


Figure 1.16: 3D reconstruction of an acto-myosin cortex (green actin) peeling off a liposome (red) over time (1.4 second between frames). The actin cortex contraction happened after the injection of Myosin II. Scale bar is 5 μm . Experiments and reconstruction done by Joël Lemière.

area can be written as

$$H = H_{ext} + H_{curv} \quad (1.3)$$

In which H_{ext} is due to the extension/compression of the membrane, and H_{curv} is due to the local curvature of the membrane.

The density of energy cost to extend the membrane H_{ext} can be written as a function of the elastic area compressibility modulus K_a and the relative variation surface of the membrane A :

$$H_{ext} = \frac{1}{2} K_a \left(\frac{\Delta A}{A} \right)^2 \quad (1.4)$$

K_a express how much energy is required to expand the surface of the lipid bilayer and is due to the exposition of more hydrophobic surface to water when expanding it. K_a is expressed in $J \cdot m^{-2}$, or N/m and is close to twice the surface tension between the lipids and water.

For closed lipid bilayers, the total curvature energy can be expressed as the sum of the curvature energy H_{curv} :

$$H_{curv} = \frac{1}{2} \kappa (c_1 + c_2 - c_0)^2 \quad (1.5)$$

In which κ is the bending modulus of the membrane and c_1, c_2 are the principal curvatures of the membrane. c_0 is the spontaneous curvature of the membrane, which is defined as the curvature the membrane would adopt when free of external constraints.

An important parameter which is introduced in membrane mechanics is the membrane tension σ which is the stress associated with an increase in membrane surface. The tension σ is linked to the energy required to expand the membrane H_{ext} by :

$$\sigma = \frac{\partial H}{\partial \left(\frac{\Delta A}{A} \right)} \quad (1.6)$$

i.e.

$$H_{ext} = \sigma \left(\frac{\Delta A}{A} \right) \quad (1.7)$$

In which

$$\sigma = K_a \left(\frac{\Delta A}{A} \right) \quad (1.8)$$

Membrane tension is a key parameter as it can be measured in cells, and is one of the parameters responsible for cell sorting [Maitre, Berthoumieux, Krens, et al. 2012]. In particular between cells, the tension of the couple (membrane+actin cortex) can be determined by using the contact angle between cell which is the angle between interfaces as defined in figure 1.17.

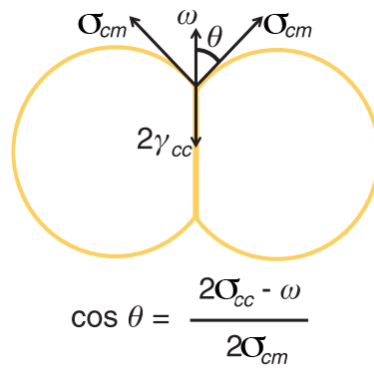


Figure 1.17: Surface tension govern doublet shape, adapted from [Maitre, Berthoumieux, Krens, et al. 2012]. The equilibrium of forces on the contact line govern the angle of contact 2θ . ω corresponds to the adhesion tension between the two cells, σ_{cm} correspond to the tension between the cell and the medium, σ_{cc} correspond to the cortex tension between the two cells.

In a later part, we use a reconstituted biomimetic system made of liposomes. The injection of myosin motors changes the tension of the acto-myosin cortex attached to a membrane. By determining the geometrical parameters of this system, and in particular the evolution of the contact angle with time, we are able to measure the variation of tension of the acto-myosin cortex due to contraction by molecular motors.

1.7 Actin networks as viscoelastic material

We have seen previously that while polymerising, G-actin assembles into F-actin filaments. The stiffness of filaments can be measured by a characteristic number called the persistence length (l_p). More precisely, the persistence length characterizes the average loss of correlation between the tangent along the considered polymer. With s the curvilinear abscissae along the polymer, and $\Theta_{(x,y)}$ the angle between the two tangent at two different abscissae (Fig 1.18):

$$\langle \Theta_{(s,s+l)} \rangle = \exp \left(\frac{-l}{l_p} \right) \quad (1.9)$$

For actin filaments, the persistence length is in the order of $10 \mu\text{m}$ [Isambert, Venier, Maggs, et al. 1995]. This means that for scales much smaller, the actin filament can be considered as rigid. This is the case in the cell cortex where the meshwork has a typical size smaller than 250 nm . In the other extreme, at length scale much bigger than l_p , filaments can be considered as flexible. While in typical cells, the filament length is rarely much bigger than the persistence length of actin, *Xenopus* eggs can be as big as 1 mm , so hundreds fold the actin persistence length. Still for the majority of cells, the typical size we are interested in is about the persistence length of an actin filament, making it neither purely rigid nor completely flexible.

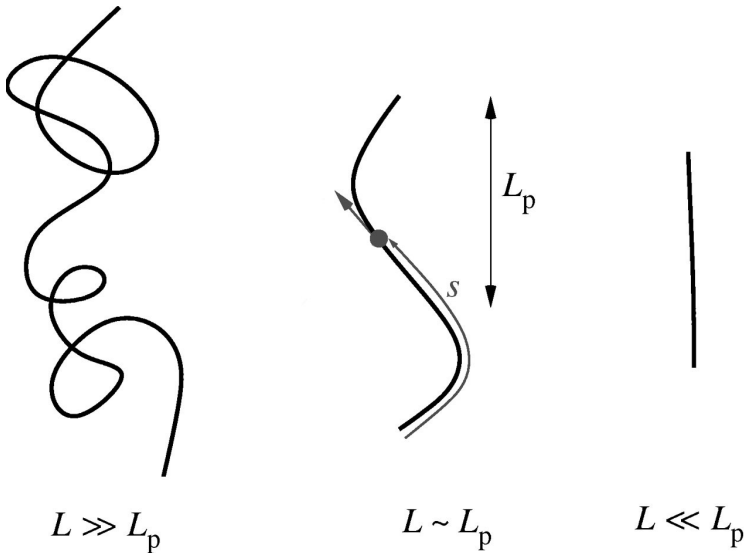


Figure 1.18: Schematic of polymers with length respectively big compared to the persistence length (A), in the order of the persistence length (B) and small compared to persistence length (C), s as defined on (B) is the *curvilinear abscissae*, that is to say the distance between two points of the polymer measured by “following” the polymer. Adapted from [Liverpool, 2006]

For the above reasons, actin solutions are often compared to semi-flexible polymers, and models that predict the behavior of actin networks often take foundation on polymers physics [Morse, 1998b] [Morse, 1998a]. Still, if these models rely on local microscopic parameters, experimental methods only have access to bulk properties of the studied material, and it is from these properties, and through the models that we can deduce possible values for the microscopic models [MacKintosh, Kas, Janmey, 1995].

1.7.1 Elastics Modulus

The elastics moduli are probably the easiest to understand. They are a characteristic of how a material will deform non-permanently under an applied force. The stiffer something is the higher its elastics moduli will be. There are two specific elastic moduli of interest in this manuscript, *Young's Modulus* and *shear modulus*. The first one describes how a material will react to compression or extension, while the second describes how a material resists shearing. For isotropic and homogeneous materials, the Young's modulus (E) and the shear models (G) are related by the Poisson ratio (ν):

$$G = \frac{E}{2(1 + \nu)} \quad (1.10)$$

Both G and E units are homogeneous to N/m^2 or Pa . It is instructive to have an idea of the order of magnitude of a few usual materials. Aluminum will have an elastic modulus $G_{Al} \simeq 70 \text{ GPa}$ while rubber will be more in the order of $G_{rubber} \simeq 0.1 \text{ GPa}$. The elastic modulus of muscle cell is in the order of $G_{muscle} \sim 10 \text{ kPa}$ and brain tissues around $G_{brain} \sim 0.1 \text{ to } 1 \text{ kPa}$ [Engler, Sen, Sweeney, Discher, 2006].

A more formal definition of the Young's modulus, is the ratio between the stress σ along the direction of the deformation and the relative deformation ϵ .

$$\begin{aligned} E &= \frac{\sigma}{\epsilon} \\ &= \frac{F/S}{\Delta L/L_0} \end{aligned} \quad (1.11)$$

In which F is the applied force, S is the cross section of the material, ΔL is the elongation and L_0 is the initial length of the considered material. (Figure 1.19 A):

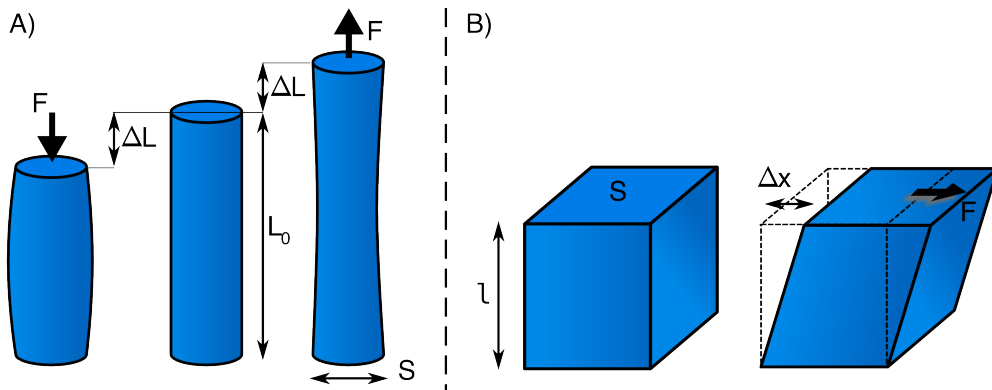


Figure 1.19: Schematic of the Young Modulus definition. F , force applied to sample, S surface of cross section when uncompressed, L_0 , length when no load applied. For both compression and extension, in the regime of small deformation, the relative change of length is proportional to the applied force. Here, the material can be seen to expand/contract in the direction orthogonal to the direction of application of the force, in the case of an incompressible material ($\nu \neq 0.5$) this can be seen as the conservation of volume of the material.

The shear modulus is defined for a deformation parallel to the surface on which it is applied :

$$\begin{aligned} G &= \frac{\tau_{xy}}{\gamma_{xy}} \\ &= \frac{F/S}{\Delta x/l} \end{aligned} \quad (1.12)$$

In which τ_{xy} is the shear stress, γ_{xy} is the shear strain, F is the applied force on the cross section of the material S . l is the thickness of the material and Δx is the transverse displacement (Fig 1.19 B).

Other characteristic numbers can also be defined, such as the bulk modulus. In the case of isotropic elastic materials, only two of those parameter are required to completely define the properties of the material.

1.7.2 Poisson Ratio

We have seen that the shear modulus is linked to the Young modulus using the Poisson ratio. The Poisson ratio is another characteristic of a material that defines how much a material will compress/expand in the

directions orthogonal to its elongation.

The Poisson ratio is the negative ratio of transverse to axial strain :

$$\nu = -\frac{d\epsilon_{trans}}{d\epsilon_{axial}} \quad (1.13)$$

In which ϵ_{axial} is the relative deformation along one of the axis of compression/elongation and ϵ_{trans} correspond to the relative deformation along an axis orthogonal to the axis of deformation.

Having volume conservation during compression or elongation require a Poisson ratio of 0.5. Such values have been found in bulk measurements of actin network at concentrations 21.5 μM of actin [Gardel, Valentine, Crocker, et al. 2003]. Materials with a Poisson ratio of 0.5 are said to be incompressible. A Poisson ratio lower 0.5 correspond to material expanding less than incompressible materials, some cell and tissues are known to have Poisson ratio lower than 0.5 [Mahaffy, Park, Gerde, et al. 2004]. Another critical value is 0, at which the material only expand or contract in the direction of the main stress.

Materials with a Poisson ratio superior to 0.5 would show a bigger deformation in the orthogonal direction than incompressible material, leading to a global increase of volume if compressed.

1.7.3 Viscosity

Like elasticity, viscosity is something tangible we are used to work with in everyday life. The more viscous a material is the more difficult it is to move something in it at high speed. And indeed, viscosity is the pendant of the elastic modulus but considering forces induced by the deformation rate instead of displacement.

$$\begin{aligned} \frac{F}{S} &= \tau_{xy} \\ &= \eta \frac{\partial v}{\partial z} \end{aligned} \quad (1.14)$$

In which τ_{xy} is the shear stress, F is the force exerted on the surface S . η is the viscosity, and is expressed in Pa.s , v is the deformation rate along the direction z .

At room temperature water has a viscosity of around 1 mPa.s, and honey of 10 Pa.s. The consideration of viscosity in problems will often depend on the timescale and deformation rate. At short timescale tissue often behaves elastic, whereas at long timescale the effect of viscosity will be seen [Thoumine, Ott, 1997]. In actin networks, the effect of viscosity at short time scale can be similar to elasticity [Gardel, Valentine, Crocker, et al. 2003].

1.7.4 Viscoelasticity

Typically, no material is purely elastic or purely viscous. While glaciers seem purely solid at the time scale of a few days, observation on longer time scale ranging from month to years show that ice is not only a solid but can also flow. Of course ice in its solid form is not the only material which is both solid and viscous. In order to describe such behavior one can use the theory of viscoelastic materials. A number of models have been and are still developed to describe viscoelastic behavior. The Kelvin-Voigt and Maxwell models are two of the simpler ones (Fig 1.20). A thought experiment to understand each of these model is to put a spring and a dash pot in parallel or series. Such model systems exhibit viscoelastic behavior.

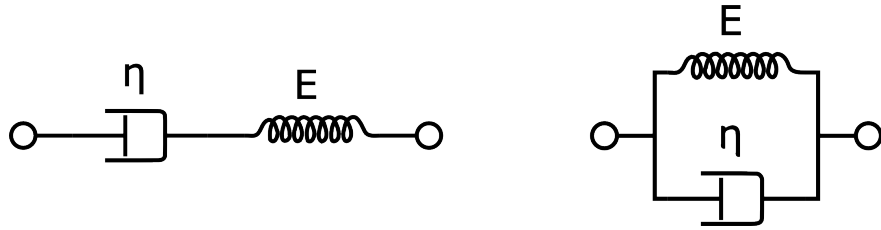


Figure 1.20: Maxwell model schematic on the left and Kelvin-Voigt model on the right. Both are simple approaches to express the properties of a viscoelastic solid. The response to a creep compliance will differ in both cases. The Maxwell model will mostly behave like a fluid with viscosity η after a long time, while the Kelvin-Voigt model will mostly reflect the elastic components at constant stress exerted. (Schematic in Public Domain, adapted from Wikimedia).

The idea for more complex models is similar, where any material can be seen like an (infinite) combination of springs (for elasticity), and dash-pots, (for viscosity).

Theory of viscoelastic materials explains the mechanical properties of a system by using a single function which is the viscoelasticity of a material. This can be done by describing E as a relaxation modulus depending on time. In the case of a linear system we can express the strain on the material at a given time as a function of its history :

$$\sigma(t) = \int_0^t E(t - \tau) \frac{du}{d\tau} d\tau \quad (1.15)$$

In which $\sigma(t)$ is the time dependent stress, and $u(t)$ is the known strain.

Using rheology, it is common to measure the properties of a material using a sinusoidal strain of known amplitude u_0 and frequency $f = \omega/2\pi$: $u(t) = u_0 \cos(\omega t)$, which also implies a sinusoidal strain rate. Using the complex notation $\dot{u} = u_0 i \omega e^{i\omega t}$ in equation (1.15), and operating the change of variable $t - \tau \rightarrow t'$ leads to :

$$\sigma(t) = u_0 \int_0^\infty E(t') i \omega e^{i\omega(t-t')} dt' \quad (1.16)$$

By factoring out the time dependent part, the rest can be rewritten as two integrals with respectively a real and imaginary prefactors :

$$\sigma(t) = u_0 e^{i\omega t} \times \left(\omega \int_0^\infty E(t') \sin(\omega t) dt' + i\omega \int_0^\infty E(t') \cos(\omega t) dt' \right) \quad (1.17)$$

The two integrals in brackets only depend on the pulsation ω and the properties of the considered material. They are both in factors of the complex strain $u(t) = u_0 e^{i\omega t}$. We thus define the storage modulus of the material as the real part of ((1.17) in bracket) E' :

$$E'(\omega) = \omega \int_0^\infty E(t') \sin(\omega t) dt' \quad (1.18)$$

And the loss modulus as the imaginary part of ((1.17) in bracket)

$$E''(\omega) = \omega \int_0^\infty E(t') \cos(\omega t) dt' \quad (1.19)$$

And define the complex frequency dependent Young's modulus as :

$$E^*(\omega) = E'(\omega) + i.E''(\omega) \quad (1.20)$$

Thus we can write (1.17) as :

$$\sigma(t) = E^*(\omega).u(t) \quad (1.21)$$

In this representation of $E^*(\omega)$, the real part will correspond to the elastic response of the material (in-phase response under oscillatory strain) and the imaginary part corresponds to the viscous response of the system (out of phase under sinusoidal strain). The complete knowledge of $E^*(\omega)$ at all frequency completely characterizes the material.

Models for actin networks have been extensively studied as viscoelastic material both theoretically [Morse, 1998a], [Kruse, Joanny, Julicher, et al. 2005] , and experimentally [Mizuno, Tardin, Schmidt, Mackintosh, 2007]. Actin networks have also been shown to exhibit linear characteristic behavior, but also and non-linear behaviour in a certain concentration ranges has been observed [Yao, Becker, Broedersz, et al. 2011], [Gardel, Valentine, Crocker, et al. 2003].

The actin networks we will study hereafter are in the condition where linear behavior is expected, thus we will use the viscoelastic theory to interpret the relation stress/strain observed in order to determine the mechanical properties of the formed actin gels.

1.8 Optical tweezer

Optical tweezers, or optical traps are a technique that allows to trap objects near the focal plane of a microscope at the focal point of a high power laser. It is a versatile technique that allows to trap both fabricated objects and part of living cell. Optical traps typically allow to apply forces up to a few tenth of pico Newton.

To understand that light can trap an object, it is instructive to keep in mind that despite having no mass, photons carry momentum, and as for any massive object, changing the trajectory requires a force. According to Newton's third law, when applying a force via a photon on an object, the object will in turn exert the opposite force on the photon, thus changing the trajectory of the photon. If a photon changes trajectory in a material, the material has to apply a force on the photon (Fig 1.21), meaning that the photon also applies a force on the material. In particular, the higher the refractive index of a material, the more light beams are deviated, and hence the more photons apply forces on material.

In particular, it can be shown that objects with a higher refractive index than the surrounding medium are attracted towards higher light intensities (Fig 1.21). In parallel laser beams, with a Gaussian intensity profile, this will lead to the object being attracted towards the center of the beam.

In addition to the lateral trapping, the laser focus leads to another intensity gradient along the direction of propagation of the beam, the intensity being at its maximum at the laser waist.

A laser coupled into a microscope objective then acts as a three dimensional potential that traps particles similar to a tweezer. Usually the trapping in parallel to the direction of the laser is only about half as strong if compared to the trapping in the lateral direction.

One of the qualities of optical traps is that in principle, multiple traps can be obtained. A simple method to generate two traps is to split the incoming light into two orthogonally polarized independent beams. Instead of sharing the laser power between the different traps by using polarisation, one can use what is known as

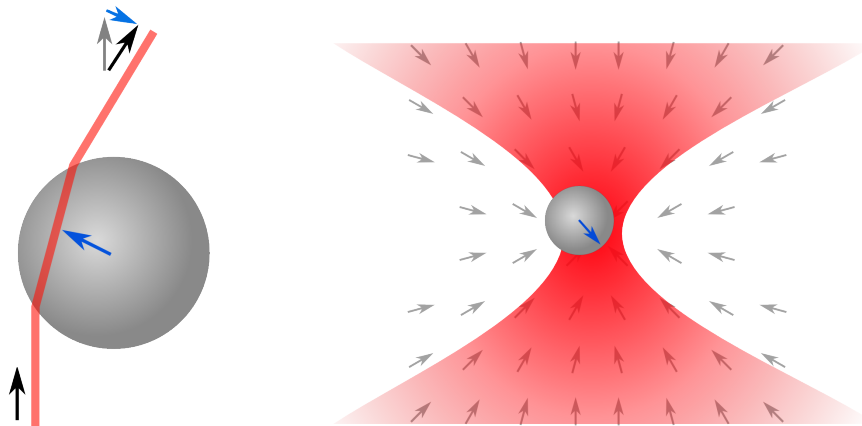


Figure 1.21: Light deflected by a transparent bead changes the momentum of light, so the light is exerting a force on the bead. The bead will be attracted towards the highest intensity. For a focused laser beam, the bead will be attracted near the focus of the laser.

multiplexing by time sharing. This is achieved by switching the laser rapidly between different positions at a speed much faster than the diffusion of the particle. By this method it is possible to virtually achieve multiple traps on the same sample.

In this work we use a multiplexed system, where the rapid switching is achieved using Accousto Optic Deflectors (aka AODs). An AOD consists of a crystal in which a high frequency sound-wave propagates perpendicular to the incoming laser beam. This sound-wave generates local changes in the refractive index of the material which act as a diffraction grating. In the right conditions, a laser passing through the crystal will be deflected by this grating under the Bragg angle.

In practice, rapidly controlling the frequency and amplitude of the sound wave in the crystal, allows direct adjustment of laser deflection and hence the trap position. Using AODs also has the advantage of controlling not only of the number and position of multiple traps, but also the individual power allocated to each trap and hence the stiffness of each trap.

A schematic of the optical setup that can be used to trap beads in the focal plane on the microscope can be found in [figure 1.22](#). The scheme also contains the detection part of the setup that is used to measure the force exerted on each bead, technique which is explained on following part.

1.8.1 Determination of trapping forces and bead displacement

In addition to allowing the objects to be hold in place, the use of a QDP (Quadrant Photo Diode, a precise position detector) with optical traps has the advantaged to acquire high frequency quantitative measurement of the displacement and force exerted on an object. Indeed, when the trapped particle is not in the trap center, the laser applies a force on the object. Reciprocally, the object applies the opposite force on the light beam, thus deflecting the light beam. Using optics and lenses correctly placed on the Fourier plane of the sample, it is hence possible to translate this change of orientation of the light beam into a displacement of a light spot onto a photo detector with hight sensitivity to applied forces.

Through careful calibration of the trap, that give the force/displacement relationship, [\[Jahnel, Behrndt, Jan-nasch, et al. 2011\]](#), [\[Vermeulen, vMameren, Stienen, et al. 2006\]](#), one can then also recover the displacement of the sample inside the optical trap.

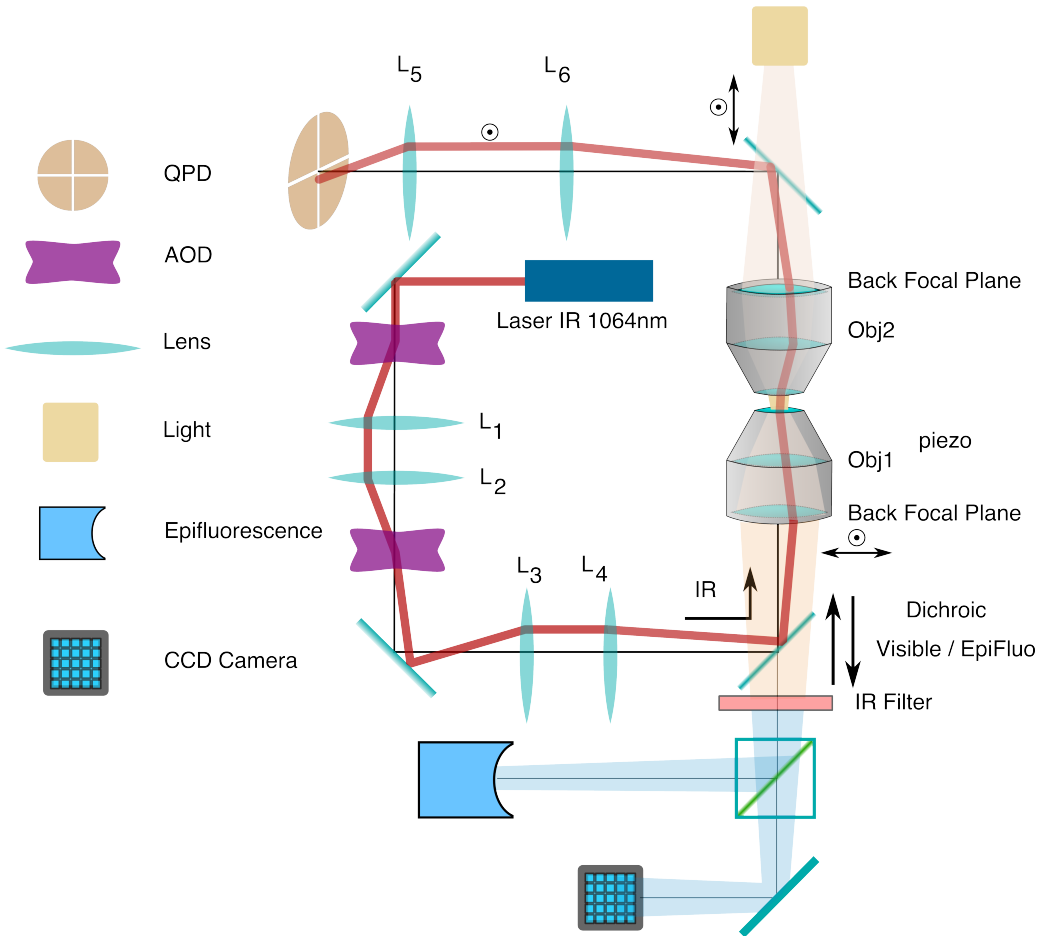


Figure 1.22: A schematic of setup used. The following elements can be distinguished. An 1064nm laser is used for trapping. It first passes through two AODs that move the position of the trap in the X and Y direction. The first couple of lenses (L₁,L₂) between AODs assure that AODs are in conjugated planes. The second pair of lens (L₃,L₄) image the AODs plane in back-focal plane of the first objective. Thus a change of angle of the light beam induce by the AOD result in a change of position of the trap. The trapping light is collected by a second objective, and illuminates a quadrant photodiode (QPD) conjugated to the back focal plane of the collecting objective. By construction QPD and AODs should be conjugated, so deviation of the light beam induced by one of the AODs is not supposed to induce any change of position of the laser spot on the QPD. Additional dichroics mirrors allow to use bright field and epifluorescence simultaneously optical tweezer.

Using optical tweezer to not only hold a particle in position, but also to get quantitative measurement of its displacement and the force exerted require to calibrated each probe particle. Polystyrene beads are common artificial probes used to achieve such a goal.

The use of polystyrene bead has multiple advantages. First, one can obtain mono-dispersed beads leading to reproducible and predictable trap stiffness. Secondly, theory can predict the shape of the potential felt by such a bead in a Gaussian beam [Nieminien, Knorer, Heckenberg, RubinszteinDunlop, 2007].

The third advantage is that beads can be functionalized, allowing specific interaction to be controlled, both *in vitro* and *in vivo*. Of course, the calibration is essential for the correct measurement of mechanical property of different system, and the choice of the bead diameter have impact both on biological side and in the physics of the measurement.

CHAPTER
TWO

MATERIALS AND METHODS

2.1 Buffers

2.1.1 G-Buffer

G-Buffer is used to conserve actin in the monomeric form. Actin is diluted in G-Buffer and kept on ice for at least 12 hours before further use. G-buffer is aliquoted and stored at -20°C. For weekly use or is thawed and conserved on ice for up to a week. G-buffer is never refrozen. pH is adjusted between 7 and 8.

Composition of G-Buffer:

- 0.2 mM $CaCl_2$
- 0.5 mM DTT (Dithiothreitol, or (2S,3S)-1,4-bis(sulfanyl)butane-2,3-diol)
- 2.0 mM Tris (tris(hydroxymethyl)aminomethane or 2-Amino-2-hydroxymethyl-propan)
- 0.2 μ M ATP (Adenosine triphosphate)

2.1.2 Polymerisation Buffer

Polymerisation buffer or X-Buffer is used for polymerisation of actin gels on beads as well as bead dilution and cleaning buffer. It is aliquoted and conserved at -20°C. During experiments it is stored on ice for up to a week. X-Buffer is never refrozen.

Composition of X-Buffer :

- 10 mM Hepes (2-[4-(2-hydroxyethyl)piperazin-1-yl]ethanesulfonic acid)
- 0.1 M KCl
- 1 mM $MgCl_2$
- 1 mM ATP (Adenosine triphosphate)
- 0.1 mM $CaCl_2$

2.1.3 X-Buffer with BSA

Same as X-Buffer with the addition of 1% BSA (10 mg/ml). BSA is used to prevent non specific adsorption. X-BSA buffer is used in place of X-Buffer for the conservation of the probe beads.

2.1.4 ATP-Mix Buffer

ATP-Mix buffer or simply *Mix* contains the ATP necessary for actin polymerisation. It is aliquoted and stored at -20°C. Kept on ice for weekly use. pH is adjusted between 7.5 and 8.0.

- 12.0 mM ATP,
- 20,0 mM DDT
- 0.88 mM Dabco
- 24.0 mM $MgCl_2$

2.2 Protein preparation

2.2.1 pWA (also called pVCA)

pWA is use as a nucleation promoting factor. It is expressed from Human pVCA (verprolin homology central and acidic domain) and expressed into Rosetta 2(DE3) pLysS (Novagen) Cell. Purified pWA is aliquoted and conserved at -80°C, never refrozen, and conserved on ice for daily use.

2.2.2 Actin

Actin and biotinylated actin are purchased from Cytoskeleton (Denver, CO, USA), and stored at -80°C. Fluorescent Alexa-488 actin is obtained from Molecular Probes, stored at -80°C, and prepared according to manufacturer recommendation.

Actin is stored in aliquots of 5 μ L at a concentration of ~238 μ M, and fluorescent actin in aliquots of 3 μ L with a concentration of ~106 μ M.

G-actin with 20% fluorescently labeled actin monomers is prepared the day before the experiment by mixing 1 aliquot of actin with 1 aliquot of fluorescently labeled actin and diluting the mix with G-Buffer until desired the concentration is reached.

2.2.3 Profilin

Human profilin is expressed by competent cells and purified in our laboratory as described in [Carvalho, Lemiere, Faqir, et al. 2013]. Profilin is conserved at 4°C for a few month and keep on ice for daily use.

2.2.4 Arp2/3

Bovine Arp2/3 complex from Bovine is purchased from Cytoskeleton prepared as recommended by the manufacturer, aliquoted at 1 μ M and conserved at -80°C. Aliquots are never refrozen and stored on ice for weekly used.

2.2.5 Capping protein

Mouse capping protein (CP; a1/b2) is purified as previously described in [Soeno, Abe, Kimura, et al. 1998]. CP was a gift from Laurent Blanchoin.

2.2.6 Myosin II

Myosin II is purified from rabbit skeletal muscle, and fluorescent myosin II is prepared as previously described in [SoareseSilva, Depken, Stuhrmann, et al. 2011]. Functionality of Myosin II is confirmed by motility assays. Gliding speed shows an average of 4.5 + 1.5 μ m/s (N = 27).

The working buffer for Myosin contains

- 25 mM imidazole
- 50 mM KCl
- 70 mM sucrose
- 1mM Tris
- 2 mM $MgCl_2$
- 1 mM ATP
- 0.1 mM DTT
- 0.02 mg/ml β -casein,

then adjusted to a pH of 7.4. In the working buffer myosin II forms minifilaments of approximately 0.7 μ m length which correspond to about 100 motors.

2.3 Lipids, reagent and proteins

Chemicals are purchased from Sigma Aldrich (St-Louis, Mo, USA) unless stated otherwise. EPC (1- α -phosphatidylcholine) and *1,2-distearoyl-sn-glycero-3-phosphoethanolamine-N-[biotinyl polyethylene glycol 2000]* (biotinylated lipids), *1,2-dioleoyl-sn-glycero-3-phosphocholine* are purchased from Avanti polar lipids (Alabaster, USA). Monomeric actin containing 10% or 20% of labeled Alexa-488 actin and 0.25 % of biotinylated actin is diluted in G-Buffer

2.4 Doublet preparation

Cell-sized liposomes are formed by electro formation [Angelova, Dimitrov, 1986]. 20 µL mix of EPC lipids and PEG-biotin lipids (present at 0.1 %, mol) with a concentration of 2.5 mg/ml in chloroform/methanol 5:3 are deposited on glass plates coated with ITO. Glass is then dried with nitrogen; placed under vacuum for 2 hours.

A chamber is formed using the ITO plates with their conductive sides facing inside, then filled with sucrose buffer (200mM sucrose, 2mM Tris adjusted at pH 7.4). Chamber is sealed with hematocrit paste (Vitrex medical, Denmark).

An alternate current voltage of 1V at 10 Hz is applied between the ITO-coated surfaces for 75minutes to form liposomes.

The same preparation is done a second time by adding 0.9µm sulphorhodamin to the sucrose buffer in order to mark liposomes inside buffer fluorescently.

The two solution are mixed in order to have the inside buffer of half the liposome marked in red and being able to distinguish the interfaced in some of the formed doublets.

Formed liposomes are incubated 15 minutes with 160 nM streptavidin in order to coat them with streptavidin. Liposomes coated with streptavidin tend to aggregates. The solution containing doublets is then diluted 30 times. Waiting 15 minutes increase the ratio doublets/single liposome by still avoiding aggregates of more liposome.

A bulk solution of 40 µM actin monomers — 10% fluo and 0.25% biotinylated — is diluted 40 times in working buffer (25 mM imidazole, 50 mM KCl, 70 mM sucrose, 1mM Tris, 2 mM $MgCl_2$, 1 mM ATP, 0.1 mM DTT, 0.02 mg/ml β -casein, adjusted at a pH 7.4) and polymerized for one hour. The adjunction of 1 µm of phalloidin after 1 hour prevent further depolymerisation

Actin filaments are diluted to 0.1 µM (10x), mixed with streptavidin-coated doublets of liposomes, and incubated for 15 min. The mix is diluted 5 times to reduce fluorescent background form actin monomers in solution.

2.5 Bead Preparation

Carboxylated polystyrene beads (Polysciences, Philadelphia, PA) of $4.34 \pm 0.239 \mu\text{m}$ (Standard deviation) diameter were used as actin-bead and probe-beads.

Beads are stored at 4°C.

Before coating by BSA (probe bead) or pWA (actin-bead), bead solution is cleaned by centrifugation at 5000 rpm, 2min. Supernatant is removed, and pellet is resuspended in X-Buffer. This procedure is repeated twice.

2.5.1 Actin-Bead Preparation

Cleaned polystyrene beads are incubated for 20 min at 20°C under agitation with 2 µM pVCA. Centrifuged at 5000rpm 2min, supernatant is removed and pellet diluted 4 times in X-buffer. The beads are stored on ice for the day.

2.5.2 Probe Bead Preparation

Cleaned polystyrene beads are incubated under agitation with 10 mg/ml BSA at room temperature for 30 minutes. Passivated beads are then centrifuged, separated from supernatant, and the pellet is resuspended in X-BSA buffer and stored at 4°C for weekly use.

2.6 Force indentation experiments

2.6.1 Preparation of sample

Equal amount of each actin and probe beads are placed in the polymerization mix consisting of :

- 2 μ L BSA at 10%
- 3 μ L of ATP-Mix Buffer
- 1.5 μ L Profilin (114 μ M)
- 1 μ L beads (50% actin-bead 50% probe bead)
- 0.5 μ L Arp2/3 (22,3 μ M)
- between 0 and 2 μ L CP (0.5 μ M)
- Completed to 15 μ L using X-Buffer.

5 μ L of G-Actin (20% fluorescent) is then added to the previous mix. This moment marks the time $t=0$ for the experiment and recording. The experimental chamber is built by 2 coverslips that are separated by VaLaP. VaLaP is a mix of vaseline (33%) Lanoline (33%) and Parafine(33%) in equal mass proportion. The chamber is prepared by gently depositing 20 μ L of the final beads mix at the center of the lower coverslip and 4 drops of VaLaP are deposited at the position where the corner of the upper (18x18mm) coverslip will rest. The VaLaP acts as a spacer and prevents the sample to be squashed. The upper coverslip is then placed on top of the sample and the chamber is sealed using VaLaP.

2.6.2 QPD positioning and calibration of microscope

The prepared sample is placed on the microscope and a drop of water is deposited on top of the upper coverslip to assure immersion of the light collecting objective. The collecting objective and the quadrant photodiode are placed on top of the sample (*Optical tweezers* (page 32)).

The trapping laser is then aligned with the photodiode while verifying that no object is trapped during the process. The conjugation of the back focal plane of the objective with the AODs and the QPD is optimized by adjusting the distance of both objectives with respect to the sample.

A trapping laser is positioned near the center of the microscope field of view using the custom written LabView program (Fig 2.1). The QPD is adjusted in X and Y direction to $\Delta X = \Delta Y = 0V$. This is done while no object trapped in the laser focus.

2.6.3 Initial bead trapping

Two maximum strength trap (~50mW/trap) are created near the center of the microscope field of view, separated by 15 to 20 μm . The sample plane is then moved in the Z-direction by displacing the 3D piezo controlled sample stage to position the traps near the middle plane of the chamber. Temporarily removing the Infra Red filter from the microscope allows to see the reflection of the trapping lasers on the upper and lower coverslip and to determine the localisation of the middle plane of the observation chamber.

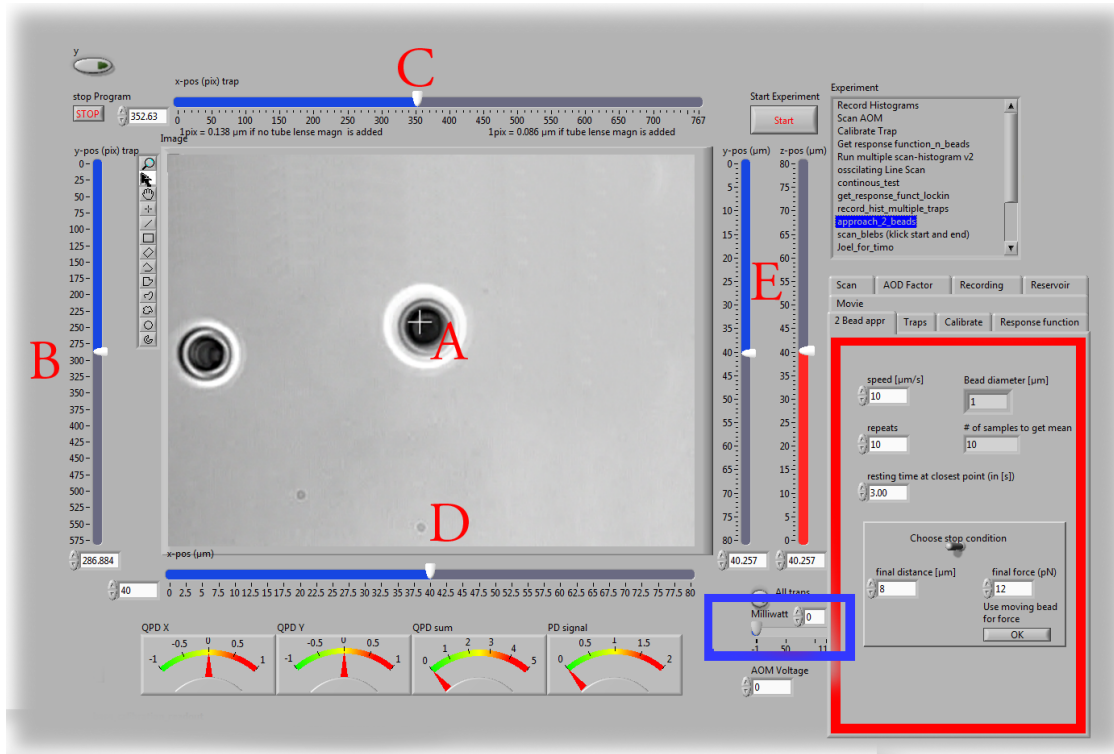


Figure 2.1: Software interface responsible for controlling the optical tweezer. Sample image showing 2 polystyrene beads and a single trap (A, white cross) holding one bead. Cursors (B,C) are available to displace the optical trap(s). Cursors can control the position of the stage in X (D), Y (E, blue) and Z (E, red). The blue rectangle highlights the slider that allows to control the trap power. The red rectangle highlights the area where the different parameters of the experiment can be set (approach speed, resting time at closest point). 3 indicators at the bottom of the screen indicate the voltage on the QPD.

The operator then captures one probe-bead and one actin-bead in each of the traps. Both types of beads can be recognized using fluorescent microscopy, as actin-beads are promptly covered with a fluorescent actin which can clearly be distinguished from the probe bead that remains dark. In the case where two identical beads are trapped one of the two traps can selectively be disabled or decreased in stiffness, letting the bead escape from the trap, and the procedure can be repeated.

The operator will then move the two traps roughly one micrometer in each direction to check that the two beads are effectively trapped in the tweezer and that no external forces act on the beads.

For practical reasons, the traps are aligned along one of the principles axis of the AOD before starting the indentation experiments.

2.6.4 Indentations

The operator sets the parameters of the experiment in the software:

- Average bead radius,
- Approach/Retraction Speed.
- Resting Time
- Laser Power

For each pair of actin/probe bead, the initial minimum approach distance of the traps is set to 5 to 8 μm before a single indentation cycle is done. If the maximum measured force between the two beads is not higher than 8 to 10 pN, the minimum approach distance is reduced by 0.25 to 1 μm and the procedure repeated. Once the maximum force measured is in the 10-15pN range the right distance is found and up to 10 automatic force-indentation experiments are performed (Fig 2.2). Before each indentation the software automatically does a “scan” of each bead to ensure correct calibration. An indentation cycle has the following step:

- Probe trap is approaching the actin-bead at constant speed until the minimal approach distance has been reached.
- At the minimal distance the traps remain stationary for the predefined (typical 3 seconds) resting time.
- Probe trap returns to its initial position at constant speed.
- Cycle is repeated as many times as set.

During this cycle the deflection of the laser induced by the probe-bead and actin-bead are recorded by the QPD.

After an indentation cycle is finished the experimenter can try to perform the indentation on the actin-bead from another direction, or release the actin-bead proceeding to a new one.

In the case where the indented actin network shows signs of inhomogeneity or symmetry breaking, the experiments are stopped and not taken into account for further analysis.

The date and time of each indentation cycle is recorded to extract the time of polymerisation for each sample.

2.7 Time Shared Optical Traps

The optical trap is built on an inverted microscope (Olympus, IX71) equipped with a fluorescence (200W mercury lamp, Osram, Munich, Germany). The sample is observed through a Olympus 60X water immersion objective (Olympus) with numerical aperture NA=1.2, that also serves as entry point for the laser of the optical tweezer. The light source is an infrared fiber laser ($\lambda = 1064\text{nm}$, YLP-1-1064, IPG, Germany). X, Y positioning and stiffness of the trapping force are controlled by 2 Acousto Optic Deflectors (AODs, AA-Optoelectronics, France) that are placed in the conjugated plane of the back focal plane of the objective. Multiple traps can be achieved by switching the laser between multiple positions within a switching time in the order of 5 μs , and resting on each position 20 μs or more.

Light refracted by the trapped sample is collected by a 40X (N.A:0.9, Olympus) water immersion objective and imaged on a quadrant photodiode (QPD) conjugated with the back focal plane of the light collection

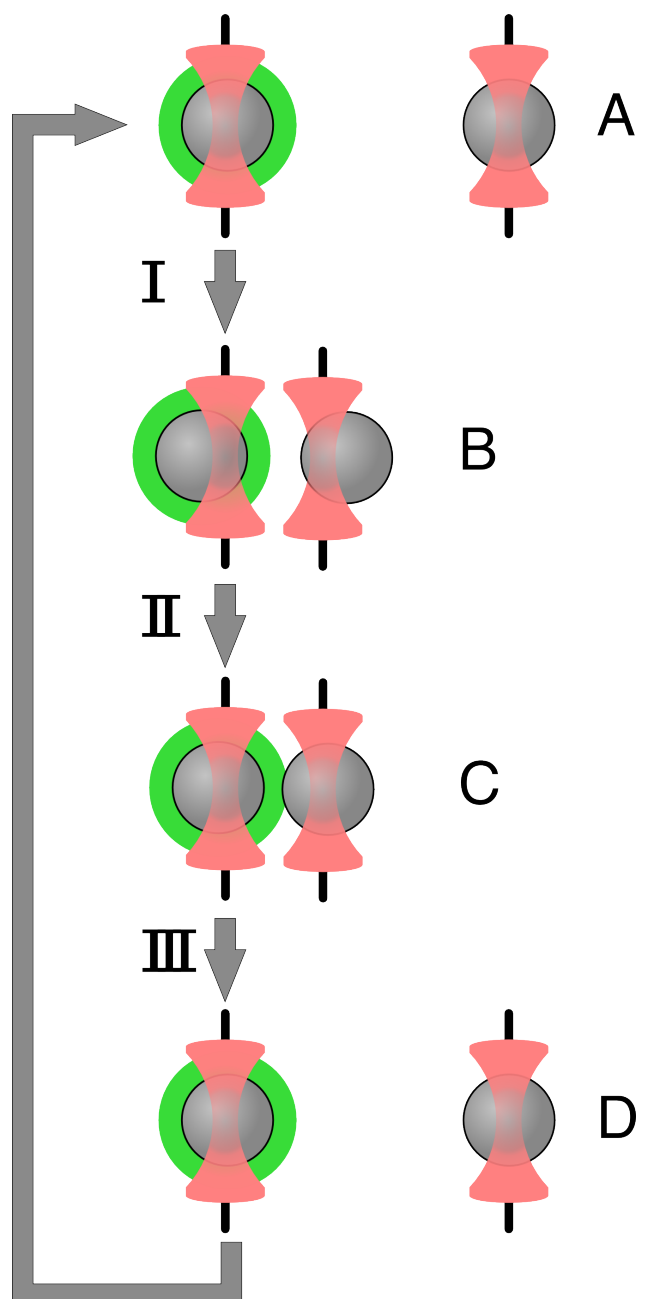


Figure 2.2: Schematic of indentation experiment. On the left is the actin-bead, covered with actin, in the static trap, on the right the probe-bead in the mobile trap. At the beginning of the experiment (A) the probe bead is situated far from the actin-bead. During the approach phase (I) the moving trap approaches the static trap at $10\mu\text{m/sec}$ until it reaches the minimal approach distance (B). The moving trap stays at the minimal approach distance for 3sec (II), which constitute the relaxation phase.C) The actin gel are relaxed, the distance between bead is smaller than on B. III) the moving trap retract at $10\mu\text{m/sec}$ back to its initial position.

objective. Signals from the QPD (ΔX , ΔY and Σ) are sampled at 500kHz, by a Digital To Analogic Aquisition card (NI PCIe-6363, National Instruments, Austin, Texas), controlled using a custom written Labview software (National Instruments) coupled with Matlab (Mathworks, Natick, MA). Raw signals are preprocessed by binning all voltage measured during the time the laser rest (typically 20 μ s) at one position. Finally the mean and standard deviation for each trap visit is stored for further processing.

The trap stiffness is inferred from bead radius, laser power, number of present traps and control experiment data. In control experiments the trap stiffness is calibrated using the power spectral density method, and was determined to be as high as 80 pN/ μ m at full laser power (119mW) for a single trap. In the case of multiplexing two traps as used in this work, both traps were calibrated before the experiment. Coarse positioning of the sample is done through a pair of micrometer precision screws capable of translating the microscope stage in X and Y. Finer positioning in X,Y and Z direction are done with the help of a 3D piezo stage with an accessible range of 80 μ m in each direction and a sub-micrometer accuracy.

2.8 Oocyte

2.8.1 Oocyte obtention

Oocyte culture, collection and micro injection where done at College de France by Maria Almonacid.

Oocytes were collected from 11 to 15 week old mice (WT), fmn2-/- as previously described in [Holubcova, Howard, Schuh, 2013] and maintained in Prophase I in M2+BSA supplemented with 1 μ M Milrinone. Oocyte are then injected with cRNA using a micro-injector Eppendorf FemtoJet. Imaging was carried out at 37°C.

MECHANICAL PROPERTIES OF A FAR REACHING ACTIN CLOUD

3.1 Introduction

We have seen that the actin cytoskeleton plays a major role in cellular mechanics. It is necessary for force generation, and a key component for cell motility. It has also been extensively studied both in cells and biomimetic systems.

Actin can form a variety of networks in cells, ranging from dense branched networks at the leading edge of the lamellipodia to bundled parallel structures forming the filopodia. Reconstruction of the actin network has been achieved in biomimetic systems using purified components [Plastino, Sykes, 2005], [Loisel, Boujemaa, Pantaloni, Carlier, 1999], [BernheimGroswasser, Wiesner, Golsteyn, et al. 2002], [Pontani, vdGucht, Salbreux, et al. 2009], and many properties of these networks have been measured.

It has been determined that the actin cortex provides mechanical support for the plasma membrane and that it extends over a few hundreds of nanometers. Many cellular processes hint for actin structures connected to this cortex to be key elements in organelle and chromosome positioning.

In this part of the manuscript we investigate how a sparse actin structure can emanate from the actin cortex, and we explore its properties. Using the *bead-motility* (page 23) biomimetic system to reconstitute the actin cortex and its dendritic structure, we show that a sparse network of actin filaments emanating from the cortex has a mechanical effect sufficient to displace objects on the size of cells organelles at distances up to tens of micrometers away from the actin cortex.

The branched structure of the actin cortex underneath the plasma membrane of cells hints for a structure governed by Arp2/3. How Arp2/3 and CP can be used to form a biomimetic actin cortex has been widely studied. In [Kawska, Carvalho, Manzi, et al. 2012], both *in vitro* measurements on reconstituted actin cortices on beads as well as simulations investigate the effect of cross-linking and Capping Protein on the formed actin gel. It can be seen both experimentally and in simulation that a network of filaments escape from what is defined as the actin cortex (Fig 3.1). The effect of these long filaments is not taken into account in the *in-silico* system where the analysis is restricted to filaments shorter than 10 μm . Only the effect of dense entangled actin networks generated from primers randomly placed on the bead surface participate in the increase of tension and contribute to symmetry breaking.

The limit of the dense network visible in epifluorescence is defined in [Kawska, Carvalho, Manzi, et al. 2012] by the position of the half-maximum fluorescent intensity (Fig 3.2). The properties of these networks are measured by [Pujol, dRoure, Fermigier, Heuvingh, 2012] using magnetic beads and actin stabilized with phalloidin. Though they do not investigate the sparse and softer actin network that originate from the visible part.

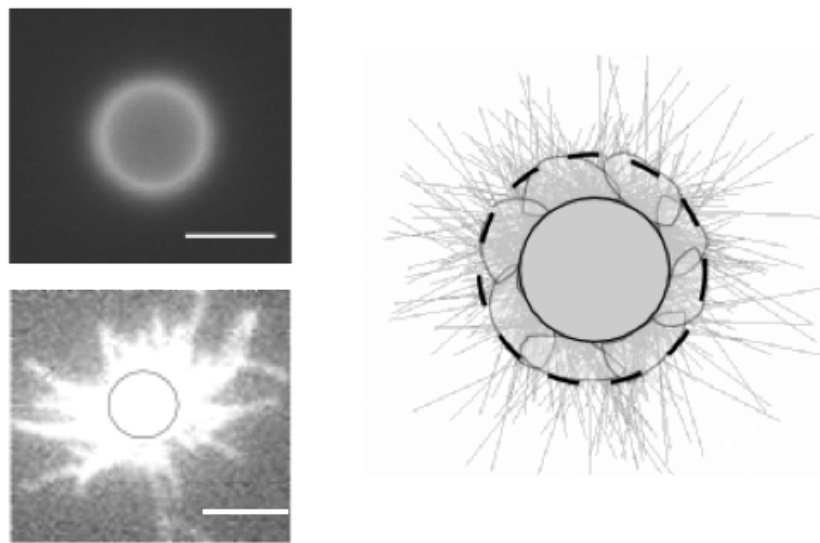


Figure 3.1: Upper Left : Fluorescence image of an actin bead with a growing actin cortex. Escaping filaments form the actin cloud that can only hardly be seen in fluorescence. Scale bar is $2 \mu\text{m}$. Lower Left: Total Internal Reflexion (TIRF) image of actin polymerising on an actin bead. Escaping filaments are directly visible. The gray circle represents the size of the bead. Right : Representation of the actin growth simulation with delimitation between the entangled branched actin network and escaping filaments. Adapted from [Kawska, Carvalho, Manzi, et al. 2012].

Using *time-shared optical tweezer* (page 43) we are able to probe the mechanics of this soft actin structure at time scale shorter than the characteristic time of actin polymerisation and forces in the pN range. We show that beyond the dense dendritic network mimicking the actin cortex which has been measured to have an *elastic modulus* (page 28) in the order of kPa [Pujol, dRoure, Fermigier, Heuvingh, 2012] the soft actin cloud is much softer with a stiffness in the Pa regime. This might explain why such a structure has not previously been seen by less sensitive techniques than optical tweezers. The size of this actin cloud and its ability to sustain forces suggest that in cells the actin cortex is not sharply delimited and that structures escaping from it may have a role in organelle positioning.

The questions we address in this part of the manuscript are : How does the far extends the soft part of the gel? What are its precise mechanical properties? How does it change over time? Is the actin cloud elastic or viscous?

3.2 Actin-Bead System

To reproduce the actin cortex and study the mechanics of actin structures emanating from it *we prepare polystyrene beads* (page 40) of $4.3 \mu\text{m}$ diameter coated with a nucleation promoting factor. These beads are placed in the *ATP mix buffer* (page 38) in presence of 25nm of Arp2/3 complex, $4 \mu\text{M}$ of monomeric actin (20% fluorescently labeled) $12 \mu\text{M}$ profilin and a variable amount of Capping Protein. *see Material and Methods* (page 37). These beads are referred to as actin-beads.

These conditions are chosen in order to grow a dense network on the surface of actin-bead as in [Kawska, Carvalho, Manzi, et al. 2012]. We place ourselves at 25nM ATP and a varying amount of Capping Protein

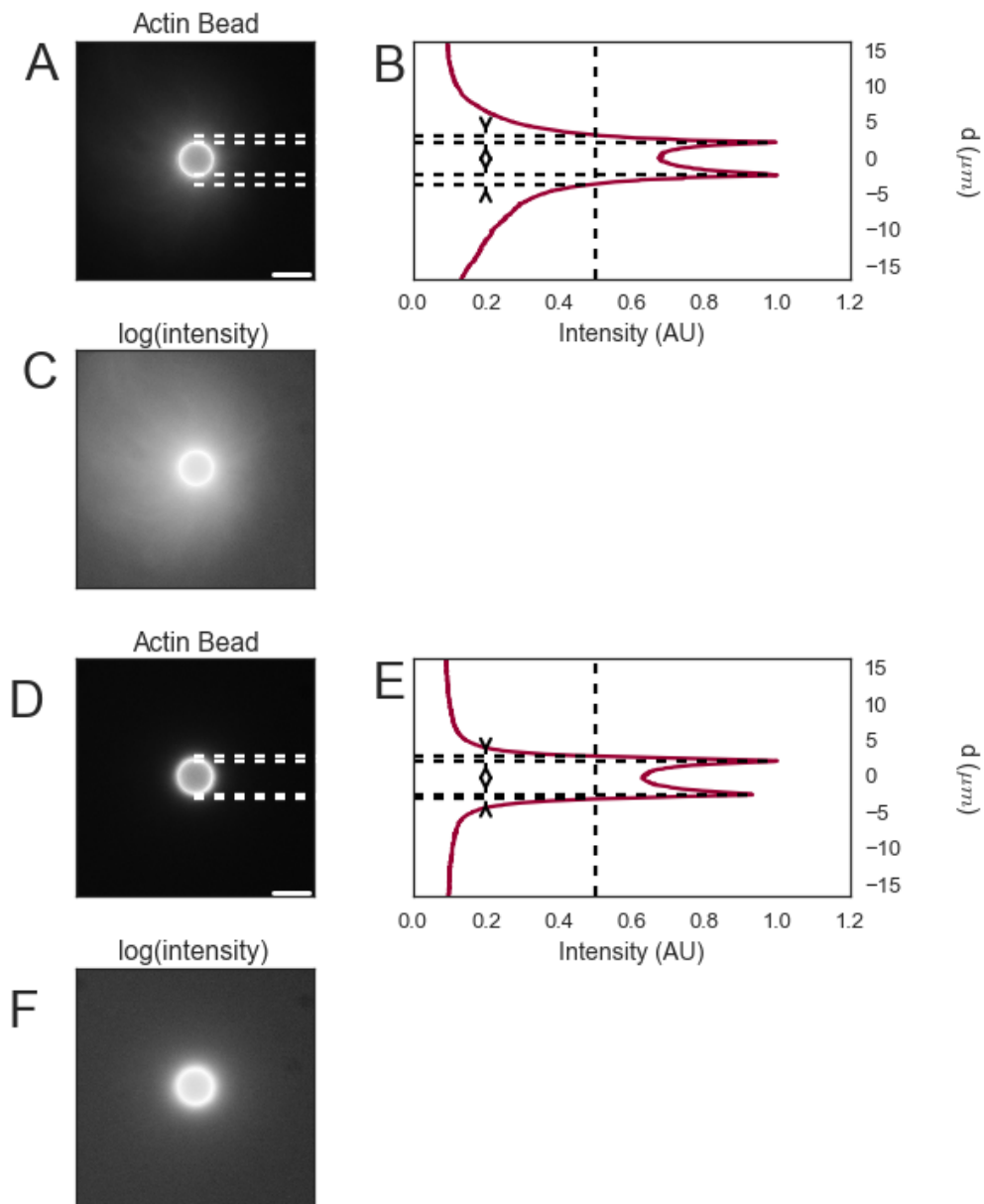


Figure 3.2: A) Epifluorescence image of polystyrene bead with a growing actin gel in presence of 25 nM of Arp2/3 and 25 nM of Capping Protein. Scale bar is 5 μm . B) Normalized intensity profile of fluorescence image with thickness of the gel shown with dashed line as defined in [Kawska, Carvalho, Manzi, et al. 2012] : Distance between maximum intensity and half-maximum intensity. C) Epifluorescence image of $\log(\text{intensity})$. D,E,F) Same as A,B,C, in absence of Capping Protein

concentration in order to cover condition where the dense gel that forms on the actin-bead is able to accumulate sufficient stress to lead to symmetry breaking (CP between 15 and 35 nM, see part *Bead Motility Assay* (page 23)). We also investigate conditions where the amount of Capping Protein is too low ($< 15\text{nM}$) or too high ($> 35\text{ nM}$) to permit symmetry breaking.

We select a bead diameter of $4.3\text{ }\mu\text{m}$ in order to get a characteristic symmetry breaking time of 20 to 40 minutes. A smaller bead radius imply a faster increase of stress and a shorter symmetry breaking time. The choice of $4.3\text{ }\mu\text{m}$ provides sufficient time to proceed with the experiments before symmetry breaking occurs.

All measurements were made on an actively growing actin network which was not stabilized and before symmetry breaking occur for Capping Protein concentration in the range 15 to 35 nM [Kawska, Carvalho, Manzi, et al. 2012].

3.3 Probe Bead System

Beside the actin-bead, the experiment requires a polystyrene bead passivated with BSA. These beads are referred to as probe-beads. The size of the probe-bead was chosen to be the same as the actin-bead, which ensure optical trapping of both beads in the same observation plane. In the case of beads with different diameters, the axial forces on the beads are different. This axial displacement of the two beads during the indentation process leads to a component along the z-axis which eventually pushes one bead out of the trap.

3.4 Experimental description

To probe the actin network we trap an actin-bead with a growing actin-network and a probe-bead using time-shared *optical trap* (page 43), and measure the forces on the actin-bead using a QPD placed in the back focal plane of the condenser (*material and methods* (page 37)).

To avoid systematic errors of force measurements on the moving trap, all force recordings used for analysis are made on the static bead, which is in our case the actin bead.

The indentation is a three step process (Fig 3.3):

- Approach phase at constant velocity $10\mu\text{m/sec}$ unless specified otherwise
- Relaxation phase of 3 second during which both traps remain static
- Retraction phase in which the probe trap move towards its initial position at $10\mu\text{m/sec}$.

3.4.1 Approach Phase

During the approach phase, the probe-trap approaches the actin-trap at constant speed ($10\text{ }\mu\text{m/s}$), as shown in figure 3.3 for times $t < t_1$. During this approach the actin bead will repel the probe bead due to the actin network growing on it. The force felt by the actin bead will progressively increase during the probe bead approach, eventually reaching the maximum as the probe-trap reaches its closest position to the actin trap. Note that during this process the force between the beads pushes the beads out of the respective trap center. The displacement of the beads in the trap remains small compared to the distance between the two beads. Hence in the following we consider that the probe-bead speed is equivalent to the trap approach speed of $10\mu\text{m/sec}$.

3.4.2 Relaxation Phase

After the approach , the trap remain static for a 3 seconds relaxation phase . The relaxation phase start at t_1 and finish at t_3 as shown on [figure 3.3](#). The duration of the relaxation phase is sufficient to allow the partial relaxation of the actin cloud but remain sufficiently short compared to the actin polymerisation speed hence the polymerisation is not expected to change the properties of the network during indentation cycle as well as during repetitive indentation ([Figure 3.6](#))

While the actin network relaxes, the forces between the two beads will slowly decrease thus leading to the beads getting closer to their trap center and closer to each other. The decrease in distance during the relaxation phase is small compared to the distance between beads. The decrease of force as well as the minimal change in distance between the two bead can be seen on [Fig 3.3](#) in the middle part.

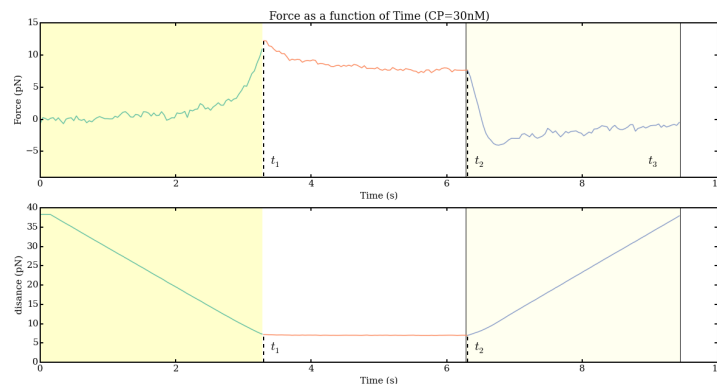


Figure 3.3: Upper graph : Force as a function of time on the actin-beads. Lower graph : distance between beads (distance between traps + displacement of beads from the trap center) as a function of time. First part of each graph (green curve, yellow back) represents the approach phase. Middle part (orange on white) corresponds to the relaxation phase, and right part (blue on pale yellow) is the retraction. Shown data is a subsample of around 1 of every 1000 points acquired. We can see on the second graph that the bead displacement on their respective trap is small compared to the displacement of the trap and justify the approximation of a probe bead speed equal to the probe trap speed.

3.4.3 Retraction part

After the three seconds of the retraction phase, the probe trap returns to it's initial position at $10 \mu\text{m/s}$ ($t > t_2$). During this phase, the force exerted between the two beads decreases, becomes negative, reaches a minimum, and eventually returns to zero as the probe bead recover its initial position (shown on [Figure 3.3](#) right part). Negative forces represent forces that tends to push the two beads towards each other.

3.4.4 Reconstitution of Force-distance-curve

From the position of he trap with time and the signal measured by the QPD the position of bead in the trap as well as the force exerted on each bead can be calculated. We can then recover the distance between bead centers as a function of time. The force-distance curve representing the force exerted by the probe bead on

the actin bead as a function of the distance can be computed and is show in [figure 3.4](#) where we can still distinguish the three phase of the indentation cycle, also marked by the color of the data.

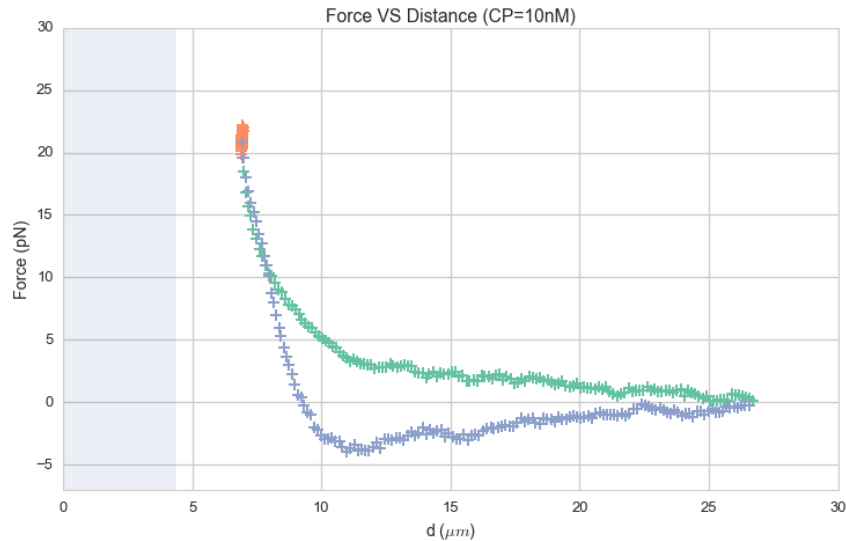


Figure 3.4: Force exerted on the actin bead as a function of the distance between the two bead centers. Color and data are the same as in [Fig 3.3](#). The probe bead starts from the far right, and gets closer while the force increases (green upper part of the curve), reaches a maximum, and enters the relaxation phase (orange part) where the force between the probe and actin bead decrease, while the distance also slightly decreases. During the retraction part (blue) the force rapidly decreases and reaches negative values while the bead returns to its initial position. Shown data is a subsample of 1 every 1000 points of acquired data. Shaded region represent areas where the two polystyrene beads would interpenetrates.

3.4.5 Repetitive indent

To check for reproducibility and non-plastic deformation of the network after indentation, the indentation cycle can be repeated several times at a few seconds interval. As the network is constantly growing during the measurement, this repeat also allows to check for possible change of network properties due to actin polymerisation. The force distance plot is shown in [Figure 3.6 , 3.5](#).

3.4.6 Effect of approach speed

[Gardel, Valentine, Crocker, et al. 2003] suggest that for frequencies higher than 0.1 Hz, force due to the viscous behavior of actin network can be in the same order as the elastic component. To test if such an relaxation effect is important we measured the effect of the approach speed on the force measurements. [Fig 3.7](#) presents the indentation speed affect the measurement by varying the approach speed from 10 to 30 $\mu\text{m/s}$ on the same actin bead.

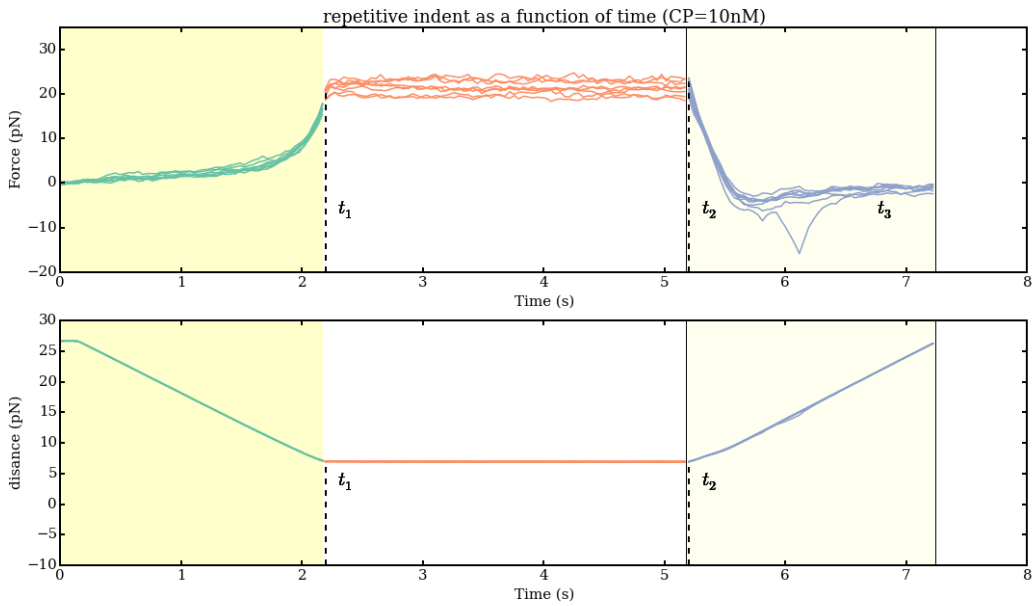


Figure 3.5: Upper graph : Force exerted on actin bead as a function of time for ten repetitive indents. In one of the cycles a sticking event can be seen in the retraction phase 6 seconds after the beginning of the cycle. Lower graph: Distance as a function of time for ten repetitive indents. The ten curves can only hardly be distinguished from one another, which shows the reproducibility of indentation curves.

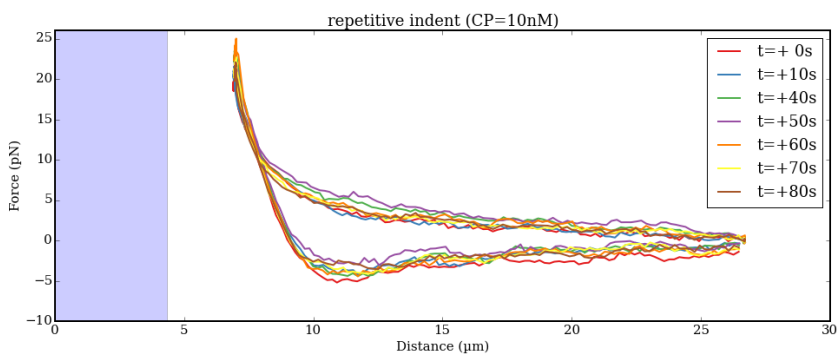


Figure 3.6: Figure showing the reproducibility of indentation process on a bead with 25nM Arp2/3 and 10nM CP Subset of data from Fig 3.5 shown with different color to represent the evolution of the indentation curve over time. Time is relative to first indentation. Shaded area represent zone where the two beads would interpenetrates.

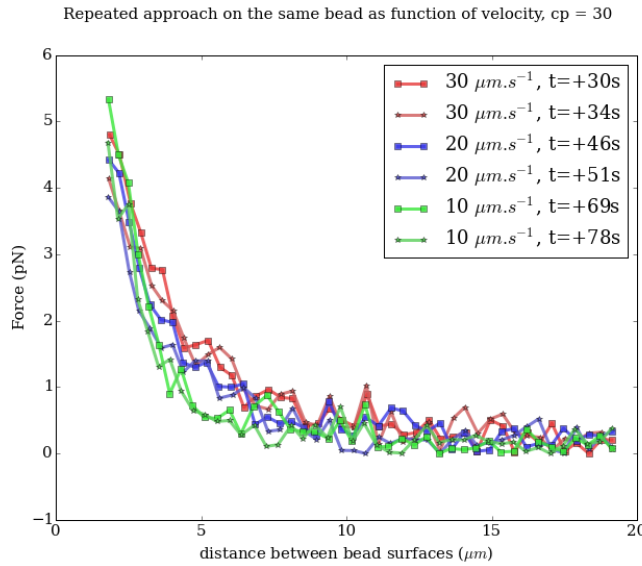


Figure 3.7: Approach phase of repetitive indents at multiple speed on the same actin-bead. The approach phase in the different conditions are similar, hinting for a negligible effect of the viscosity in the actin cloud at the speed considered.

3.5 Experimental observations

Using the bead system, we are able to reconstruct actin cortices *in vitro* and to investigate the mechanical properties inaccessible to other microscopy techniques like TIRF. Beyond the visible actin cortex we can detect the presence of an actin structure that has mechanical effects starting at distances of $> 10\mu\text{m}$, hence far beyond the thickness of the actin cortex ($\sim 1\mu\text{m}$). Figure 3.8 presents a video showing qualitatively that the actin cloud growing on actin beads is able to repel free floating probe beads before they reach the visible reconstituted cortex.

To quantify the distance at which the probe beads are first affected by the actin-cloud we measure the experimental noise by looking at the fluctuations of the trapped probe bead.

During the indentation we defined d_0 as the distance at which the average force felt by the probe bead is higher than the experimental noise. Typically the standard deviation is 2pN.

The repartition of d_0 with the concentration of Capping Protein is plotted in figure 3.9.

3.5.1 Approach phase modeling

To extract mechanical properties using the three phases of the experiment we decided to model each part (approach, relaxation and retraction) independently. In particular, we fit force-distance curve of the approach phase using a power law with 3 fit parameters α, β, δ :

$$F(d) = \beta \times (d - \delta)^\alpha \quad (3.1)$$

In which F represent the force exerted on the probe bead, and d is the distance between bead centers. The powerlaw exponent α is expected to be negative as the force decreases with the distance d , and characterizes

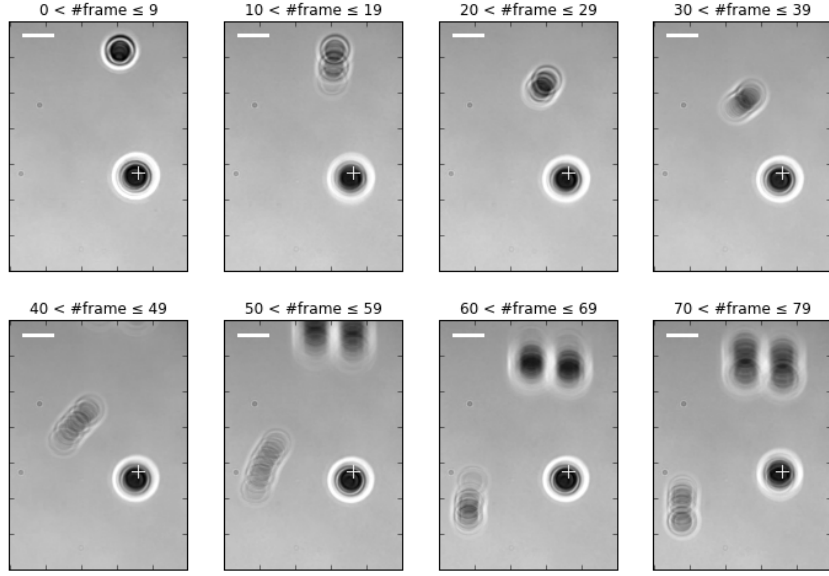


Figure 3.8: Chronophotography representing the displacement a trapped actin bead in a solution with probe bead. During this experiment, the actin bead is kept static in the optical trap (marked by the cross) while the stage is moved. Scale bar is 5 micrometers. Total movie duration is 21 seconds.

how fast the force increase as the two beads approaches each other. The prefactor β acts as a scaling factor of the force. The offset parameter δ shifts the curve on the distance axis. This phenomenological model has the particularity that the force on the probe bead tends to $+\infty$ when the distance d get to δ . The force is undefined for values of $d < \delta$. Hence, the offset distance δ practically describe the distance at which the optical trap is not able to indent the network anymore.

In the case of a hard sphere the value of α would tend towards $-\infty$ leading to a infinite force increase at the contact between the two hard-spheres of same diameter and a value of δ equal to the diameter of the hard sphere. In this case $F(d > \delta) = 0$ and $F(d < \delta) = \infty$

The optical tweezer we use can apply forces up to 20pN, and the beads we use have a diameter of $4.34\mu\text{m}$, hence we determine a cross-sectional surface of surface of roughly $14.7\mu\text{m}^2$. Before escaping the trap, the probe bead can move up to $1\mu\text{m}$ from its trap center. To estimate the maximal stiffness that can be measured, we approximate that we can provide a clear measure of deformation in the order of $1/10$ of μm , this leads to a maximum detectable Young's modulus of :

$$\begin{aligned} E_{max} &\sim \frac{F_{max}L_{0,max}}{A_0.\Delta L} \\ &\sim \frac{50.10^{-12} \times 1.10^{-5}}{(\pi \times 2.17 \times 10^{-6})^2 \times 1.10^{-7}} \\ &\sim 300\text{Pa} \end{aligned} \tag{3.2}$$

Any material with a stiffness much higher than 300 Pa can be considered as infinitely rigid.

The elasticity of dense actin gels around polystyrene beads has been measured in [Pujol, dRoure, Fermigier,

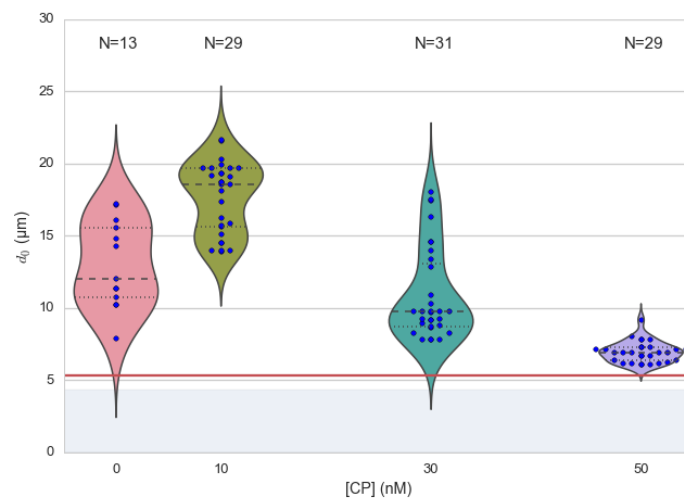


Figure 3.9: Repartition of the bead-center distance at which the actin cloud exert a force higher than the noise (d_0) on the probe bead, as a function of Capping Protein. Shaded region represent the position of the bead surface ($4.34 \mu\text{m}$) and the red line represent the bead surface+ $1\mu\text{m}$ (upper bound for the in vitro Capping Protein concentration. The shaded region represents the position of the bead surface ($4.34 \mu\text{m}$) and the red line represents the bead surface+ $1\mu\text{m}$ (upper bound for the in vitro reformed actin cortex measured in [Kawska, Carvalho, Manzi, et al. 2012]). We see in this graph that for symmetry breaking conditions (CP 10 nM and 30 nM) the distance at which the actin cloud starts to apply forces on the probe bead is large compare to the thickness of the actin cortex. The distance at which the probe bead is able to detect the presence of the actin cloud decreases when increasing the concentration of Capping Protein that restricts actin filament growth. The condition in the absence of Capping Protein are a particular case as no dense actin network forms on the surface of the actin bead.

Heuvingh, 2012] and found to be in the order of kPa. Therefore the optical tweezers are not able to probe the mechanics of the dense gel on the surface of the bead. The value of δ is expected to be $> 4.34\mu m$ as it include partially the dense actin gel.

The model can be fitted independently on each experimental approach phase. An example of such a fit is shown in figure 3.10 and the quality of fit can be measure by the coefficient R^2 which has a media value of 0.97 across all fits.

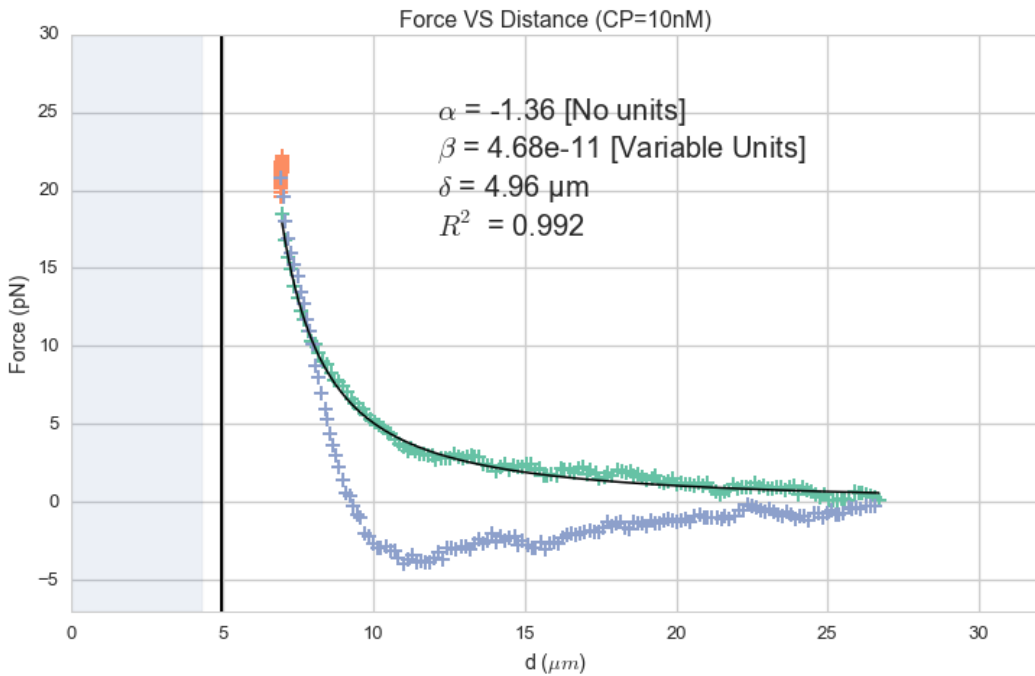


Figure 3.10: Power law model fitted on the approach phase data for one experiment in the presence of $[CP]=10nM$, with the particular values found for the fit parameters. The vertical line represent the point at which the model diverges and the force goes to infinity, that is to say δ . The shaded region corresponds to the distance at which the two beads would interpenetrates. Relaxation (orange) and retraction (blue) data are not fitted.

The approach phase data can be corrected for the distance offset δ and plot in a log-log scale allowing for a better appreciation of the fit result (Fig 3.11). The corrected distance is noted with c indices $d_c = d - \delta$. In the model the force tends to infinity at $d_c = 0$.

In our experiments, the polystyrene beads have an average diameter of $4.34\mu m$, thus we expect δ to be higher than the bead diameter since the beads cannot interpenetrates. Data with δ values lower than $4.34\mu m$ (21 out of 127) are considered as unphysical and were removed from further analysis.

As expected we find negative values for α . Surprisingly the value of alpha does not vary significantly when comparing experiments with different amount of Capping Protein and stay close to -1, with a mean value of -1.10, and a standard deviation of 0.38. The distribution of the power law exponent can be seen on figure 3.12

Due to the scale invariance of the inverse power law found above, all the approach phases data can be

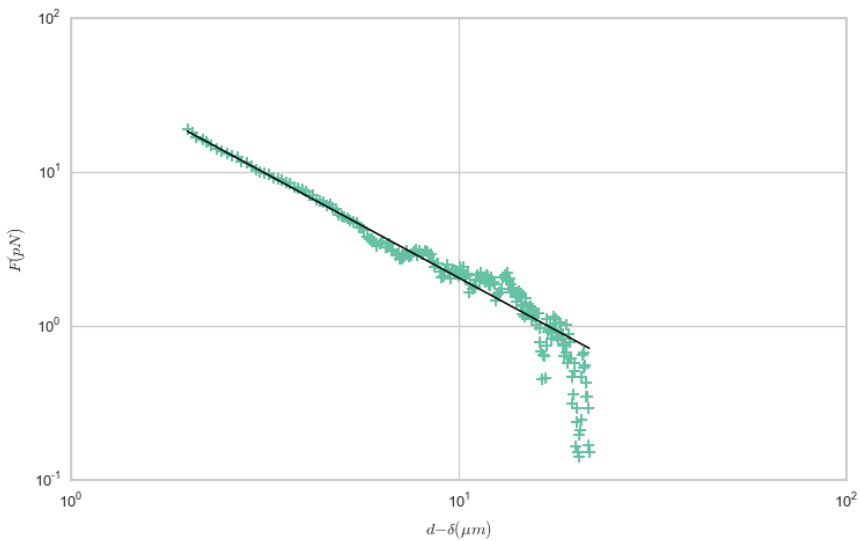


Figure 3.11: Force on the actin bead during the approach phase as a function of bead distance minus distance offset δ plotted on a log-log scale. Black line represents the power law model with correction of the offset distance. Same data as Fig 3.4 but showing only approach phase.

rescaled into a single master-curve (Fig 3.13). This is done by dividing the force by the maximum force F_{max} reached during the approach and rescaling the distance by the minimum approach distance from which δ is subtracted.

The rescaled data confirm an average power law exponent of ~ -1 , the breakdown of the average exponent beyond $d_c/d_{c,min} = 10$ can be explained by the statistical effect of having less data for long distance.

3.5.2 Variation of parameters with Capping Protein

At the chosen concentration of Arp2/3 the bead system can show symmetry breaking in the correct range of concentration of Capping Protein of 10 to 30 μM . In absence of Capping Protein the dense dendritic network does not form on the surface [Kawska, Carvalho, Manzi, et al. 2012]. At low Capping Protein concentrations ($< 10 \mu\text{M}$) it seem not to be able to generate enough stress to rupture, and at too high concentration ($> 35 \text{nM}$) the visible gel is thin and do not break symmetry either. We then investigated the variation of each of the fit parameters for concentrating of Capping Protein ranging from 0 to 50 nM.

We have already seen previously that the powerlaw exponent factor α didn't vary with the amount of Capping Protein in solution (Fig 3.12). The two other parameters investigated are the prefactor β . For the same value of α and δ , the higher β is the stronger the interaction between the two beads for the same distance d_c . We can see on figure 3.14 that the average value for the prefactor decreases with increasing Capping Protein concentration.

The last parameter of our model is δ , the distance at which the force diverges. It can be seen in Figure 3.15 that with the exception of zero Capping Protein, the distance at which the model diverges gets closer to the diameter of the polystyrene bead as the concentration of Capping Proteins in the medium increases. It is interesting to see that the distance offset δ is very close from the bead diameter in the absence of Capping Protein, when no biomimetic actin cortices forms.

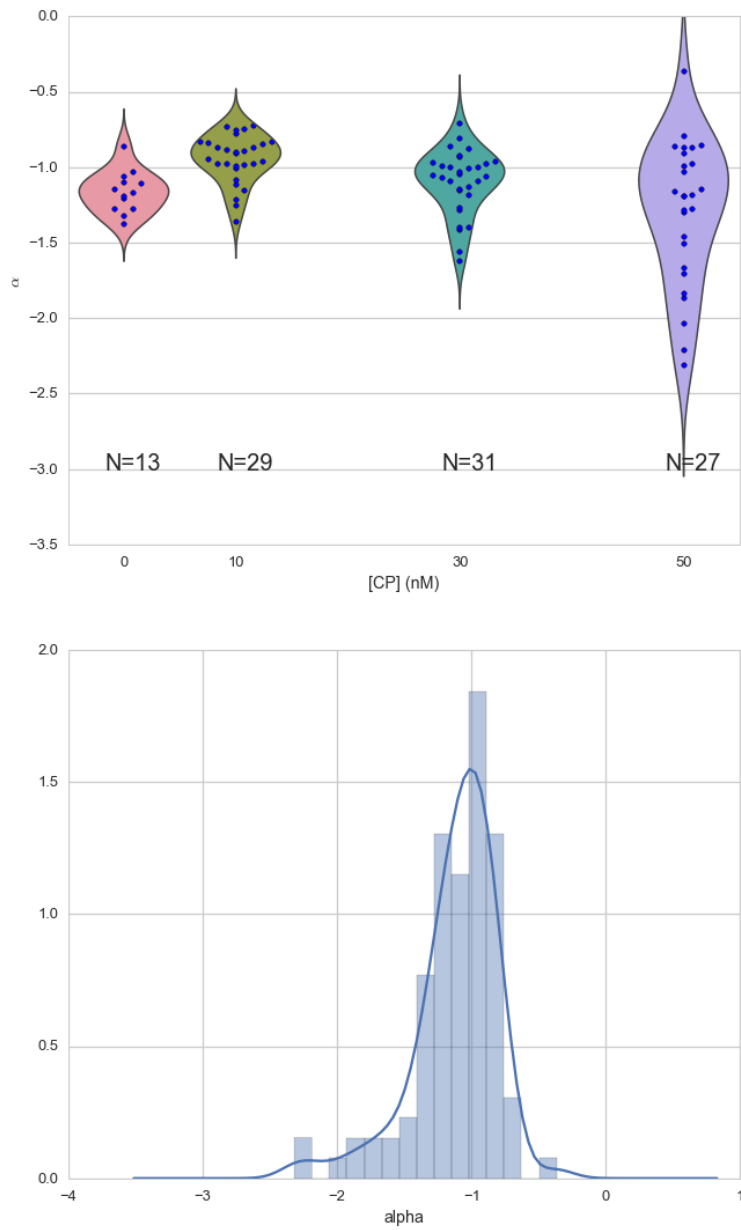


Figure 3.12: Right : Violin plot showing the repartition of power law exponents with the concentration of Capping Protein. Left: distribution of power law exponent α regardless of the concentration in Capping Protein. Value of exponent lies close to -1 .

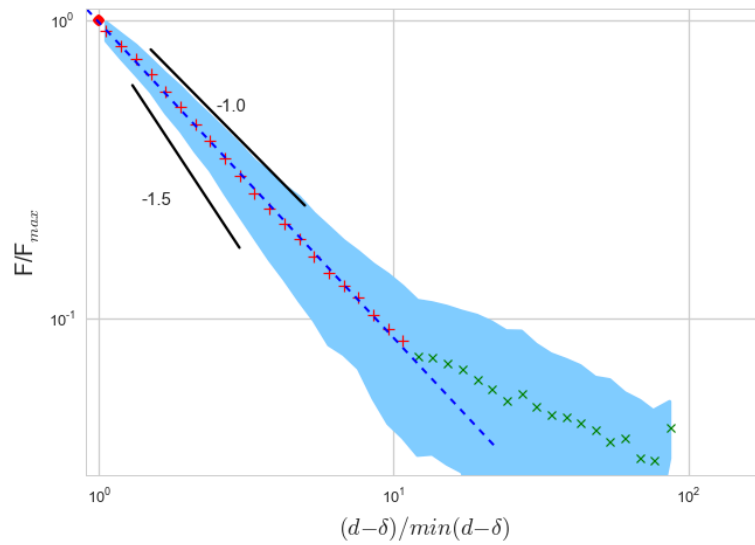


Figure 3.13: Representation of rescale approach data on a log-log scale. Red and green crosses correspond to average values. Blue area corresponds to average +/- standard deviation for each average bin. Red dot in the upper right corner corresponds to the point (1,1) with respect to which all data has been rescaled.

Blue dashed line shows a powerlaw fit of the average data for $d_c/d_{c,min} < 10$ (red cross), fitted slope is -1.06 . As an eye guide, slope of -1 and -1.5 have been represented.

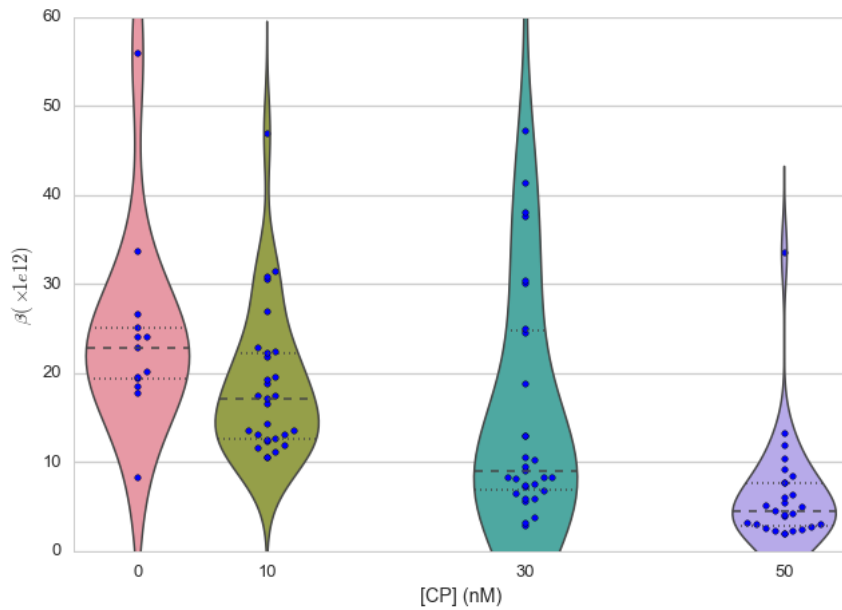


Figure 3.14: Violin plot showing the repartition of the prefactor with the quantity of Capping Protein. Decrease of prefactor with increasing amount of Capping Protein indicates a lower force between the probe bead and the actin bead for the same corrected distance between bead centers.

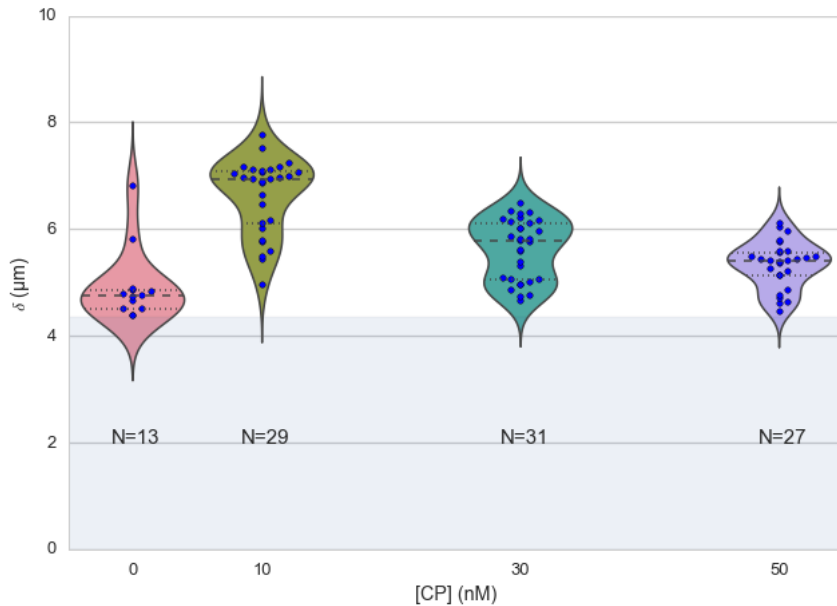


Figure 3.15: Violin plot showing the variation of the offset distance δ with the Capping Protein concentration. The shaded area represents the non-physical region which would correspond to a diverging force beyond the contact of the two polystyrene beads. Experimental data with δ value in this regions have been excluded from further analysis.

3.5.3 Determination of Young's Modulus

To determine the mechanical properties of the gel between the actin and the probe bead, we model it as a purely elastic material. The viscous effects are neglected in the approach part as the approach at different speed show no clear effect on the approach curves (Figure 3.7). We consider the compression of the material between the two beads. The surface of the compressed material is approximated by the projected surfaces of the bead along the direction of compression (πR^2). The thickness of the compressed material is taken as being the distance between bead centers corrected by the distance offset δ as any material below delta can be considered as infinitively rigid for the optical tweezer.

The stress exerted onto the material projected onto the bead surface or radius R can be written :

$$\sigma = \frac{F}{\pi R^2} \quad (3.3)$$

For small deformation the local strain of the material u can be written as a function of the corrected bead position d_c and the considered location along the axis between the two bead center x :

$$u(x) = \frac{d_c - x}{d_c} \quad (3.4)$$

We can express the local differential strain around the position d_c of the bead : $\partial u = -\partial x / \partial d_c$ in which the minus sign reflect the choice of the coordinate system: a decrease in x with a positive Young's modulus E

should lead to an increase of the exerted force. The locally felt Young's modulus at the distance d_c is then

$$E(d_c) = \frac{\partial \sigma}{\partial u} \Big|_{d_c} \quad (3.5)$$

By injecting the expression of u and σ this lead to :

$$\begin{aligned} E(d_c) &= -\frac{d_c}{\pi R^2} \times \left(\frac{dF}{dx} \right) \Big|_{x=d_c} \\ &= E_0 d_c^\alpha \end{aligned} \quad (3.6)$$

In which the value of E_0 can be expressed as function of the power law exponent α and the prefactor β :

$$E_0 = -\frac{\alpha \beta}{\pi R^2} \quad (3.7)$$

Experimentally, the probed Young's modulus corresponds to the average mechanical properties of the actin cloud between the surface of the actin bead and the surface of the probe bead and do not reflect the variation of the mechanical properties of the uncompressed actin cloud with position. Physically E_0 correspond to the Young's modulus as a corrected distance of $d_c = 1\mu m$ (See Fig 3.16) The geometry of the system and the fluorescence signal suggest a decrease of the density of the actin cloud with the distance from the actin-bead center. All values reported later represent estimation of elasticity of an effective Young's modulus. The value of this effective Young's modulus are 3 orders of magnitude smaller than the known elasticity of dendritic gels formed on beads that has been measured to be in the order of kPa [Marcy, Prost, Carlier, Sykes, 2004].

This difference in elasticity might explain why the mechanical actions of this actin cloud as not been seen before in other measurement like micro-pipette aspiration, micro needle deformation or Atomic Force Microscopy indentation that have sensitivities in the order of nN while the forces exerted by this actin cloud are in the order of pN.

Nonetheless, [Gardel, Valentine, Crocker, et al. 2003] show that such low moduli can be obtain using sparse entangle actin network, and confirm the idea that the actin-cloud seen with the optical-tweezer indent experiments has a fundamentally different structure than the dense dendritic network on the actin bead surface.

3.5.4 Mechanical properties

To investigate the mechanical properties of the network that should arise from a $\alpha = -1$ power law, we model the deformation of the actin cloud by the theory of semi-flexible entangled polymer networks ([Isambert, Maggs, 1996], [MacKintosh, Kas, Janmey, 1995], [Morse, 1998a]).

The Young's modulus of semi-flexible filaments in a 3D environment can be expressed as a function of filament contour length density ρ and the entanglement length L_e as [Morse, 1998b]:

$$E = \frac{2.(1+\nu).7.k_B T \rho}{5L_e} \quad (3.8)$$

In which ν is the Poisson ratio that allows the conversion from shear to elastic modulus. Previous studies have investigated the non-linear stiffening of such actin network for large deformation [Semmrich, Larsen, Bausch, 2008] and found that in our condition, the linear description of theses networks holds to describe the actin-cloud.

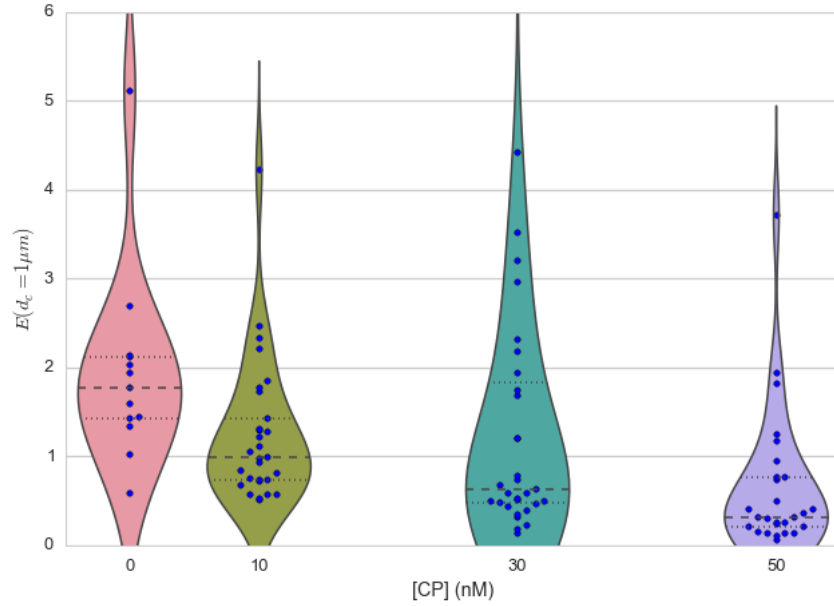


Figure 3.16: Young's Modulus prefactor as a function of Capping Protein show a decrease of average Young's modulus with an increase of Capping Protein concentration.

Similar to [Morse, 1998a] we express the entanglement length as a function of persistence length and filament density: $L_e \approx L_p^{1/5} \rho^{-2/5}$. We can reduce the expression of the Young's modulus to a function of the following parameters :

- The Poisson Ratio ν ,
- The persistence length of actin filaments L_p
- The mesh size of the network $\xi_0^2 = \rho_0$
- The “size” of the cloud, for which we use the distance at which the force is first significant d_0

We need also to consider that for a general compressible material, the only variable that changes during compression is the density ρ which can be expressed as a function of the corrected distance $\rho \rightarrow \rho(d_c)$

Thus leading to :

$$E(d_c) = \frac{(1 + \nu) \cdot 14 \cdot k_B T}{5L_p^{1/5}} \times \rho(d_c)^{7/5} \quad (3.9)$$

The scaling exponent of E in equation (3.9) with d_c should match the exponent of the experimentally found power law α . Thus the density can be expressed in the following form :

$$\rho(d_c) = \rho_0 (d_c/d_0)^{5/7 \times \alpha} \quad (3.10)$$

By the definition of ρ in [Morse, 1998a] which is the filament contour length per unit volume, we can determine the mesh-size ξ_0 of the undeformed network:

$$\xi_0 = 1/\sqrt{\rho_0} \quad (3.11)$$

By comparing this to the phenomenological fit we can express the elastic modulus as a function of the distance and the mesh size, as a function of the fit parameters and characteristic scales of the system.

$$E(d_c) = \frac{(1 + \nu) \cdot 14 \cdot k_B T}{5 L_p^{1/5} \xi_0^{14/5} d_0^\alpha} \times d_c^\alpha. \\ = E'_0 \times d_c^\alpha \quad (3.12)$$

In which E'_0 can be identified as E_0 in (3.9) to extract the closed form solution for the mesh size ξ_0 :

$$\xi_0 = \left(-\frac{(2 - \frac{5}{7}\alpha) \cdot k_B T \pi R^2}{5\alpha\beta L_p^{\frac{1}{5}} d_0^\alpha} \right)^{\frac{5}{14}} \quad (3.13)$$

The found mesh size is in the order of 0.3 to 0.4 μm which is consistent with previous findings :Morse1998b. The variation of the mesh size can be seen on figure 3.17 and does not seem to have a correlation with the concentration of Capping Protein.

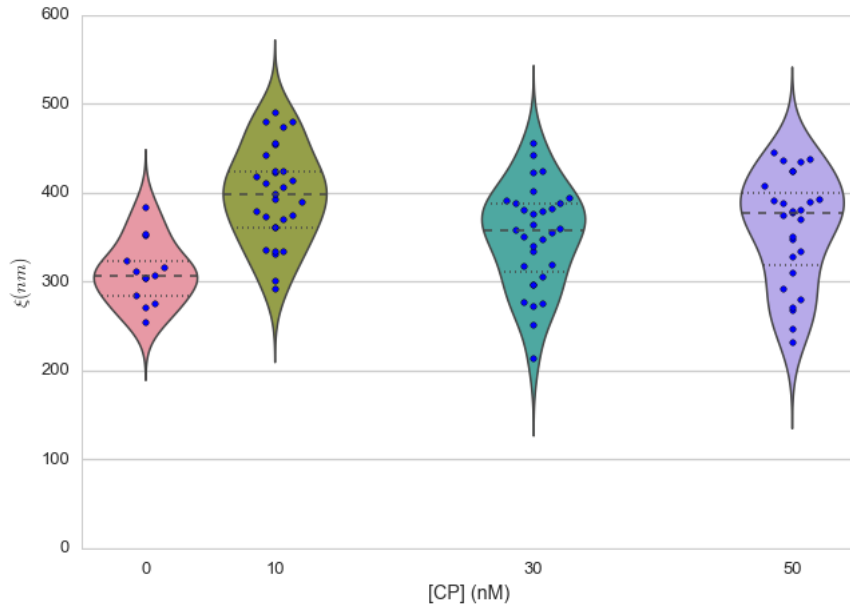


Figure 3.17: Meshsize vs Capping plot.

We explore the correlation between the mesh size and δ by plotting the mesh size again the distance offset δ (Fig 3.18). Figure 3.19 shows the relation between the mesh size and the offset distance δ independently for each concentration of Capping Protein.

From (3.9) and (3.12) by identifying the prefactor it is also possible to extract the Poisson ratio (ν) of the compressed material :

$$\nu = \frac{1}{2} \times \left(\frac{5}{7} \cdot \alpha + 1 \right) \quad (3.14)$$

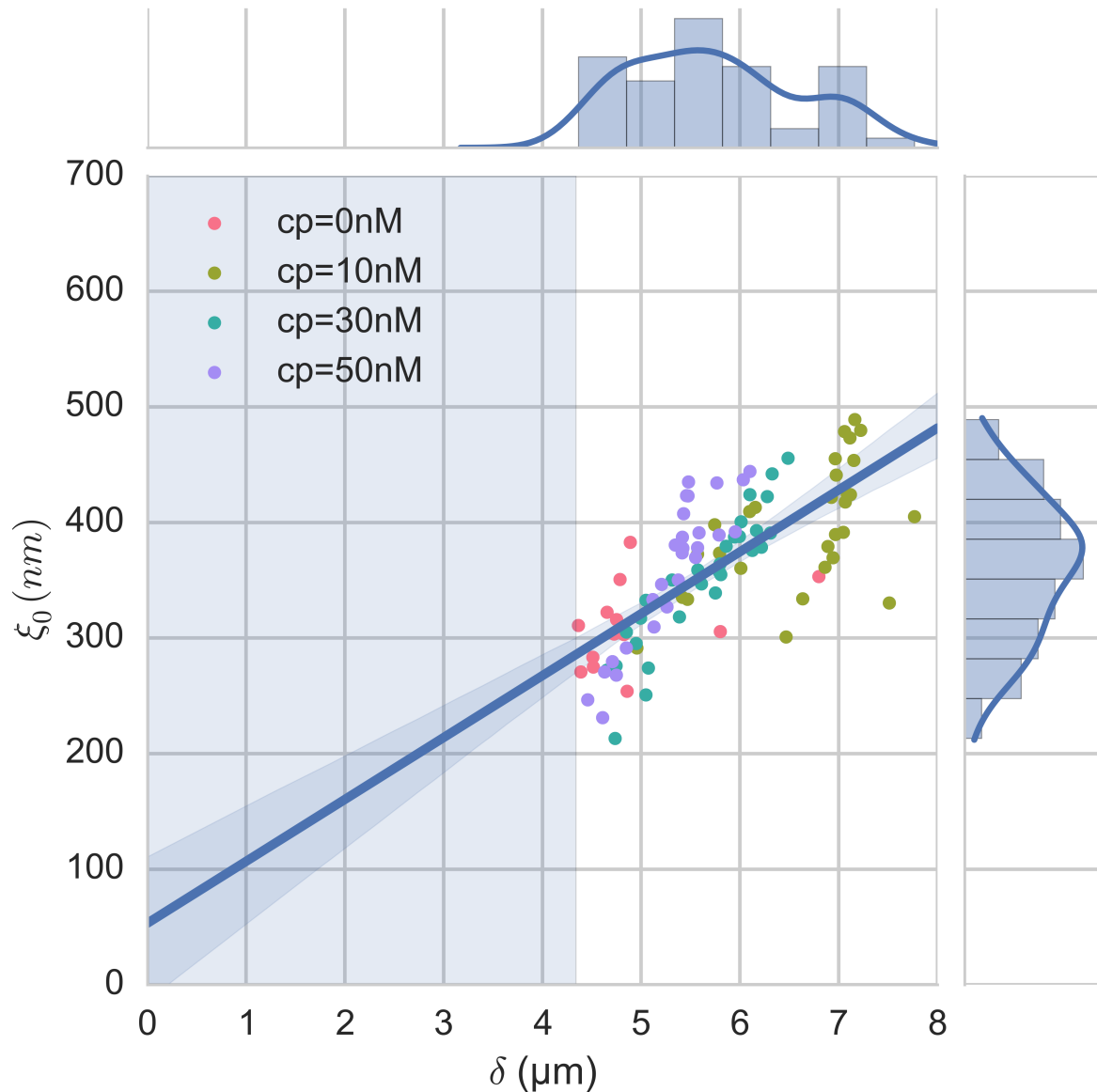


Figure 3.18: Correlation of the meshsize ξ_0 with the distance offset δ , with marginal distribution as histogram on the side and on the top. Shaded regions represent confidence interval at 95%.

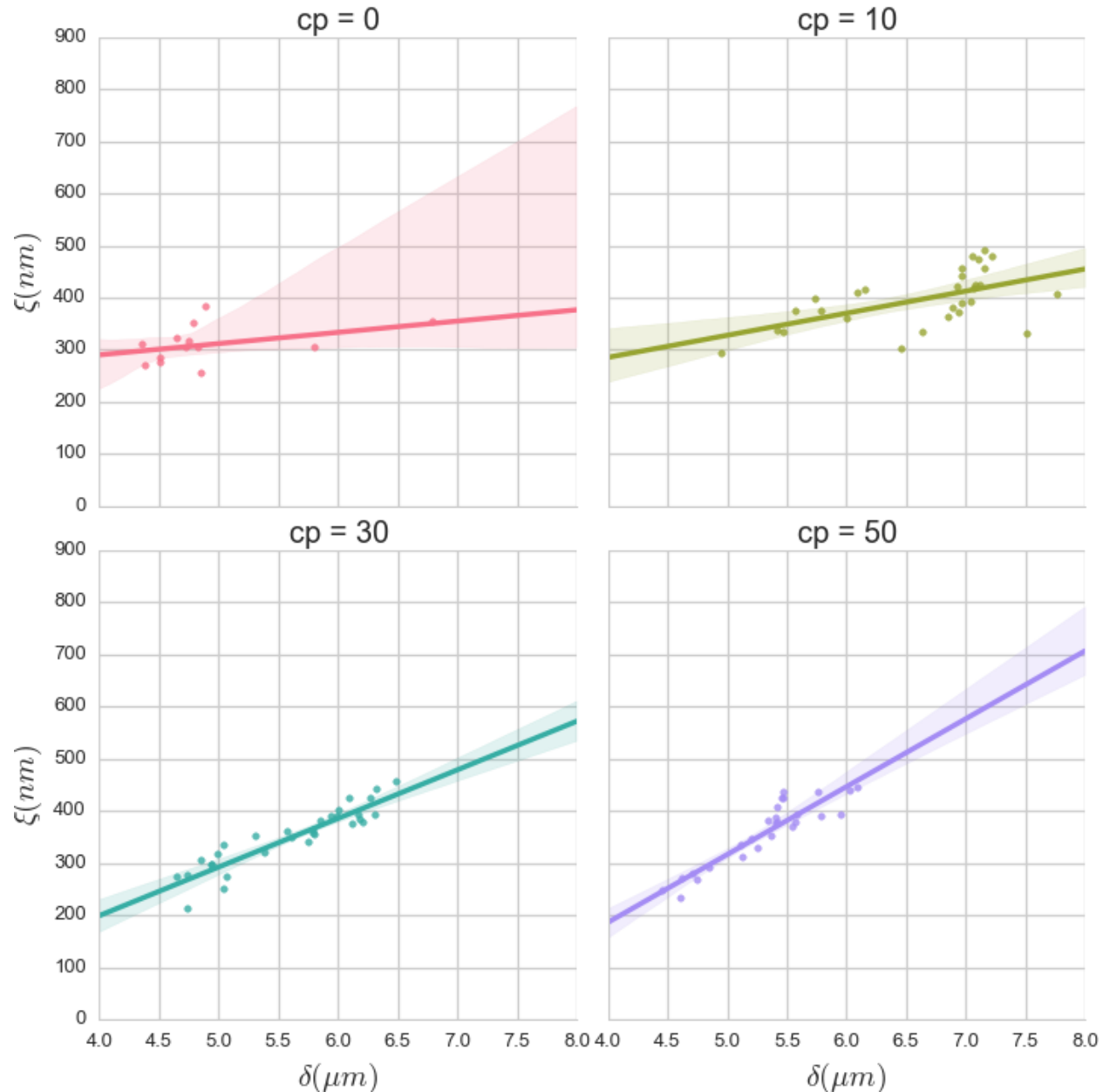


Figure 3.19: Same figure as [Fig 3.18](#) for each concentration of Capping Protein, with linear regression and confidence intervals at 95%.

The Poisson ratio depends only on the powerlaw exponent and thus varies little with the amount of Capping Protein concentration. We found value of the Poisson ratio that are between 0.1 and 0.2 corresponding to compressible foam-like materials that do not expand highly in the direction orthogonal to the compression axis. Previous study of bulk actin network find a Poisson ration of 0.5 (incompressible material) for actin concentration of 21.5 μM . We suspect that the low actin concentration used in our experiments (4 μM) is the reason for the low Poisson Poisson Ratio. Also the local structure of filaments emanating from the bead may explain the large compressibility of our actin cloud.

3.5.5 Interpretation

The results of our data analysis lead to the interpretation that a dense actin gel of elasticity close to $\sim 1\text{kPa}$ is polymerized on the surface of the actin bead. This stiff gel cannot be indented by the optical tweezer. Beyond this dense gel a soft actin cloud with an effective elastic modulus of 1 Pa and below is present and extends on distances that are several times bigger than the thickness of the reconstituted actin cortex (Fig 3.20). The structure of this actin cloud is expected to be quite different from the dendritic gel and be mostly constituted of loosely entangle actin filaments.

In this model, the offset distance δ correspond to the limit of the dense dendritic actin network mimicking the actin cortex that grows on actin beads. The high elastic modulus of this gel makes it impenetrable by the small forces generated by the optical tweezer we use. The value of δ we found are coherent with the measured thickness $e \simeq \delta - 2.R_{\text{bead}}$ of the biomimetic actin cortex as measured by epifluorescence in [Kawska, Carvalho, Manzi, et al. 2012] and found to be in the range of 1 to 2 μm . The decrease of δ with Capping Protein is also coherent with the decrease of gel thickness.

The filaments composing the actin cloud emanate directly from the actin cortex in which the nucleation of actin polymerisation started at the surface of the bead. Eventually, a few filaments can escape from the network and are capped by the Capping Protein only when the growing extremity is already several micrometers from the bead surface.

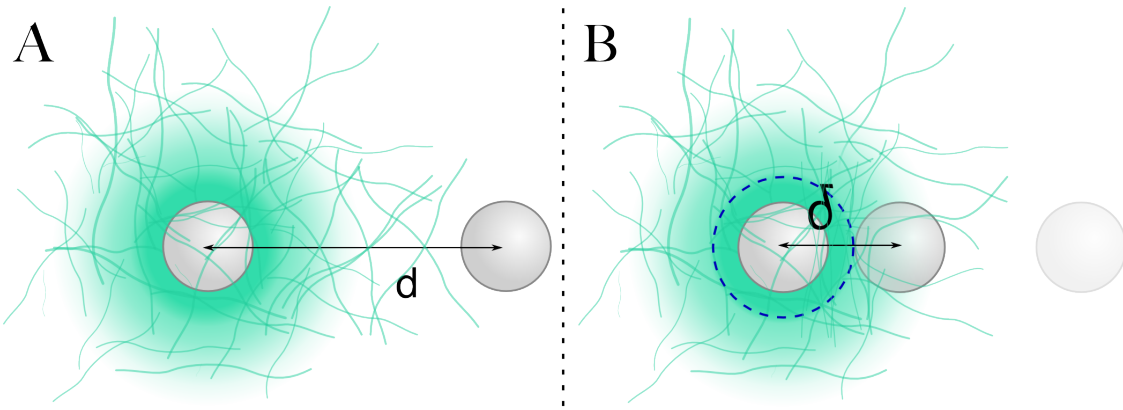


Figure 3.20: A) Schematic of an actin cloud. Left: The actin bead triggers actin polymerisation. Right Probe Bead. On the surface of the actin bead a dense and dendritic network forms a biomimetic actin cortex with an elastic modulus close to the kPa (Dark Green). From this actin cortex emanates a softer actin structure : The actin cloud . The actin cloud is a loosely entangled network formed by the filaments escaping from the bead's actin cortex and extending over several micrometers. The actin cloud has an average elastic modulus which is several order of magnitude softer than the actin cortex. B) From the point of view of the probe bead in optical tweezer, the system (actin-bead+actin cortex) behave as a hard-sphere of radius $\delta - R$

The thickness of the actin cortex e as measured in [Kawska, Carvalho, Manzi, et al. 2012] increases with time during the polymerisation of actin. We can predict that the offset distance δ should increase with time, except in the absence of Capping Protein where no actin cortices form. This can be verified on figure 3.21 that shows the evolution of δ as a function of polymerisation time.

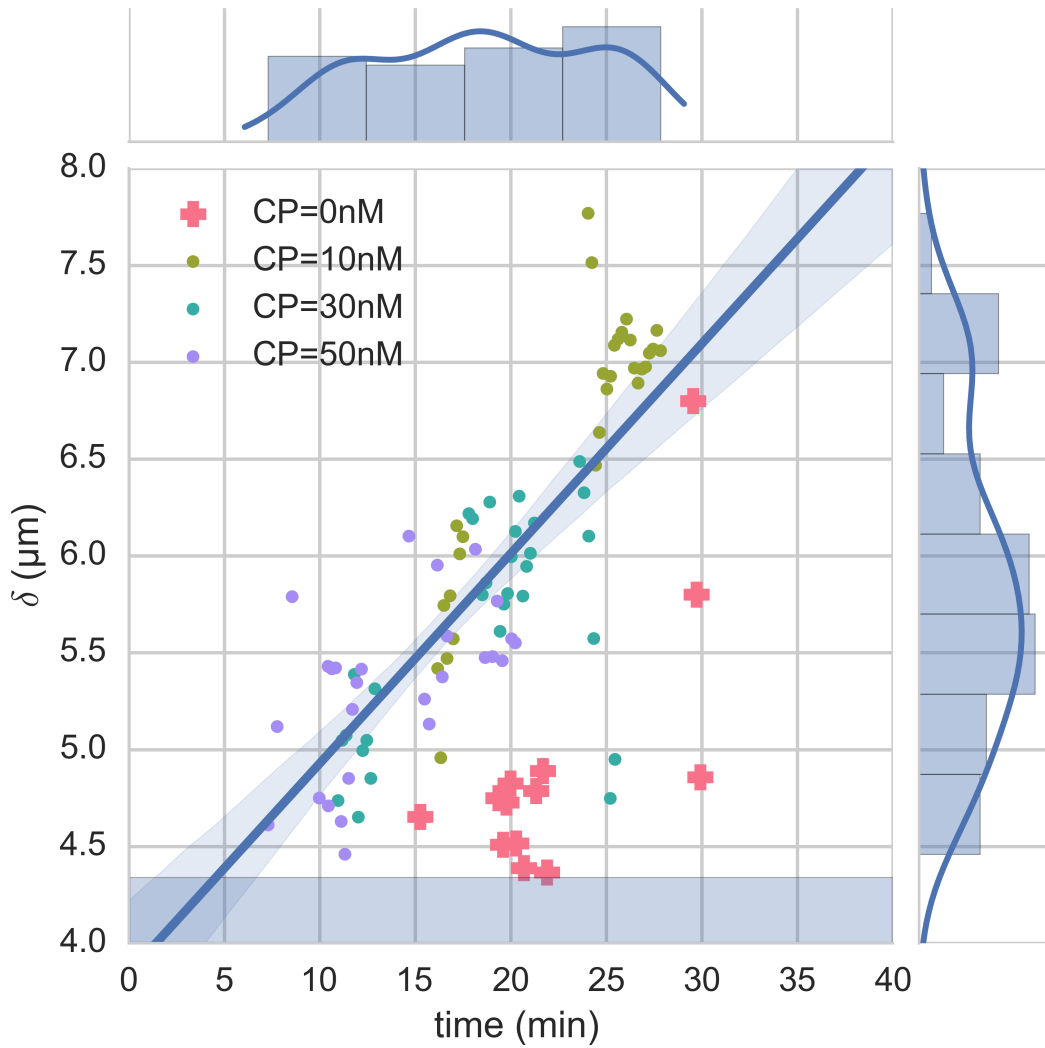


Figure 3.21: Distance offset δ as a function of time (min) since mix of actin, ATP and beads. Linear fit with confidence interval at 95% (light shaded area) and bead surface (dark shaded area). Samples taken in the absence of Capping Protein are not taken into account in the regression (Pink +). The increase of δ with time is coherent with the measured increase of the gel thickness e as measured in [Kawska, Carvalho, Manzi, et al. 2012]

3.6 Relaxation phase

The approach phase of the indentation cycle has been modeled with a purely elastic mode. However, the force distance plot shows a significant dissipation marked by an hysteresis Fig 3.4. The repetitive indent cycle giving the same force-distance curves (Fig 3.6) allow to exclude a plastic deformation. We can hence reject the hypothesis of ruptures of the actin meshwork or breakage near the entanglement points.

The theory of entangled filaments networks that allowed us to understand the link between the phenomenological model and the mechanical properties of the network also proposes a relation to explain the relaxation of the network.

In this model [Morse, 1998a], the visco elastic modulus E is a function of time and can be written as $E(t) = E \times \chi(t)$ with

$$\chi(t) = \sum_{n,odd} \frac{8}{n^2\pi^2} \exp\left(-\frac{n^2\pi^2 t}{\tau_{rep}}\right) \quad (3.15)$$

In which $\tau_{rep} = \frac{l_f^2}{D_{rep}}$ is a single fit parameter that depends on diffusion constant for filament reptation D_{rep} and the filaments length l_f . In this form, χ is a sum of exponential decays with well defined characteristic timescales and amplitudes that decrease as $1/n^2$. To fit this model to the data of the relaxation phase, we can limit ourselves to the first 40 terms of the sum as any of the subsequents terms represent timescales we cannot reach with our experimental resolution.

It should be noted that the value of $\chi(t = 0)$ is 1 and should be treated particularly in order to insure continuity of the force applied on the actin-bead in the model.

Using this sum of exponential decays is coherent with the common findings of power-laws found in the frequency-dependant shear modulus of both *in vivo* and *in vitro* actin networks as well as the relaxation behavior found in cells.

In order to determine τ_{rep} , the Young's modulus determined in the approach phase is used and the model is fitted against the relaxation data. A result of such a fit can be seen on figure 3.22. The value of τ_{rep} are highly variable and the fit can be difficult when the relaxation is slow or in the order of the measured noise. Variation of τ_{rep} with the concentration in Capping Protein can be seen on figure 3.23, and one example of fit on the figure 3.22

We can see here that the polymer model introduced in [Morse, 1998a] allows to completely fit the succession of approach and relaxation phases. To check if the fit parameters give realistic value, we can estimate the diffusion constant for filament reptation D_{rep} .

$$D_{rep} = \frac{k_b T}{\gamma l_f} \quad (3.16)$$

In which $\gamma \approx 2\pi\eta_s/\ln(\xi_0/d_f)$ is the friction coefficient per unit length. γ depends on the solvent viscosity η_s , the mesh-size ξ_0 and the filament diameter d_f (7nm for actin). We use $\eta_s = 10^{-3} Pa \times s$ for water and a mesh size in the order of 400nm as determined from the approach phase (Fig 3.23). Using τ_{rep} given by the fit, this lead to filaments length ranging from 3 to 8 μm , which is consistent with TIRF experiments and simulation as done in [Kawska, Carvalho, Manzi, et al. 2012].

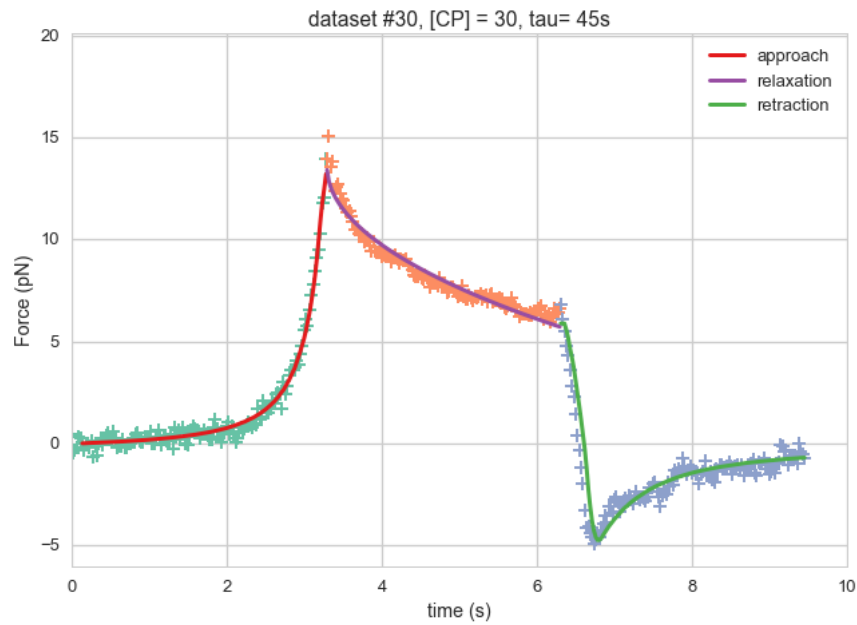


Figure 3.22: Force as a function of time as well as fit for the 3 phases, approach, relaxation and retraction.

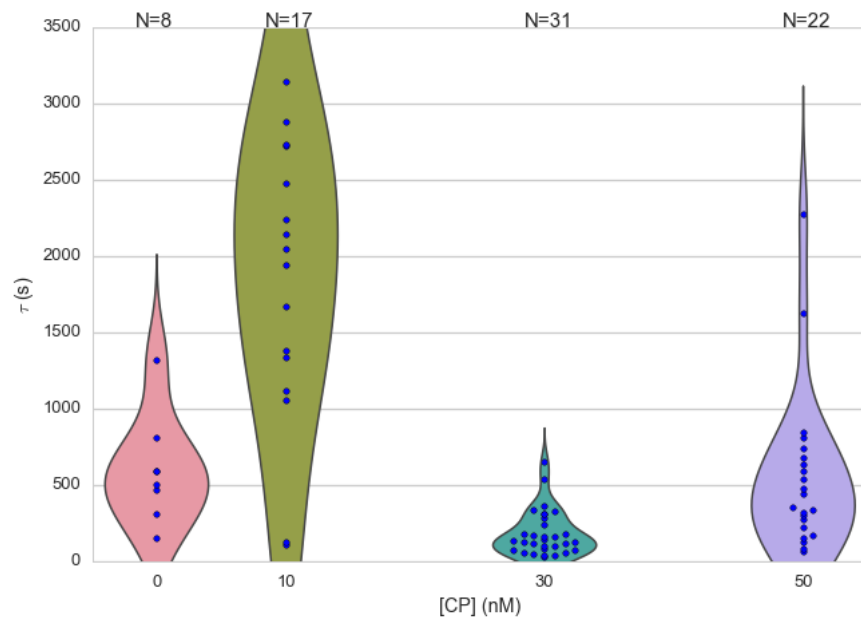


Figure 3.23: Violin plot showing the repartition of τ_{rep} as a function of capping protein. Outlier (τ_{rep} negative or greater than tens of minutes removed)

3.6.1 Retraction Phase

During the retraction phase the force decreases, becomes negative after a retraction of 3 to 4 μm , and show a slow return to 0 at large distance. Sticking events can be seen when the force becomes abruptly negative before relaxing as fast. [Figure 3.24](#) shows such a sticking even happening during an indentation cycle.

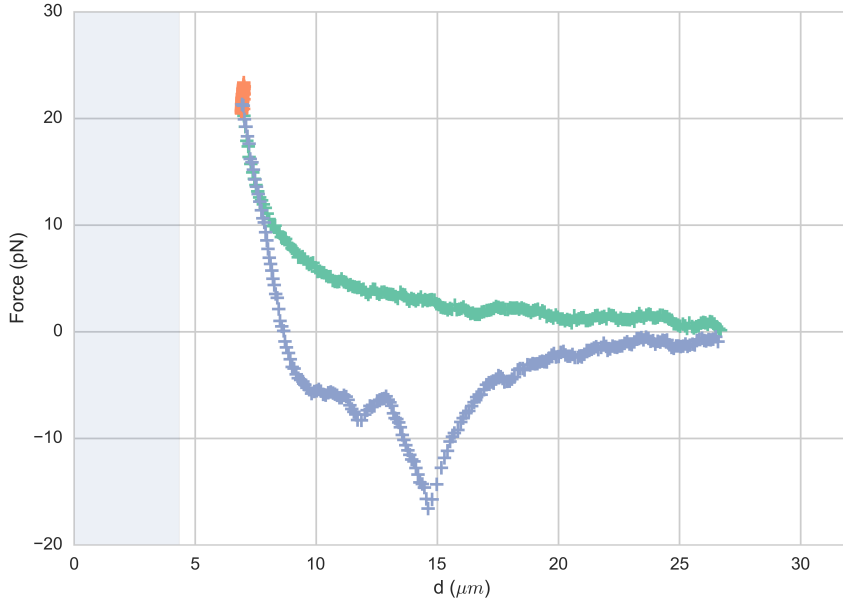


Figure 3.24: A sticking event at $d = 15\mu\text{m}$ where the force can be seen decreasing rapidly up to -18 pN before quickly returning to its normal value. A second smaller sticking even is present at $d = 12\mu\text{m}$. Sticking even appear roughly 20% of the experiments.

We assume that the sticking events are characteristic to non-specific interaction between the probe bead and the actin cloud. In the case when no sticking event is present, we assume partial closing of the actin cloud beyond the probe bead during the relaxation phase and model the retraction curve as a transition between the damped-approach curve and a penetration of the probe bead through the closing actin cloud.

During the approach phase the force exerted on the actin-bead is $F(d) = \beta(d - \delta)^\alpha$. During the relaxation phase the force decrease from $F(t_1)$ to $F(t_2)$ with the relation :

$$\frac{F(t_2)}{F(t_1)} = \chi(t_2 - t_1) \quad (3.17)$$

We can write that the force exerted on the actin-bead during the retraction can be written as a sum of the force felt during the approach, damped during the relaxation (F_{da}), plus a force due to the closing of the actin network behind the bead $F_{closing}$.

$$\begin{aligned} F_{ret}(d) &= F_{da}(d) + F_{closing}(d) \\ F_{ret}(d) &= \chi(t_2 - t_1) \cdot \beta(d - \delta)^\alpha + F_{closing}(d) \end{aligned} \quad (3.18)$$

$F_{closing}$ is computed using the fit parameter α , β , δ and τ_{rep} ([Fig 3.25](#)).

On a double logarithmic scale and at long distance $F_{closing}$ also seem to follow a power law (F_{plaw}), when no sticking events are present.

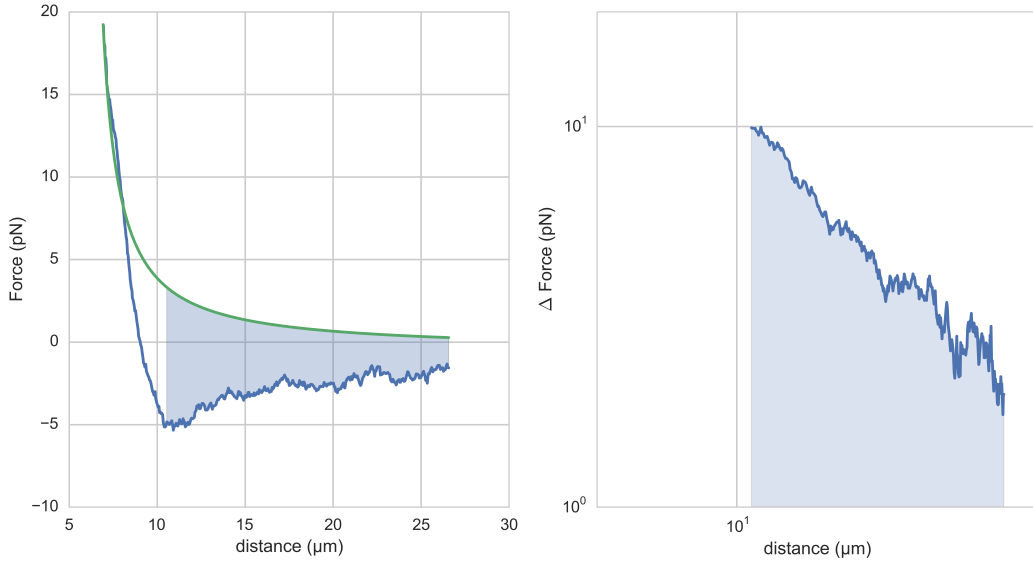


Figure 3.25: Left : Retraction phase with approach phase fit damped by $\chi(t_2 - t_1)$ in green. Blue area under the curve is plotted on a log-log scale on the right, follow a powerlaw.

$F_{ret}(d)$ seems though to follow the force felt during the approach phase, damped by $\chi(t)$ (F_{da}) for $d \simeq D_{bead}$ and $F_{da} + F_{plaw}$ for $d > 10\mu m$. The typical size of the bead being D_{bead} we expect the transition from one regime to the other to be done on a length scale of D_{bead} . Thus we use a smoothing function which is a convolution between the projected bead area and a linear ramp function which can be seen on [figure 3.26](#)

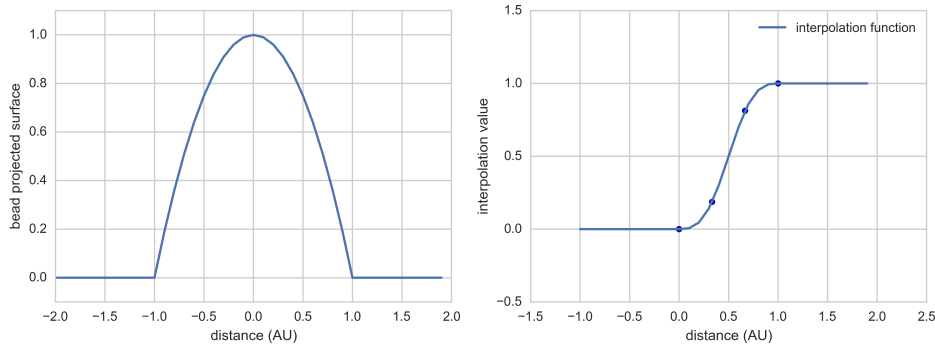


Figure 3.26: Interpolation function used to smooth the transition from F_{da} to $F_{da} + F_{plaw}$

The complete retraction force can be seen on [figure 3.22](#) and is equal to

$$F_{ret}(d) = F_{da}(d) \times (1 - S(d)) + F_{plaw}(d) \times S(d) \quad (3.19)$$

Where $S(d)$ is the interpolation function for a bead of $4.34 \mu\text{m}$ diameter. We can see that the model represents correctly the retraction and especially the position and value of the minimum of the retraction function without fitting parameters when we use the diameter of the probe bead as a typical scale for the transition when changing direction.

3.7 Discussion

The actin cytoskeleton plays an important role in many cellular functions. The actin cortex, just beneath the cell membrane is not only a crucial structure for cell motility and the mechanical properties of the cell, it is also an essential component in cell division and the positioning of the spindle. Other actin structures, that spawn from the nucleus to the cell membrane are responsible for cell organelle positioning like in plants where the nucleus is found towards the anticlinal wall of the cell [Iwabuchi, Takagi, 2010], or during nurse cell maturation where the nucleus is pushed away from the dumping channel:cite:Huelsmann2013. The mechanical link from the outside of the cells to the nucleus using actin bundles has already been show previously [Jaalouk, Lammerding, 2009]. We show here that these actin structure should not be the only one taken into account to explain organelles positioning.

Our experiments show the existence of a sparse and stiff actin cloud emanating from a biomimetically reconstituted actin cortex. This actin cloud is capable of staining forces of tens of pico Newtons, enough to hold organelles in place. Using polymer physics we are able to model the behavior of such an actin cloud and measure many of its mechanical properties. It provides an actin scaffold capable of deforming non-plastically. At time scale of few seconds if behaves mostly elastically with an elastic module of a few Pascal. The Poisson ratio of the actin cloud varies from 0.1 to 0.2 hinting for a sparse structure of loosely entangle filaments forming a meshwork with a typical mesh size of 300 to 400 nm.

The filaments at the origin of this loosely entangled network would emanate from the dense actin cortex that can be seen and simulated on actin-beads [Kawska, Carvalho, Manzi, et al. 2012] and the evolution of parameters of this actin cloud are coherent with the preceding studies on biomimetically reconstituted actin cortices. Recently, the role of actin networks with similar properties as the actin cloud have been described in cells such as *Xenopus* Oocyte [Feric, Brangwynne, 2013]. Poisson ratios of actin networks have been measured in bulk to be higher [Gardel, Valentine, Crocker, et al. 2003] but are not inconsistent with our measurement at lower actin concentration.

The actin cloud provides a novel structure that should be studied further to understand the positioning of organelles in cells and to study which role this sparse actin structure plays in the formation of other actin networks inside cells.

In particular microrheology experiments could be performed on the growing actin cloud in order to further characterize the frequency dependence of the mechanical properties of the actin cloud. The effect of cross linking and network branching is crucial for the occurrence of symmetry breaking on bead systems, and would likely play a role in the structure of the actin cloud. A confined geometry and direct polymerisation on membrane, or the effect of myosin motors might allow to alter the properties of the actin cloud.

All these could be cellular mechanisms to use the actin cloud in order to efficiently form structures needed for its function. Further studies of the actin cloud on biomimetic or *in vivo* system are challenging, but would lead to a better understanding of the mechanics of the cells and its control.

A Paper based on this study has been accepted for publication in Biophysical Journal and is added for information as appendix of this manuscript.

CORTICAL TENSION MEASURED ON LIPOSOME DOUBLETS

4.1 Introduction

We have seen that in cells the actin cytoskeleton is a key component to form structures like the actin cortex that serve to transmit forces and gives mechanical rigidity to cells. In order to drive shape changes, cells regulate the mechanical properties of the sub-micrometer thick actin cortex that is found beneath the membrane [Clark, Dierkes, Paluch, 2013]. The dynamics of the actin cortex drives cell shape changes [Salbreux, Charras, Paluch, 2012] and the presence of the molecular motor myosin II plays a fundamental role for the tension of the acto-myosin cortex [Tinevez, Schulze, Salbreux, et al. 2009]. Cortical tension can be measured on cells to vary between 50 and 4000 pN/ μ m depending the activity of actin and myosin. These changes of the cortical tension are also affected by cell-cell adhesions [Maitre, Berthoumieux, Krens, et al. 2012] which have been shown to play a main role in cell sorting.

Recently, such acto-myosin cortices have been reconstructed on cell-sized liposomes [Carvalho, Lemiere, Faqir, et al. 2013] which showed that the attachment of the actin cortex to the membrane plays a crucial role in the behavior and contractility of the acto-myosin network.

In the present study, I collaborated with Kévin Carvalho and Joël Lemière to further extend the previously developed system [Carvalho, Lemiere, Faqir, et al. 2013] with the aim to monitor the cortical tension changes in a biomimetic actin cortex formed on liposomes. My principal contribution was the analysis of the 3D data that was acquired using Spinning Disk Microscopy. For the analysis I developed a novel method to get an precise and unbiased measure of the geometrical parameter.

To determine the role of cortical tension in cells, recent work used cell doublets [Maitre, Berthoumieux, Krens, et al. 2012]. Here we form similar doublets from liposomes around which we polymerize an actin cortex *in vitro* (Fig 4.1). The shape changes of these liposome doublets allow the time dependent monitoring of cortical tension in a non-invasive way. In this project we hence develop a method for the precise acquisition of doublet deformation in order to determine accurately the increase of tension induced by the injection of myosin motor on the preformed actin cortex.

4.2 Experimental description

4.2.1 Formation of liposomes doublets

Liposomes are obtain by electro-formation (see *Material and methods* (page 40)) from a mix of EPC and PEG-biotin lipids. The presence of streptavidin in the working buffer allow liposomes to naturally stick

together to form doublets after 15 minutes (Fig 4.1).

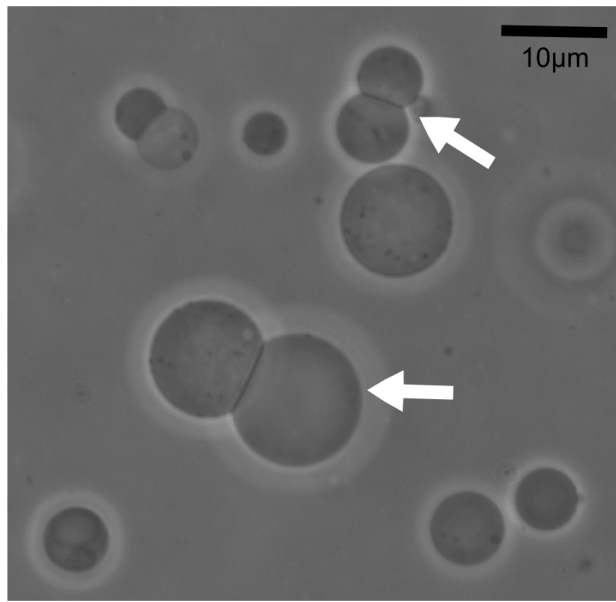


Figure 4.1: Cell-sized liposome doublets. Doublets are indicated by white arrows in the field of view of a phase contrast microscope.

4.2.2 Formation of actin cortex on doublets

Formation of the actin network on doublets is done similar as described recently [Carvalho, Lemiere, Faqir, et al. 2013]. Briefly, actin filaments including biotinylated monomers are stabilized by phalloidin and linked to PEG-Biotin lipids (see *materials and methods* (page 37)) via streptavidin that is present in the solution (Fig 4.3). Besides linking the actin to the membrane, it also cross-links the filaments. Such a network has already been characterized recently [Carvalho, Lemiere, Faqir, et al. 2013]. Note that as the actin filaments are only added after the formation of the doublets, the interface between the two liposomes composing the doublets remains free of F-actin (Fig 4.4, 4.2). As the actin added is fluorescent, the absence of actin at the liposome interface can be checked by epifluorescence as it appears dark compared to the rest of the doublet (Fig 4.4).

4.2.3 Visualisation of the interface

To visualise the interface between the liposomes, and to avoid the use of fluorescent lipids that may affect the membrane mechanics [Sandre, Moreaux, BrochardWyart, 1999] the inside buffer of approximately half the liposomes are labeled with 0.9 μ M of sulphorhodamin B (SRB) eventually leading to half of the doublets containing a single fluorescent liposome (Fig 4.4 i and iii).

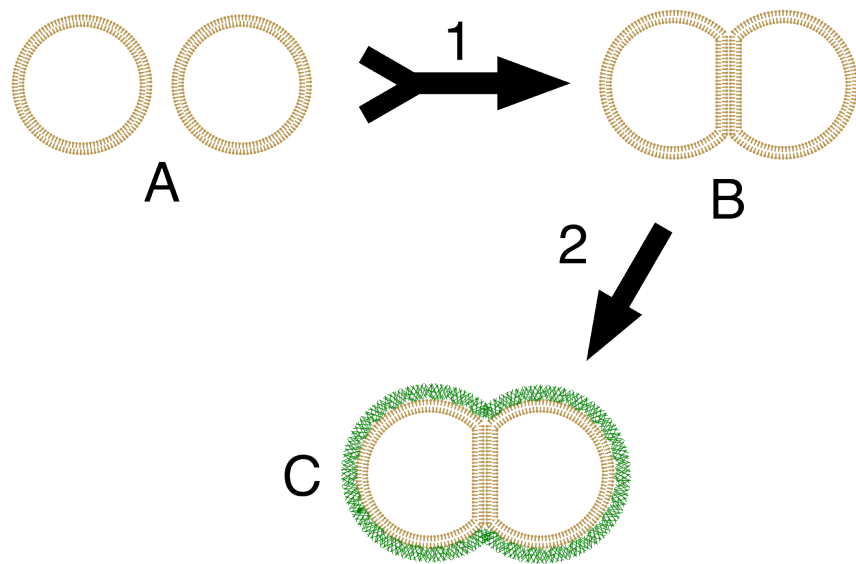


Figure 4.2: Formation of doublets: 1) In the presence of streptavidin, single liposome (A) aggregate into doublets. (B) The addition of biotinylated actin filaments stabilized with phalloidin (2) forms liposome doublets covered with a micrometer-sized actin network (C). The interface between the two liposome is a double lipid bilayer free of actin filaments.

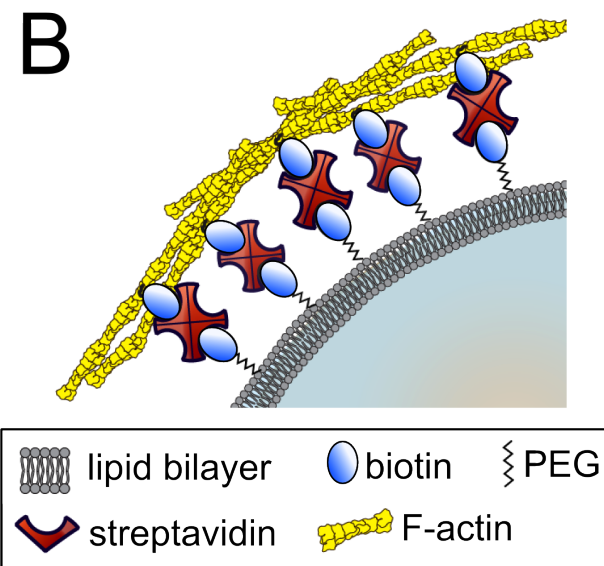


Figure 4.3: Schematic of the stabilized actin cortex at the membrane (proteins not to scale).

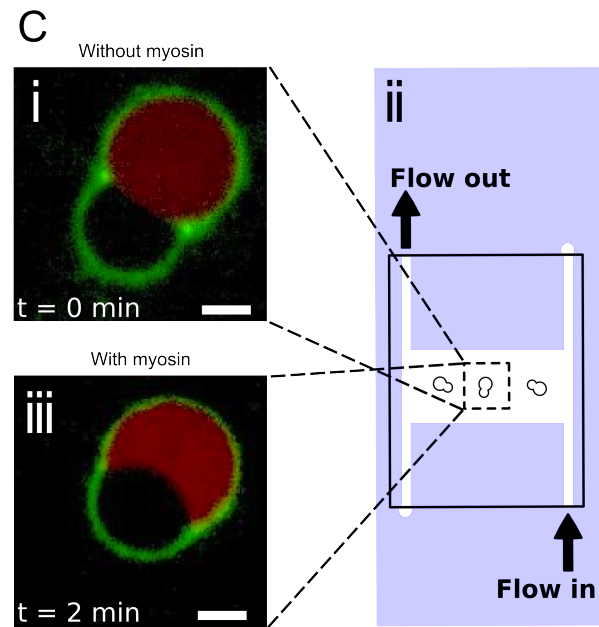


Figure 4.4: i) Flow-chamber designed for buffer exchange. Doublets are visualized in the middle horizontal channel of the H shape chamber to avoid movement during the buffer exchange. Spinning disk images of the doublet before i) or after iii) myosin II injection. One liposome contains the fluorophore SRB (red) to visualize the interface of the doublet. The actin cortex is labeled in green. Scale bar 5 μ m.

4.2.4 Geometrical parameters

To study the doublet geometry we model each liposome as well as the interface between them as two spherical caps with their respective center and radius, as sketched in [figure 4.5](#).

The center position in 3D (X,Y,Z) and the radius (R) of the three spherical caps completely determine the doublet geometry, though it is interesting to look at other parameters of the doublets which are :

- the total volume of the liposome doublets V
- the contact angle between the two liposomes
- Each of the “half”-contact angles which are the angle between the interface and each of the liposomes θ_1, θ_2
- The distance between the liposome centers.

4.3 Experimental Observations

4.3.1 Effect of myosin-II injection

We image the liposomes doublets in an open chamber either in phase contrast and epifluorescence, or spinning disk microscopy in the red (sulphorhodamin) and green (actin) channel.

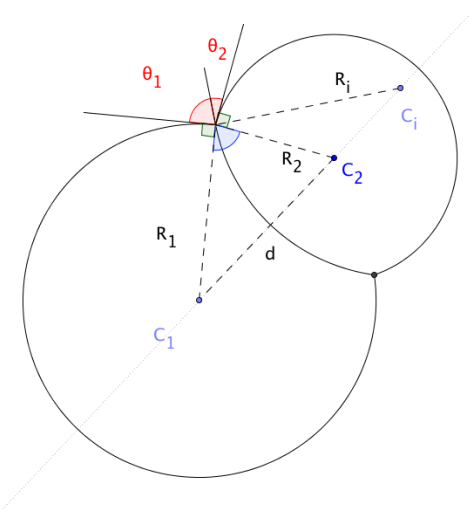


Figure 4.5: Notation of parameters for the doublet model: R_1 , R_2 , R_i are respectively the radius of the liposome 1, the liposome 2 and the interface. d is the distance between the liposome centers. θ_1 and θ_2 are the angles between the tangents of the liposome surface and the tangent to the interface at the contact line. The total contact angle θ is the sum of θ_1 and θ_2 .

Muscle Myosin II that forms *bipolars filaments* (page 14) is carefully injected into the chamber, and leads within minutes to a shape change (Fig 4.6) of the doublets due to the contraction of the actin cortex.

The distance between the liposome centers decreases as the total angle $\theta = \theta_1 + \theta_2$ increases. The contact angle and other parameters of the doublets are obtained by fitting spherical caps onto the 2D epifluorescence images or on the 3D confocal stack as *described later* (page 87). In the absence of myosin, the contact angle θ is measured to be $\theta = 64 \pm 16^\circ$ ($n=18$) whereas in the presence of myosin II (200 nM) we find a value of $\theta = 86 \pm 21^\circ$ ($n=5$). Measurements of the contact angle after myosin II injection are done before the cortex ruptures as characterized in [Carvalho, Lemiere, Faqir, et al. 2013].

4.3.2 Relation between the angles and tension

Each liposome has its respective tension τ_1 , and τ_2 . In the absence of the biomimetic acto-myosin cortex these tensions correspond only to the tension of the liposome membrane. The interface between the two liposomes is formed by two lipid bilayers, and the inter-facial tension is composed of two contributions: The tension of the lipid bilayer, noted τ_i , and the adhesion energy per surface unit W due to the biotin-streptavidin-biotin link between the two lipid bilayers. The total tension at the interface can thus be written $\tau_t = \tau_i - W$ [Maitre, Berthoumieux, Krens, et al. 2012].

As the movement of the contact line during the contraction is slow (order of $\mu\text{m}/\text{min}$) compared to pressure equilibration across the doublet, we can consider the contact line between the liposomes and the interface to be at equilibrium. Hence, we can apply Young's equation:

$$\sum_{k \in \text{interfaces}} \tau_k \cdot \vec{t}_k = \vec{0} \quad (4.1)$$

$$\tau_i \vec{t}_i + \tau_1 \vec{t}_1 + \tau_2 \vec{t}_2 = \vec{0}$$

In which t_k are the vectors tangent to the interface at the point of contact, as described in figure 4.7

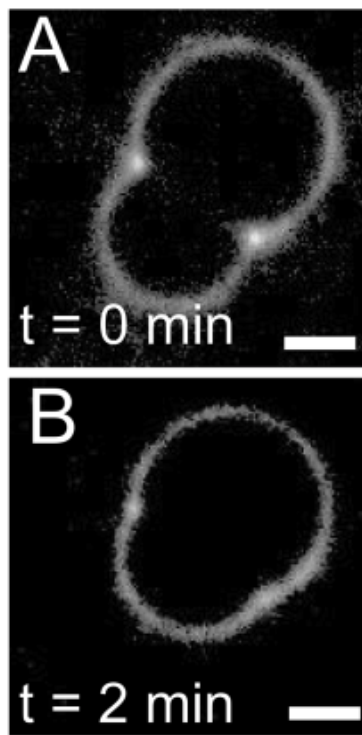


Figure 4.6: Doublets contraction showing green channel (actin): (A) doublet before myosin II injection. (B) doublet during contraction due to myosin II. Time=0 corresponds to myosin II injection. Scalebar is 5 μm

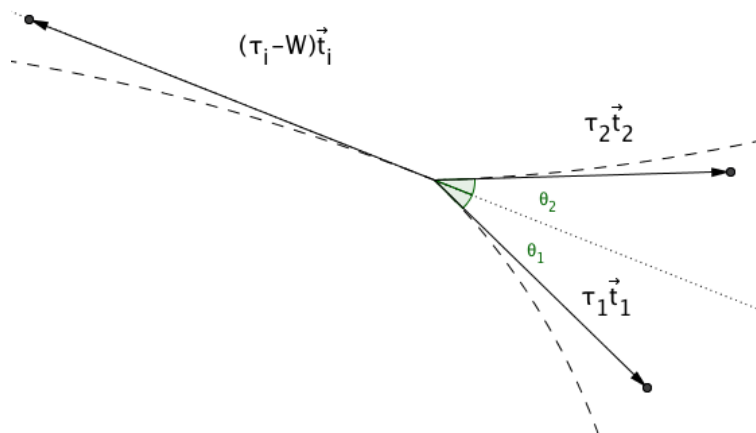


Figure 4.7: Equilibrium of the contact line. Each interfaces pull on the line with a force proportional to its tension. As the contact line is at equilibrium the some of the force compensate which allow to get a relation between the tensions and the contact angles.

This allows to relate the tension of each of the lipid layers and the angle between them at each instance of the contraction. We can in particular project the result of this equation onto the direction of the contact surface tangent (dotted line on figure 4.7):

$$\tau_i - W = \tau_1 \cos(\theta_1) + \tau_2 \cos(\theta_2) \quad (4.2)$$

And on the direction perpendicular to it :

$$\tau_1 \sin(\theta_1) = \tau_2 \sin(\theta_2) \quad (4.3)$$

These equations link the tension to the contact angle both before, during and after the contraction and hence remain correct during the experiment. In the following we will mark the values before the contraction phase by the suffix 0. Thus, for example $\tau_{i,0}$ refers to the tension of the interface before the addition of myosin, and τ_i refers to the tension of the interface at any instant of the contraction.

4.3.3 Contact angle dispersion

The value of the contact angle θ varies across different doublets both before and after the addition of myosin II. This reflects initial variations of tension in $\tau_{i,0}$, $\tau_{1,0}$, and $\tau_{2,0}$ from doublet to doublet. Such variations could be due to a difference in the liposome tension acquired during the different preparations, but also due to a variation of adhesion energy between doublets, or alternatively an effect of tension build-up during the formation of the actin shell. As the dispersion in contact angle is in the same order as the increase in angle upon addition of myosin, a statistical analysis of the contact angle before and during contraction is problematic. Thus to avoid this effect of dispersion, we follow the evolution of θ each individual doublet during time.

4.3.4 Tension of actin-shell

In order to investigate the increase of tension due to the acto-myosin network on liposomes, we first characterise the increase that is only due to the addition of the actin-shell in the absence of myosin. By destroying the F-actin via photo-bleaching (Fig 4.8) we compare the shape of the same doublets in the presence and absence of the actin-shell. It should be noted that it is established that the actin filaments are destroyed by bleaching as this process frees oxygen radicals that denature the actin monomers. Hence, the bleaching process actually destroys the actin cortex ([vdGucht, Paluch, Plastino, Sykes, 2005]). This investigation showed that the total contact angle changes by $3.4 \pm 2.0^\circ$ ($n=7$) after disruption (Fig 4.9) of the actin network. Thus we conclude that the change of tension due of the actin-shell is small and negligible compared to the change in tension we see with myosin.

4.4 3D observation

Three dimensional imaging of the doublets is necessary to get the correct contact angle. This requirement comes from the fact that in simple 2D epifluorescence images, the focal plane would have to correspond to the equatorial plane of the doublets for correct analysis. If this is not the case, the fit will produce a systematic underestimation of the contact angle. This is especially the case when doublets are of different radii as typically found in our experiments, where the liposomes composing the doublets have a ratio of R_1/R_2 between 1.15 and 1.82.

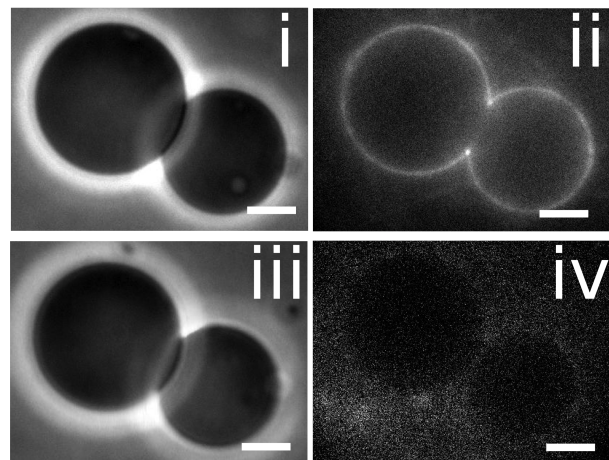


Figure 4.8: Image of an individual doublet coated with fluorescent F-actin before i) ii) and after iii) iv) actin cortex disruption. The actin cortex is visualized by epifluorescence ii) iv) and the doublet by phase contrast i) iii). Scale bar 5 μ m.

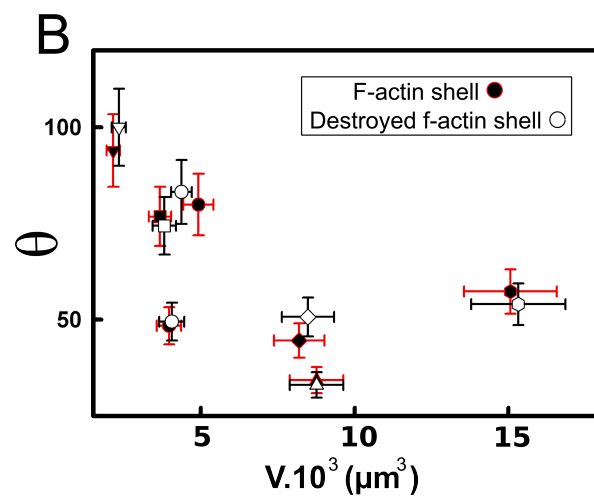


Figure 4.9: Measurement of the contact angle between the two liposomes forming the doublet before (black) and after (white) disruption of the stabilized actin cortex as a function of their volume.

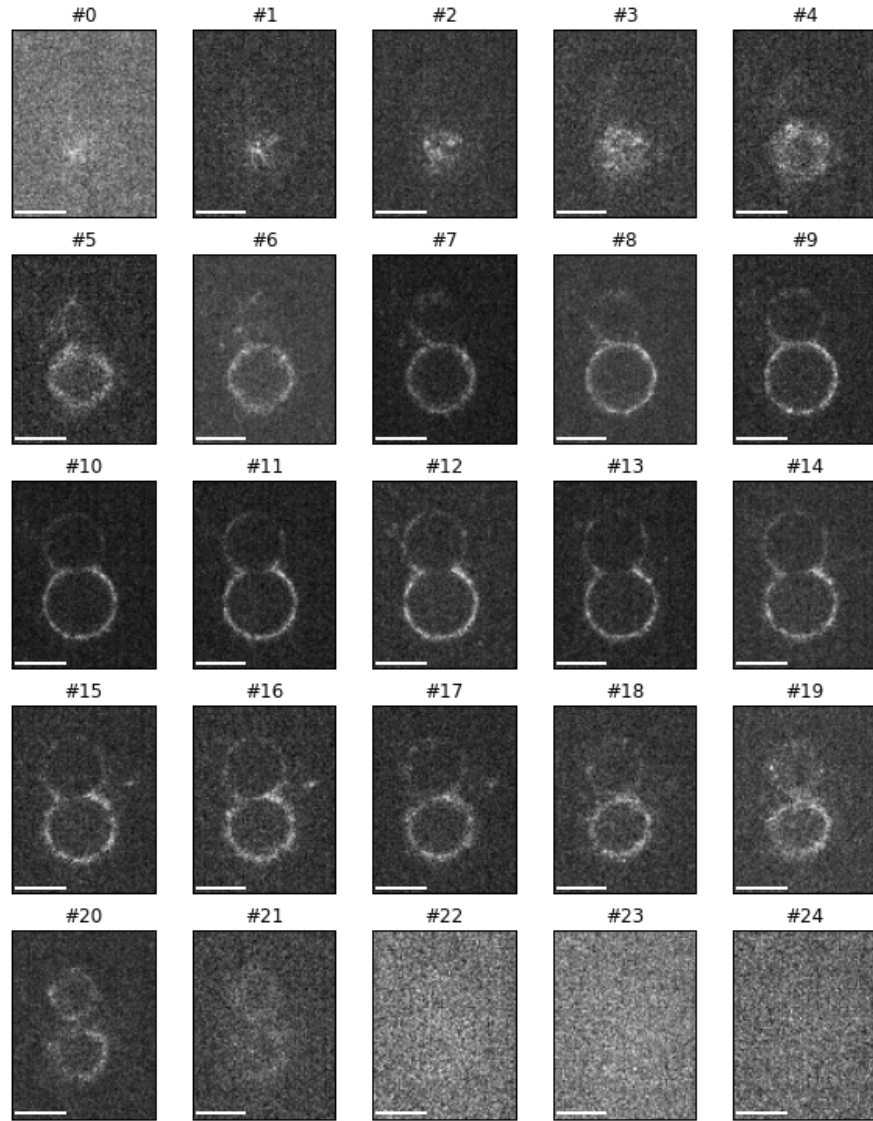


Figure 4.10: Confocal stack of an liposome doublet actin channel, 3D reconstruction in [figure 4.11](#). Note that there is no actin at the interface between the liposomes (Frames #11-#14). The distance between each image is $\Delta z = 0.85 \mu\text{m}$.

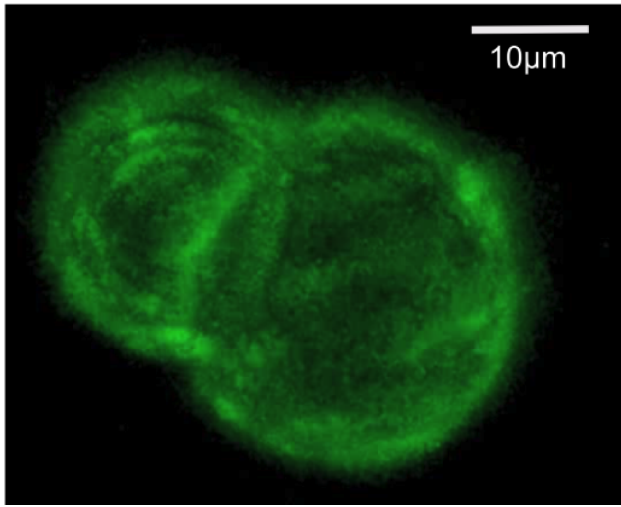


Figure 4.11: 3D reconstruction of a doublet surrounded by actin. The absence of actin on the interface can be seen more easily on [figure 4.10](#).

Time resolved 3D Spinning disk stacks ([Fig 4.10](#) with 3D reconstruction [Fig 4.11](#)) are recorded with a time resolution of less than 5 seconds per stack for an accurate determination of the different parameters of the doublet over time. The analysis reveals the contact angle θ ([Fig 4.12](#)), the volume of the doublet V ([Fig 4.14](#)) and the distance between liposome centers d ([Fig 4.13](#)). All these parameters are obtained by fitting spherical 3D caps on the 3D stack as explained [later](#) (page 87).

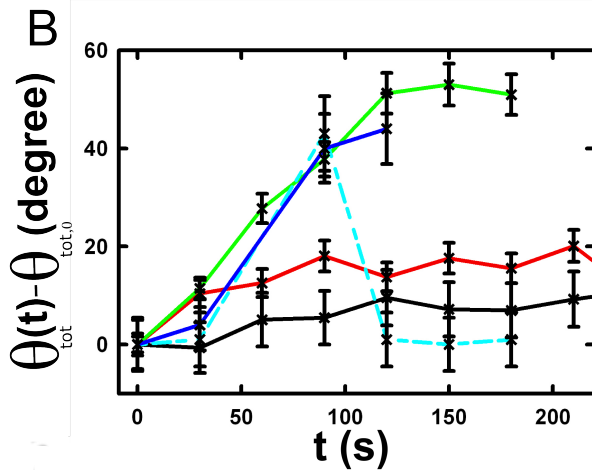


Figure 4.12: Evolution of the contact angle compared to its initial value as a function of time. Each doublet is represented by a different colors. The color code corresponds to the doublet shown in figure [4.13](#), [4.14](#) and [4.15](#). A special case is shown in the blue dashed line, where the actin cortex on the doublet ruptured, and the cortex is peeled off. The analysis of this case showed that the contact angle after rupture recovers its initial value.

During contraction triggered by myosin, we observe that the contact angle θ increases while the distance between liposome centers d decreases. During this process the volume remains constant within the error of 10%. These results are consistent with the measure of contact angle in freely adhering cell doublet

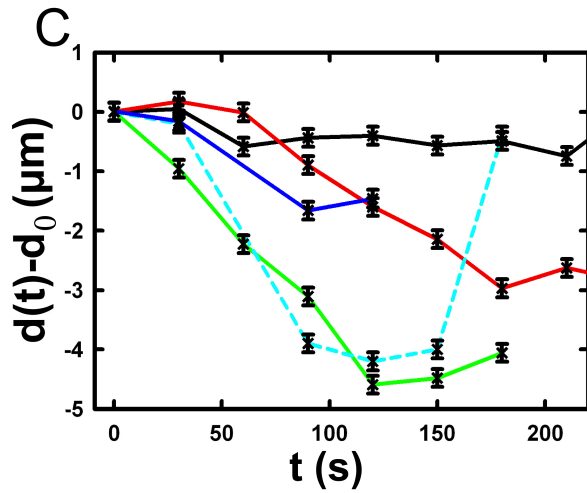


Figure 4.13: Evolution of the distance between liposome centers as a function of time. Same color code for same doublets as in figure 4.12, 4.14 and 4.15. Again the doublet with the ruptured cortex recovers its initial parameter values.

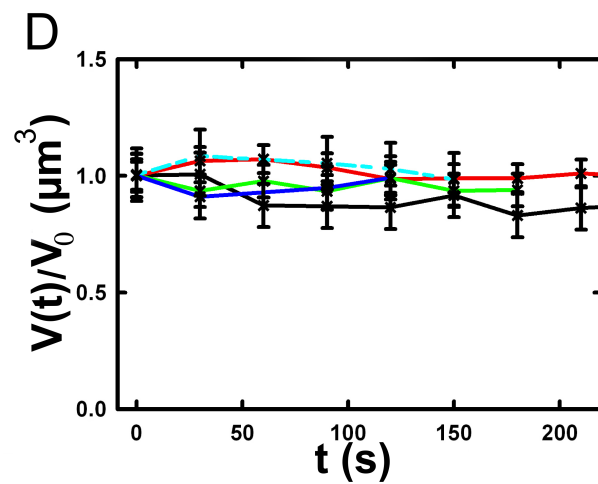


Figure 4.14: Evolution of the volume ratio over time. Same color code for same doublets as in figure 4.12, 4.13 and 4.15.

experiments done previously [Maitre, Berthoumieux, Krens, et al. 2012].

4.5 Discussion

4.5.1 Cortical tension is homogeneous for single doublet

Combining equation (4.3) with the finding that $\theta_1 = \theta_2 = \theta/2$ allows to infer the equality of tension on both side of the doublet during all the experiments. We can hence write $\tau_1 = \tau_2 = \tau$. This result is consistent with the fact that actin is distributed continuously all around the liposome doublet. Hence, myosin II minifilaments pull on a continuous shell. In these conditions equation (4.2) simplifies to :

$$\tau_i - W = 2.\tau(t).\cos(\theta(t)/2) \quad (4.4)$$

Where $\tau(t)$ and $\theta(t)$ are the tension and the angle at the time t after myosin injection. Assuming that $\tau_i - W$ may depend on a variability of the initial adhesion between liposomes. Since myosin does not operate at the interface between liposome as this is free from actin, it is reasonable to consider the tension and adhesion energy constant for a given doublets over time $\tau_i - W = \tau_{i,0} - W_0$. Therefore we obtain an expression of the tension $\tau(t)$ during the acto myosin contraction that reads :

$$\begin{aligned} \tau(t) &= \frac{\tau_i - W}{2.\cos(\theta/2)} \\ &= \frac{cst}{2.\cos(\theta/2)} \end{aligned} \quad (4.5)$$

Hence we can evaluate the tension relative to its initial value over time :

$$\frac{\tau(t)}{\tau_0} = \frac{\cos(\theta_0/2)}{\cos(\theta(t)/2)} \quad (4.6)$$

4.5.2 Relative increase in cortical tension

Interaction of myosin II filaments with a biomimetic actin cortex induces tension build up. The cortical tension, normalized to its initial value, increases and reaches a plateau where $\tau(t) = \tau_{peeling}$ (Fig 4.15) with the same trend as θ . Note that if the acto-myosin shell breaks and peels, the doublet recovers its initial shape (see dashed blue line for d and θ on Fig 4.12, 4.13, 4.14). The average relative tension is found to be $\tau_{peeling}/\tau_0 = 1.56 \pm 0.56$ ($n=5$) in 3D and $\tau_{peeling}/\tau_0 = 1.25 \pm 0.15$ ($n=5$) in epifluorescence, in agreement with discussed expected underestimation of the contact angle in epifluorescence measurements.

4.5.3 Cortical tension increase in doublets and in cells

In cells, cortical tension can be as low as 50 pN/ μ m in fibroblast progenitor cells [Krieg, ArboledaEstudillo, Puech, et al. 2008] and can go up to 4000 pN/ μ m for dictyostelium [Schwarz, Neuhaus, Kistler, et al. 2000]. Surprisingly, when myosin activity is affected, either by drugs or by genetic manipulation, the cortical tension only decreases by a factor of about 2. Cells are also observed to round up during division in which an increase of tension by a factor of two is sufficient [Stewart, Helenius, Toyoda, et al. 2011], [Kunda, Pelling, Liu, Baum, 2008]. Our *in vitro* reconstruction is able to reproduce similar changes of cortical tension as we observe a cortical tension increase by a factor of up to 2.4.

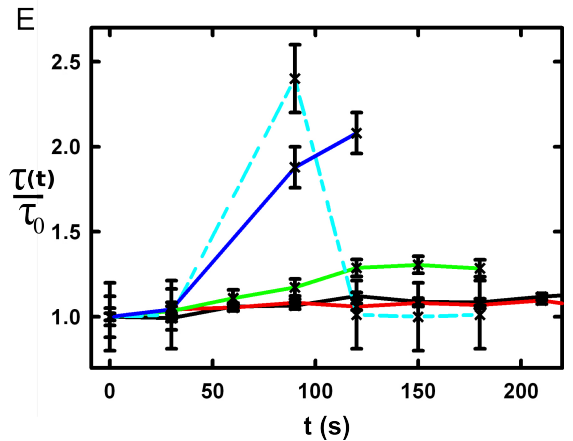


Figure 4.15: Increase of the tension ratio between the tension $\tau(t)$ at time t and the initial one τ_0 . Same color code for same doublets as in figure 4.12, 4.13 and 4.14. The actin cortex rupture in the blue dashed line also presents the highest relative tension increase.

4.5.4 Different contributions for cortical tension

Cortical tension is the sum of the membrane tension and the tension due to the acto myosin cortex. We question how the membrane contributes to cortical tension and in our assay we show that it may account for approximately 50% of the cortical tension in some cases. In suspended fibroblast cells, membrane tension is estimated to be 10% of the cortical tension [Tinevez, Schulze, Salbreux, et al. 2009]. When polymerisation of actin is stimulated, the cortical tension is multiplied by a factor of 5 showing a strong dependence also with actin dynamics [Tinevez, Schulze, Salbreux, et al. 2009]. Hence the residual tension in cells might be due to actin dynamics which is absent in our experiments. How actin contribute to cortical tension is still an open question that needs to be addressed in the cell geometry. Whereas actin polymerisation outside a liposome has been shown to generate inward pressure, how this can be translated to tension in a different geometry is not yet clear. *In vitro* assays are on their way to mimic actin dynamics in cells [AbuShah, Keren, 2014] and will allow to unveil the mechanisms of tension build up by actin dynamics, which is the remaining module that needs to be understood. The effect of myosin and of the membrane being clarified in this study.

4.5.5 Conclusion

We provide a biomimetic reconstitution of the tension build up by acto-myosin contractility using liposome doublets. Cortical tension changes are visualized *in situ* over time by analyzing doublet shape changes. This method allows us to directly quantify the relative increase in tension due to myosin, separately from the one due to actin dynamics. Understanding the contraction of composite systems that are rebuilt brick by brick to finally model a living cell will hopefully lead the way towards for a reconstitution of complex systems like tissues.

4.6 3D fitting

Obtaining the geometrical parameter of doublets remains challenging as in classical phase contrast and epifluorescence microscopy the acquired images only capture a single focal plane of the doublets. This

makes the analysis difficult as the observation plane should be the equatorial plane of the doublet.

In order to achieve good precision in the measurements of the contact angle we decided to use confocal microscopy and acquire evenly spaced z-stacks. From these stacks the 3D structure of a doublet was reconstituted. Using the 3D structure of the doublets allows to recover the geometrical parameters and the contact angle.

To determine the geometrical parameters of the doublets we modeled the doublets as two intersecting spheres, determined the expected 3D images and adjusted the parameters of the model to resemble the obtained experimental data.

I was responsible for developing a fast and precise method to reliably and automatically recover the geometrical parameters of the liposome doublets based in the image stacks acquired using spinning disk microscopy. In the following part I will develop the principle of this method and the result on liposomes doublets.

4.6.1 First step: Fitting a single liposome

In this part we show the principle that allow us to determine the 8 geometrical parameter that characterise a doublet: 2 centers (X,Y,Z) and 2 radii (R_1 and R_2).

As the principle for finding the geometrical parameter does not differ with the number of dimensions, the presented methods can be applied even in higher dimensions (e.g. deformed ellipsoid liposome, or multi channel imaging). Furthermore, the principles remain the same also in a space with less dimensions, so we will restrict our discussion to a single liposome in a 2D plane (X,Y position of centers and R, radius) hence reducing the parameters to be determined to six instead of eight.

Experimentally, liposomes are observed using fluorescently labeled actin that forms an homogeneous micrometer sized actin shell. In the observation plane, the liposome is a bright ring of given thickness (we will refer to this as the *expected signal*), on top of this image is the experimental noise where the principal noise sources are identified to be the presence of fluorescent actin monomers in the buffer solution and electronic noise from the CCD camera. Eventually, the noise in the outside buffer due to monomeric actin can be higher than inside which is free of actin.

The signal from a liposome and the addition of noise can be replicated numerically as seen on [figure 4.16](#).

The *expected signal* can be modeled numerically using several parameters of the system (center and radius of liposome, point spread function of microscope, ...).

To find the correct parameters for the doublets we will numerically correlate the acquired data with the numerical model and search for the correlation that correspond best to the real image. The correlation between the model and the images data can be written.

$$r_{xy} = \frac{\sum_{i=1}^n (x_i - \bar{x})(y_i - \bar{y})}{(n - 1)s_x s_y} \quad (4.7)$$

In which x_i are luminosity values of each of the n pixels in the acquired data, y_i are the luminosity of the pixels in the model \bar{x}, \bar{y} correspond to average values over the images, s_x and s_y are the standard deviation of the luminosity values.

As the monomeric fluorescently labeled actin and the electronic noise are dominant in the acquired images, we can assume a uniform noise on top of the *expected signal*. The correlation between the model and the

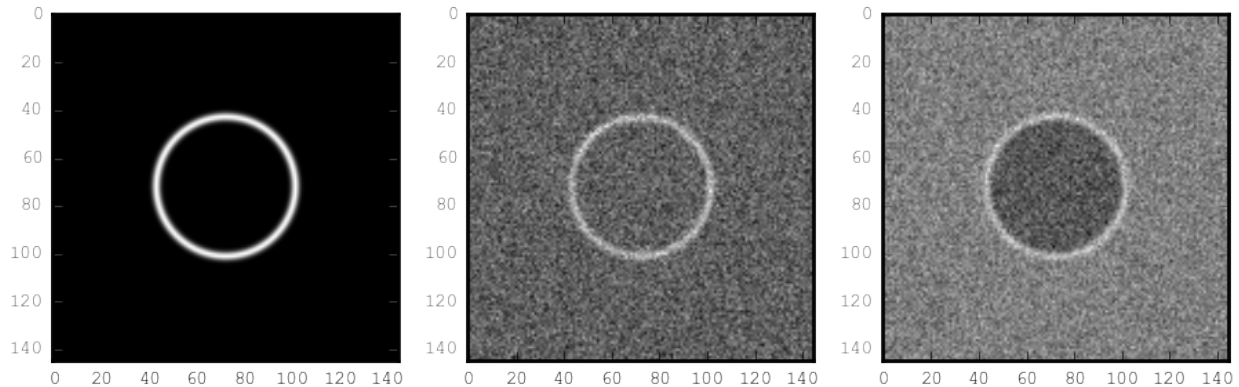


Figure 4.16: Left : A simulation of liposome fluorescent image consisting of an uniform shell or membrane (*expected signal*). Middle: Same Image Adding Gaussian noise. This simulates one plane of a confocal Z-stack. Right: Simulation of liposome with fluorescently labeled actin shell in a fluorescent external buffer and non fluorescent inside buffer.

noise is in average uniform.

$$r_{noise,model(params)} = cst \quad (4.8)$$

And the correlation between the *expected signal* and the model is expected to be maximal for the parameters of the model that equal the real geometrical parameters of the doublets.

$$\arg \max_p (r_{data,model(p)}) = \arg \max_p (r_{expectedSignal,model(p)}) \quad (4.9)$$

In which $\arg \max_p$ stands for the argument of the maximum, that is to say, the set of points of the given argument for which the given function reaches its maximum value. Thus searching for parameter values that maximize the correlation between the model and the data implies finding the geometrical parameters we are interested in.

We can test the ability to do this numerically by generating data, adding noise to it and trying to recover the parameters of the *expected signal*.

By looking at the value of the correlation between the generated data and the model as a function of model parameters, we can check that the correlation values are maximal when the model center value correspond to the *expected signal* center value (Fig 4.17), and when the radius of the model liposome has the same radius in the model correspond to the radius in the generated data (Fig 4.18).

Using minimisation techniques we can search the parameter space of the model and maximise the correlation between the model and the experimental data. We then recover the geometrical parameters of the liposomes. This can be done by efficiently computing the value of the correlation within a few hundreds of points and which gives access to the liposomes' geometrical parameters, here position and radius.

4.6.2 Fitting a doublet

The determination of the contact angle on epifluorescence images or phase contrast images often results in an underestimation as the imaging plane is not necessarily one of the doublets equatorial planes. Moreover, most determination of the contact angle on phase contrast and epifluorescence images are done manually

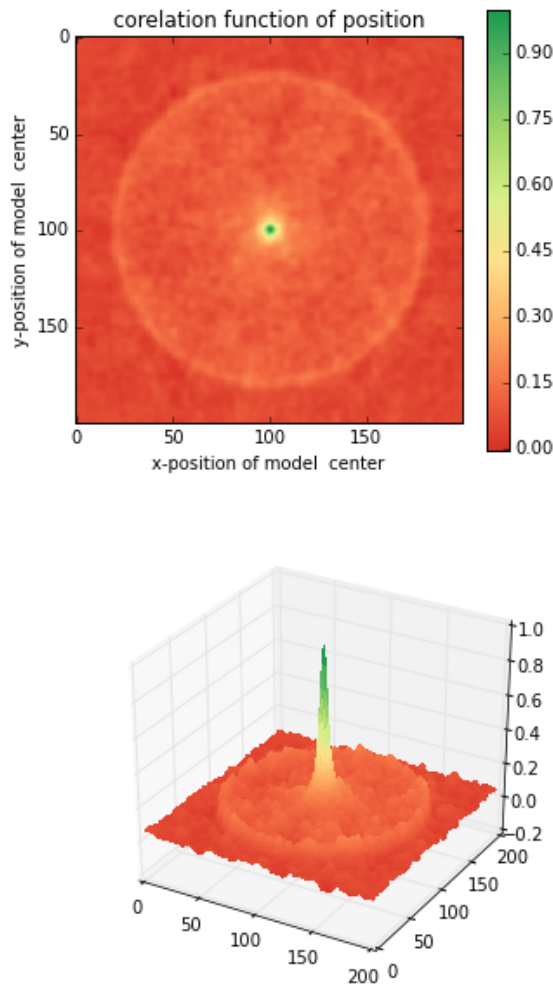


Figure 4.17: Value of the correlation as a function (arbitrary units) of two of the fit parameters. The radius of the liposome in the model is taken as equal to the value of the *expected signal*, and the position of the center is varied in the X and Y direction. The value of the correlation is maximal for the position of the center in the model that equals the center of the *expected signal*. We can see local maxima on the 3D representation that are well below the value of the global maximum. The peak at the global maxima is sharp, hinting that the search of the maxima need relatively good initial parameters (lower than $\sim 1/10$ of liposome radius). The sharpness of the peak point that corresponds to the best fit parameters on experimental data should be robust.

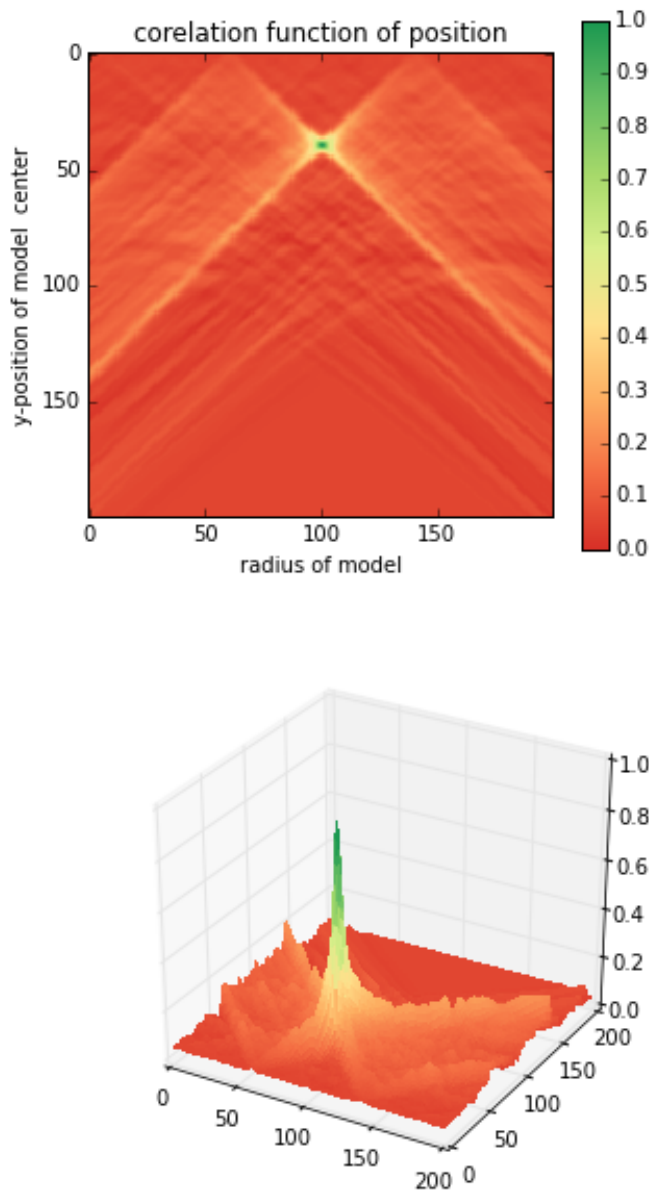


Figure 4.18: Same as [figure 4.17](#) with Y position of the center taken as equal to the expected signal, variating X position of the model and radius of the liposome. The graph shows the same properties as before.

[Maitre, Berthoumieux, Krens, et al. 2012] and are subject to experimenter bias as the experimenter draws the tangent lines at the contact point between the liposomes. Thus we decided to develop fitting routines for the acquired 3D confocal stacks. In our case we avoid the usage of fluorescent lipids that could artificially change the tension of the membrane.

As sketched in figure 4.2, the doublets are covered with a thin micrometer-thick layer of fluorescent actin filaments, which we image by confocal spinning disk microscopy. As the actin-layer is attached to the membrane and the contact angle is defined as the angle between the lipid bilayer, imaging the actin-layer corresponds to the angle between the inner surfaces of the two actin networks present on each liposome.

Thus in order to determine the geometrical parameters of the doublets we need to also model the actin shell. As the liposomes in contact are two spherical caps the uniform actin layer will also form two spherical caps with a given thickness. The total image is thus the union of two spherical caps blurred by the point spread function of the microscope. This can be seen on figure 4.19. We can see on this image that the doublet is here lying on the chamber surface. We checked in this case that the contact surface between the chamber and the doublet did not change during experiments.

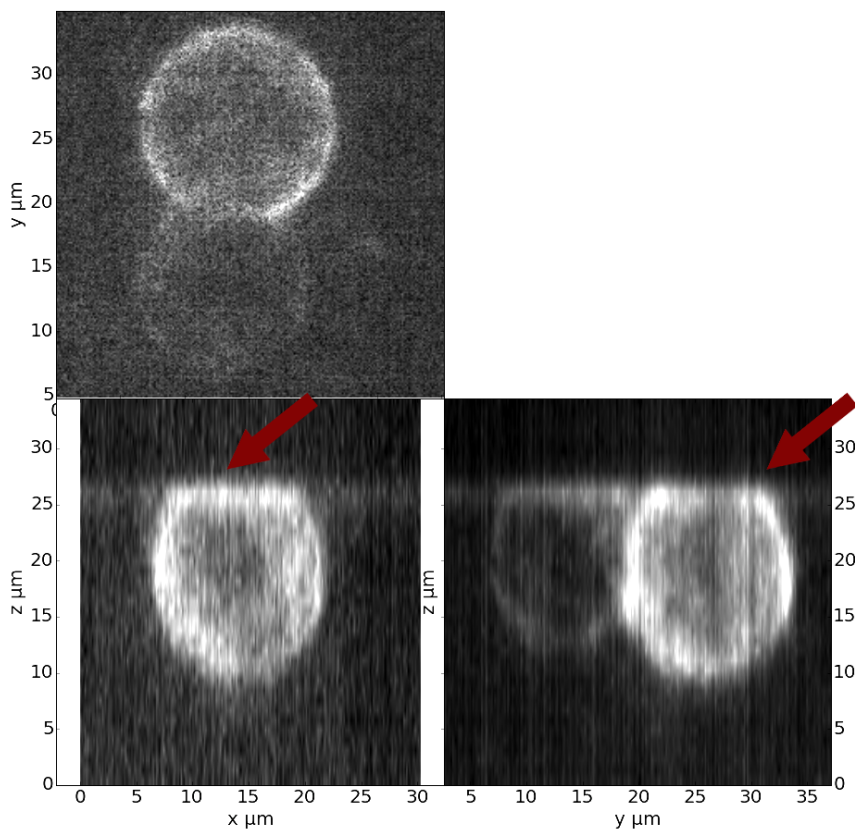


Figure 4.19: Maximum projection along X, Y and Z of recorded stacks, green channel represents actin. One can see that the liposome doublets are lying on the surface of the observation chamber (arrows).

As the contraction of the doublets is rapid, and the recorded 3D stacks contain a large number of frames. Hence it is crucial to be able to compute the model and the correlation in a reasonable time (less than an hour per images). To achieve this besides calculating the model as efficiently as possible one can replace the exact calculation of two spherical cap and the point spread function of the microscope by the union and subtraction of pre calculated spheres followed by a 3D numerical Gaussian blur (Fig 4.20).

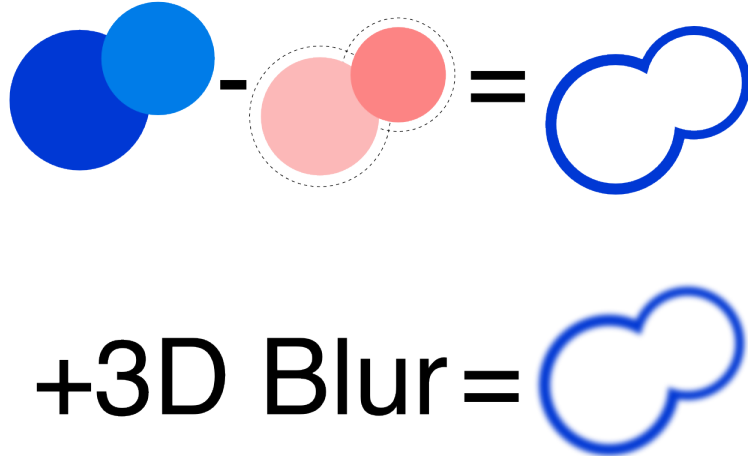


Figure 4.20: Principe of numerically approximating the two spherical caps as intersection of two spheres, followed by a 3D numerical Gaussian blur. The numerical speed-up compared to the exact calculation of the fluorescent density allows to make fits on doublets in minutes instead of hours.

However, the use of such numerical techniques is not without artifacts. In the case of discrete Z-stack that are not sufficiently spaced, the different radii in the fluorescent rings within subsequent stacks can lead to a “ring-artifact” (Fig 4.21) when using numerical Gaussian blur. In the case of a too pronounced “ring-artifact” a “ghost” spheres can appear around each liposome which can cause the fitting process of the doublets to fall into a local maximum of correlation, thus leading to wrong value of the geometrical parameters.

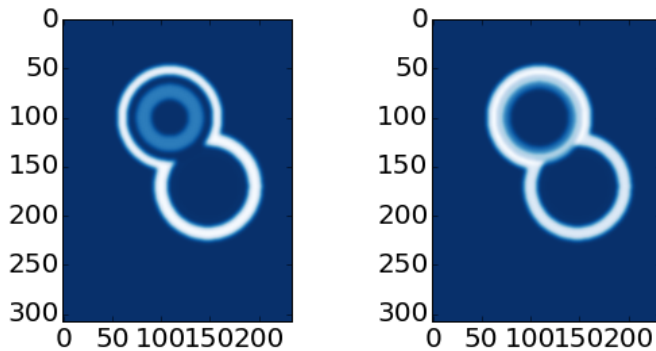


Figure 4.21: Left : One plane of the numerical model with an exaggerated ring artifact due to an under sampling of the model in the Z-direction, stacks from “Far” Z leak onto the current Z-plane and form a ring. Right : Same plane of the model with enough sampling plane in the Z-direction do not show the ring artifact. In this case we use a sampling equal to the number of slice than the recorded data. (X,Y in arbitrary units)

In our case we have a sufficient number of planes per stack so that the numerical model with the same

sample size as the data do not show the ring artefact and have smooth transition near the position of the spherical cap. Though the ring artifact can be eliminated by oversampling/interpolating the model before the numerical Gaussian blur and under sampling afterwards to arrive at the correct number of pixels.

The size of the Gaussian blur can also be adjusted to be higher which will act as a regularisation function for the value of the correlation between the model and the acquired data (see Fig 4.22), thus smoothing or eliminating local maxima, but reducing the precision in the position of the maxima.

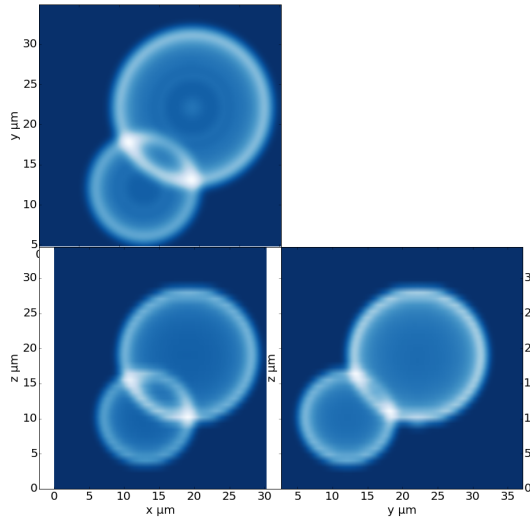


Figure 4.22: Maximum projection along X,Y and Z of numerical model, the “ring” effect can still slightly be seen near the pole of each liposome, but is not sufficient for the fit to be stuck in a local minimum.

The value of the correlation between the model and the experimentally recorded data can be maximised using already available functions, in particular we used the Nelder–Mead simplex algorithm as implemented in `scipy.optimize` python library. This gives us the 8 parameters of the doublets. Result of the fits are show in figure 4.23.

Using the fast Cython code ([Seljebotn, 2009]) also allowed to also speed up fitting to a reasonable time: one Z-stack of 3 millions pixels can be fitted in about 40 seconds. Thus allowing the fitting of a full 3D movie of a doublets contraction to be done in less than an hour for 30 to 40 frames.

To ensure robustness of the fits to doublet center displacement during acquisition, the initial parameter of the fit where chosen manually for each first frame of each sequences. The final fit parameters of each frame are reused as initial fit parameter for the subsequent frame.

In order to test robustness of the fit, the initial fit parameters where randomly modified by an amount of $\pm 1\mu\text{m}$, and we checked that the final parameters did not vary.

For a couple of parameters, the values of the correlation function can be plotted to check for the regularity of the function and the absence of local maxima. Figure 4.24 and figure 4.25 show the resulting correlation values.

The correctness of the fit is also checked visually to prevent errors in the procedure. The fit was found to

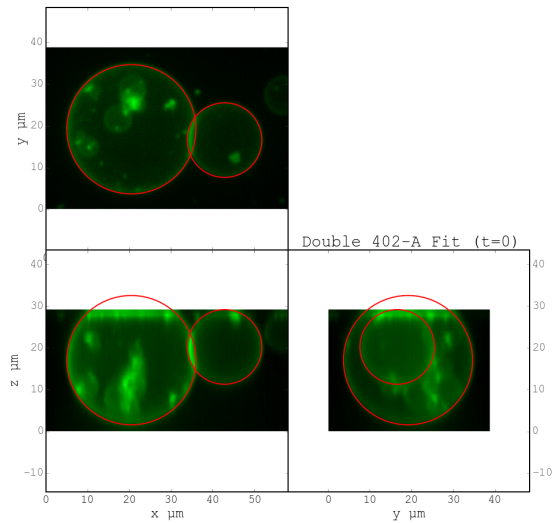


Figure 4.23: Maximum projection of confocal images in the X,Y and Z projection as well as the result of the fits shown as equatorial circles for the three direction of projection.

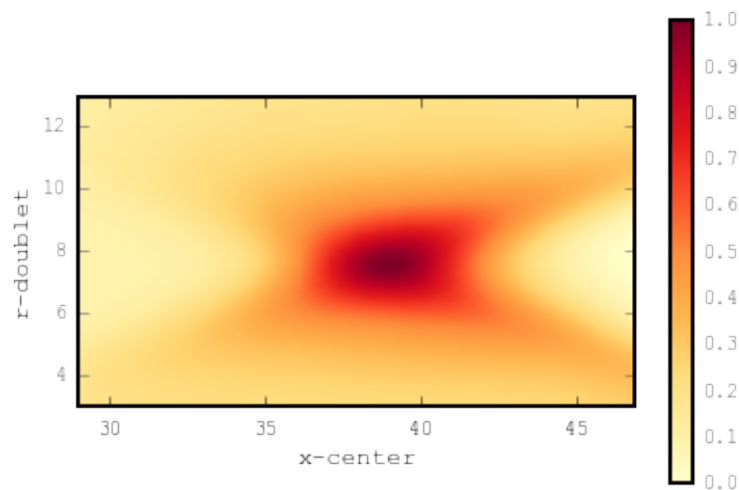


Figure 4.24: Correlation of the model and the data as a function of the center position of one of the model spherical caps along the X axis and the radius of this same spherical cap. Vertical axis in arbitrary unit.

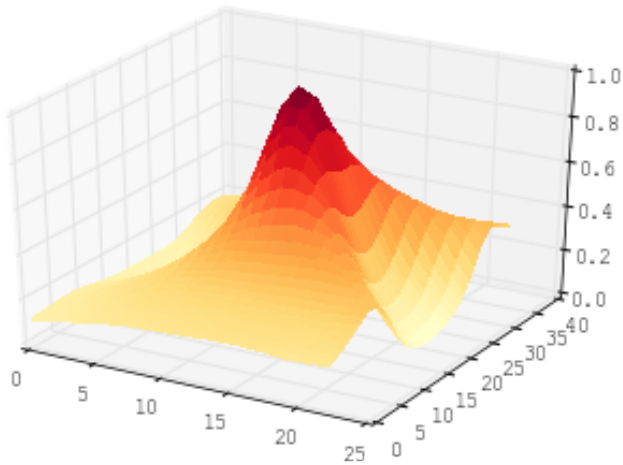


Figure 4.25: 3D representation of the data in figure 4.24, the shape of the function is the same as the simulation done with the *expected signal* in figure 4.17 and 4.18

be always accurate and coherent with manual measurements of the contact angle. When the red channel was also present and liposomes contained sulphorhodamin B, fits were additionally visually checked by using maximum projection of the red channel. (see Fig 4.26).

4.6.3 Discussion

In this part we show that by modeling the liposome doublet and using fluorescently labeled actin we are able to develop a technique that automatically and robustly determine the geometrical properties of the liposome doublets.

We note that the red fluorescent dye present in the inside buffer of the liposome could be used conjointly to the green channel in order to improve the quality of the fit, though this would require the extra parameters of the interface radius. As the computation time needed to fit the doublets increase rapidly with the number of parameters, this solution was found to be impractical. Moreover, the curvature of the interface being relatively small and the difference between the curved interface and a flat plane being close to the optical resolution, hence the fits risk to become unstable. The use of fluorescently labeled lipids for the liposome membrane also suffers from the same issues of extra parameter if one wants to recover the position of the interface.

4.6.4 Conclusion

We developed a robust and automated method to determine the geometrical parameters of liposome doublets. This allows to determine robustly the geometrical parameters of liposome doublets without experimenter measurement bias due to the selection of the illumination plane, resolution of optics and luminosity scale.

We have seen that liposome doublets with reconstituted acto-myosin cortices are a biomimetic system that allows to measure the changes in cortical tension with time. 3D fitting helped to quantify the tension by obtaining the corresponding contact angles.

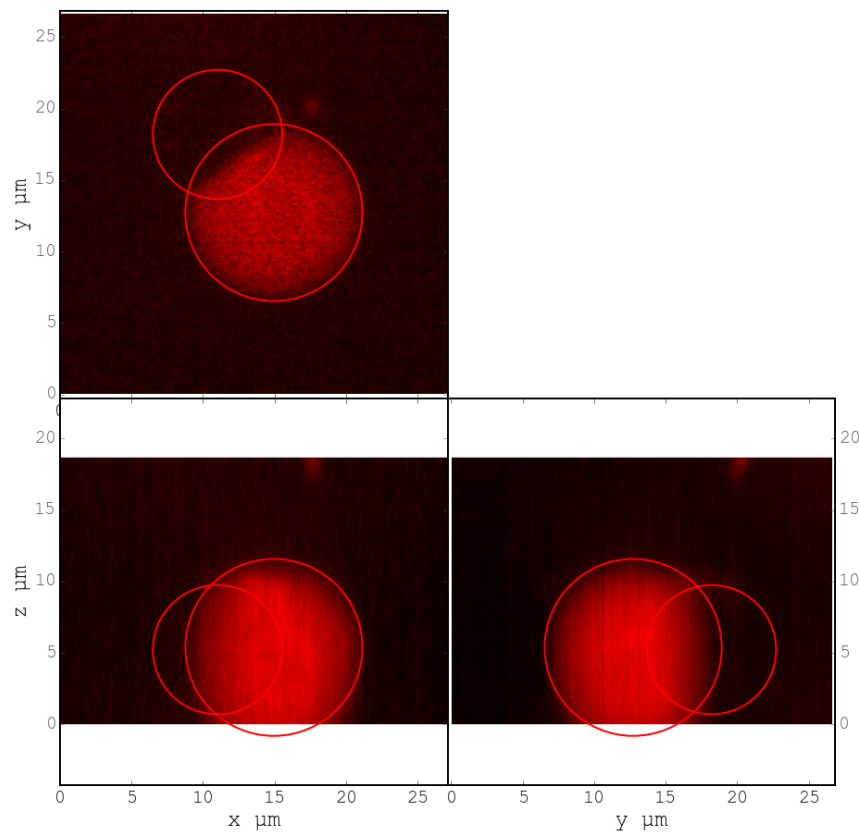


Figure 4.26: Maximum projection of the red channel (*sulphorhodamin*) and the fitted parameter for the doublet.

Actin Gels dynamics,

Observing the contraction of multiple liposomes doublets simultaneously and the ability to automatically determine the geometrical parameters allows more sample to be collected. Faster and more reliable data acquisition on actin network contractions will allow for a better understanding of the effect of actin network *in vitro* which also pave the way to reconstitution of more complex system.

ACTIVE CYTOPLASM MOVEMENT IN MOUSE OOCYTES

5.1 Introduction

Mouse oocyte are big spherical cells with a diameter of about 80 μm . Previous work has shown that the spindle positioning during meiotic cell division in oocytes depends on an actin meshwork that is present in the cell's cytoplasm [Schuh, Ellenberg, 2008]. This actin meshwork is regulated by formin that is localized to endogenous vesicles. Additionally, these vesicles recruit the myosin-Vb motor protein, that are known to drive the active movement of the vesicles in the cytoplasm [Holubcova, Howard, Schuh, 2013]. In a collaborative project with the group of Marie-Hélène Verlhac and her Postdoc Maria Almonacid at the Collège de France, I designed a way to measure cytoplasmic activity in mouse oocyte.

In figure 5.1 a typical mouse oocyte is presented where the nucleus can be seen to be positioned at the center of the cell. Current questions in this system relate to the mechanical processes during meiosis such as the chromosome migration, the asymmetric cell division and the positioning of organelles by the dynamic remodelling of the actin network. While our team did active and passive microrheology measurements on the timescales of 10 seconds, I developed a method that is suitable for longer timescales in the order of minutes, that are more relevant for the process of meiosis.

5.2 Oocytes

The cytosolic actin meshwork in oocytes is controlled by the activity of formins (Fmn2) that nucleate actin polymerisation and by the activity of the vesicle bound molecular motor protein myosin Vb that controls the dynamic movement of the vesicles in the actin meshwork. Hence it is of interest to study oocytes that have formin and myosin Vb deficits. In particular, we focused on three types: 1) Wild type oocyte, 2) oocytes prepared from Formin 2 invalidated female (Fnm2 $^{-/-}$) that lack the actin meshwork and 3) oocytes injected with the RNA coding for the dominant-negative tail of Myosin Vb (Fig 5.2), thus replacing the active myosin Vb on the vesicles.

5.3 Measure of activity

The diffusive like motion of actin positive vesicles that can be observed during oocyte meiosis is reduced in Fmn2 $^{-/-}$ and MyosinVb-tails oocytes when compared to the wild type. While the use of particle tracking algorithms to measure vesicle motion in oocyte is possible, it remains a complex process especially as the

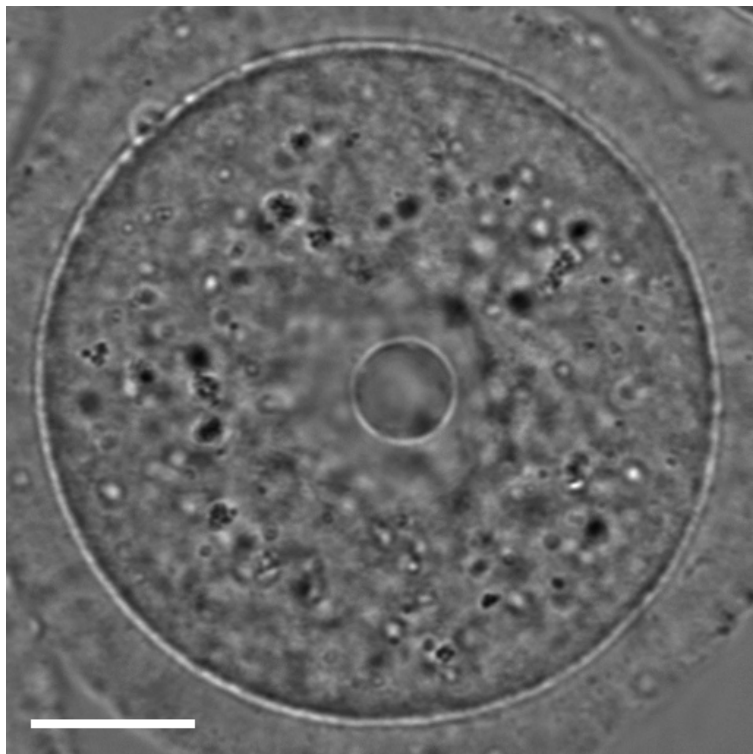


Figure 5.1: Bright field image of a mouse oocyte before meiosis (scale bar is 20 μm). The cell diameter is about 80 μm . The nucleus is positioned at the center of the oocyte during meiosis I by the help of the actin network. The positioning is a crucial factor for the normal division of the oocyte. The oocytes are a good reference system as they provide a clean spherical symmetry and due to their size give a good spatial differences between the cortex and the cytosol which helps in measuring spatial variations of mechanical properties and vesicle movement. Image Credit to Maria Almonacid, Collège de France.

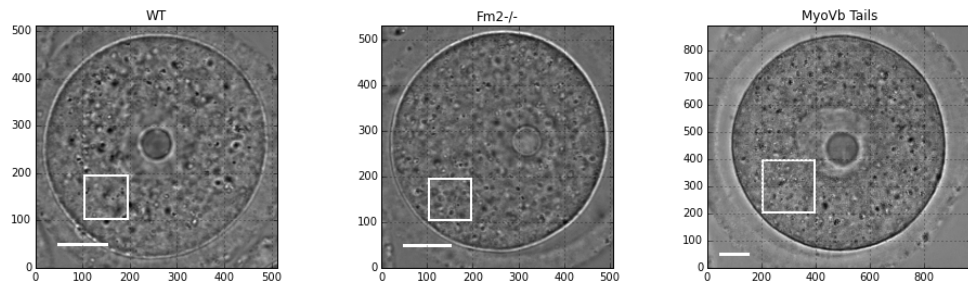


Figure 5.2: Bright field image microscopy of the 3 kinds of oocytes (Credit to Maria Almonacid, Collège de France). WT) Image of Wild Type Oocyte, Scale bar is 20 μm . Fmn2-/-) Oocytes extracted from females with invalidated Formin 2, theses oocytes lack the actin meshwork. MyosinVb Tails) Oocyte injected with the RNA coding for Myosin Vb dominant negative tails. These cells have a less active vesicle population. The white square gives an example of the region that is used for the analysis presented in this chapter.

vesicles may move outside the focal plane of the microscope. As a simple approach to measure the vesicle activity we decided to investigate the temporal variations of the bright field images in mouse oocytes.

We can compute the time dependent difference between predefined region of interest (ROI) in an image series to see how fast the bright field images change. Then we compare the result between wild type, Formin Knockout and MyosinVb dominant negative tails (Fig 5.3).

To get a quantitative measurement of the speed at which the difference of the images changes, we can compute the autocorrelation of bright field images thought time. The correlation of two images A and B of same dimension is defined as :

$$r_{AB} = \frac{\sum_{i=1}^n (A_i - \bar{A})(B_i - \bar{B})}{(n - 1)s_A s_B} \quad (5.1)$$

In which A_i and B_i are luminosity values of each of the n pixels of the images, \bar{A} , \bar{B} correspond to average luminosity values over the images, s_A and s_B are the standard deviations of the luminosity values. The correlation will give us a single value that characterise the similarity of the images. A correlation of 1 mean the images are identical, a correlation of 0, mean that the images have nothing in common, a negative value of correlation mean that the second image is globally dark where the first one is bright and bright when the first one is dark. We can thus obtain a measurement of similarity of images over time, that should start at 1 for $\Delta t = 0\text{s}$ between images. We expect it to decrease until it eventually reaches zero.

We can compare the decrease of correlation over time depending on the type of oocyte. In order to extract a single value that represents the activity, we can phenomenologically fit the correlation as a decaying exponential with an offset :

$$r(t) = (1 - off).e^{(-t/\tau)} + off \quad (5.2)$$

In which t is time, and τ is a characteristic time representing the correlation decay. The offset off represent the value of the correlation at infinite time to take into account artifacts in the chosen region of interest, and defects in the image that will not decorrelate over time.

Figure 5.4 gives typical examples of the result of the measured autocorrelation over time, and a single exponential decay fit.

The results show that the values of the characteristic time increases when the actin network is disrupted in Fnm2/- cells or when the source of its dynamics is removed by inactivating Myosin Vb. We can then use the inverse of τ as an indicator of activity.

Once we have define the activity of a region of the cytoplasm of the cell, we can repeat the measurement on different areas of the cytoplasm. This allows to reproduce a map of the activity in the cell as a function of the position (Fig 5.5).

The measure of the correlation characteristic decay time can also be done on a time sliding widows. This allows for the determination of activity of a particular area of the cytoplasm with time.

5.4 Conclusion

In this part we developed a method that allows to determine the cytoplasmic activity in oocytes by a non-invasive image analysis. This method also allows to measure the spatial and temporal variation of this

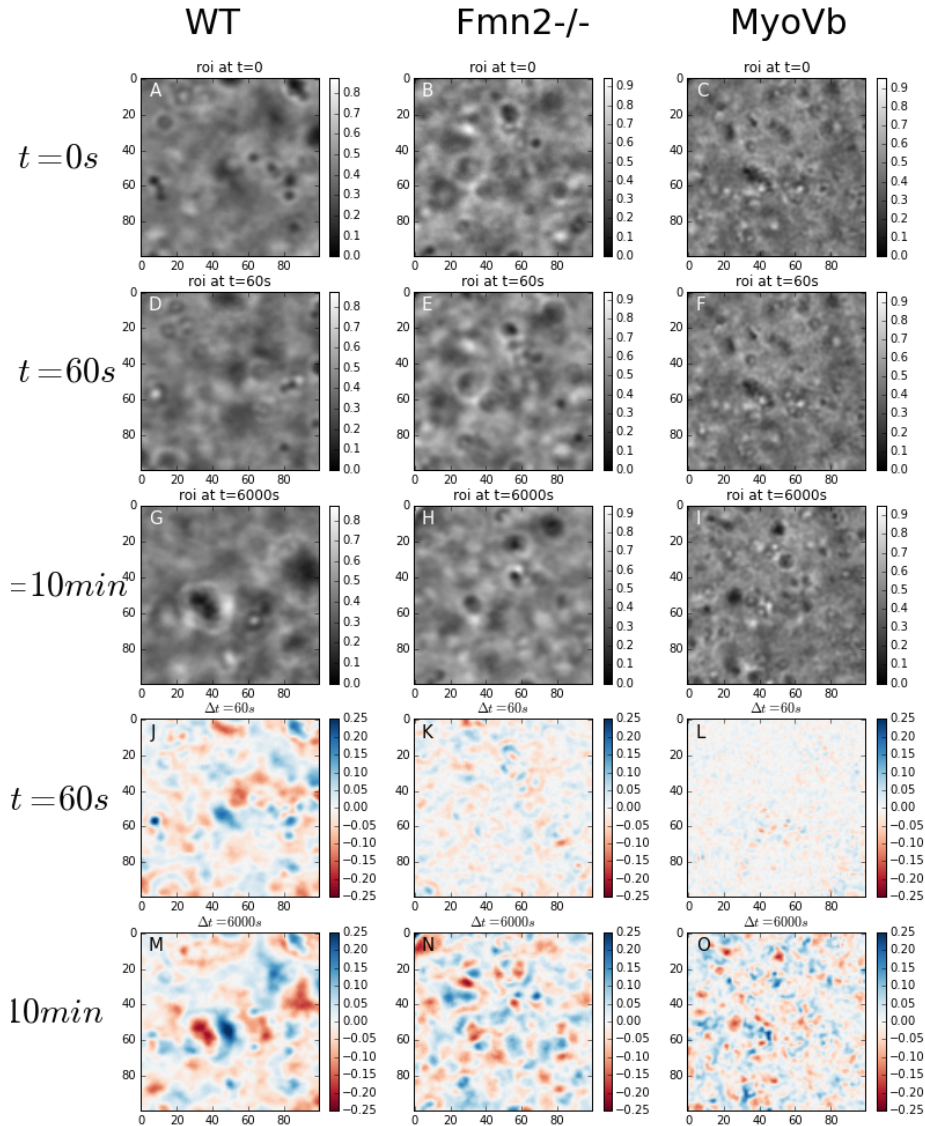


Figure 5.3: Bright field images of 3 types of mouse oocyte : Wild type in first column, Formin knockout in second, Myosin Tail dominant negative in the third. Row 1 to 3 represent the region of interest of [figure 5.2](#) ($20 \mu\text{m}$ side) for each kind of oocyte. Row 1 show region of interest at $t=0\text{s}$, row 2 at $t=1\text{min}$ and row 3 at $t=10\text{min}$. The color-coded difference between images at $t=0\text{s}$ and 60s are shown on row 4, and between $t=0\text{s}$ and 10min row 6. Blue indicate that the later image is brighter than the original one and red indicate that it is darker. For wild type oocyte, the difference of images reaches rapidly its maximum value (Image J and M similar), Whereas for Fmn2-/- and MyoVb the difference between images separated by 60 seconds (K,L) is much smaller than after 10 minutes (N,O) which can be seen as the (K) is whiter than (N) and (L) is whiter than (O). The change in cytoplasm is thus much faster in WT oocyte ($< \text{min}$) while it takes significantly longer in Fmn2-/- and MyosinVb oocytes.

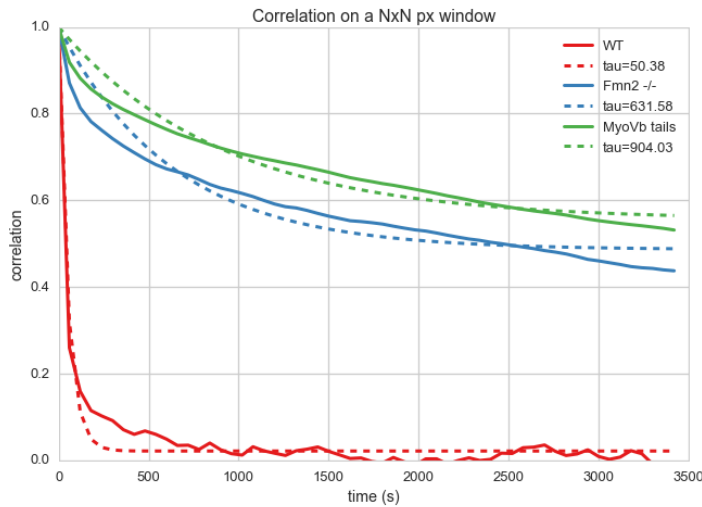


Figure 5.4: Decreasing autocorrelation of images intensity (solid line) over time, with exponential decay (dotted lines) as in (5.2). The characteristic decay time of the fit τ in the legend. We can see in the plot that the correlation of the images decrease much faster in wild type oocyte (red curves, $\tau \sim \text{minute}$) in compared to Fmn2-/- (blue lines $\tau > \text{hour}$) that lack the actin meshwork, or to dominant negative myosin Vb tails (green $\tau > \text{hour}$). While the fit quality is not impressively good, the overall change in the timescales is well captured.

cytoplasmic activity. A further advantage of this method is its flexibility regarding the timescales that are probed reaching from the second up to hours, noting that this is similar to the timescales relevant for oocyte maturation. Measurements on timescales of minutes are also complementary to techniques like active optical tweezer based micro-rheology that have difficulties in probing timescale beyond tens of seconds due to thermal drift and cell movement, but reach on the other hand much shorter timescales of below ms.

The proposed technique is currently actively applied by Marie-Hélène Verlhac and Maria Almonacid at the Collège de France. It is used to measure the activity of actin networks in oocyte and determine their effect on the meiosis of mouse oocyte and the organelle positioning.

1/ τ map for a wild type oocyte

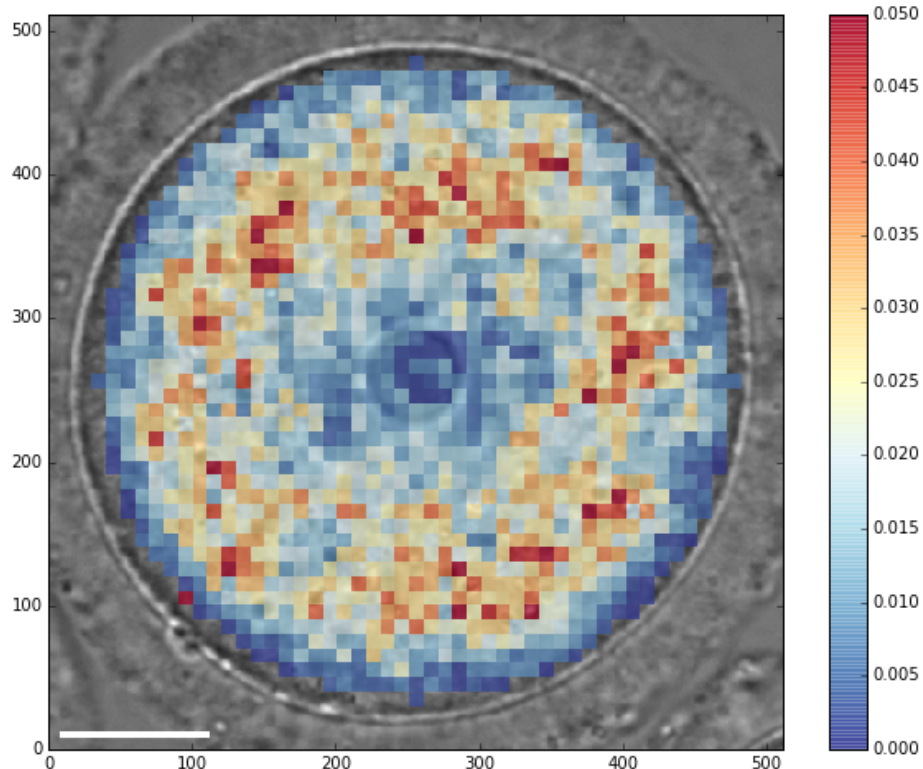


Figure 5.5: Activity for different region of 10 by 10 pixels of a wild type oocyte. Value of $1/\tau$ plotted as color square overlaying the analysed bright field image. Scale bar is 20 μm . We can see that the activity is near the nucleus is lower (blue) than in the middle of the cytoplasm.

CHAPTER

SIX

CONCLUSION

During my PhD I have investigated the mechanics of different actin networks found in living and biomimetic cells.

In the first part, the reconstitution of biomimetic cortices on polystyrene beads allowed to study the actin filaments that emanate from a thin reconstituted cortex. We determine that the mechanical effect of these actin filaments can be already perceived 10 to 15 μm from the bead surface, well beyond the surface of the reconstituted actin cortex ($\sim 1\mu\text{m}$). We coin these extending filaments “actin cloud”, which appears to be mostly elastic at the time scale of tens of second, and have a elasticity of a few Pascals at the most, which is several orders of magnitude smaller than the actin gel visible on the surface of the beads which has been measured to provide elastic moduli of kPa. Nonetheless, this actin cloud appears to be able to sustain forces sufficient to move organelles and seem coherent with several observation made *in-vivo* in cells.

We also studied the change in mechanical properties of this actin cloud under variable biochemical conditions, and in particular as a function of Capping Protein concentration. Using established polymer physics models, we are able to derive information about the structure of the network, like mesh-size and filaments length. We show that the evolution of the model parameters with the concentration of Capping Protein are coherent with previously observed phenomena: The distance offset δ in our model corresponds to the measured gel thickness by the position of the half fluorescence maximum.

Our description thus extends the current knowledge of reconstituted actin cortices. It shows a transition zone beyond the typically studied dense gels forming on the membrane. In this transition we find soft structures with different properties than found in the cortex. These properties have direct impact on the cells mechanics and could be directly involved in the positioning of organelles in cells. This work was recently accepted for publication in Biophysical Journal, with Matthias Bussonnier as the lead author.

The mechanical properties of cells and the actin cortex is not only driven by the dynamics of actin polymerisation. The effect of molecular motors is crucial to understand the well known change in acto-myosin cortex tension that has been shown to contribute to cell-cell adhesion and cell sorting.

In a second project of my PhD I focused on the measurement of cortical tension changes. In order to address the evolution of cortical tension over time, we developed a new biomimetic system composed of liposome doublets. Time resolved 3D imaging allowed the tracking of the key geometrical parameters over time to measure the relative increase of the cortex tension after the addition of myosin motors to a preformed actin cortex. I focused on the development of an automated method to measure the geometrical parameters of liposomes doublets to obtain accurate and robust measurement of contact angle independent from experimenter bias. This non-invasive measurement is a step towards a better understanding of the effect of myosin motors on the cortical tension in cells and its potential consequences on cell motility.

Actin Gels dynamics,

The mechanics and dynamics of the actin network is decisive for cells. In the case of mouse oocytes during meiosis, the actin meshwork is necessary for the correct positioning of different structure of the cells like the mitotic spindle and the nucleus. Without a correct actin network, or without the network dynamics driven by myosin, the oocyte meiosis is severely hindered, leading to non viable cells.

The third part of my PhD was done on these oocytes. In a collaboration with the group of Marie-Helene Verlhac at Collège de France, we used image analysis as a complementary technique to determine the evolution of cytoplasmic activity. In particular we measured the time dependent autocorrelation of bright field image series to determine how fast the cytosol arrangement changes, which is dependent of the overall organelle movement. We investigated the characteristic decay time of the autocorrelation function under different types of oocytes. Our results show that the overall activity strongly depends on the presence of the actin network and the molecular motor myosin Vb. The method developed also allows to determine the temporal and spatial change in activity in the mouse oocyte cytosol. It thus provides a simple method that can extract changes in network dynamics of living cells. This will allow a better understanding of the different phenomenon at the origin of organelle positioning in cells and the role of actin networks.

**CHAPTER
SEVEN**

APPENDIX

7.1 Mechanical detection of a long range actin network emanating from a biomimetic cortex Preprint

Preprint of paper on the actin cloud accepted for publication in biophysical journal under the reference *2014BIOPHYSJ303916R* and entitled *Mechanical detection of a long range actin network emanating from a biomimetic cortex*.

Mechanical detection of a long range actin network emanating from a biomimetic cortex

Matthias Bussonnier^{1,2,3,4,#}, Kevin Carvalho^{1,3,4,#}, Joël Lemière^{1,2,3,4}, Jean-François Joanny^{1,3,4}, Cécile Sykes^{1,3,4}, Timo Betz^{1,3,4,*}

1 Institut Curie, Centre de Recherche, F-75248 Paris, France

2 Univ Paris Diderot, Sorbonne Paris Cité F-75205, Paris, France

3 Sorbonne Universités, UPMC Univ Paris 06, UMR 168, F-75005, Paris, France

4 CNRS, UMR168, F-75248, Paris, France

Abstract

Actin is an ubiquitous globular protein that polymerizes into filaments and forms networks that participate in the force generation of eukaryotic cells. Such forces are used for cell motility, cytokinesis and tissues remodeling. Among those actin networks we focus on the actin cortex, a dense branched network beneath the plasma membrane that is of particular importance for the mechanical properties of the cell. Here we reproduce the cellular cortex by activating actin filament growth on a solid surface. We unveil the existence of a sparse actin network that emanates from the surface and extends over a distance that is at least ten times larger than the cortex itself. We call this sparse actin network the "actin cloud" and characterize its mechanical properties with optical tweezers. We show, both experimentally and theoretically that the actin cloud is mechanically relevant and that it should be taken into account as it can sustain forces as high as several pN. In particular, it is known that in plant cells, actin networks similar to the actin cloud have a role in positioning the nucleus, in large oocytes they play a role in driving chromosome movement and recent evidence shows that such networks even prevent granule condensation in large cells.

Insert Received for publication Date and in final form Date.

MB and KC contributed equally to this work.

* Corresponding author , E-mail: timo.betz@curie.fr

1 Introduction

The actin cytoskeleton plays a major role in cellular mechanics (1), force generation (2) and cell motility (3). Its mechanical properties have been extensively studied in the past decades (4). The detailed characterization and modeling of the actin cytoskeleton has proven to be a complex task, mainly due to the different structures formed by the actin biopolymer in cells. A major experimental approach to understand the architecture and detailed properties of the actin cytoskeleton is to reconstitute the structures commonly found in cells using purified components (5–8). Such controlled *in vitro* studies gave detailed insights into the mechanical properties of cytoskeletal structures like actin bundles (9), actin stress fibers (10) and cortical actin networks (7, 11).

Of particular importance is the mechanical contribution of the actin cortex, which provides a mechanical barrier supporting the plasma membrane against extracellular forces, but also acts as a steric obstacle for intracellular organelles. The actin cortex in cells was estimated to extend over a thickness of a few hundred nanometer underneath the cell membrane (12, 13). However, actin structures connected with the actin cortex appear to be key elements for organelle positioning in plant cells (14, 15) and nuclear positioning in oocytes (14, 16). Moreover, nuclear actin dynamics is involved in the movement of chromosomal foci in large cells like oocytes (17). A recent study shows even that such networks can prevent the condensation of nuclear droplets in large cells (18). How could these actin networks be connected to the cortex and can we envision that they could emanate from the actin cortex are the questions we address here.

How this cortical actin network is nucleated at the membrane is still a debate (19): whereas fluorescence techniques did not allow to detect the presence of the Arp2/3 complex and formins as nucleating agent of the actin network at the membrane (20), the branched structure that is observed under the plasma membrane hints for a contribution of Arp2/3 (12). Therefore, it is important to understand how networks produced by the Arp2/3 complex branching mechanism can impact cell mechanics and behavior. Such a branched and entangled actin network can be reproduced at the surface of beads covered with an activator of the Arp2/3 complex (11). The thickness of such an actin network was detected by epifluorescent microscopy and defined as the distance of the bead surface from the half-maximum intensity position along a radial profile. However, in these experiments, the drop of fluorescence away from the bead is not abrupt as shown in Fig.1A,B (11). This is what we explore here, by characterizing the mechanical and structural organization of this actin network further away from the zone detected by fluorescence. Our experimental system, based on the high force sensitivity of optical tweezers (see Fig.1C), allows to detect a mechanically relevant actin network that is inaccessible to direct visualization. This actin network emanates from the epifluorescence-visible part, which represents only a tenth of the full network size, and opposes resistance to indentation, thus revealing its important mechanical role.

The originality of our work is that we show that the Arp2/3 complex can give rise to a mechanically resistant actin cloud that spans over distances bigger than the dense and branched network close to the Arp2/3 activation. We characterize its mechanical parameters and show that this actin cloud allows sustaining forces able to displace objects on a cellular length-scale. Our findings suggest that even few filaments that may emanate from the actin cortex can lead to sufficient resistance and can generate forces that may explain the role of actin in organelle positioning within the cell. Similar filaments have been recently described to emanate from an nuclear actin cortex in starfish oocytes (21).

2 Materials and Methods

Proteins

Products are obtained from Sigma-Aldrich (St. Louis, MO) unless stated otherwise. Actin and the Arp2/3 complex are purchased from Cytoskeleton (Denver, US), and used without further purification. Fluorescent Alexa-488 actin is obtained from Molecular Probes (Eugene, OR). Capping protein (CP), profilin and pVCA are purified as previously described in (5, 22). Monomeric actin containing 10% molar of labeled Alexa-488 actin in G-Buffer (2mM Tris, 0.2 mM CaCl₂, 0.2 mM DTT at pH 8.0) at a concentration of 40 μM is obtained by keeping the solution one night on ice at 4°C before experiments.

Bead coating

Carboxylated polystyrene beads (Polysciences, Philadelphia, PA) of 4.34 ± 0.239 μm (Standard deviation) diameter were used from for actin and probe-beads.

Probe-beads: polystyrene beads are incubated for 20 min at 20°C under agitation with 10 mg/ml BSA at room temperature for 30 minutes in the working buffer (pH 7.4, 10 mM Hepes, 100 mM KCl, 1 mM MgCl₂, 0.1 mM CaCl₂, 1.8 mM ATP and 1 mg/ml BSA) and stored a few days at 4°C.

Actin-beads: polystyrene beads are first incubated for 20 min at 20°C under agitation with 2 μM pVCA and stored in working buffer (as above) for the day. Then they are placed in the polymerization mix, which is a solution of 4 μM G-actin, 12 μM profilin, 25 nM of Arp2/3 complex and various concentration of CP (0 to 50 nM) in the working buffer. 15 μL of this mix is sealed between coverslips.

Experimental procedure and data analysis

For the bead approach experiments, the pVCA coated beads which will later polymerize actin, are mixed with BSA-passivated probe-beads. Polymerization of actin on the beads is triggered by adding the bead mixture to the polymerization mix. Approximately 15 μL of the mix is sealed between two coverslips and observed in an inverse microscope (Olympus, IX71) using a 60 × water immersion objective (NA=1.2). Optical tweezers are used to trap and manipulate the beads in three dimensions by the gradient forces of a focused infrared fiber laser ($\lambda = 1064\text{ nm}$, YLP-1-1064, IPG, Germany). XY position and trapping forces are controlled by acousto optical deflectors (AODs, AA-Optoelectronics, France). Multiple traps are realized by time-sharing where the laser is switched within ≈ 6 μs between two positions, while resting 20 μs on each position. Position and force applied on each bead are measured using a quadrant photodiode (QPD) positioned in the back focal plane of the condenser (Fig.1). The trap stiffness is calibrated using the power spectral density (PSD) of trapped beads (23), and determined to be 34 pN/μm with the laser power of 119 mW as used during all experiments. The signal from the QPD is recorded with a

sampling rate of 500 kHz using a commercial data acquisition card (NI PCIe-6363, National Instruments, Austin, Texas), and processed using Labview (National Instruments) and Matlab (Mathworks, Natick, MA). Data acquisition and trap positioning are synchronized to recover the individual data for each bead. The signal from the QPD is converted to both the force exerted by the trap on the bead, and the bead position in the trap thanks to previous calibration.

To measure the viscoelastic properties we perform a force-indentation experiment. An actin and a probe-bead are selected, trapped and checked for compromising adhesion to the upper or lower coverslip. The presence of the actin network is confirmed using fluorescence microscopy (200W mercury lamp, Osram, Munich, Germany). All measurements are made on the dynamically polymerizing system, before symmetry breaking of the actin network.

To avoid too strong forces on the beads, which could push them out of the trap, single approach/retraction cycle were done while decreasing the minimal approach distance stepwise by 0.2 to 0.5 μm until the maximum force reached 8 to 10 pN. In these conditions the experimental protocol was stable and multiple consecutive approach experiments were done.

For the approach phase, the 3 fit parameters α , β and δ are estimated using a Levenberg-Marquardt algorithm as provided by Matlab. To facilitate stability in the fit algorithms, distances are expressed in μm and forces in pN.

Phenomenological fit of retraction curve

To fit the retracting part we introduce the function $A(d) = R\beta(d_c)^\alpha$ with $R : 0 \leq R \leq 1$, which corresponds to the elastic part of the actin-cloud, and is hence the discussed forces-distance curve Eq.2 scaled with the relaxation R as described in the main text (Fig.S4, dashed line, and Eq.9). $A(d)$ is fully determined form the approach and the relaxation data. For the plot in the retraction phase, we use the difference between the actual data and the expected elastic forces $A(d)$ to estimate the force that results from the actin cloud that has closed behind the bead. This is attributed for by a second powerlaw function $B(d) = -Z(d_c)^w$ (Fig.S4, red) which is fitted to the difference between the measured force during the retraction and $A(d)$ for the long distance (after force minimum is the retraction phase was reached).

To determine the curve plotted in Fig.4, we smoothly converge from $A(d)$ to $B(d)$ by using a the smoothing function $S(x) = \int_{\mathbb{R}} (1 - (x - t)^2) \times L(t)dt$ that corresponds to a convolution between the projected bead area and a linear ramp function L that is 0 for $t \leq 0$ and 1 for $t \geq 1$. The final model then reads:

$$F(d) = A(d) \times (1 - S(d)) + (A(d) + B(d)) \times S(d) \quad (1)$$

3 Results

Bead system

Polystyrene beads of 4.3 μm diameter are first coated with a nucleation promoting factor, pVCA, which is the VCA domain of N-WASP with the addition of a proline rich region (24). Beads coated with pVCA are then placed in the mix of purified proteins, containing 25 nM of the Arp2/3 complex, 4 μM actin, 12 μM profilin and various amounts of capping protein (CP). In these conditions, a network of actin filaments grows from the bead surface. In the following, these beads, once covered with their actin network, are called "actin-beads" (Fig.2A).

In the absence of CP actin filaments grow with their barbed ends away from the surface (24). The presence of CP limits the filament growth. In a spherical geometry of a bead, a stress builds up since new branches are formed at the surface of the bead, and symmetry breaks in a concentration range of CP from 15 to 35 nM (11, 25).

The choice of a bead diameter of 4.3 μm allows us to do measurements on an actin network that is homogeneous in the angular direction, hence before the appearance of heterogeneities which are a signature of symmetry breaking (Fig.1B). A characteristic symmetry-breaking time for those beads is indeed about 20 minutes (11). As our experiments are performed before symmetry-breaking, both the actin gel and the actin cloud are still growing, and no steady state has been reached. However, as previously investigated (11), the growth velocity is with about 0.1 $\mu\text{m}/\text{min}$ small, so that during the 2 minutes required for the approach experiments the actin-gel grows of about 200nm, negligible compared to the typical distances in the order of 10 μm studied in this work.

Experiment description

Using optical tweezers, the probe-bead is moved toward an actin-bead and the forces on each bead are monitored as shown in Fig.1C. Time shared optical tweezers are used to trap the probe- and actin- beads, see Materials and Methods for more details (26). The displacement of each bead from its trap center is recorded using a quadrant photodiode (QPD) as shown in

Fig.1C. For further analysis we exclusively use forces determined from the stationary trap that holds the actin bead, to avoid systematic errors that might arise from the trap displacement. The absence of interaction between bead and glass cover slip is probed before each experiment by moving it in all directions using the tweezers. A typical experiment starts as follows: the distance between traps is at least set to 20 μm , and beads are positioned at the trap centers. Then, the probe trap approaches the actin-bead at a constant velocity of $v=10 \mu\text{m/s}$ ($0 \leq t \leq t_1$, Fig.2A, left part). During this process, as soon as the actin-bead feels the force exerted by the probe-bead, it becomes off-centered in its trap (Fig.2A, $t \lesssim t_1$). The approach phase is followed by two other phases, a relaxation phase ($t_1 \leq t \leq t_2$; Fig.2A, middle part, white background), and a retraction phase ($t_2 \leq t \leq t_3$, Fig.2A, right part, light yellow background). During the retraction phase, the probe bead returns to its initial position with the same absolute velocity of 10 $\mu\text{m/s}$ as in the approach phase. The duration of the relaxation phase ($t_2 - t_1 = 3\text{s}$) is chosen to be long enough to allow relaxation to happen, and short enough for actin polymerization not to change the properties of the network. The time-dependent force on the actin-bead (Fig.2A) is converted into a force-distance curve as shown in Fig.2B,C where d is the distance between the surfaces of the actin-bead and the probe-bead. The force distance curve Fig.2B reads as follows : i) ($t \leq t_1$) the force between beads starts from an asymptotic zero value at long distance and increases as the distance decreases (green points), ii) ($t_1 \leq t \leq t_2$) the probe-bead stops and relaxation occurs. During the relaxation, the force decreases with a very little distance decrease (red points, up left in Fig.2B). iii) ($t_2 \leq t \leq t_3$) the force decreases, becomes negative, and eventually reaches asymptotically zero again when distance increases (blue points). Those curves are repeatable and show only small changes if multiple approach-retraction cycles are probed (see Fig.2C). Previous experiments suggest that for frequencies higher than 0.1 Hz, viscous relaxation becomes comparable to the elastic properties (27). To check the importance of stress relaxation during the approach phase we verify that the probe trap velocity did not affect the force-distance curves by performing experiments at variable velocities ranging from 5 to 30 $\mu\text{m/sec}$ (Fig.S1 in the Supporting Material). These experiments did not show any striking differences in the recorded measurements, and hence for the analysis of the approach phase we use an elastic model.

4 Experimental observations

Approach phase

The bead system provides a way to reconstruct actin cortices *in vitro*. Moreover, these reconstituted systems can be manipulated to investigate 3D mechanical properties of a biomimetic actin cortex in experimental conditions inaccessible to other microscopy techniques typically used to investigate single actin filament dynamics, like total internal reflection (TIRF). Optical tweezer and force measurements on the bead allow us to precisely probe for the actin network emanating from a bead in a 3D environment. To approximate the size of the actin cloud, we determine the distance d_0 (Tab.1, Fig.2B, dotted lines) where the forces on the probed bead become higher than the experimental noise of the force detection (2pN). The found values for d_0 remain large compared to the fluorescent actin gel thickness. Indeed, the probe bead already feels the presence of actin filaments at a distance from 13 μm to about 4 μm (Fig.1A,B; Tab. 1). This distance depends on CP concentration (Tab.1), but is always much larger than 1 μm , which has been established as an upper estimation of the actin network thickness e , previously measured as the distance of half-maximum fluorescence intensity (11) and Fig.1A.

As the bead distance decreases, the force gradually increases, until the trap stops at the minimal displacement distance. The force-distance data are fitted by a power law with fit parameters β , α and δ (Fig.2A,B).

$$F(d) = \beta \times (d - \delta)^\alpha \quad (2)$$

where we obtain a high fit quality measured by a median $R^2 = 0.97$. Since the power-law exponent, α , is found to be negative (Tab.1), δ corresponds to the offset distance between bead surfaces at which the force would diverge (vertical black line in Fig.2B).

We experimentally find a negative power law exponent close to -1 with a statistical distribution of $\langle \alpha \rangle = -1.10 \pm 0.38$ ($n=103$, mean \pm std) for all CP concentration probed (Fig.2D, inset).

This inverse relation hints for a far reaching network, or "actin cloud", which is mechanically evidenced here. In our experiments it is detectable over distances that are larger than the fluorescence estimated thickness of around 1 μm (Movie S1).

Due to the scale invariance of the power law, we can collapse all 103 experimental curves into a single master curve by normalizing the force with the point of maximal force (F_{max}) reached at t_1 , and the distance between bead surface at the minimal approach (d_{t_1} , Fig.2D). This rescaling procedure allows us to determine the power law exponent of all averaged data curves to be ($\alpha_{rs} = -1.06$) which confirms the -1 exponent.

Nonlinear elastic modulus

To determine the Young's modulus from the force distance curves, we use its definition as given by Hooke's law: $E = \sigma/u$, where $\sigma = F/(\pi R^2)$ is the stress on the projected bead surface, R the bead radius, $u = (d_c - x)/d_c$ the strain where we define $d_c = (d - \delta)$ and x as the the experimentally controlled bead position for the small deformations. Hence $du = -dx/d_c$ where the minus sign reflects the choice of the coordinate system for the deformation, which has to be consistent with the direction of the force to ensure a positive elastic modulus. Here we study the situation in which a predeformation of the gel of d_c is applied, and then we apply a stress σ and strain u when displacing the probe-bead by a small distance. In such a situation, the global Young's modulus as function of d_c reads $E(d_c) = (d\sigma/du)|_{d_c}$. The deformation-dependent Young's modulus can hence be expressed as the derivative of the force with respect to the deformation at the distance d_c to yield:

$$E(d_c) = -\frac{d_c}{\pi R^2} \times \left(\frac{dF}{dx} \right) \Big|_{x=d_c} \quad (3)$$

$$= E_0 \times d_c^\alpha \quad (4)$$

where $E_0 = -\alpha\beta/(\pi R^2)$. In this expression we use the fit function of Eq.2 to calculate the derivative. Interestingly, using the strain at a position d_c gives rise to the same power-law between the nonlinear Young's modulus and the measured force. It should be noted that experimentally we can only access the average mechanical properties between the probe- and the actin-bead. Hence, all reported values present mean values of the material between these two beads. The discussed model describes the reported mean values, and assumes an effectively averaged Young's modulus. Here $E(d_c)$ is then this global Young's modulus that measures the material properties of the actin cloud that is confined between the two beads. These values (Tab.1) are 3 orders of magnitudes smaller than the elasticity of the actin gel generated from an Arp2/3 activated bead (known to be $\approx 1\text{kPa}$ (28)). This large difference in rigidity might explain why the actin cloud was not observed in previous mechanical measurements such as micropipette, micro-needle deformation or AFM indentation that were sensitive to large forces in the nN regime. However, such small moduli are commonly found in loosely entangled actin networks (27). It also shows that the actin cloud is of a fundamentally different network type that results in such a drastic change of mechanical properties as compared to the dense actin gel found at the bead surface. Optical tweezers are the optimal measurement technique to determine such small elastic parameters.

Relaxation phase

In the 3-second resting phase, we observe that the beads move toward the center of their traps, corresponding to a force relaxation (Fig.2A, central part) during which the beads get closer to each other (Fig.2A, $t = t_1$ and $t = t_2$). The force-drop during the relaxation is typically of 20% (see Fig.S3).

Retraction phase

We observe a rapid decrease of the force towards negative forces leading to two different behaviors that may add up. First, a general tendency is that the rapid drop of the force is followed by a slow force increase through an inflection point (Fig.2B lower curve). Second, and only in $\approx 25\%$ of the experiments, we find evidence of rapid detachments that are identified by a sawtooth shape of the force-distance curve (Fig.S2).

Irreversibility

An important finding is that the approach phase does not superimpose with the relaxation and retraction phases, which indicates dissipation of energy during a cycle of approach and retraction. Apart from the relaxation phase, a contribution to this dissipation is the negative force that is reminiscent of the sticky behavior similar to AFM indentation/retraction experiments.

Influence of capping protein concentration

Actin filament length is controlled by the amount of CP in the protein mix (24). To check the influence of the CP concentration on the actin cloud we analyze experiments at 0, 10, 30 and 50 nM CP. As shown in Fig.3 and Tab.1, the value of the power law exponent α does not change significantly with CP concentration. In contrast, we find that the distance offset δ changes under variable conditions and the parameter β decreases five fold when CP concentration increases from 0 to 50nM.

5 Discussion

Approach Phase: Interpretation of the power-law

To further investigate this power-law exponent (of $\simeq -1$), we model the deformation of the actin cloud by the established theory of semiflexible, entangled polymer networks (29–31). In the approach phase, we focus on the elastic properties quantified by the deformation-dependent Young's modulus $E(d_c)$ and neglect any viscous term given that the force in this phase does not depend significantly on the approach speed. The Young's modulus E of semiflexible filaments is well studied and can be expressed as a function of filament contour length density ρ and the entanglement length L_e as $E = 2.(1+\nu).7.k_B T \rho / (5L_e)$ (31). The prefactor is model-dependent and includes the transition from shear to Young's modulus using the Poisson ratio. Previous studies have investigated the non-linear stiffening of actin gels for large deformations comparable to the presented approach protocol (32). For actin concentrations similar to the concentration used in our study, these previous experiments show that a linear description holds, and hence the proposed model should correctly describe the mechanics of the polymer network.

The entanglement length itself can be expressed as a function of density ρ and persistence length L_p as $L_e \approx L_p^{1/5} \rho^{-2/5}$ (31). For the general case of a compressible material, the only variable that might change under the strong deformation is $\rho \rightarrow \rho(d_c)$. Hence, we can express the Young's modulus as a function of density ρ that depends on the compression of the network, therefore noted $\rho(d_c)$:

$$E(d_c) = \frac{(1+\nu).14.k_B T}{5L_p^{1/5}} \times (\rho(d_c))^{7/5} \quad (5)$$

Using the experimentally found power-law, Eq.5 allows to infer a relation for the density $\rho \propto d_c^{5/7 \times \alpha}$. Using the scaling arguments that at the distance d_0 , which corresponds to the undeformed actin cloud, the density is ρ_0 , we can directly express $\rho(d_c) = \rho_0(d_c/d_0)^{5/7 \times \alpha}$. These changes in the density can be also used to estimate the Poisson's ratio of the actin cloud, which connects the distance dependent density and the deformation by $\rho(d_c) = \rho_0(d_c/d_0)^{2\nu-1}$. Hence, we infer for the Poisson's ratio: $\nu = 1/2(1 + 5/7\alpha)$. Due to the definition of ρ which corresponds to the filament contour length per unit volume, we can determine the average mesh-size ξ_0 of the undeformed network by $\rho_0 = 1/\xi_0^3$. Combining these expressions then leads to

$$E(d_c) = \frac{(1+\nu).14.k_B T}{5L_p^{1/5}\xi_0^{14/5} d_0^\alpha} \times d_c^\alpha. \quad (6)$$

$$= E'_0 \times d_c^\alpha \quad (7)$$

To determine the expected mesh-size, we can set E_0 as found in Eq.3 equal to Eq.6:

$$\xi_0 = \left(- \frac{(2 - \frac{5}{7}\alpha).k_B T \pi R^2}{5\alpha\beta L_p^{\frac{1}{5}} d_0^\alpha} \right)^{\frac{5}{14}} \quad (8)$$

The resulting values of ξ_0 are listed in Tab.1, which are in the order of 0.3-0.4 μm . Such average values are consistent with other rheology experiments and have been described previously (31). Unlike previous studies of bulk actin networks that find a bulk Poisson ratio of 0.5 for actin gels formed at actin concentration of 21.5 μM (27), we find that the actin cloud can almost collapse under the applied forces, with approximated Poisson's ratios of 0.1 to 0.2. The difference may be explained by the lower actin concentration (4 μM) or by the geometrical arrangement of the actin network used in our experiments.

Approach Phase: Interpretation of distance offset δ

The third fit parameter in the power-law of Eq.2 is δ , which marks the position at which the power-law diverges. As the actin network around the bead is known to have an elastic modulus of ≈ 1 kPa (28, 33) the forces provided by our optical tweezers (max. 30 pN) are unable to deform this network. This suggests that in our measurements, the actin network close to the bead acts as a rigid object, which in turn suggests to interpret δ as the thickness of the actin network defined by epifluorescence (Fig.1B). As shown in Tab.1, δ decreases with increasing CP concentration. The determined values of $\approx 1 - 2 \mu\text{m}$ are consistent with previous measurements of the actin thickness e by fluorescence microscopy (11). This general dependence is not found in the absence CP, where the system is in a completely different regime because the filament growth away from the

bead is only limited by the amount of G-actin. Indeed, in the absence of capping protein filaments grow mainly away from the bead (11), leading to the absence of symmetry breaking. Therefore, without CP it remains difficult to define an actin shell thickness, as the increasing number of filaments growing away from the bead surface changes the overall structure of the gel, which does not allow to interpret δ .

Relaxation phase

The apparent mechanical effect of the actin cloud shows a dominant elastic component, while the force-distance plot gives a significant dissipation marked by the hysteresis. The repeatable approach-retraction excludes a significant plastic deformation, like breakage of the filaments or rupture of the sparse actin network. To understand the relaxation and the retraction behavior, we further follow the approach inspired by Morse (31), and investigate the proposed relaxation function $\chi(t)$, which determines the time dependence of $E(t) = E \times \chi(t)$:

$$\chi(t) = \sum_{n,odd} \frac{8}{n^2 \pi^2} \exp(-n^2 \pi^2 t / \tau_{rep}) \quad (9)$$

where $\tau_{rep} = \frac{l_f^2}{D_{rep}}$. In this model, the relaxation is a sum of exponential decays with well defined decay times for a reptation dominated relaxation. The unknown parameters are the diffusion constant for filament reptation D_{rep} and the filament length l_f , that are combined in the single fit parameter (τ_{rep}). We limit the fit to the first 40 terms of the sum in eq. 9, since the higher modes relax faster than can be observed with the experimental resolution. Such a sum of exponentials remains consistent with the common finding of a power-law behavior of the shear modulus in *in vitro* actin networks (27) and the relaxation behavior found in cells (34).

To check if the resulting fit parameter gives realistic values, we estimate $D_{rep} = k_b T / (\gamma l_f)$, where $\gamma \approx \frac{2\pi\eta_s}{\ln(\xi/d_f)}$ is the friction coefficient per unit length that depends on the solvent viscosity η_s , the mesh-size ξ , which has been estimated in Eq.8, and the filament diameter d_f . We can also use $\eta_s = 10^{-3}$ Pa·s, $d_f = 7$ nm and the mesh-size in the order of 400nm. Knowing the value of the relaxation parameter τ_{rep} given by the fit, we can estimate the filament length l_f from the two previous expressions in the different CP conditions and determine values in the order of $\approx 3 - 8$ μm (see Tab.1). Interestingly these values are very close to the size of the actin cloud d_0 which we determine independently by the first measurable mechanical signature of the cloud.

Hence, the found values of the fit are directly consistent with the predictions of a decrease of filament length when CP concentration is increased (24). The model of entangled actin filaments can therefore explain both the approach and the relaxation part.

Retraction phase

During the retraction phase we observe two types of events: i) sticking events (Fig.S2), where the force becomes abruptly negative until a threshold value is reached and then quickly relaxes, ii) a continuous decrease of the force that becomes negative after an average retraction of 3.5 μm and returns to zero at large distances. While the sticking can be explained by interaction between the probe-bead and the actin, the second case can be modeled phenomenologically assuming a partial closure of the actin network behind the bead as sketched in Fig.4 (right part of the graph). The details of the fit function are given in the methods section. Briefly, we assume a transition between the elastic force generated by the actin cloud between the two beads and an additional viscoelastic contribution that accounts for the partially closed actin cloud behind the bead during the resting phase.

Biological relevance of the actin cloud emanating from cortical actin

The actin cytoskeleton is involved in many cellular events spanning from setting cell shape to the regulation of gene expression. Further experiments hint for a possible direct mechanical transmission of forces from the outside towards the nucleus via the actin cytoskeleton. Especially since the actin cytoskeleton is already known to be important in the positioning of the nucleus, and hence presents a force transmission role in cells, it can be speculated that such force transmission may directly or indirectly trigger changes in gene expression. The mechanical link from extracellular environment to the nucleus is established by actin bundles that connect integrins and proteins of the nuclear envelope (35). However, to explain the role of actin in organelle and nucleus positioning (14, 15), not only such actin bundles should be taken into account. Our experiments highlight that an actin network emanating from the actin cortex can sustain forces in the range of 10 pN. A force of 10pN

is sufficient for dragging organelles inside cells. Moreover, the capacity of Arp2/3 branched networks to reorganize in para structure, as well as nucleators as formins (6), can allow a constantly polymerizing cortical network to push throughout the inside of a cell and exert sufficient forces to move organelles and chromosomes (17). Indeed, networks observed inside cells are generally anchored to cortical actin network (14, 36–38). Since we show that mechanical parameters of filaments far away from nucleation sites may sustain forces up to 15 pN, we anticipate that unbranched actin filaments connected to cortical actin may provide as a mechanical scaffold for a general mechanism of positioning and long range interplay between organelles in oocytes (39, 40) or even in large scale systems like drosophila development (16). Recently, the role of an actin network with similar properties as the here described actin cloud had been identified in large cells such as *Xenopus* oocytes, which directly shows the mechanical relevance of the actin cloud in intracellular organization (18).

6 Conclusion

The transition from a dense actin network, which is polymerized off an Arp2/3 complex activated surface, to the bulk medium is not abrupt and we identify and characterize a large transition zone, the actin cloud. These actin clouds are very soft compared to the dense actin network that is formed at the location of the Arp2/3 complex activation. Our *in vitro* experiments show that this actin cloud also gives a mechanical support with a far reaching mechanical effect that scales inverse to the distance, a property that can be explained by polymer theory. The predicted viscoelastic properties and extracted material properties are in good agreement with our measurements. The actin cloud can not be ignored in the context of cellular events, like nucleus positioning and oocyte maturation, that have been shown to happen on force scales of several pN (18). Moreover, we enlighten a general mechanical feature of sparse actin networks that can serve as a useful mechanism to displace and organize the different cellular compartments.

Acknowledgments

The authors would like to thank Klaus Kroy, Claus Heussinger and Herv Isambert for helpful discussion. K.C. was supported by ARC, M.B. and J.L. were supported by Axa Research Fund. This work was also founded by the federation "dynamique des systemes complexes" of the University Paris 6 and supported by French Agence Nationale de la Recherche (ANR) Grants ANR-11-JSV5-0002, ANR-09-BLAN-0283 and ANR 12BSV5001401, Fondation pour la Recherche Médicale Grant DEQ20120323737

References

- [1] Fletcher, D. A., and R. D. Mullins, 2010. Cell mechanics and the cytoskeleton. *Nature* 463:485–492. <http://www.nature.com/gate1.inist.fr/nature/journal/v463/n7280/full/nature08908.html>.
- [2] Lecuit, T., P.-F. Lenne, and E. Munro, 2011. Force Generation, Transmission, and Integration during Cell and Tissue Morphogenesis. *Annual Review of Cell and Developmental Biology* 27:157–184. <http://www.annualreviews.org/doi/abs/10.1146/annurev-cellbio-100109-104027>.
- [3] Betz, T., D. Koch, Y.-B. Lu, K. Franze, and J. A. Ks, 2011. Growth cones as soft and weak force generators. *Proceedings of the National Academy of Sciences* 108:13420–13425. <http://www.pnas.org/content/108/33/13420.abstract>.
- [4] Salbreux, G., G. Charras, and E. Paluch, 2012. Actin cortex mechanics and cellular morphogenesis. *Trends in Cell Biology* 22:536–545. <http://www.sciencedirect.com/science/article/pii/S0962892412001110>.
- [5] Bernheim-Grosbawsser, A., S. Wiesner, R. M. Golsteyn, M.-F. Carlier, and C. Sykes, 2002. The dynamics of actin-based motility depend on surface parameters. *Nature* 417:308311. <http://dx.doi.org/10.1038/417308a>.
- [6] Reymann, A.-C., J.-L. Martiel, T. Cambier, L. Blanchoin, R. Boujemaa-Paterski, and M. Thry, 2010. Nucleation geometry governs ordered actin networks structures. *Nature Materials* 9:827–832. <http://www.nature.com/gate1.inist.fr/nmat/journal/v9/n10/full/nmat2855.html>.
- [7] Pontani, L.-L., J. van der Gucht, G. Salbreux, J. Heuvingh, J.-F. Joanny, and C. Sykes, 2009. Reconstitution of an Actin Cortex Inside a Liposome. *Biophysical Journal* 96:192198.
- [8] Carvalho, K., J. Lemire, F. Faqir, J. Manzi, L. Blanchoin, J. Plastino, T. Betz, and C. Sykes, 2013. Actin polymerization or myosin contraction: two ways to build up cortical tension for symmetry breaking. *Philosophical Transactions of the Royal Society B: Biological Sciences* 368:20130005.
- [9] Strehle, D., J. Schnau, C. Heussinger, J. Alvarado, M. Bathe, J. Ks, and B. Gentry, 2011. Transiently crosslinked F-actin bundles. *European Biophysics Journal* 40:93–101. <http://link.springer.com/article/10.1007/s00249-010-0621-z>.
- [10] Thoresen, T., M. Lenz, and M. Gardel, 2013. Thick Filament Length and Isoform Composition Determine Self-Organized Contractile Units in Actomyosin Bundles. *Biophysical Journal* 104:655–665. <http://www.sciencedirect.com/science/article/pii/S0006349512051764>.

- [11] Kawska, A., K. Carvalho, J. Manzi, R. Boujemaa-Paterski, L. Blanchoin, J.-L. Martiel, and C. Sykes, 2012. How actin network dynamics control the onset of actin-based motility. *Proceedings of the National Academy of Sciences* <http://www.pnas.org/content/early/2012/08/16/1117096109>.
- [12] Morone, N., T. Fujiwara, K. Murase, R. S. Kasai, H. Ike, S. Yuasa, J. Usukura, and A. Kusumi, 2006. Three-dimensional reconstruction of the membrane skeleton at the plasma membrane interface by electron tomography. *The Journal of Cell Biology* 174:851–862. <http://jcb.rupress.org/content/174/6/851>.
- [13] Clark, A., K. Dierkes, and E. Paluch, 2013. Monitoring Actin Cortex Thickness in Live Cells. *Biophysical Journal* 105:570–580. <http://www.sciencedirect.com/science/article/pii/S0006349513006450>.
- [14] Iwabuchi, K., R. Minamino, and S. Takagi, 2010. Actin Reorganization Underlies Phototropin-Dependent Positioning of Nuclei in Arabidopsis Leaf Cells. *Plant Physiology* 152:1309–1319. <http://www.plantphysiol.org/content/152/3/1309>.
- [15] Sturmer, K., O. Baumann, and B. Walz, 1995. Actin-dependent light-induced translocation of mitochondria and ER cisternae in the photoreceptor cells of the locust *Schistocerca gregaria*. *Journal of Cell Science* 108:2273–2283. <http://jcs.biologists.org/content/108/6/2273>.
- [16] Huelsmann, S., J. Ylne, and N. H. Brown, 2013. Filopodia-like Actin Cables Position Nuclei in Association with Perinuclear Actin in *Drosophila* Nurse Cells. *Developmental Cell* 26:604–615. [http://www.cell.com/developmental-cell/abstract/S1534-5807\(13\)00483-8](http://www.cell.com/developmental-cell/abstract/S1534-5807(13)00483-8).
- [17] Kumaran, R. I., R. Thakar, and D. L. Spector, 2008. Chromatin Dynamics and Gene Positioning. *Cell* 132:929–934. [http://www.cell.com/abstract/S0092-8674\(08\)00334-6](http://www.cell.com/abstract/S0092-8674(08)00334-6).
- [18] Feric, M., and C. P. Brangwynne, 2013. A nuclear F-actin scaffold stabilizes ribonucleoprotein droplets against gravity in large cells. *Nature Cell Biology* 15:1253–1259. <http://www.nature.com.gate1.inist.fr/ncb/journal/v15/n10/full/ncb2830.html>.
- [19] Smith, B. A., S. B. Padrick, L. K. Doolittle, K. Daugherty-Clarke, I. R. Corral, M.-Q. Xu, B. L. Goode, M. K. Rosen, and J. Gelles, 2013. Three-color single molecule imaging shows WASP detachment from Arp2/3 complex triggers actin filament branch formation. *eLife* 2. <http://elife.elifesciences.org/content/2/e01008>.
- [20] Charras, G. T., C.-K. Hu, M. Coughlin, and T. J. Mitchison, 2006. Reassembly of contractile actin cortex in cell blebs. *The Journal of Cell Biology* 175:477490.
- [21] Mori, M., K. Somogyi, H. Kondo, N. Monnier, H. J. Falk, P. Machado, M. Bathe, F. Ndlec, and P. Lnrt, 2014. An arp2/3 nucleated f-actin shell fragments nuclear membranes at nuclear envelope breakdown in starfish oocytes. *Current biology: CB* 24:1421–1428.
- [22] Paluch, E., J. van der Gucht, and C. Sykes, 2006. Cracking up: symmetry breaking in cellular systems. *The Journal of Cell Biology* 175:687692.
- [23] Gittes, F., and C. F. Schmidt, 1998. Interference model for back-focal-plane displacement detection in optical tweezers. *Optics Letters* 23:7–9. <http://ol.osa.org/abstract.cfm?URI=ol-23-1-7>.
- [24] Achard, V., J.-L. Martiel, A. Michelot, C. Gurin, A.-C. Reymann, L. Blanchoin, and R. Boujemaa-Paterski, 2010. A Primer-Based Mechanism Underlies Branched Actin Filament Network Formation and Motility. *Current Biology* 20:423428. [http://www.cell.com/current-biology/abstract/S0960-9822\(10\)00052-7](http://www.cell.com/current-biology/abstract/S0960-9822(10)00052-7).
- [25] Sykes, C., and J. Plastino, 2010. Cell biology: actin filaments up against a wall. *Nature* 464:365–366.
- [26] Lemire, J., K. Guevorkian, C. Campillo, C. Sykes, and T. Betz, 2013. -Hemolysin membrane pore density measured on liposomes. *Soft Matter* 9:3181–3187.
- [27] Gardel, M. L., M. T. Valentine, J. C. Crocker, A. R. Bausch, and D. A. Weitz, 2003. Microrheology of Entangled F-Actin Solutions. *Physical Review Letters* 91:158302. <http://link.aps.org/doi/10.1103/PhysRevLett.91.158302>.
- [28] Marcy, Y., J. Prost, M.-F. Carlier, and C. Sykes, 2004. Forces generated during actin-based propulsion: A direct measurement by micromanipulation. *Proceedings of the National Academy of Sciences of the United States of America* 101:5992–5997. <http://www.pnas.org/content/101/16/5992.abstract>.
- [29] Isambert, H., and A. C. Maggs, 1996. Dynamics and Rheology of Actin Solutions. *Macromolecules* 29:10361040. <http://dx.doi.org/10.1021/ma946418x>.
- [30] MacKintosh, F. C., J. Kas, and P. A. Janmey, 1995. Elasticity of semiflexible biopolymer networks. *Physical Review Letters* 75:4425–4428.
- [31] Morse, D. C., 1998. Viscoelasticity of Concentrated Isotropic Solutions of Semiflexible Polymers. 2. Linear Response. *Macromolecules* 31:7044–7067. <http://dx.doi.org/10.1021/ma980304u>.
- [32] Semmrich, C., R. J. Larsen, and A. R. Bausch, 2008. Nonlinear mechanics of entangled F-actin solutions. *Soft Matter* 4:1675.
- [33] Pujol, T., O. d. Roure, M. Fermigier, and J. Heusinger, 2012. Impact of branching on the elasticity of actin networks. *Proceedings of the National Academy of Sciences* 109:10364–10369. <http://www.pnas.org/content/109/26/10364>.
- [34] Fabry, B., G. N. Maksym, J. P. Butler, M. Glogauer, D. Navajas, and J. J. Fredberg, 2001. Scaling the microrheology of living cells. *Phys Rev Lett* 87:148102.
- [35] Jaalouk, D. E., and J. Lammerding, 2009. Mechanotransduction gone awry. *Nature Reviews Molecular Cell Biology* 10:63–73. <http://www.nature.com.gate1.inist.fr/nrm/journal/v10/n1/full/nrm2597.html>.
- [36] Schuh, M., and J. Ellenberg, 2008. A New Model for Asymmetric Spindle Positioning in Mouse Oocytes. *Current Biology* 18:1986–1992. <http://www.sciencedirect.com/science/article/pii/S0960982208015029>.
- [37] Chaigne, A., C. Campillo, N. S. Gov, R. Voituriez, J. Azoury, C. Umaa-Diaz, M. Almonacid, I. Queguiner, P. Nassoy, C. Sykes, M.-H.

- Verlhac, and M.-E. Terret, 2013. A soft cortex is essential for asymmetric spindle positioning in mouse oocytes. *Nature Cell Biology* 15:958–966. <http://www.nature.com/ncb/journal/v15/n8/full/ncb2799.html>.
- [38] Lnr, P., C. P. Bacher, N. Daigle, A. R. Hand, R. Eils, M. Terasaki, and J. Ellenberg, 2005. A contractile nuclear actin network drives chromosome congression in oocytes. *Nature* 436:812–818. <http://www.nature.com/nature/journal/v436/n7052/full/nature03810.html>.
- [39] Li, H., F. Guo, B. Rubinstein, and R. Li, 2008. Actin-driven chromosomal motility leads to symmetry breaking in mammalian meiotic oocytes. *Nature cell biology* 10:1301–1308.
- [40] Azoury, J., K. W. Lee, V. Georget, P. Hikal, and M.-H. Verlhac, 2011. Symmetry breaking in mouse oocytes requires transient F-actin meshwork destabilization. *Development* 138:2903–2908. <http://dev.biologists.org/content/138/14/2903>.

Table 1: Listing of the fit parameters found for different CP concentrations. N represents the number of data-points for each CP concentration. Exponent of the model α , prefactor in the model β , distance offset δ and $E_{1\mu m}$ the elastic modulus at a distance of 1 μm . ξ_0 is the average mesh size as calculated for an homogeneous network. ν is the Poisson's ratio. d_0 the distance at which the average force is over 2pN. The viscoelastic model used also allows to predict the average filament length l_f from the relaxation behaviors. The median R^2 values are given to quantify the fit quality for the different conditions.

CP [nM]	0	10	30	50
N	13	29	31	30
α	-1.2±0.1	-0.9±0.2	-1.1±0.2	-1.2±0.5
$\beta[pN\mu m]$	24.3±10.7	18.7±8.1	16.9±16.0	6.1±5.9
$\delta[\mu m]$	0.5±0.6	2.2±0.7	1.2±0.6	1.0±0.5
ν	0.1±0.05	0.2±0.06	0.1±0.07	0.1±0.2
$E_{1\mu m}[Pa]$	1.93 ± 1.05	1.24 ± 0.78	1.39 ± 1.61	0.59 ± 0.76
$\xi_0[nm]$	310	397	350	376
$d_0[\mu m]$	8.6 ± 2.9	13.3 ± 2.4	6.5 ± 3.1	3.7 ± 6.3
$l_f[\mu m]$	10.8±2.2	9.1±5.5	2.5±0.5	3.1±3.8
median(R^2)	0.982	0.989	0.936	0.850

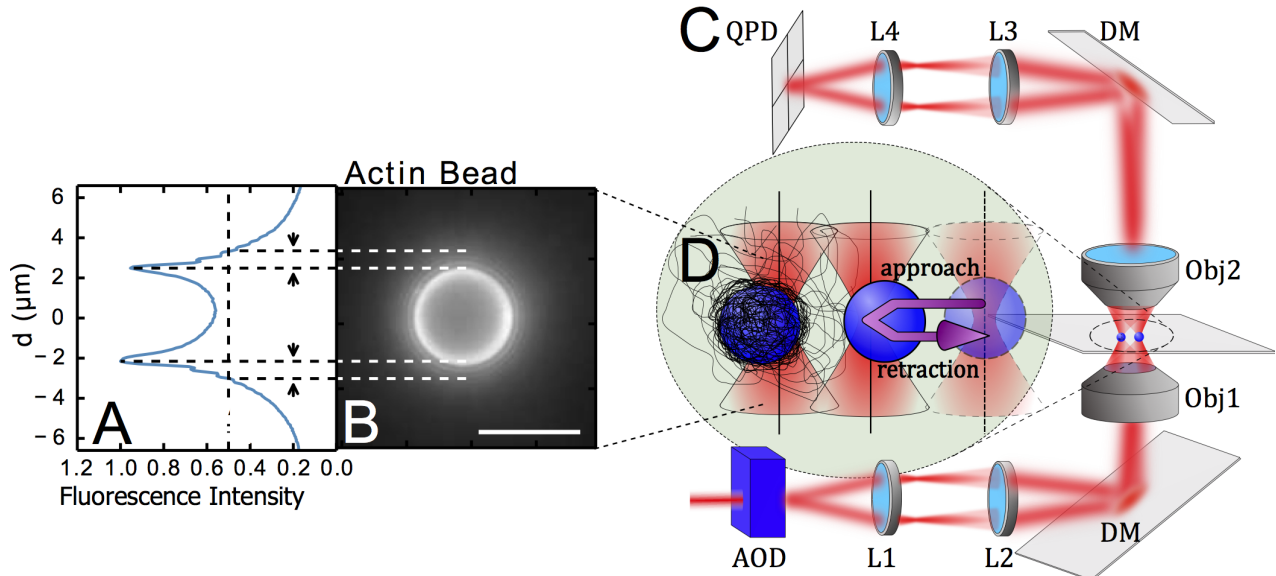


Figure 1: Sketch describing the experimental situation: **A)** Normalized intensity profile of the fluorescent actin cortex shown in B, taken along the bead diameter. Arrowheads represent gel thickness measured as the half maximal intensity of the epifluorescence signal. **B)** Fluorescence Image of a $4.3 \mu\text{m}$ actin-bead, 25 nM Arp2/3, 10 nM CP after 30 min. Bar is $5 \mu\text{m}$. **C)** To probe the mechanics of the actin cloud we use multiplexed optical tweezers generating 2 traps. A 1 W IR fiber laser (IPG Photonics, $\lambda=1064 \text{ nm}$) is steered by 2 acousto optical deflectors (AOD) and multiplexed by time-sharing. The resulting beams are imaged in the back focal plane of a water immersion objective (Obj1, 60X, NA=1.2), by a 2 fold magnification telescope (with focal of the L_x lenses being $f_{L1} = 10 \text{ cm}$, $f_{L2} = 20 \text{ cm}$). The light is coupled in the optical path of an Olympus IX71 microscope by a dichroic mirror (DM). After interaction with the beads, the light is collected by a water immersion objective (Obj2, 40X, NA=0.9) and the back focal plane of Obj2 is imaged onto a quadrant-photo-diode (QPD) via 2 lenses ($f_{L3} = 6 \text{ cm}$, $f_{L4} = 3 \text{ cm}$). **D)** The lasers trap the actin-bead (left) and the probe bead. During the experiments, the probe bead is approaching the actin-bead and moved from an initial position (light, right) to a final position at a velocity v , resting 3 s at the closest proximity (middle) and retracting back to the original position (movement indicated by the purple arrow). The displacement of the two beads from their respective trap center (marked by a straight line) is recorded by the QPD during the whole time. Optical forces are calculated using the calibrated trap stiffness.

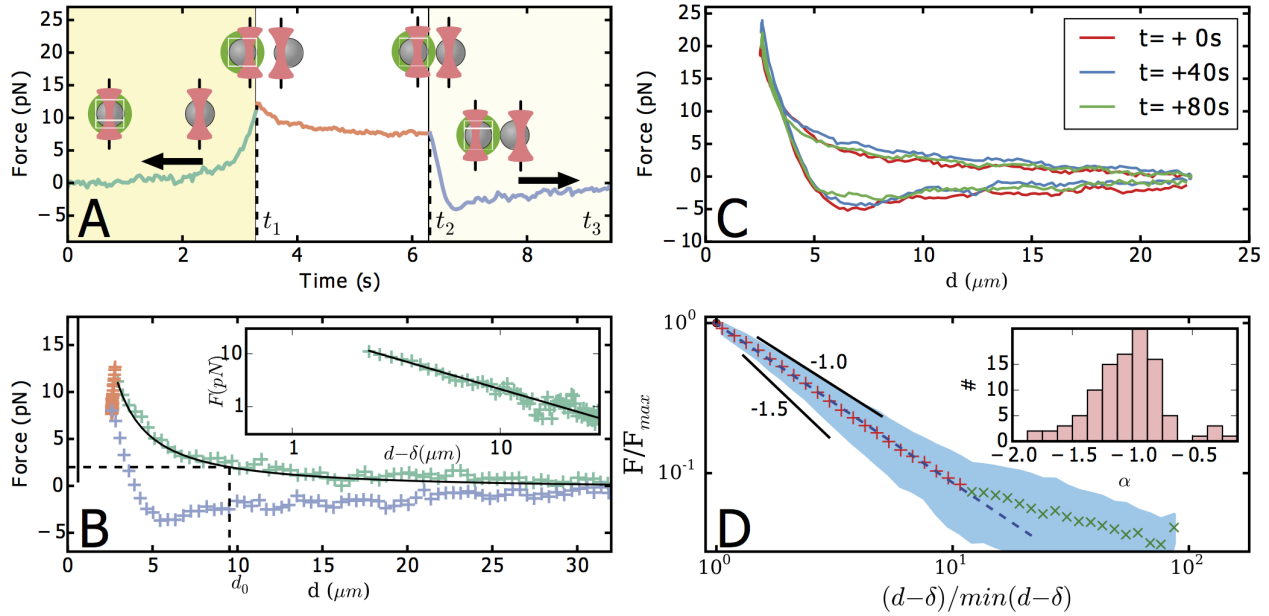


Figure 2: A) Force of an actin-bead as a function of time in the presence of 30 nM CP. t_1 and t_2 respectively correspond to the beginning of the relaxation and retraction phases. Here, the sample is measured 12 min after adding actin to bead mix. Color of the points marks the different phases of approach (green), relaxation (red) and retraction (blue). **B)** Force on an actin-bead as a function of the distance d between bead surfaces of the data presented in A. The zero force is fixed by the average of force at large distance. d_0 is the distance at which the mean force is higher than the standard deviation measured for the resting bead (before the approach). We use this distance d_0 as size of the actin cloud for the presented analysis. However, it should be noted that this measure may depend on the measurement method and the size of the probe beads. The color code used corresponds to panel A. The sample was measured 17 min after adding actin to the bead mix. The straight black line represents δ , the distance at which the force extrapolated by the fit would be infinite. Inset: Power-law fit of the approach (solid line) and log-log representation. Examples of graph A and B for different amount of capping protein are available in Fig. S5, S6, S7. **C)** Repeated approach-retraction experiments (3 out of 8 shown) give reproducible data. The example shown was acquired under 10nM CP concentration. **D)** Log-log representation of the rescaled experimental data. Red and green crosses (+, \times), correspond to mean values and the filled blue area corresponds to average plus/minus standard deviation for each averaged bin. Blue dashed line (---) correspond to a linear fit of the data, $(d - \delta)/(d - \delta)_{min} < 10$, slope is -1.06 . Slopes of $-1, -1.5$ are represented as visual guides. Inset: Distribution of power law exponent values obtained for each approach experiment for all CP concentration value ($n=103$). We excluded 24 experiments out of 127, that gave fit results with negative and non-physical value for δ .

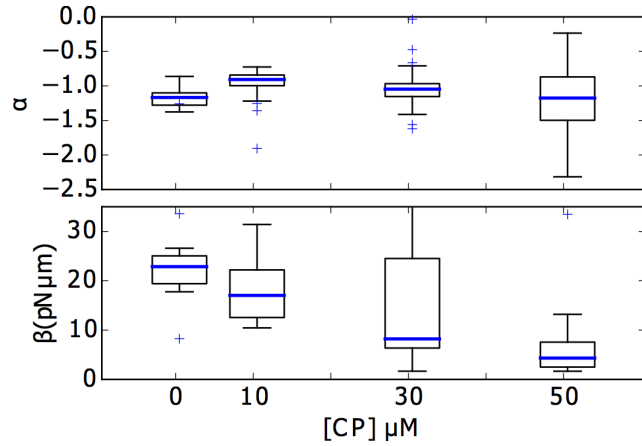


Figure 3: **Distribution of power exponent α and prefactor β for different concentrations in CP (see Tab.1).**

Box plot: blue line defines mean, box limit represent first(q1) and third(q3) quartiles, whiskers extend to the most extreme data point within $1.5 \times (q3 - q1)$ data range. None of the value of α are statistically different than the value for $[\text{CP}] = 50 \mu\text{M}$

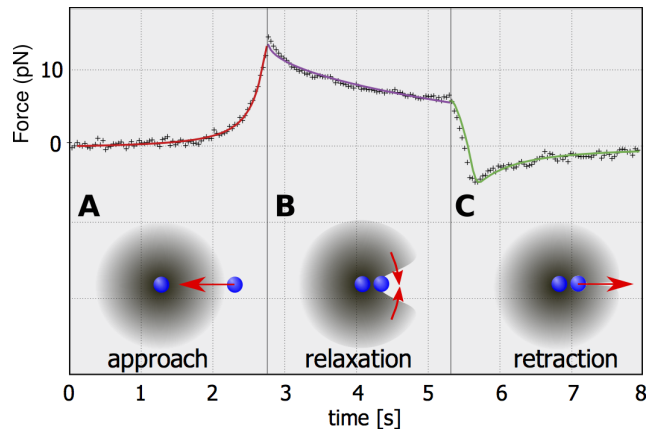


Figure 4: **Model and example of a full fit for the measured force-evolution.** A) (red) While approaching, the bead deforms the full actin cloud between the two beads leading to the measured forces that are fitted by the model of polymer elasticity including the discussed nonlinear Young's modulus. B) (violet) subsequent viscoelastic relaxation of the network between the two beads following the theory of polymer relaxation of sparse actin networks as discussed in Eq.9. To understand the negative forces in the retracting phase we imply that the network behind the bead is starting to relax into the void that has been created by the bead during the approach phase (red arrows). C) (green) This leads then to an additional elastic constraint while the bead returns to the initial position, hence explaining the negative force during the return phase.

Supplementary Information

June 11, 2014

Repeated approach on same bead as function of velocity, cp = 30

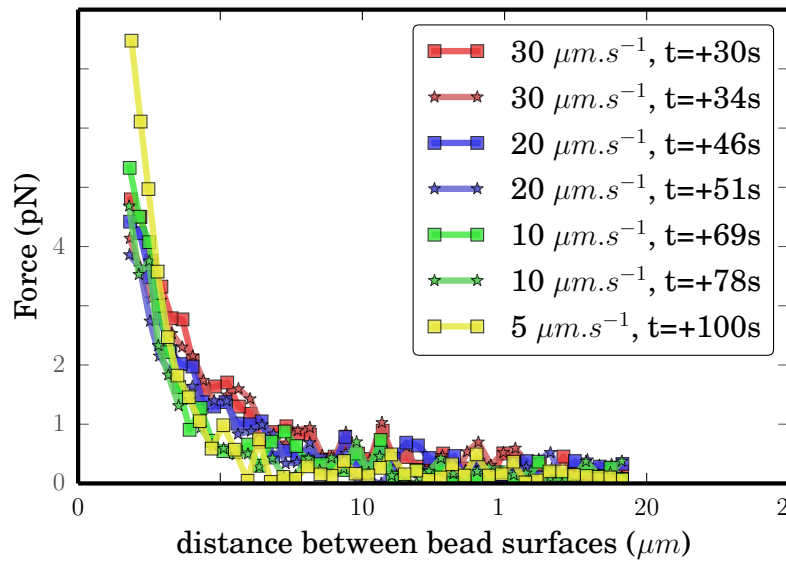


Figure 1: S1: Repeated approach curves at difference speeds (30, 20, 10 and $5\mu\text{m/s}$) on the same bead, by decreasing velocity. Indentation time t represents the instant at which the probe-bead started approaching the actin-bead, where $t=0$ corresponds to the time at which both beads were trapped. Starting distance and minimal approach distance where kept the same across all speed. The difference of maximum force between the first indentation (30 $\mu\text{m/s}$) and the last indentation (5 $\mu\text{m/s}$) can be explained by the fact that the actin is still growing on the bead surface.

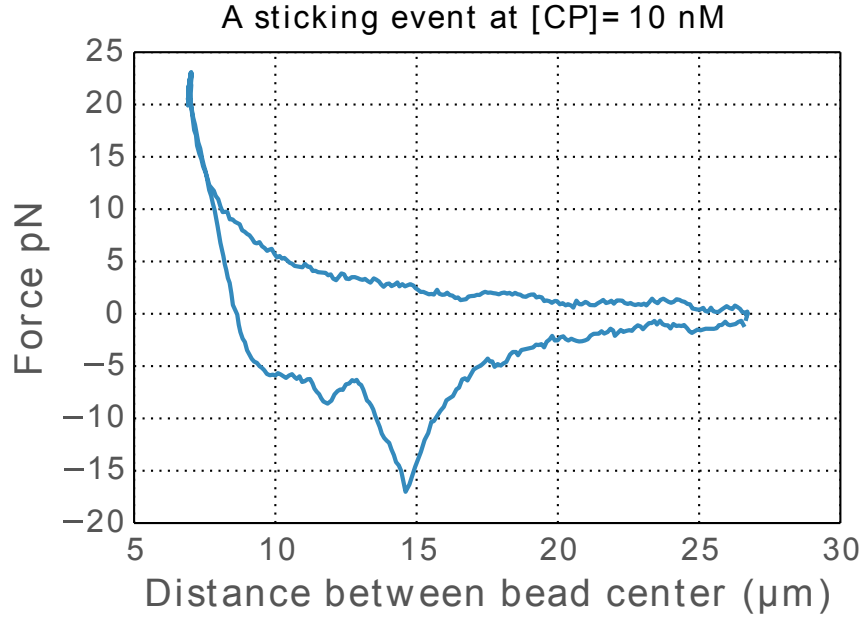


Figure 2: S2: Sawtooth like sticking events as observed for $\approx 25\%$ of experiments.

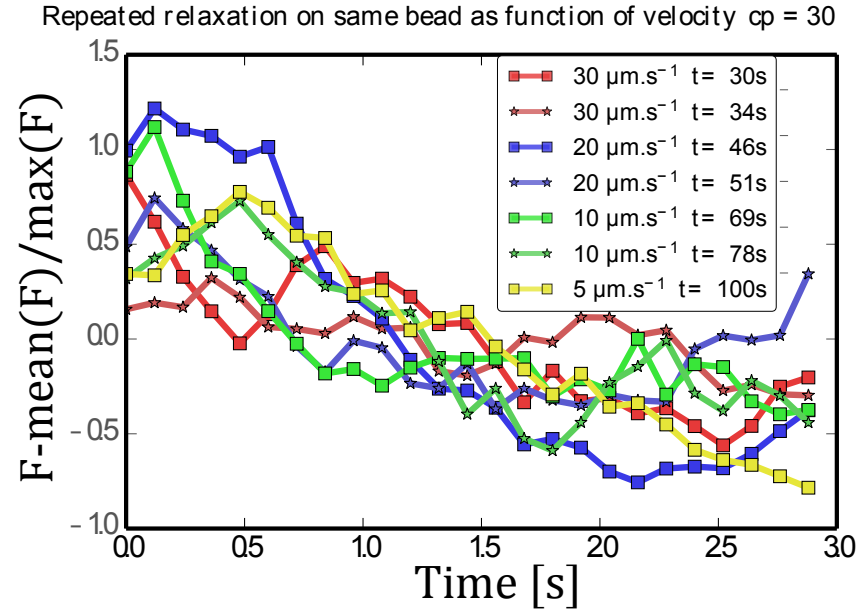


Figure 3: S3: Renormalized relaxation at different speeds for the same experiment as presented in Fig. S1.

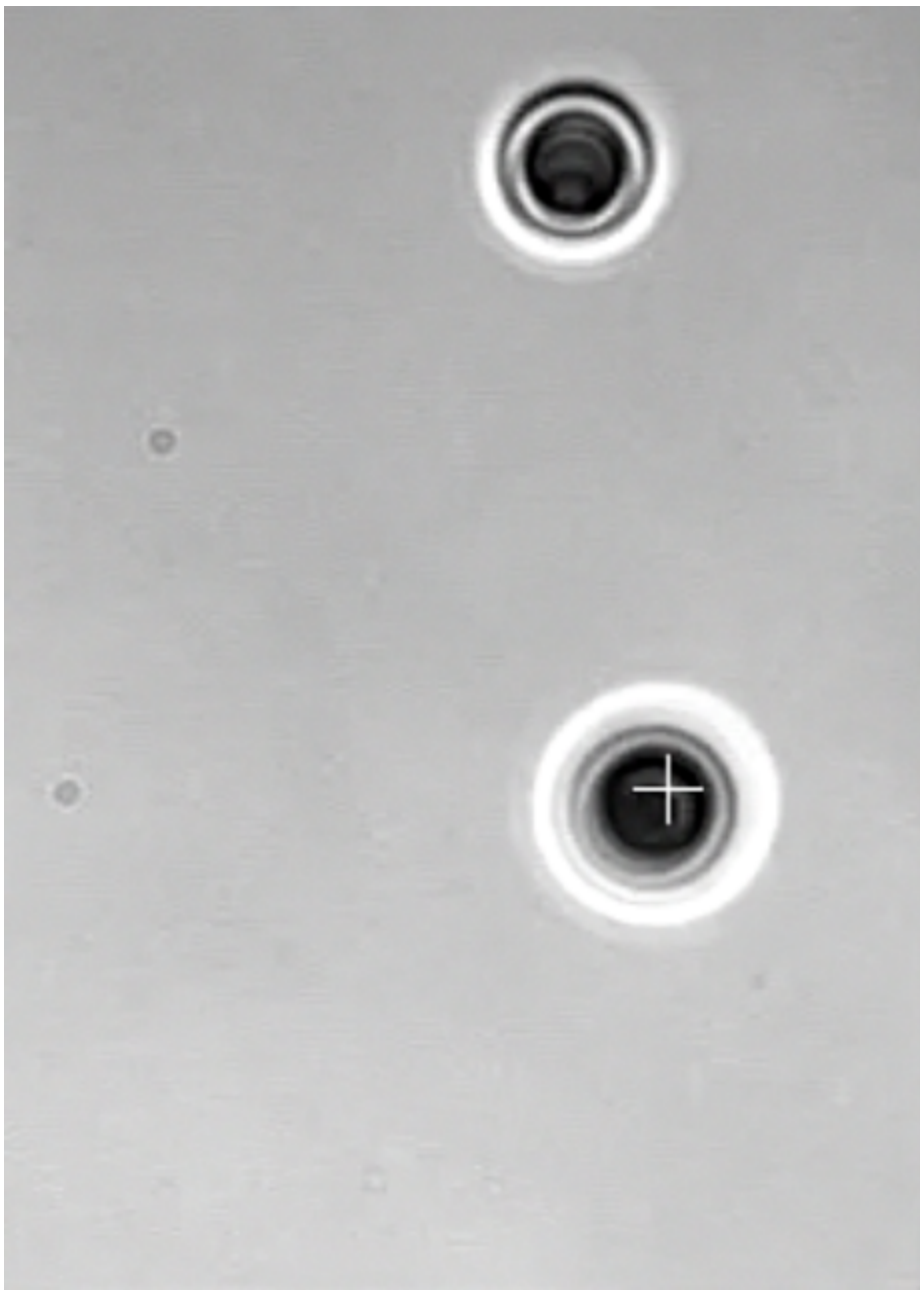


Figure 4: Video S4 : Actin bead trapped by an optical tweezer (white cross). When the stage is displaced. neighbouring particles experience a repulsive force. Timescale is realtime.

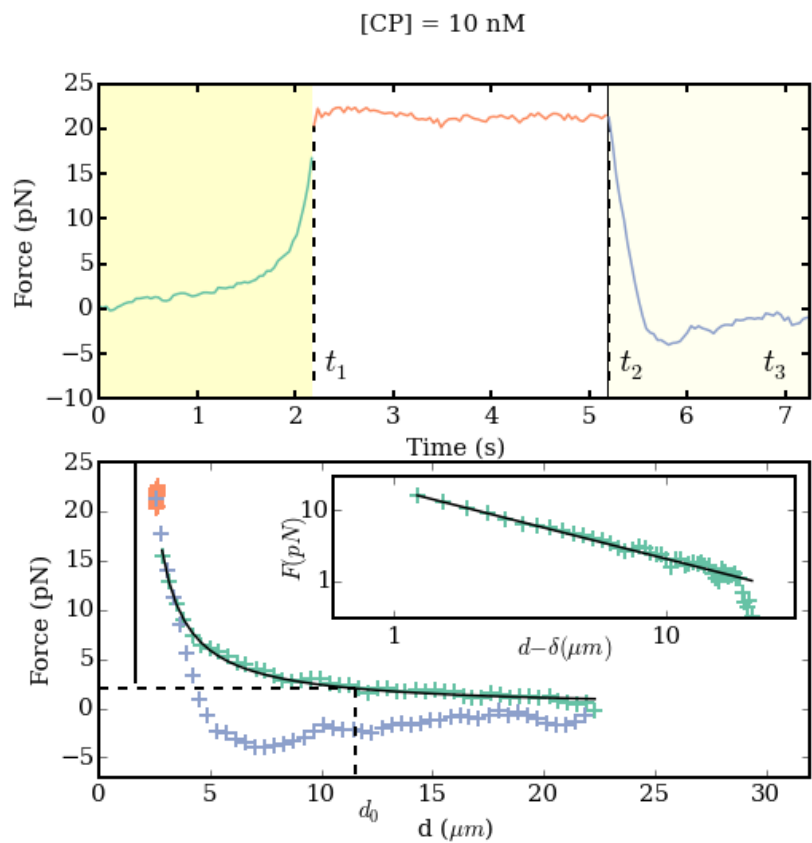


Figure 5: S5:One sample of the approach-retraction curves shown both as a function of time and distance for concentration of capping protein of 10nM.

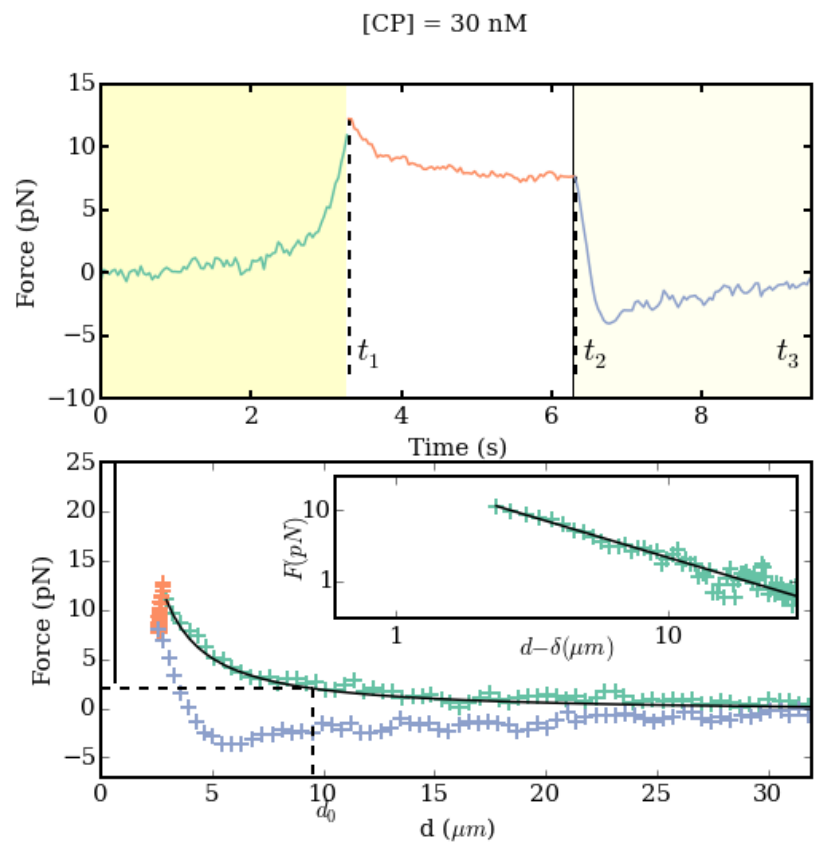


Figure 6: S6:One sample of the approach-retraction curves shown both as a function of time and distance for concentration of capping protein of 30nM.

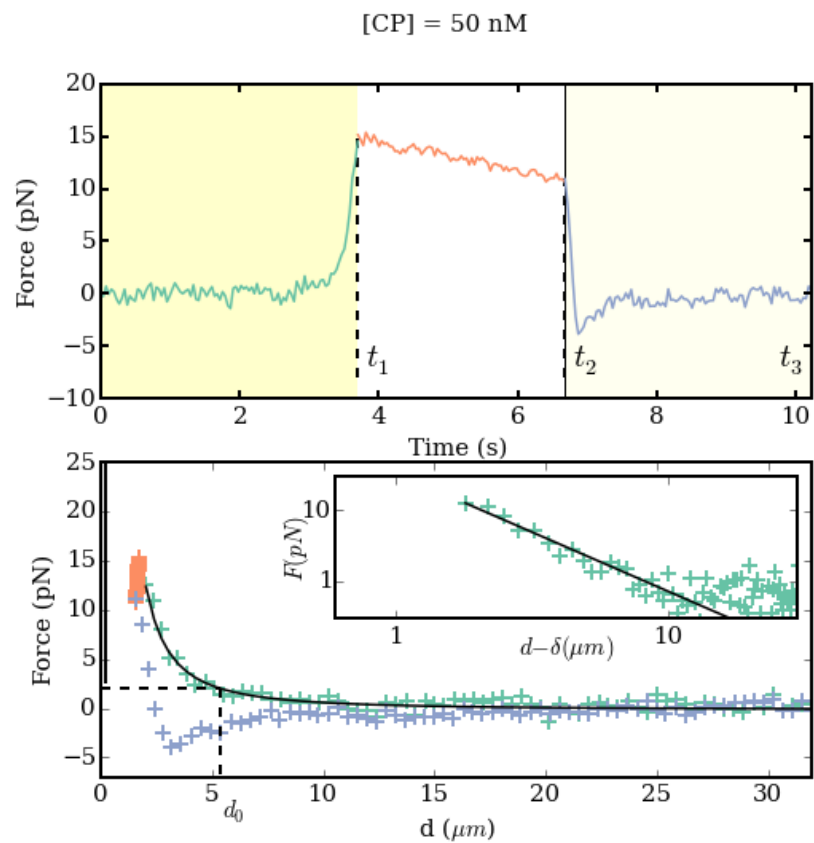


Figure 7: S7:One sample of the approach-retraction curves shown both as a function of time and distance for concentration of capping protein of 50.

7.2 Cell-sized liposome doublets reveal active cortical tension build up Draft

The part on liposomes doublets used to measure the increase of cortical tension on biomimetic cortices is subject of a draft :

Cell-sized liposome doublets reveal active cortical tension build up

Joël Lemière^{a,b,c,d}, Matthias Bussonnier^{a,b,c,d}, Timo Betz^{a,b,c}, Cécile Sykes^{a,b,c} & Kevin Carvalho^{a,b,c}

^a Institut Curie, Centre de Recherche, Paris, F-75248 France

^b CNRS, UMR 168, Paris, F-75248 France

^c Sorbonne Universités, UPMC Univ Paris 06, UMR 168, Paris, F-75005 France

^d Univ Paris Diderot, Sorbonne Paris Cité, Paris, F-75205 France

Abstract

Cells are able to generate contractile forces and modulate their shape to fulfill their specific functions. The cell cortex, a thin actin shell bound to the plasma membrane, mediates these essential behaviours. It is the substrate for myosin activity which contributes to cortical tension build up, together with actin dynamics. Here, we dissect the sole effect of myosin II on cortical tension increase with a non-invasive method. Cell-sized biomimetic liposomes are arranged in doublets and covered with a stabilized actin cortex anchored to the membrane. The addition of myosin II minifilaments to this doublet triggers a shape change unambiguously related to cortical-tension increase. Our assay paves the way for a quantification of cortical-tension changes triggered by various actin-associated proteins in a cell-sized system.

Introduction

Cells are highly dynamic and need to change their shape in almost all cellular events spanning from division and motility to tissue remodeling. One of the major components involved in these processes is the contractile actin cytoskeleton arranged in a sub-micrometer thick network linked to the plasma membrane and called the acto-myosin cortex [1]. It drives cell-shape changes as well as cell polarization [2] and governs tissue remodeling [3]–[6]. This cortex insures tension in cells, called cortical tension [7]–[9], where the interactions with the plasma membrane and myosins are the essential modulators for this tension. Micromanipulation of cells allows to measure the cortical tension, which was found to be between 50 and 4000 pN/ μ m depending on cell type, myosin activity and actin dynamics [7], [10]–[12]. Moreover, as shown for cell doublets, cell-cell adhesion is able to modulate cortical tension [13], a mechanism that is involved in cell sorting for tissue formation [14]. Recently, acto-myosin cortices have been reconstructed on supported lipid bilayers [15] and on cell-sized liposomes [16] where those reconstructions allowed to understand how crosslinking, attachment to the membrane, and actin-filament length influence contraction by myosin activity and actin polymerization [17].

In this study, we determine cortical-tension changes by the use of cell-sized doublet liposomes around which an acto-myosin cortex is reproduced *in vitro*. Changes in cortical tension are quantified by analyzing doublet-shape change. This approach is reminiscent of cell-cell doublets used to uncover the role of cell adhesion in cortical-tension change [14]. Our assay allows isolating the role of myosin motors on cortical-tension build up, independently of actin dynamics and membrane tension.

Results

Formation of liposome doublets

Liposomes are obtained by electroformation [18] from a mixture of egg-phosphatidylcholine (EPC) and biotin-PEG lipids (**See Material and methods**). We take the advantage of biotin PEG lipids to stick liposomes together by adding streptavidin to the liposome solution (**see MM**). In these conditions, several doublets are formed within 15 minutes (**Fig 1A**).

Attachment of actin on doublet liposomes

Phalloidin-stabilized fluorescent actin filaments, obtained in the presence of biotinylated actin monomers, stick to the membrane of the preformed doublets through a biotin-streptavidin-biotin link (**Fig 1B**) and form a crosslinked homogeneous coat, as already characterized on liposomes [16]. Note that the interface between the two liposomes is free of actin filaments (**Fig 1C - i**). To avoid the use of fluorescent lipids that may affect membrane mechanics [19], this interface is visualized by fluorescently labeling the inside buffer of only one of the liposomes with 0.9 μ M of sulforhodamin B (SRB) (**see MM and Fig 1C - i**).

Effect of myosin injection

Myosin II motors, which assemble into bipolar filaments, are injected in the observation chamber by exchanging the external solution using an H-shaped flow chamber where doublets are imaged (**Fig 1C - ii**). Myosin II motors trigger a shape change of the doublets within minutes (**Fig 1C - iii**) and the following geometrical characteristics of the liposome doublets are modified: the distance between liposome centers (d), the radii R_1 and R_2 of the liposomes 1 and 2, respectively ($R_1 > R_2$), the

radius of curvature of the interface R_i , the volume of the doublet V , the angles between the interface and the liposome 1 or 2, θ_1 and θ_2 respectively. We define the total contact angle $\theta_{tot} = \theta_1 + \theta_2$ (**Fig 1D**). These parameters are geometrically linked (**Fig 1D**), and obtained by adjusting two spherical caps in contact, either in 2D-(phase contrast and epifluorescence) images or 3D-(spinning disk) stacks (**see MM**). We use the total contact angle θ_{tot} as a reporter for shape change. We find that myosin addition produces an increase of θ_{tot} . Indeed, on epifluorescence images and in the absence of myosin, we measure a total contact angle θ_{tot} of $(64 \pm 16)^\circ$ ($n=18$) whereas in the presence of 200 nM myosin and before the actin cortex ruptures, we find a θ_{tot} value of $(86 \pm 21)^\circ$ ($n=5$). This difference is statistically significant ($p=0.0186$)

Angles are related to tensions

Liposomes 1 and 2 have a uniform tension τ_1 and τ_2 , respectively. Tension refers to the sole membrane tension in the absence of actin and myosin, and to cortical tension in the presence of actin and myosin. The tension at the interface between liposome 1 and 2 has two components: a membrane tension τ_i and the adhesion energy per unit surface W which is due to biotin-streptavidin-biotin adhesion, and reads $(\tau_i - W)$. The Young's equation, which relates tensions and angles, can be applied to the contact line between the two doublet liposomes (**Fig1 D**). When projected on the contact surface tangent, the Young's equation reads:

$$\tau_i - W = \tau_1 \cos \theta_1 + \tau_2 \cos \theta_2 \quad (1)$$

When projected orthogonally to the contact surface tangent, one finds:

$$\tau_1 \sin \theta_1 = \tau_2 \sin \theta_2 \quad (2)$$

Contact-angle dispersion

Dispersion in θ_{tot} , in a population of doublets before myosin injection is $\pm 16^\circ$. It reflects a difference in tension, which could be due either to the dispersion of tension during the liposome preparation, to a difference in adhesion at the interface between doublet liposomes, or to contribution of the actin shell in tension build up. Contact angle increase upon myosin addition is on the same order of this dispersion, which prompted us to characterize many individual doublets as a function of time.

The sole presence of an actin shell does not modify the contact angle

We now investigate how the actin shell affects the contact angle, and thus the tension, in the absence of myosin. We compare the shape of the same doublet in the presence or in the absence of an actin shell by photo-damaging the actin filamentous network (**Fig 2A**) [20]. The total contact angle changes only by $(3.4 \pm 2)^\circ$ ($n = 7$), (**Fig 2B**) which is negligible compared to the change due to myosin activity (see above).

3D observations

Since the liposomes forming the doublets have size ratios R_1/R_2 that vary between 1.15 and 1.82, the plane of epifluorescence images is generally not parallel to the doublet equatorial plane, hence leading to an underestimate of the angle θ_{tot} . Therefore, 3D spinning disk image stacks are recorded (**Fig 3A**) for an accurate determination of θ_{tot} , V and d (see above for definition) which are obtained by fitting spherical caps on 3D stacks (**see mat and meth**). All initial values before myosin

addition are noted θ_{tot}^I , V^I , d^I and $\theta_{tot}(t)$, $V(t)$, $d(t)$ after addition of myosin at $t=0$. We observe that $\theta_{tot}(t)$ increases, whereas $d(t)$ decreases when myosin filaments are added. During these geometric changes, the volume remains constant within 10% consistent with cell doublet experiments [14], [21] (**Fig 3D**).

Visual inspection of our images reveals that the interface between liposome 1 and 2 only differs from a flat interface by a few pixels (**Fig SI**). The curvature $1/R_i$ (**Fig 1D**) is generally much smaller than $1/R_1$ and $1/R_2$, which are comparable. This observation leads to the assumption that $\theta_1 = \theta_2 = \theta$ within our resolution.

Discussion

Cortical tension is homogeneous for a single doublet

The use of **equation (2)** with $\theta_1(t) = \theta_2(t) = \theta_{tot}(t)/2$ leads to the equality of tensions on both sides of the doublet, thus, $\tau_1(t) = \tau_2(t) = \tau(t)$. This result is consistent with the fact that actin is distributed continuously all around the liposome doublet. Thus, myosin II mini-filaments contract a continuous shell. Under these conditions, **equation (1)** simplifies to:

$$\tau_i - W = 2\tau(t) \cdot \cos \theta(t) \quad (3)$$

Where $\theta(t) = \frac{\theta_{tot}(t)}{2}$ with a reasonable assumption that $\tau_i - W$ may depend on the variability of initial adhesion in our experiments, but is considered constant over time for a given doublet. Therefore, we obtain an expression of the tension $\tau(t)$ that varies during acto-myosin contraction and reads

$$\tau(t) = \frac{\text{cst}}{2 \cdot \cos \theta(t)} \quad (4)$$

Therefore, the tension relative to its initial value over time reads:

$$\frac{\tau(t)}{\tau^I} = \frac{\cos\theta^I}{\cos\theta(t)} \quad (5)$$

Relative increase of cortical tension

Interaction of myosin II filaments with a biomimetic actin cortex induces tension build up. The cortical tension, normalized to its initial value $\frac{\tau(t)}{\tau^I}$, increases and reaches a maximal value $\frac{\tau^{max}}{\tau^I}$ (**Fig 3E**). Note that if the actomyosin shell breaks and peels, the doublet recovers its initial shape (**see dashed blue line for d and θ Fig3**). The relative maximal change in tension is found to be $\frac{\tau^{max}}{\tau^I} = 1.56 \pm 0.56$ (n=5) in 3D and $\frac{\tau^{max}}{\tau^I} = 1.25 \pm 0.15$ (n=5) in epifluorescence, in agreement with the expected underestimates of the contact angle in epifluorescence (see above).

Cortical tension increase in doublets and in cells

In cells, cortical tension can be as low as 50 pN/ μ m in fibroblast progenitor cells [10] and can go up to 4000 pN/ μ m for dictyostelium [11]. Surprisingly, when myosin activity is affected, either by drugs or by genetic manipulation the cortical tension only decreases by a factor of about 2 [7], [10], [11], [22]. Our *in vitro* reconstruction is able to capture this feature in the change of cortical tension. Indeed, we observe the cortical tension of the doublets to increase by a factor 1.1 to 2.4.

Different contributions for cortical tension

Cortical tension is the sum of the membrane tension and the tension due to the actomyosin cortex. In our assay, membrane contributes about 50% to the cortical

tension. In suspended fibroblast cells however, membrane tension is estimated to be only 10% of the cortical tension [7]. This difference may be explained by the absence of actin dynamics in our assay. Actin dynamics is confirmed to have a role on cortical tension that is multiplied by a factor of 5 when polymerization of actin is stimulated [7], [13]. How actin polymerization contributes to cortical tension is still an open question that needs to be addressed in the geometry of the cell. Whereas actin polymerization outside a liposome has been clearly shown to generate inward pressure, is not yet clear how this can be translated into tension in a different geometry. *In vitro* assays are on their way to mimic actin dynamics in cells [23], [24] and will allow unveiling the mechanism of tension build up by actin dynamics. This is the remaining module that needs to be understood, while the effect of myosin is distinguish from the one of membrane in this study.

Conclusion

We provide a biomimetic reconstitution of tension build up through actomyosin contractility using liposome doublets. Cortical tension is visualized *in situ* over time by analyzing doublet shape changes. This method allows us to directly quantify the relative increase in tension due to myosin, separately from the one due to actin dynamics. Understanding contraction of composite systems built brick by brick on the model of a cell tile the road for the reconstitution of complex systems like tissues.

Acknowledgments: This work was supported by the French Agence Nationale pour la Recherche (ANR), grant ANR 09BLAN0283, ANR 12BSV5001401 and ANR-11-JSV5-0002, and by the Fondation pour la Recherche Médicale (FRM), grant

DEQ20120323737. We thank Dr Agnieszka Kawska at IlluScientia for schemes. JL and MB thank the AXA Research Fund for doctoral fellowships. JL and KC were also supported by la Fondation ARC pour la recherche sur le cancer. We thank Thomas Risler and Clément Campillo for critical reading of the manuscript

Material and methods.

Lipids, reagents and proteins. Chemicals are purchased from Sigma Aldrich (St. Louis, MO, USA) unless specified otherwise. L-alpha-phosphatidylcholine (EPC) and 1,2-distearoyl-sn-glycero-3-phosphoethanolamine-N-[biotinyl polyethylene glycol 2000] (biotinylated lipids), 1,2-dioleoyl-sn-glycero-3-phosphocholine are purchased from Avanti polar lipids (Alabaster, USA). Actin and biotinylated actin are purchased from Cytoskeleton (Denver, USA) and used with no further purification. Fluorescent Alexa-488 actin is obtained from Molecular Probes. Monomeric actin containing 10% or 20% of labeled Alexa-488 actin and 0.25% of biotinylated actin is diluted in G-Buffer (2mM Tris, 0.2mM CaCl₂, 0.2mM DTT at pH 8.0). Myosin II is purified from rabbit skeletal muscle and fluorescent myosin II is prepared as previously described [25] and its functionality is confirmed by motility assays showing an average gliding speed of $4.5 \pm 1.5 \mu\text{m/s}$ ($N = 27$) [26]. The working buffer contains 25 mM imidazole, 50 mM KCl, 70 mM sucrose, 1mM Tris, 2 mM MgCl₂, 1 mM ATP, 0.1 mM DTT, 0.02 mg/ml β -casein, adjusted to pH 7.4. All proteins are mixed in the working buffer and myosin II forms minifilaments of approximately 0.7 micrometer length with about 100 motors [27].

Formation of liposome doublets, actin cortices on doublets. Liposomes are electroformed [18]. Briefly, 20 μ L of a mixture of EPC lipids and biotin PEG lipids present at 0.1 molar ratio with a concentration of 2.5 mg/ml in chloroform/methanol 5:3 (v:v) are spread on ITO-coated plates and dried under nitrogen flow, then placed under vacuum for 2 hours. A chamber is formed using the ITO plates (their conductive sides facing each other) filled with sucrose buffer (200mM sucrose, 2mM Tris adjusted at pH 7.4, containing or not sulforhodamin B 0.9 μ M), and sealed with hematocrit paste (Vitrex medical, Denmark). Liposomes are formed by applying an alternate current voltage (1V - 10 Hz) for 1hour and 15 minutes. Then liposomes are incubated with 160 nM streptavidin for 15 min and diluted 30 times. Note that for the observation of the interface between the doublet liposomes, we prepare separately liposomes in the presence or in the absence of sulforhodamin B, and mix them at equal volume before incubation with streptavidin. At this stage we have doublets coated with streptavidin. Waiting more than 15 min would increase the quantity of liposome aggregates and decrease the quantity of doublets and single liposomes. A bulk solution of 40 μ M actin monomers (Cytoskeleton, Denver USA) containing 10% fluorescently labeled actin and 1/400 biotinylated actin monomers is polymerized at 1 μ M by diluting 40 times in the working buffer (25 mM imidazole, 50 mM KCl, 70 mM sucrose, 1mM Tris, 2 mM MgCl₂, 1 mM ATP, 0.1 mM DTT, 0.02 mg/ml β -casein, adjusted at a pH 7.4) for 1 hour in the presence of 1 μ M of phalloidin (to prevent depolymerization). Actin filaments are then diluted 10-fold to 0.1 μ M, mixed with streptavidin-coated doublets of liposomes, and incubated for 15 min. The mix is diluted 5 times for observation to reduce background fluorescence from actin filaments.

Observation chamber design, formation and myosin II injection. Observation chambers are made by heating Parafilm stripes (as spacer) with an H-shape between two coverslips. The solution containing doublets is injected in the chamber and let few minutes in order to let the doublets sediment (**Fig 1C**). Then myosin II filaments are injected in the chamber and the H-shape and doublets are imaged over time in the middle of the chamber (**Fig 1C**). Conditions (streptavidin, actin filament length) are the same as in [16] but observations are made before breakage of the acto-myosin shell.

Observation of doublets. Epifluorescence and phase contrast microscopy are performed using an IX70 Olympus inverted microscope with a 100x or a 60x oil-immersion objective. Spinning-disk confocal microscopy is performed on a Nikon Eclipse T1 microscope with an Andor Evolution Spinning Disc system and a 60x water immersion objective and a z distance of xx μm between z-slices.

Image processing and data analysis. 2D- images: the contact angle is measured by adjusting two circles on binarized liposome images taken by phase contrast or epifluorescence microscopy. 3D-images: The geometrical parameters of the doublets are determined by optimizing the correlation between simulated and acquired 3D recording. Simulated 3D stacks, using [Python], [Numpy] and [Cython] are obtained by creating two spherical caps in contact and reproducing the fluorescent signal of actin at the external surface. Optimizing the correlation between simulated and acquired data is done using [Python] and [SciPy] (Nelder–Mead simplex method from the "optimize" submodule). Initial fit parameters of the first frame of each timelapse are determined visually. For the subsequent frame, we use the optimized parameters as initial parameters. Robustness of fit is checked by several repeats while changing the initial fit parameters by a random amount drawn from a normal distribution (mean

$0\mu\text{m}$ and standard deviation $0.5\mu\text{m}$). The obtained eight parameters (2 centers with X,Y,Z coordinate and 2 liposomes radii) geometrically define the contact angle and the distance between centers. All the data processing was done in an [IPython] environment.

Bibliography

- [1] A. G. Clark, K. Dierkes, E. K. Paluch, « Monitoring Actin Cortex Thickness in Live Cells », *Biophys. J.*, vol. 105, n° 3, p. 570-580, 2013.
- [2] G. Salbreux, G. Charras, E. Paluch, « Actin cortex mechanics and cellular morphogenesis », *Trends Cell Biol.*, 2012.
- [3] E. Munro, J. Nance, J. R. Priess, « Cortical flows powered by asymmetrical contraction transport PAR proteins to establish and maintain anterior-posterior polarity in the early *C. elegans* embryo », *Dev. Cell*, vol. 7, n° 3, p. 413-424, 2004.
- [4] T. Lecuit, P.-F. Lenne, « Cell surface mechanics and the control of cell shape, tissue patterns and morphogenesis », *Nat. Rev. Mol. Cell Biol.*, vol. 8, n° 8, p. 633-644, 2007.
- [5] M. Rauzi, P.-F. Lenne, T. Lecuit, « Planar polarized actomyosin contractile flows control epithelial junction remodelling », *Nature*, vol. 468, n° 7327, p. 1110-1114, 2010.
- [6] M. Rauzi P.-F. Lenne, « Cortical forces in cell shape changes and tissue morphogenesis », *Curr. Top. Dev. Biol.*, vol. 95, p. 93-144, 2011.
- [7] J.-Y. Tinevez, U. Schulze, G. Salbreux, J. Roensch, J.-F. Joanny, E. Paluch, « Role of cortical tension in bleb growth », *Proc. Natl. Acad. Sci. U. S. A.*, vol. 106, n° 44, p. 18581-18586, 2009.
- [8] R. Nambiar, R. E. McConnell, M. J. Tyska, « Control of cell membrane tension by myosin-I », *Proc Natl Acad Sci U S A*, vol. 106, n° 29, p. 11972-11977, 2009.
- [9] D. Raucher, T. Stauffer, W. Chen, K. Shen, S. Guo, J. D. York, M. P. Sheetz, T. Meyer, « Phosphatidylinositol 4,5-bisphosphate functions as a second messenger that regulates cytoskeleton-plasma membrane adhesion », *Cell*, vol. 100, n° 2, p. 221-228, 2000.

- [10] M. Krieg, Y. Arboleda-Estudillo, P.-H. Puech, J. Käfer, F. Graner, D. J. Müller, C.-P. Heisenberg, « Tensile forces govern germ-layer organization in zebrafish », *Nat. Cell Biol.*, vol. 10, n° 4, p. 429-436, 2008.
- [11] E. C. Schwarz, E. M. Neuhaus, C. Kistler, A. W. Henkel, T. Soldati, « Dictyostelium myosin IK is involved in the maintenance of cortical tension and affects motility and phagocytosis », *J. Cell Sci.*, vol. 113 (Pt 4), p. 621-633, 2000.
- [12] T. Luo, K. Mohan, P. A. Iglesias, D. N. Robinson, « Molecular mechanisms of cellular mechanosensing », *Nat. Mater.*, vol. 12, n° 11, p. 1064-1071, 2013.
- [13] W. Engl, B. Arasi, L. L. Yap, J-P. Thiery, V. Viasnoff, « Actin dynamics modulate mechanosensitive immobilization of E-cadherin at adherens junctions », *Nat. Cell Biol.*, vol. 16, n° 6, p. 587-594, 2014.
- [14] J.-L. Maître, H. Berthoumieux, S. F. G. Krens, G. Salbreux, F. Jülicher, E. Paluch, C.-P. Heisenberg, « Adhesion Functions in Cell Sorting by Mechanically Coupling the Cortices of Adhering Cells », *Science*, vol. 338, n° 6104, p. 253-256, 2012.
- [15] M. P. Murrell M. L. Gardel, « F-actin buckling coordinates contractility and severing in a biomimetic actomyosin cortex », *Proc. Natl. Acad. Sci.*, 2012.
- [16] K. Carvalho, F. C. Tsai, E. Lees, R. Voituriez, G. H. Koenderink, C. Sykes, « Cell-sized liposomes reveal how actomyosin cortical tension drives shape change », *Proc. Natl. Acad. Sci.*, 2013.
- [17] K. Carvalho, J. Lemière, F. Faqir, J. Manzi, L. Blanchoin, J. Plastino, T. Betz, C. Sykes, « Actin polymerization or myosin contraction: two ways to build up cortical tension for symmetry breaking », *Philos. Trans. R. Soc. B Biol. Sci.*, vol. 368, n° 1629, 2013.
- [18] M. Angelova, D. Dimitrov, « Liposome electroformation », *Faraday Discuss.*, vol. 81, p. 303+, 1986.
- [19] O. Sandre, L. Moreaux, F. Brochard-Wyart, « Dynamics of transient pores in stretched vesicles », *Proc. Natl. Acad. Sci. U. S. A.*, vol. 96, n° 19, p. 10591-10596, 1999.
- [20] J. van der Gucht, E. Paluch, J. Plastino, C. Sykes, « Stress release drives symmetry breaking for actin-based movement », *Proc. Natl. Acad. Sci. U. S. A.*, vol. 102, n° 22, p. 7847-7852, 2005.

- [21] J. Sedzinski, M. Biro, A. Oswald, J.-Y. Tinevez, G. Salbreux, E. Paluch, « Polar actomyosin contractility destabilizes the position of the cytokinetic furrow », *Nature*, vol. 476, n° 7361, p. 462-466, 2011.
- [22] P. Kunda, A. E. Pelling, T. Liu, B. Baum, « Moesin controls cortical rigidity, cell rounding, and spindle morphogenesis during mitosis », *Curr. Biol. CB*, vol. 18, n° 2, p. 91-101, 2008.
- [23] E. Abu Shah, K. Keren, « Symmetry breaking in reconstituted actin cortices », *eLife*, vol. 3, p. e01433, 2014.
- [24] T. Luo, V. Srivastava, Y. Ren, D. N. Robinson, « Mimicking the mechanical properties of the cell cortex by the self-assembly of an actin cortex in vesicles », *Appl. Phys. Lett.*, vol. 104, n° 15, p. 153701, 2014.
- [25] G. H. Koenderink, Z. Dogic, F. Nakamura, P. M. Bendix, F. C. MacKintosh, J. H. Hartwig, T. P. Stossel, D. A. Weitz, « An active biopolymer network controlled by molecular motors », *Proc. Natl. Acad. Sci. U. S. A.*, vol. 106, n° 36, p. 15192-15197, 2009.
- [26] Y. Y. Toyoshima, S. J. Kron, E. M. McNally, K. R. Niebling, C. Toyoshima, J. A. Spudich, « Myosin subfragment-1 is sufficient to move actin filaments in vitro », *Nature*, vol. 328, n° 6130, p. 536-539, 1987.
- [27] M. S. E. Silva, M. Depken, B. Stuhrmann, M. Korsten, F. C. Mackintosh, G. H. Koenderink, « Active multistage coarsening of actin networks driven by myosin motors », *Proc. Natl. Acad. Sci. U. S. A.*, 2011.

Figure 1

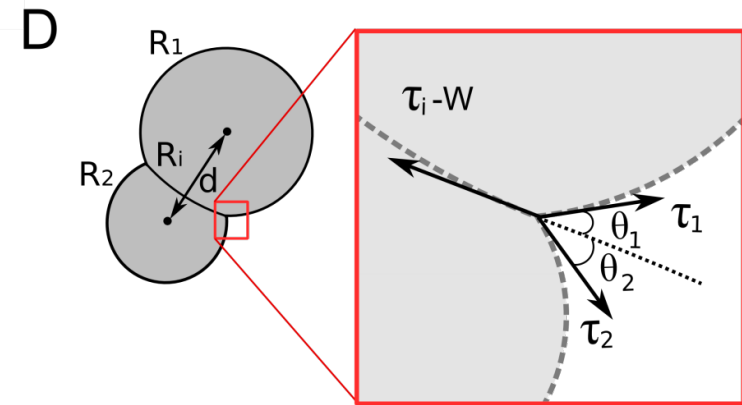
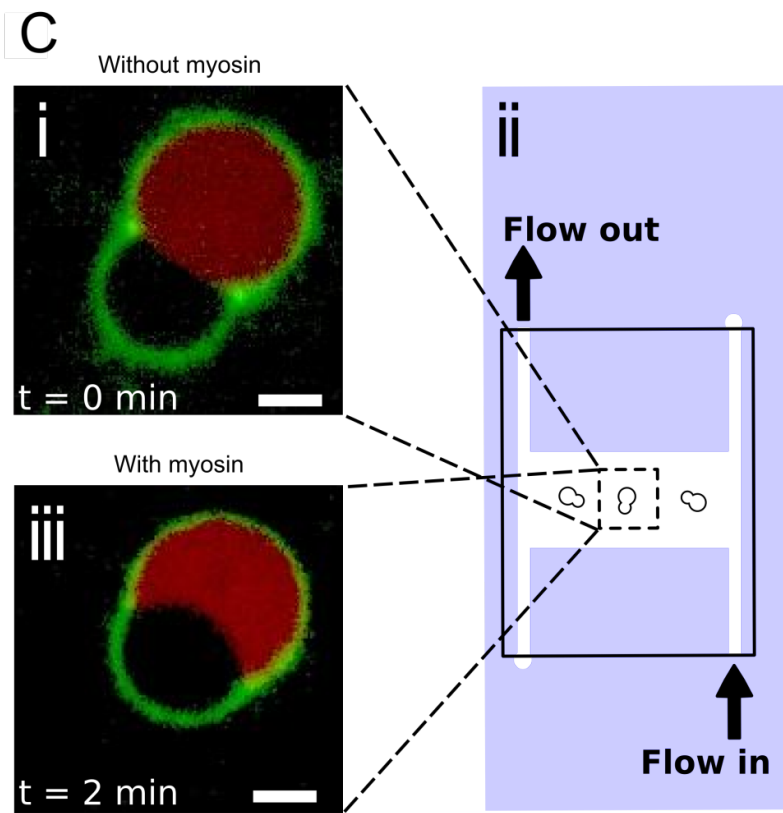
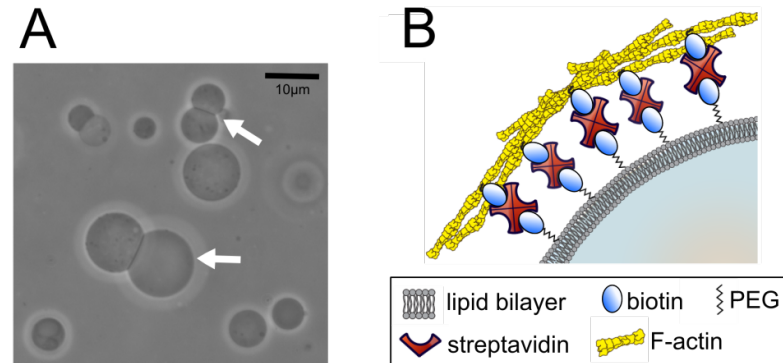
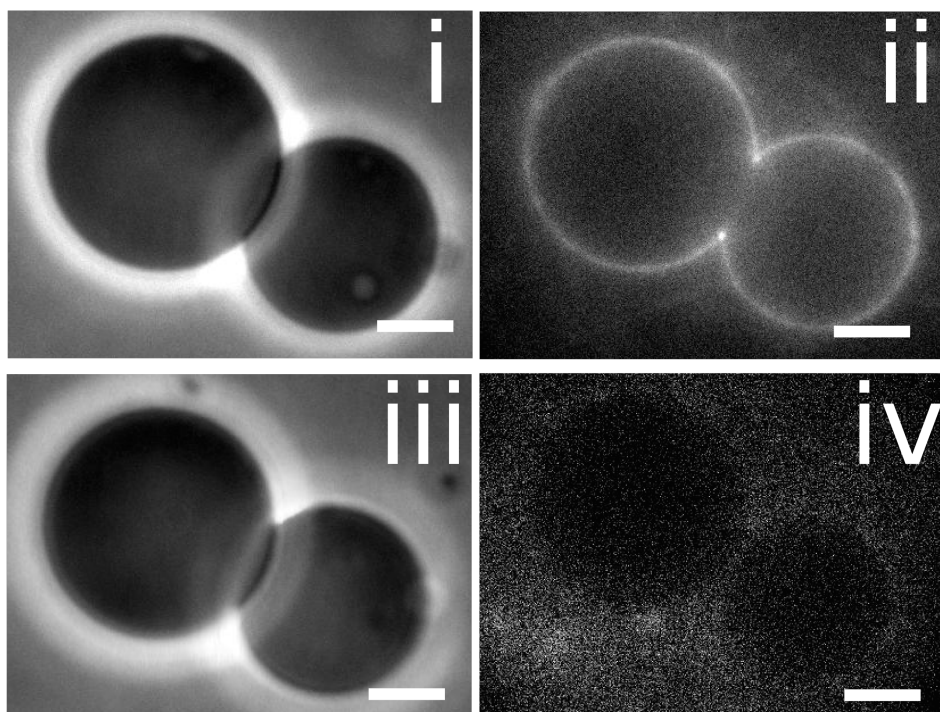


Figure 2

A



B

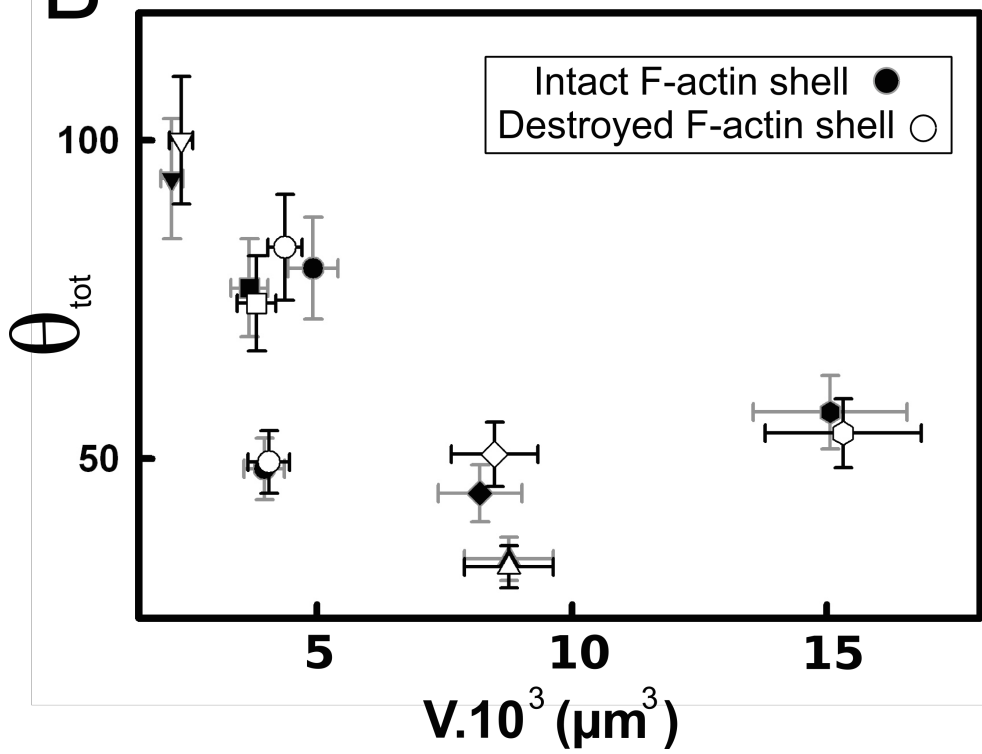
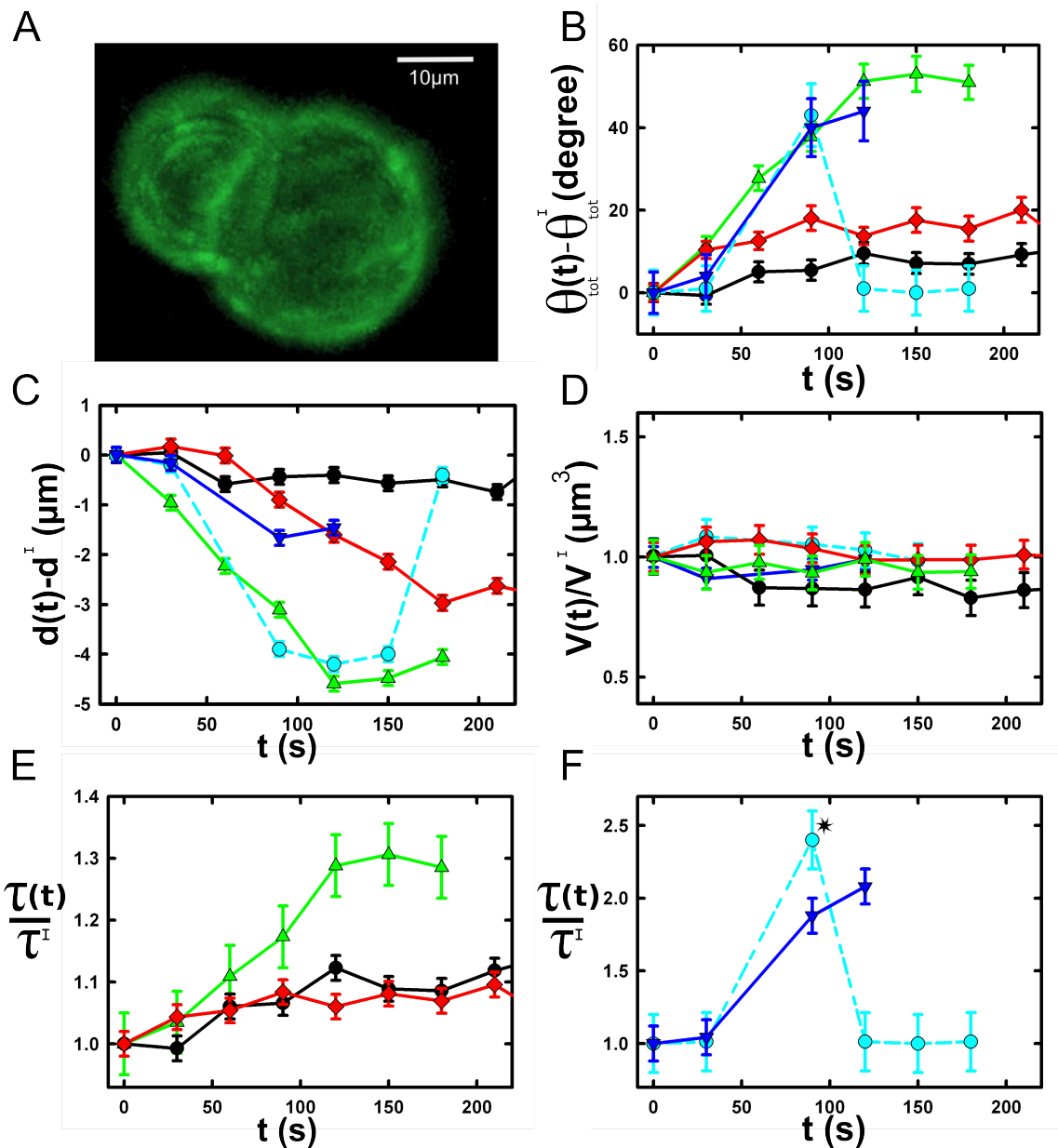


Figure 3



Supplementary figure

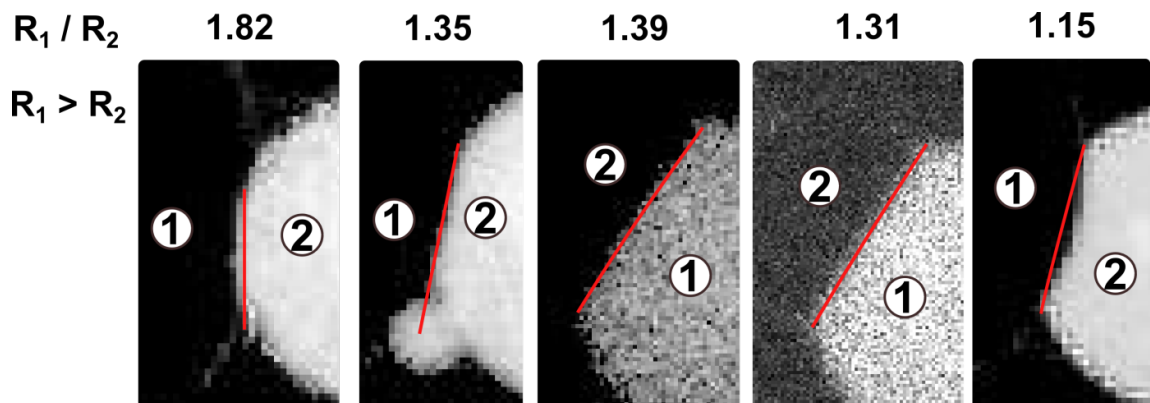
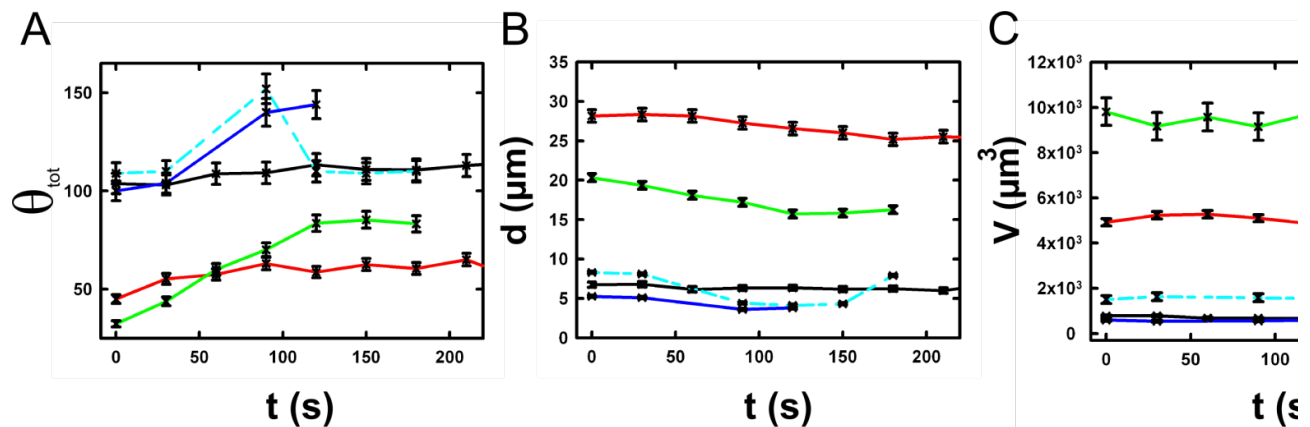


Figure Captions

Figure 1: Cell-sized liposome doublets. A) Doublets, indicated by white arrows, in the field of view of a phase contrast microscope. B) Schematic of the stabilized actin cortex at the membrane (proteins not to scale). C) i) Macrofluidics chamber designed to exchange the outside buffer. Doublets are visualized in the middle horizontal channel of the H shape chamber to avoid movement during the buffer exchange. Spinning disk images of the doublet before i) or after iii) myosin II injection. One liposome contains SRB (red) to visualize the interface of the doublet, the actin cortex is labeled in green. Scale bar 5 μ m. D) Simplification of the doublet with the three characteristic radii. Inset: enlargement of the contact interface between the two liposomes with the Young's tension vector and the contact angle.

Figure 2: Effect of an actin cortex on the doublet's shape. A) Image of the same doublet coated with fluorescent actin before i) ii) and after iii) iv) actin cortex disruption. The actin cortex is visualized by epifluorescence ii) iv) and the doublet by phase contrast i) iii). Scale bar 5 μ m. B) Measurement of the contact angle between the two liposomes as a function of their volume, before (black) and after (white) disruption of the stabilized actin cortex.

Figure 3: Geometrical parameters over time: A) 3D reconstruction of a doublet surrounded by actin. Note that there is no actin at the interface between the liposomes. B) Evolution of the contact angle compare to the initial one as a function of time. Each doublet is represented by a different line color. C) Evolution of the

distance between the two liposomes center over time. D) Evolution of the volume ratio over time. E) Increase of the tension ratio between the tension $\tau(t)$ at time t and the initial one τ^i . Note that the blue dashed line A-B-C-D corresponds to the evolution of geometrical parameters of the same doublet, analyzed even after actin cortex rupture. It recovers its initial parameter values.

This version of the manuscript is based on the source files repository version 698b3be62d1ac63210da5f0cd79c4d6b2817cae4, available on [github¹](#), and [bitbucket²](#). It is also available [online³](#) as HTML and epub.

¹<http://github.com/carreau/phd-dissertation/>

²<https://bitbucket.org/Carreau/dissertation>

³<http://matthiasphd.herokuapp.com/html>

BIBLIOGRAPHY

- [Alberts, Johnson, Lewis, et al. 2008] B Alberts, A Johnson, J Lewis, M Raff, K Roberts, and P And Walter. *Molecular Biology of the Cell*. volume 54. Garland, 2008. URL: <http://discovery.ucl.ac.uk/109973/>⁴.
- [Angelova, Dimitrov, 1986] Miglena I. Angelova and Dimiter S. Dimitrov. Liposome electroformation. *Faraday Discussions of the Chemical Society*, 81:303, 1986. URL: <http://xlink.rsc.org/?DOI=dc9868100303>⁵, doi:10.1039/dc9868100303⁶.
- [Azoury, Lee, Georget, et al. 2011] Jessica Azoury, Karen Wingman Lee, Virginie Georget, Pascale Hikal, and Marie-Hélène Verlhac. Symmetry breaking in mouse oocytes requires transient F-actin meshwork destabilization.. *Development (Cambridge, England)*, 138(14):2903–8, July 2011. URL: <http://dev.biologists.org/content/138/14/2903.long>⁷, doi:10.1242/dev.060269⁸.
- [BernheimGroswasser, Wiesner, Golsteyn, et al. 2002] Anne Bernheim-Groswasser, Sébastien Wiesner, Roy M. Golsteyn, Marie-France Carlier, and Cecile Sykes. The dynamics of actin-based motility depend on surface parameters. *Nature*, 417(6886):308–311, May 2002. URL: <http://dx.doi.org/10.1038/417308a> <http://www.nature.com/nature/journal/v417/n6886/full/417308a.html>⁹, doi:10.1038/417308a¹⁰.
- [Berridge, 2012] Michael J. Berridge. Cell Signalling Biology: Module 4 - Sensors and Effectors. 2012. doi:10.1042/csb0001004¹¹.
- [Bornschlogl, 2013] Thomas Bornschlogl. How filopodia pull: what we know about the mechanics and dynamics of filopodia.. *Cytoskeleton (Hoboken, N.J.)*, 70(10):590–603, October 2013. URL: <http://www.ncbi.nlm.nih.gov/pubmed/23959922>¹², doi:10.1002/cm.21130¹³.
- [Buss, KendrickJones, 2008] Folma Buss and John Kendrick-Jones. How are the cellular functions of myosin VI regulated within the cell?. *Biochemical and biophysical research communications*, 369(1):165–175, April 2008.

⁴<http://discovery.ucl.ac.uk/109973/>

⁵<http://xlink.rsc.org/?DOI=dc9868100303>

⁶<http://dx.doi.org/10.1039/dc9868100303>

⁷<http://dev.biologists.org/content/138/14/2903.long>

⁸<http://dx.doi.org/10.1242/dev.060269>

⁹<http://dx.doi.org/10.1038/417308a> <http://www.nature.com/nature/journal/v417/n6886/full/417308a.html>

¹⁰<http://dx.doi.org/10.1038/417308a>

¹¹<http://dx.doi.org/10.1042/csb0001004>

¹²<http://www.ncbi.nlm.nih.gov/pubmed/23959922>

¹³<http://dx.doi.org/10.1002/cm.21130>

URL: [http://www.sciencedirect.com/science/article/pii/S0006291X07025508¹⁴](http://www.sciencedirect.com/science/article/pii/S0006291X07025508),
doi:10.1016/j.bbrc.2007.11.150¹⁵.

[Carlier, Laurent, Santolini, et al. 1997] M F Carlier, V Laurent, J Santolini, R Melki, D Didry, G X Xia, Y Hong, N H Chua, and D Pantaloni. Actin depolymerizing factor (ADF/cofilin) enhances the rate of filament turnover: implication in actin-based motility.. *The Journal of cell biology*, 136(6):1307–22, March 1997. URL: [http://www.ncbi.nlm.nih.gov/pubmed/2132522&tool=pmcentrez&rendertype=abstract¹⁶](http://www.ncbi.nlm.nih.gov/pubmed/2132522&tool=pmcentrez&rendertype=abstract).

[Carvalho, Lemiere, Faqir, et al. 2013] Kevin Carvalho, Joël Lemière, Fahima Faqir, John Manzi, Laurent Blanchoin, Julie Plastino, Timo Betz, and Cécile Sykes. Actin polymerization or myosin contraction: two ways to build up cortical tension for symmetry breaking.. *Philosophical transactions of the Royal Society of London. Series B, Biological sciences*, 368(1629):20130005, January 2013. URL: [http://www.ncbi.nlm.nih.gov/pubmed/24062578¹⁷](http://www.ncbi.nlm.nih.gov/pubmed/24062578), doi:10.1098/rstb.2013.0005¹⁸.

[Carvalho, Tsai, Lees, et al. 2013] Kevin Carvalho, Feng-Ching Tsai, Edouard Lees, Raphaël Voituriez, Gijsje H Koenderink, and Cecile Sykes. Cell-sized liposomes reveal how actomyosin cortical tension drives shape change.. *Proceedings of the National Academy of Sciences of the United States of America*, 110(41):16456–61, October 2013. URL: <http://www.pnas.org/content/110/41/16456> [http://www.ncbi.nlm.nih.gov/articlerender.fcgi?artid=3799374&tool=pmcentrez&rendertype=abstract¹⁹](http://www.ncbi.nlm.nih.gov/articlerender.fcgi?artid=3799374&tool=pmcentrez&rendertype=abstract), doi:10.1073/pnas.1221524110²⁰.

[Chaigne, Campillo, Gov, et al. 2013] Agathe Chaigne, Clément Campillo, Nir S Gov, Raphaël Voituriez, Jessica Azoury, Claudia Umaña-Díaz, María Almonacid, Isabelle Queguiner, Pierre Nassoy, Cécile Sykes, Marie-Hélène Verlhac, and Marie-Emilie Terret. A soft cortex is essential for asymmetric spindle positioning in mouse oocytes.. *Nature cell biology*, 15(8):958–66, August 2013. URL: <http://dx.doi.org/10.1038/ncb2799> [http://www.ncbi.nlm.nih.gov/pubmed/23851486²¹](http://www.ncbi.nlm.nih.gov/pubmed/23851486), doi:10.1038/ncb2799²².

[Charras, Paluch, 2008] Guillaume Charras and Ewa Paluch. Blebs lead the way: how to migrate without lamellipodia.. *Nature reviews. Molecular cell biology*, 9(9):730–6, September 2008. URL: <http://dx.doi.org/10.1038/nrm2453> [http://www.ncbi.nlm.nih.gov/pubmed/18628785²³](http://www.ncbi.nlm.nih.gov/pubmed/18628785), doi:10.1038/nrm2453²⁴.

[Clark, Dierkes, Paluch, 2013] Andrew G. Clark, Kai Dierkes, and Ewa K. Paluch. Monitoring actin cortex thickness in live cells.. *Biophysical journal*, 105(3):570–80, August 2013. URL: [http://www.ncbi.nlm.nih.gov/pubmed/23931305²⁵](http://www.ncbi.nlm.nih.gov/pubmed/23931305), doi:10.1016/j.bpj.2013.05.057²⁶.

[Dabiri, Sanger, Portnoy, Southwick, 1990] G A Dabiri, J M Sanger, D A Portnoy, and F S Southwick. Listeria monocytogenes moves rapidly through the host-cell cyto-

¹⁴<http://www.sciencedirect.com/science/article/pii/S0006291X07025508>

¹⁵<http://dx.doi.org/10.1016/j.bbrc.2007.11.150>

¹⁶<http://www.ncbi.nlm.nih.gov/articlerender.fcgi?artid=2132522&tool=pmcentrez&rendertype=abstract>

¹⁷<http://www.ncbi.nlm.nih.gov/pubmed/24062578>

¹⁸<http://dx.doi.org/10.1098/rstb.2013.0005>

¹⁹<http://www.pnas.org/content/110/41/16456> <http://www.ncbi.nlm.nih.gov/articlerender.fcgi?artid=3799374&tool=pmcentrez&rendertype=abstract>

²⁰<http://dx.doi.org/10.1073/pnas.1221524110>

²¹<http://dx.doi.org/10.1038/ncb2799> <http://www.ncbi.nlm.nih.gov/pubmed/23851486>

²²<http://dx.doi.org/10.1038/ncb2799>

²³<http://dx.doi.org/10.1038/nrm2453> <http://www.ncbi.nlm.nih.gov/pubmed/18628785>

²⁴<http://dx.doi.org/10.1038/nrm2453>

²⁵<http://www.ncbi.nlm.nih.gov/pubmed/23931305>

²⁶<http://dx.doi.org/10.1016/j.bpj.2013.05.057>

plasm by inducing directional actin assembly.. *Proceedings of the National Academy of Sciences of the United States of America*, 87(16):6068–72, August 1990. URL: <http://www.ncbi.nlm.nih.gov/pmc/articles/PMC36942/>²⁷, doi:10.1073/pnas.87.16.6068²⁸.

[Engler, Sen, Sweeney, Discher, 2006] Adam J. Engler, Shamik Sen, H. Lee Sweeney, and Dennis E. Discher. Matrix elasticity directs stem cell lineage specification.. *Cell*, 126(4):677–89, August 2006. URL: <http://www.ncbi.nlm.nih.gov/pubmed/16923388>²⁹, doi:10.1016/j.cell.2006.06.044³⁰.

[Faix, Rottner, 2006] Jan Faix and Klemens Rottner. The making of filopodia.. *Current opinion in cell biology*, 18(1):18–25, February 2006. URL: <http://www.sciencedirect.com/science/article/pii/S095506740500178X>³¹, doi:10.1016/j.ceb.2005.11.002³².

[Feric, Brangwynne, 2013] Marina Feric and Clifford P Brangwynne. A nuclear F-actin scaffold stabilizes ribonucleoprotein droplets against gravity in large cells. *Nature Cell Biology*, 15:1253–1259, 2013. URL: <http://dx.doi.org/10.1038/ncb2830>³³, doi:10.1038/ncb2830³⁴.

[Fletcher, Mullins, 2010] Daniel A Fletcher and R Dyche Mullins. Cell mechanics and the cytoskeleton.. *Nature*, 463(7280):485–92, January 2010. URL: <http://dx.doi.org/10.1038/nature08908>³⁵, doi:10.1038/nature08908³⁶.

[Gardel, Valentine, Crocker, et al. 2003] M. L Gardel, M. T Valentine, J. C Crocker, A. R Bausch, and D. A Weitz. Microrheology of entangled F-actin solutions.. *Physical review letters*, 91(15):158302, October 2003. URL: <http://www.ncbi.nlm.nih.gov/pubmed/14611506> <http://link.aps.org/doi/10.1103/PhysRevLett.91.158302>³⁷, doi:10.1103/PhysRevLett.91.158302³⁸.

[Goley, Welch, 2006] Erin D Goley and Matthew D Welch. The ARP2/3 complex: an actin nucleator comes of age.. *Nature reviews. Molecular cell biology*, 7(10):713–26, October 2006. URL: <http://dx.doi.org/10.1038/nrm2026>³⁹, doi:10.1038/nrm2026⁴⁰.

[Hartman, Spudich, 2012] M. A. Hartman and J. A. Spudich. The myosin superfamily at a glance. *Journal of Cell Science*, 125(7):1627–1632, May 2012. URL: <http://jcs.biologists.org/content/125/7/1627.full> <http://jcs.biologists.org/cgi/doi/10.1242/jcs.094300>⁴¹, doi:10.1242/jcs.094300⁴².

²⁷<http://www.ncbi.nlm.nih.gov/pmc/articles/PMC36942/>

²⁸<http://dx.doi.org/10.1073/pnas.87.16.6068>

²⁹<http://www.ncbi.nlm.nih.gov/pubmed/16923388>

³⁰<http://dx.doi.org/10.1016/j.cell.2006.06.044>

³¹<http://www.sciencedirect.com/science/article/pii/S095506740500178X>

³²<http://dx.doi.org/10.1016/j.ceb.2005.11.002>

³³<http://dx.doi.org/10.1038/ncb2830>

³⁴<http://dx.doi.org/10.1038/ncb2830>

³⁵<http://dx.doi.org/10.1038/nature08908>

³⁶<http://dx.doi.org/10.1038/nature08908>

³⁷<http://www.ncbi.nlm.nih.gov/pubmed/14611506> <http://link.aps.org/doi/10.1103/PhysRevLett.91.158302>

³⁸<http://dx.doi.org/10.1103/PhysRevLett.91.158302>

³⁹<http://dx.doi.org/10.1038/nrm2026>

⁴⁰<http://dx.doi.org/10.1038/nrm2026>

⁴¹<http://jcs.biologists.org/content/125/7/1627.full> <http://jcs.biologists.org/cgi/doi/10.1242/jcs.094300>

⁴²<http://dx.doi.org/10.1242/jcs.094300>

- [Helfrich, 1973] W Helfrich. Elastic properties of lipid bilayers: theory and possible experiments.. *Zeitschrift für Naturforschung. Teil C: Biochemie, Biophysik, Biologie, Virologie*, 28(11):693–703, 1973. URL: <http://www.ncbi.nlm.nih.gov/pubmed/4273690>⁴³.
- [Holubcova, Howard, Schuh, 2013] Zuzana Holubcová, Gillian Howard, and Melina Schuh. Vesicles modulate an actin network for asymmetric spindle positioning.. *Nature cell biology*, 15(8):937–47, August 2013. URL: <http://www.pubmedcentral.nih.gov/articlerender.fcgi?artid=3797517&tool=pmcentrez&rendertype=abstract>⁴⁴, doi:10.1038/ncb2802⁴⁵.
- [Huelsmann, Ylanne, Brown, 2013] Sven Huelsmann, Jari Yläne, and Nicholas H Brown. Filopodia-like actin cables position nuclei in association with perinuclear actin in Drosophila nurse cells.. *Developmental cell*, 26(6):604–15, September 2013. URL: <http://www.pubmedcentral.nih.gov/articlerender.fcgi?artid=3791400&tool=pmcentrez&rendertype=abstract>⁴⁶, doi:10.1016/j.devcel.2013.08.014⁴⁷.
- [Isambert, Maggs, 1996] H. Isambert and A. C. Maggs. Dynamics and Rheology of Actin Solutions. *Macromolecules*, 29(3):1036–1040, January 1996. URL: <http://dx.doi.org/10.1021/ma946418x> <http://pubs.acs.org/doi/abs/10.1021/ma946418x> <http://pubs.acs.org/doi/full/10.1021/ma946418x> <http://pubs.acs.org/doi/pdf/10.1021/ma946418x>⁴⁸, doi:10.1021/ma946418x⁴⁹.
- [Isambert, Venier, Maggs, et al. 1995] H. Isambert, P. Venier, A. Maggs, A. Fattoum, R. Kassab, D. Pantaloni, and M. Carlier. Flexibility of actin filaments derived from thermal fluctuations. Effect of bound nucleotide, phalloidin, and muscle regulatory proteins. *Journal of Biological Chemistry*, 270(19):11437–11444, May 1995. URL: <http://www.jbc.org/content/270/19/11437.short>⁵⁰, doi:10.1074/jbc.270.19.11437⁵¹.
- [Iwabuchi, Takagi, 2010] Kosei Iwabuchi and Shingo Takagi. Actin-based mechanisms for light-dependent intracellular positioning of nuclei and chloroplasts in Arabidopsis.. *Plant signaling & behavior*, 5(8):1010–3, August 2010. URL: <http://www.plantphysiol.org/content/152/3/1309>⁵², doi:10.1104/pp.109.149526⁵³.
- [Jaalouk, Lammerding, 2009] Diana E Jaalouk and Jan Lammerding. Mechanotransduction gone awry.. *Nature reviews. Molecular cell biology*, 10(1):63–73, January 2009. URL: <http://www.pubmedcentral.nih.gov/articlerender.fcgi?artid=2668954&tool=pmcentrez&rendertype=abstract>⁵⁴, doi:10.1038/nrm2597⁵⁵.
- [Jahnel, Behrndt, Jannasch, et al. 2011] Marcus Jahnel, Martin Behrndt, Anita Jannasch, Erik Schäffer, and Stephan W. Grill. Measuring the complete force field of an optical trap. *Op-*
-
- ⁴³<http://www.ncbi.nlm.nih.gov/pubmed/4273690>
- ⁴⁴<http://www.pubmedcentral.nih.gov/articlerender.fcgi?artid=3797517&tool=pmcentrez&rendertype=abstract>
- ⁴⁵<http://dx.doi.org/10.1038/ncb2802>
- ⁴⁶<http://www.pubmedcentral.nih.gov/articlerender.fcgi?artid=3791400&tool=pmcentrez&rendertype=abstract>
- ⁴⁷<http://dx.doi.org/10.1016/j.devcel.2013.08.014>
- ⁴⁸<http://dx.doi.org/10.1021/ma946418x> <http://pubs.acs.org/doi/abs/10.1021/ma946418x> <http://pubs.acs.org/doi/full/10.1021/ma946418x> <http://pubs.acs.org/doi/pdf/10.1021/ma946418x>
- ⁴⁹<http://dx.doi.org/10.1021/ma946418x>
- ⁵⁰<http://www.jbc.org/content/270/19/11437.short>
- ⁵¹<http://dx.doi.org/10.1074/jbc.270.19.11437>
- ⁵²<http://www.plantphysiol.org/content/152/3/1309>
- ⁵³<http://dx.doi.org/10.1104/pp.109.149526>
- ⁵⁴<http://www.pubmedcentral.nih.gov/articlerender.fcgi?artid=2668954&tool=pmcentrez&rendertype=abstract>
- ⁵⁵<http://dx.doi.org/10.1038/nrm2597>

- tics Letters*, 36(7):1260–1262, April 2011. URL: <http://ol.osa.org/abstract.cfm?URI=ol-36-7-1260> <http://www.opticsinfobase.org/ol/abstract.cfm?URI=ol-36-7-1260>⁵⁶, doi:10.1364/OL.36.001260⁵⁷.
- [Kawska, Carvalho, Manzi, et al. 2012] Agnieszka Kawska, Kévin Carvalho, John Manzi, Rajaa Boujema-Paterski, Laurent Blanchoin, Jean-Louis Martiel, and Cécile Sykes. How actin network dynamics control the onset of actin-based motility.. *Proceedings of the National Academy of Sciences of the United States of America*, 109(36):14440–5, September 2012. URL: <http://www.pnas.org/content/109/36/14440.short>⁵⁸, doi:10.1073/pnas.1117096109⁵⁹.
- [Krieg, Arboleda-Estudillo, Puech, et al. 2008] M Krieg, Y Arboleda-Estudillo, P-H Puech, J Käfer, F Graner, D J Müller, and C-P Heisenberg. Tensile forces govern germ-layer organization in zebrafish.. *Nature cell biology*, 10(4):429–36, April 2008. URL: <http://dx.doi.org/10.1038/ncb1705>⁶⁰, doi:10.1038/ncb1705⁶¹.
- [Kruse, Joanny, Julicher, et al. 2005] Karsten Kruse, J F Joanny, Frank Jülicher, J Prost, and K Sekimoto. Generic theory of active polar gels: a paradigm for cytoskeletal dynamics.. *The European physical journal. E, Soft matter*, 16(1):5–16, January 2005. URL: <http://link.springer.com/article/10.1140/epje/e2005-00002-5> <http://www.ncbi.nlm.nih.gov/pubmed/15688136>⁶², doi:10.1140/epje/e2005-00002-5⁶³.
- [Kunda, Pelling, Liu, Baum, 2008] Patricia Kunda, Andrew E Pelling, Tao Liu, and Buzz Baum. Moesin controls cortical rigidity, cell rounding, and spindle morphogenesis during mitosis.. *Current biology : CB*, 18(2):91–101, January 2008. URL: <http://www.ncbi.nlm.nih.gov/pubmed/18207738>⁶⁴, doi:10.1016/j.cub.2007.12.051⁶⁵.
- [Liverpool, 2006] Tanniemola B Liverpool. Active gels: where polymer physics meets cytoskeletal dynamics.. *Philosophical transactions. Series A, Mathematical, physical, and engineering sciences*, 364(1849):3335–55, December 2006. URL: <http://www.ncbi.nlm.nih.gov/pubmed/17090463>⁶⁶, doi:10.1098/rsta.2006.1897⁶⁷.
- [Loisel, Boujemaa, Pantaloni, Carlier, 1999] T P Loisel, R Boujemaa, D Pantaloni, and M F Carlier. Reconstruction of actin-based motility of Listeria and Shigella using pure proteins.. *Nature*, 401(6753):613–6, October 1999. URL: <http://www.ncbi.nlm.nih.gov/pubmed/10524632>⁶⁸, doi:10.1038/44183⁶⁹.
- [Lenart, Bacher, Daigle, et al. 2005] Péter Lénárt, Christian P Bacher, Nathalie Daigle, Arthur R Hand, Roland Eils, Mark Terasaki, and Jan Ellenberg. A contractile nuclear actin network drives chromosome congression in oocytes.. *Nature*, 436:812–818, 2005. doi:10.1038/nature03810⁷⁰.

⁵⁶<http://ol.osa.org/abstract.cfm?URI=ol-36-7-1260> <http://www.opticsinfobase.org/ol/abstract.cfm?URI=ol-36-7-1260>

⁵⁷<http://dx.doi.org/10.1364/OL.36.001260>

⁵⁸<http://www.pnas.org/content/109/36/14440.short>

⁵⁹<http://dx.doi.org/10.1073/pnas.1117096109>

⁶⁰<http://dx.doi.org/10.1038/ncb1705>

⁶¹<http://dx.doi.org/10.1038/ncb1705>

⁶²<http://link.springer.com/article/10.1140/epje/e2005-00002-5> <http://www.ncbi.nlm.nih.gov/pubmed/15688136>

⁶³<http://dx.doi.org/10.1140/epje/e2005-00002-5>

⁶⁴<http://www.ncbi.nlm.nih.gov/pubmed/18207738>

⁶⁵<http://dx.doi.org/10.1016/j.cub.2007.12.051>

⁶⁶<http://www.ncbi.nlm.nih.gov/pubmed/17090463>

⁶⁷<http://dx.doi.org/10.1098/rsta.2006.1897>

⁶⁸<http://www.ncbi.nlm.nih.gov/pubmed/10524632>

⁶⁹<http://dx.doi.org/10.1038/44183>

⁷⁰<http://dx.doi.org/10.1038/nature03810>

- [Machesky, Mullins, Higgs, et al. 1999] L. M. Machesky, R. D. Mullins, H. N. Higgs, D. A. Kaiser, L. Blanchoin, R. C. May, M. E. Hall, and T. D. Pollard. Scar, a WASp-related protein, activates nucleation of actin filaments by the Arp2/3 complex. *Proceedings of the National Academy of Sciences*, 96(7):3739–3744, March 1999. URL: [http://www.pnas.org/content/96/7/3739.full⁷¹](http://www.pnas.org/content/96/7/3739.full), doi:10.1073/pnas.96.7.3739⁷².
- [MacKintosh, Kas, Janmey, 1995] F. MacKintosh, J. Käs, and P. Janmey. Elasticity of Semiflexible Biopolymer Networks. *Physical Review Letters*, 75(24):4425–4428, December 1995. URL: [http://link.aps.org/doi/10.1103/PhysRevLett.75.4425⁷³](http://link.aps.org/doi/10.1103/PhysRevLett.75.4425), doi:10.1103/PhysRevLett.75.4425⁷⁴.
- [Mahaffy, Park, Gerde, et al. 2004] R E Mahaffy, S Park, E Gerde, J Käs, and C K Shih. Quantitative analysis of the viscoelastic properties of thin regions of fibroblasts using atomic force microscopy.. *Biophysical journal*, 86(3):1777–93, March 2004. URL: <http://www.ncbi.nlm.nih.gov/pmc/articles/PMC1304012/>&tool=pmcentrez&rendertype=abstract⁷⁵, doi:10.1016/S0006-3495(04)74245-9⁷⁶.
- [Maitre, Berthoumieux, Krens, et al. 2012] Jean-Léon Maitre, Hélène Berthoumieux, Simon Frederik Gabriel Krens, Guillaume Salbreux, Frank Jülicher, Ewa Paluch, and Carl-Philipp Heisenberg. Adhesion functions in cell sorting by mechanically coupling the cortices of adhering cells.. *Science (New York, N.Y.)*, 338(6104):253–6, October 2012. URL: <http://www.sciencemag.org.rproxy.sc.univ-paris-diderot.fr/content/338/6104/253.long> <http://www.ncbi.nlm.nih.gov/pubmed/22923438> [http://www.sciencemag.org/content/338/6104/253.abstract⁷⁷](http://www.sciencemag.org/content/338/6104/253.abstract), doi:10.1126/science.1225399⁷⁸.
- [Marcy, Prost, Carlier, Sykes, 2004] Yann Marcy, Jacques Prost, Marie-France Carlier, and Cécile Sykes. Forces generated during actin-based propulsion: a direct measurement by micromanipulation.. *Proceedings of the National Academy of Sciences of the United States of America*, 101(16):5992–7, April 2004. URL: <http://www.pnas.org/content/101/16/5992.abstract> [http://www.pnas.org/content/101/16/5992.full.pdf⁷⁹](http://www.pnas.org/content/101/16/5992.full.pdf), doi:10.1073/pnas.0307704101⁸⁰.
- [McCullough, Grintsevich, Chen, et al. 2011] Brannon R. McCullough, Elena E. Grintsevich, Christine K. Chen, Hyeran Kang, Alan L. Hutchison, Arnon Henn, Wenxiang Cao, Cristian Suarez, Jean Louis Martiel, Laurent Blanchoin, Emil Reisler, and Enrique M. De La Cruz. Cofilin-linked changes in actin filament flexibility promote severing. *Biophysical Journal*, 101:151–159, 2011. doi:10.1016/j.bpj.2011.05.049⁸¹.
- [Mizuno, Tardin, Schmidt, Mackintosh, 2007] Daisuke Mizuno, Catherine Tardin, C. F. Schmidt, and F C Mackintosh. Nonequilibrium mechanics of active cytoskeletal networks.. *Science (New York, N.Y.)*, 315(5810):370–3, January 2007. URL: <http://www.sciencemag.org/content/315/5810/370.abstract>

⁷¹<http://www.pnas.org/content/96/7/3739.full>

⁷²<http://dx.doi.org/10.1073/pnas.96.7.3739>

⁷³<http://link.aps.org/doi/10.1103/PhysRevLett.75.4425>

⁷⁴<http://dx.doi.org/10.1103/PhysRevLett.75.4425>

⁷⁵<http://www.ncbi.nlm.nih.gov/pmc/articles/PMC1304012/>&tool=pmcentrez&rendertype=abstract

⁷⁶[http://dx.doi.org/10.1016/S0006-3495\(04\)74245-9](http://dx.doi.org/10.1016/S0006-3495(04)74245-9)

⁷⁷<http://www.sciencemag.org.rproxy.sc.univ-paris-diderot.fr/content/338/6104/253.long> <http://www.ncbi.nlm.nih.gov/pubmed/22923438>

<http://www.sciencemag.org/content/338/6104/253> <http://www.sciencemag.org/content/338/6104/253.abstract>

⁷⁸<http://dx.doi.org/10.1126/science.1225399>

⁷⁹<http://www.pnas.org/content/101/16/5992.abstract>

<http://www.pnas.org/content/101/16/5992.full>

<http://www.pnas.org/content/101/16/5992.full.pdf>

⁸⁰<http://dx.doi.org/10.1073/pnas.0307704101>

⁸¹<http://dx.doi.org/10.1016/j.bpj.2011.05.049>

<http://www.sciencemag.org/content/315/5810/370.short> [http://www.ncbi.nlm.nih.gov/pubmed/17234946⁸²](http://www.ncbi.nlm.nih.gov/pubmed/17234946), doi:10.1126/science.1134404⁸³.

[Morone, Fujiwara, Murase, et al. 2006] Nobuhiro Morone, Takahiro Fujiwara, Kotono Murase, Rinshi S Kasai, Hiroshi Ike, Shigeki Yuasa, Jiro Usukura, and Akihiro Kusumi. Three-dimensional reconstruction of the membrane skeleton at the plasma membrane interface by electron tomography.. *The Journal of cell biology*, 174(6):851–62, September 2006. URL: <http://www.pubmedcentral.nih.gov/articlerender.fcgi?artid=2064339&tool=pmcentrez&rendertype=abstract> [http://jcb.rupress.org/content/174/6/851.long⁸⁴](http://jcb.rupress.org/content/174/6/851.long), doi:10.1083/jcb.200606007⁸⁵.

[Morse, 1998a] David C Morse. Viscoelasticity of concentrated isotropic solutions of semi-flexible polymers. 2. Linear response. *Macromolecules*, 9297(98):7044–7067, 1998. URL: [http://pubs.acs.org/doi/abs/10.1021/ma980304u⁸⁶](http://pubs.acs.org/doi/abs/10.1021/ma980304u).

[Morse, 1998b] David C. Morse. Viscoelasticity of Concentrated Isotropic Solutions of Semi-flexible Polymers. 1. Model and Stress Tensor. *Macromolecules*, 31(20):7030–7043, October 1998. URL: <http://pubs.acs.org/doi/abs/10.1021/ma9803032> [http://dx.doi.org/10.1021/ma9803032⁸⁷](http://dx.doi.org/10.1021/ma9803032), doi:10.1021/ma9803032⁸⁸.

[Nieminen, Knöner, Heckenberg, RubinszteinDunlop, 2007] Timo A Nieminen, Gre-gor Knöner, Norman R Heckenberg, and Halina Rubinsztein-Dunlop. Physics of optical tweezers.. *Methods in cell biology*, 82:207–36, January 2007. URL: [http://www.sciencedirect.com/science/article/pii/S0091679X06820066⁸⁹](http://www.sciencedirect.com/science/article/pii/S0091679X06820066), doi:10.1016/S0091-679X(06)82006-6⁹⁰.

[Noguera, 2012] Philippe Noguera. *Etude du rôle de la protéine VASP dans la dynamique et la mécanique des réseaux d'actine avec un système biomimétique de la motilité cellulaire*. PhD thesis, Paris 7, September 2012. URL: [http://tel.archives-ouvertes.fr/tel-00834288⁹¹](http://tel.archives-ouvertes.fr/tel-00834288).

[Parekh, Chaudhuri, Theriot, Fletcher, 2005] Sapun H Parekh, Ovijit Chaudhuri, Julie A Theriot, and Daniel A Fletcher. Loading history determines the velocity of actin-network growth.. *Nature cell biology*, 7(12):1219–23, December 2005. URL: <http://www.nature.com/gate1.inist.fr/ncb/journal/v7/n12/full/ncb1336.html> [http://www.ncbi.nlm.nih.gov/pubmed/16299496⁹²](http://www.ncbi.nlm.nih.gov/pubmed/16299496), doi:10.1038/ncb1336⁹³.

[Plastino, Sykes, 2005] Julie Plastino and Cécile Sykes. The actin sling-shot. *Current Opinion in Cell Biology*, 17(1):62–66, 2005. URL: [http://www.sciencedirect.com/science/article/pii/S0955067404001693⁹⁴](http://www.sciencedirect.com/science/article/pii/S0955067404001693).

⁸²<http://www.sciencemag.org/content/315/5810/370.abstract> <http://www.ncbi.nlm.nih.gov/pubmed/17234946>

⁸³<http://dx.doi.org/10.1126/science.1134404>

⁸⁴<http://www.pubmedcentral.nih.gov/articlerender.fcgi?artid=2064339&tool=pmcentrez&rendertype=abstract>

<http://jcb.rupress.org/content/174/6/851.long>

⁸⁵<http://dx.doi.org/10.1083/jcb.200606007>

⁸⁶<http://pubs.acs.org/doi/abs/10.1021/ma980304u>

⁸⁷<http://pubs.acs.org/doi/abs/10.1021/ma9803032> <http://dx.doi.org/10.1021/ma9803032>

⁸⁸<http://dx.doi.org/10.1021/ma9803032>

⁸⁹<http://www.sciencedirect.com/science/article/pii/S0091679X06820066>

⁹⁰[http://dx.doi.org/10.1016/S0091-679X\(06\)82006-6](http://dx.doi.org/10.1016/S0091-679X(06)82006-6)

⁹¹<http://tel.archives-ouvertes.fr/tel-00834288>

⁹²<http://www.nature.com/gate1.inist.fr/ncb/journal/v7/n12/full/ncb1336.html> <http://www.ncbi.nlm.nih.gov/pubmed/16299496>

⁹³<http://dx.doi.org/10.1038/ncb1336>

⁹⁴<http://www.sciencedirect.com/science/article/pii/S0955067404001693>

- [Pollard, 1986] T D Pollard. Rate constants for the reactions of ATP- and ADP-actin with the ends of actin filaments.. *The Journal of cell biology*, 103(6 Pt 2):2747–54, December 1986. URL: <http://www.ncbi.nlm.nih.gov/pmc/articles/2114620/>&tool=pmcentrez&rendertype=abstract⁹⁵, doi:10.1083/jcb.103.6.2747⁹⁶.
- [Pollard, Blanchoin, Mullins, 2000] T D Pollard, L Blanchoin, and R D Mullins. Molecular mechanisms controlling actin filament dynamics in nonmuscle cells.. *Annual review of biophysics and biomolecular structure*, 29:545–76, January 2000. URL: <http://www.ncbi.nlm.nih.gov/pmc/articles/10940259/>⁹⁷, doi:10.1146/annurev.biophys.29.1.545⁹⁸.
- [Pollard, Borisy, 2003] Thomas D. Pollard and Gary G. Borisy. Cellular motility driven by assembly and disassembly of actin filaments.. *Cell*, 112(4):453–65, February 2003. URL: <http://linkinghub.elsevier.com/retrieve/pii/S009286740300120X> <http://www.ncbi.nlm.nih.gov/pmc/articles/12600310/>⁹⁹, doi:10.1016/S0092-8674(03)00120-X¹⁰⁰.
- [Pontani, vdGucht, Salbreux, et al. 2009] Léa-Laetitia Pontani, Jasper van der Gucht, Guillaume Salbreux, Julien Heuvingh, Jean-François Joanny, and Cécile Sykes. Reconstruction of an actin cortex inside a liposome.. *Biophysical journal*, 96(1):192–8, January 2009. URL: [http://www.cell.com/biophysj/abstract/S0006-3495\(08\)00038-6](http://www.cell.com/biophysj/abstract/S0006-3495(08)00038-6) http://www.sciencedirect.com/science?_ob=MImg&_i¹⁰¹, doi:10.1016/j.bpj.2008.09.029¹⁰².
- [Pring, Evangelista, Boone, et al. 2003] Martin Pring, Marie Evangelista, Charles Boone, Changsong Yang, and Sally H Zigmond. Mechanism of formin-induced nucleation of actin filaments.. *Biochemistry*, 42(2):486–96, January 2003. URL: <http://dx.doi.org/10.1021/bi026520j>¹⁰³, doi:10.1021/bi026520j¹⁰⁴.
- [Pruyne, Evangelista, Yang, et al. 2002] David Pruyne, Marie Evangelista, Changsong Yang, Erfei Bi, Sally Zigmond, Anthony Bretscher, and Charles Boone. Role of formins in actin assembly: nucleation and barbed-end association.. *Science (New York, N.Y.)*, 297(5581):612–5, July 2002. URL: <http://www.science.org/content/297/5581/612.abstract>¹⁰⁵, doi:10.1126/science.1072309¹⁰⁶.
- [Pujol, dRoure, Fermigier, Heuvingh, 2012] Thomas Pujol, Olivia du Roure, Marc Fermigier, and Julien Heuvingh. Impact of branching on the elasticity of actin networks.. *Proceedings of the National Academy of Sciences of the United States of America*, 109(26):10364–9, June 2012. URL: <http://www.pnas.org/content/early/2012/06/05/1121238109>¹⁰⁷, doi:10.1073/pnas.1121238109¹⁰⁸.
- [Salbreux, Charras, Paluch, 2012] Guillaume Salbreux, Guillaume Charras, and Ewa Paluch. Actin cortex mechanics and cellular morphogenesis.. *Trends in cell biology*, 22(10):536–45,

⁹⁵<http://www.ncbi.nlm.nih.gov/pmc/articles/2114620/>&tool=pmcentrez&rendertype=abstract

⁹⁶<http://dx.doi.org/10.1083/jcb.103.6.2747>

⁹⁷<http://www.ncbi.nlm.nih.gov/pmc/articles/10940259/>

⁹⁸<http://dx.doi.org/10.1146/annurev.biophys.29.1.545>

⁹⁹<http://linkinghub.elsevier.com/retrieve/pii/S009286740300120X> <http://www.ncbi.nlm.nih.gov/pmc/articles/12600310/>

¹⁰⁰[http://dx.doi.org/10.1016/S0092-8674\(03\)00120-X](http://dx.doi.org/10.1016/S0092-8674(03)00120-X)

¹⁰¹[http://www.cell.com/biophysj/abstract/S0006-3495\(08\)00038-6](http://www.cell.com/biophysj/abstract/S0006-3495(08)00038-6) http://www.sciencedirect.com/science?_ob=MImg&_i

¹⁰²<http://dx.doi.org/10.1016/j.bpj.2008.09.029>

¹⁰³<http://dx.doi.org/10.1021/bi026520j>

¹⁰⁴<http://dx.doi.org/10.1021/bi026520j>

¹⁰⁵<http://www.science.org/content/297/5581/612.abstract>

¹⁰⁶<http://dx.doi.org/10.1126/science.1072309>

¹⁰⁷<http://www.pnas.org/content/early/2012/06/05/1121238109>

¹⁰⁸<http://dx.doi.org/10.1073/pnas.1121238109>

October 2012. URL: <http://www.sciencedirect.com/science/article/pii/S0962892412001110> [http://www.ncbi.nlm.nih.gov/pubmed/22871642¹⁰⁹](http://www.ncbi.nlm.nih.gov/pubmed/22871642), doi:10.1016/j.tcb.2012.07.001¹¹⁰.

[Sandre, Moreaux, BrochardWyart, 1999] O Sandre, L Moreaux, and F Brochard-Wyart. Dynamics of transient pores in stretched vesicles.. *Proceedings of the National Academy of Sciences of the United States of America*, 96(19):10591–6, September 1999. URL: [http://www.pubmedcentral.nih.gov/articlerender.fcgi?artid=17927&tool=pmcentrez&rendertype=abstract¹¹¹](http://www.pubmedcentral.nih.gov/articlerender.fcgi?artid=17927&tool=pmcentrez&rendertype=abstract).

[Schafer, 2004] Dorothy A Schafer. Cell biology: barbed ends rule.. *Nature*, 430(7001):734–5, August 2004. URL: [http://www.nature.com.rproxy.sc.univ-paris-diderot.fr/nature/journal/v430/n7001/full/430734a.html¹¹²](http://www.nature.com.rproxy.sc.univ-paris-diderot.fr/nature/journal/v430/n7001/full/430734a.html), doi:10.1038/430734a¹¹³.

[Schuh, Ellenberg, 2008] Melina Schuh and Jan Ellenberg. A new model for asymmetric spindle positioning in mouse oocytes.. *Current biology : CB*, 18(24):1986–92, December 2008. URL: [http://www.ncbi.nlm.nih.gov/pubmed/19062278¹¹⁴](http://www.ncbi.nlm.nih.gov/pubmed/19062278), doi:10.1016/j.cub.2008.11.022¹¹⁵.

[Schwarz, Neuhaus, Kistler, et al. 2000] E C Schwarz, E M Neuhaus, C Kistler, A W Henkel, and T Soldati. Dictyostelium myosin IK is involved in the maintenance of cortical tension and affects motility and phagocytosis.. *Journal of cell science*, 113 (Pt 4):621–33, February 2000. URL: [http://www.ncbi.nlm.nih.gov/pubmed/10652255¹¹⁶](http://www.ncbi.nlm.nih.gov/pubmed/10652255).

[Seljebotn, 2009] Dag Sverre Seljebotn. Proceedings of the Python in Science Conference (SciPy): Fast numerical computations with Cython. 2009. URL: [http://conference.scipy.org/proceedings/SciPy2009/paper_2/¹¹⁷](http://conference.scipy.org/proceedings/SciPy2009/paper_2/).

[Semmrich, Larsen, Bausch, 2008] Christine Semmrich, Ryan J. Larsen, and Andreas R. Bausch. Nonlinear mechanics of entangled F-actin solutions. *Soft Matter*, 4(8):1675, 2008. URL: [http://xlink.rsc.org/?DOI=b800989a¹¹⁸](http://xlink.rsc.org/?DOI=b800989a), doi:10.1039/b800989a¹¹⁹.

[Soeno, Abe, Kimura, et al. 1998] Y Soeno, H Abe, S Kimura, K Maruyama, and T Obinata. Generation of functional beta-actinin (CapZ) in an *E. coli* expression system.. *Journal of muscle research and cell motility*, 19(6):639–46, August 1998. URL: [http://www.ncbi.nlm.nih.gov/pubmed/9742448¹²⁰](http://www.ncbi.nlm.nih.gov/pubmed/9742448).

[Stewart, Helenius, Toyoda, et al. 2011] Martin P Stewart, Jonne Helenius, Yusuke Toyoda, Subramanian P Ramanathan, Daniel J Muller, and Anthony A Hyman. Hydrostatic pressure and the actomyosin cortex drive mitotic cell rounding.. *Nature*, 469(7329):226–30, January 2011. URL: <http://dx.doi.org/10.1038/nature09642> [http://www.ncbi.nlm.nih.gov/pubmed/21196934¹²¹](http://www.ncbi.nlm.nih.gov/pubmed/21196934), doi:10.1038/nature09642¹²².

¹⁰⁹<http://www.sciencedirect.com/science/article/pii/S0962892412001110> <http://www.ncbi.nlm.nih.gov/pubmed/22871642>

¹¹⁰<http://dx.doi.org/10.1016/j.tcb.2012.07.001>

¹¹¹<http://www.pubmedcentral.nih.gov/articlerender.fcgi?artid=17927&tool=pmcentrez&rendertype=abstract>

¹¹²<http://www.nature.com.rproxy.sc.univ-paris-diderot.fr/nature/journal/v430/n7001/full/430734a.html>

¹¹³<http://dx.doi.org/10.1038/430734a>

¹¹⁴<http://www.ncbi.nlm.nih.gov/pubmed/19062278>

¹¹⁵<http://dx.doi.org/10.1016/j.cub.2008.11.022>

¹¹⁶<http://www.ncbi.nlm.nih.gov/pubmed/10652255>

¹¹⁷http://conference.scipy.org/proceedings/SciPy2009/paper_2/

¹¹⁸<http://xlink.rsc.org/?DOI=b800989a>

¹¹⁹<http://dx.doi.org/10.1039/b800989a>

¹²⁰<http://www.ncbi.nlm.nih.gov/pubmed/9742448>

¹²¹<http://dx.doi.org/10.1038/nature09642> <http://www.ncbi.nlm.nih.gov/pubmed/21196934>

¹²²<http://dx.doi.org/10.1038/nature09642>

[Sturmer, Baumann, Walz, 1995] K Stürmer, O Baumann, and B Walz. Actin-dependent light-induced translocation of mitochondria and ER cisternae in the photoreceptor cells of the locust *Schistocerca gregaria*.. *Journal of cell science*, 108 (Pt 6):2273–2283, 1995.

[Thoumine, Ott, 1997] O Thoumine and A Ott. Time scale dependent viscoelastic and contractile regimes in fibroblasts probed by microplate manipulation.. *Journal of cell science*, 110 (Pt 1):2109–16, September 1997. URL: <http://www.ncbi.nlm.nih.gov/pubmed/9378761>¹²³.

[Tinevez, Schulze, Salbreux, et al. 2009] Jean-Yves Tinevez, Ulrike Schulze, Guillaume Salbreux, Julia Roensch, Jean-Francois Joanny, and Ewa Paluch. Role of cortical tension in bleb growth. *Proceedings of the National Academy of Sciences of the United States of America*, 106(44):18581–18586, November 2009. URL: <http://www.ncbi.nlm.nih.gov/pmc/articles/PMC2765453/> <http://www.ncbi.nlm.nih.gov/pmc/articles/PMC2765453/pdf/zpq04409018581.pdf>¹²⁴, doi:10.1073/pnas.0903353106¹²⁵.

[Valiron, Caudron, Job, 2001] O. Valiron, N. Caudron, and D. Job. Microtubule dynamics. *Cellular and Molecular Life Sciences*, 58(14):2069–2084, December 2001. URL: <http://link.springer.com/10.1007/PL00000837>¹²⁶, doi:10.1007/PL00000837¹²⁷.

[vdGucht, Paluch, Plastino, Sykes, 2005] Jasper van der Gucht, Ewa Paluch, Julie Plastino, and Cécile Sykes. Stress release drives symmetry breaking for actin-based movement. *Proceedings of the National Academy of Sciences of the United States of America*, 102(22):7847 –7852, May 2005. URL: <http://www.pnas.org/content/102/22/7847.abstract> <http://www.pnas.org/content/102/22/7847.full.pdf> <http://www.pnas.org/content/102/22/7847.short>¹²⁸, doi:10.1073/pnas.0502121102¹²⁹.

[Vasilev, Chun, Gragnaniello, et al. 2012] Filip Vasilev, Jong T. Chun, Giovanni Gragnaniello, Ezio Garante, and Luigia Santella. Effects of ionomycin on egg activation and early development in starfish.. *PloS one*, 7(6):e39231, January 2012. URL: <http://www.pubmedcentral.nih.gov/articlerender.fcgi?artid=3377674&tool=pmcentrez&rendertype=abstract>¹³⁰, doi:10.1371/journal.pone.0039231¹³¹.

[Vermeulen, vMameren, Stienen, et al. 2006] Karen C Vermeulen, Joost van Mameren, Ger J. M Stienen, Erwin J. G Peterman, Gijs J. L Wuite, and Christoph F Schmidt. Calibrating bead displacements in optical tweezers using acousto-optic deflectors. *Review of Scientific Instruments*, 77(1):013704, January 2006. URL: http://rsi.aip.org/resource/1/rsinak/v77/i1/p013704_s1?isAuthorized=no <http://scitation.aip.org/content/aip/journal/rsi/77/1/10.1063/1.2165568>¹³², doi:10.1063/1.2165568¹³³.

[Yao, Becker, Broedersz, et al. 2011] Norman Y Yao, Daniel J Becker, Chase P Broedersz, Martin Depken, Frederick C Mackintosh, Martin R Pollak, and David A Weitz. Nonlinear viscoelasticity of actin transiently cross-linked with mutant α -actinin-4.. *Journal of molecular biology*, 411(5):1062–71,

¹²³<http://www.ncbi.nlm.nih.gov/pubmed/9378761>

¹²⁴<http://www.ncbi.nlm.nih.gov/pmc/articles/PMC2765453/> <http://www.ncbi.nlm.nih.gov/pmc/articles/PMC2765453/pdf/zpq04409018581.pdf>

¹²⁵<http://dx.doi.org/10.1073/pnas.0903353106>

¹²⁶<http://link.springer.com/10.1007/PL00000837>

¹²⁷<http://dx.doi.org/10.1007/PL00000837>

¹²⁸<http://www.pnas.org/content/102/22/7847.abstract> <http://www.pnas.org/content/102/22/7847.full.pdf>

<http://www.pnas.org/content/102/22/7847.short>

¹²⁹<http://dx.doi.org/10.1073/pnas.0502121102>

¹³⁰<http://www.pubmedcentral.nih.gov/articlerender.fcgi?artid=3377674&tool=pmcentrez&rendertype=abstract>

¹³¹<http://dx.doi.org/10.1371/journal.pone.0039231>

¹³²http://rsi.aip.org/resource/1/rsinak/v77/i1/p013704_s1?isAuthorized=no <http://scitation.aip.org/content/aip/journal/rsi/77/1/10.1063/1.2165568>

¹³³<http://dx.doi.org/10.1063/1.2165568>

September 2011. URL: <http://www.sciencedirect.com/science/article/pii/S0022283611007376>¹³⁴, doi:10.1016/j.jmb.2011.06.049¹³⁵.

[Yarmola, Bubb, 2009] Elena G Yarmola and Michael R Bubb. How depolymerization can promote polymerization: the case of actin and profilin.. *BioEssays : news and reviews in molecular, cellular and developmental biology*, 31(11):1150–60, November 2009. URL: <http://www.ncbi.nlm.nih.gov/pubmed/19795407>¹³⁶, doi:10.1002/bies.200900049¹³⁷.

[AbuShah, Keren, 2014] E. Abu Shah and K. Keren. Symmetry breaking in reconstituted actin cortices. *eLife*, 3:e01433–e01433, April 2014. URL: <http://elifesciences.org/content/3/e01433.abstract>¹³⁸, doi:10.7554/eLife.01433¹³⁹.

[DosRemedios, Chhabra, Kekic, et al. 2003] C G Dos Remedios, D Chhabra, M Kekic, I V De dova, M Tsubakihara, D A Berry, and N J Nosworthy. Actin binding proteins: regulation of cytoskeletal microfilaments.. *Physiological reviews*, 83(2):433–73, April 2003. URL: <http://www.ncbi.nlm.nih.gov/pubmed/12663865>¹⁴⁰, doi:10.1152/physrev.00026.2002¹⁴¹.

[SoareseSilva, Depken, Stuurmann, et al. 2011] Marina Soares e Silva, Martin Depken, Björn Stuurmann, Marijn Korsten, Fred C MacKintosh, and Gijsje H Koenderink. Active multistage coarsening of actin networks driven by myosin motors.. *Proceedings of the National Academy of Sciences of the United States of America*, 108(23):9408–13, June 2011. URL: <http://www.pnas.org/content/108/23/9408>¹⁴², doi:10.1073/pnas.1016616108¹⁴³.

¹³⁴<http://www.sciencedirect.com/science/article/pii/S0022283611007376>

¹³⁵<http://dx.doi.org/10.1016/j.jmb.2011.06.049>

¹³⁶<http://www.ncbi.nlm.nih.gov/pubmed/19795407>

¹³⁷<http://dx.doi.org/10.1002/bies.200900049>

¹³⁸<http://elifesciences.org/content/3/e01433.abstract>

¹³⁹<http://dx.doi.org/10.7554/eLife.01433>

¹⁴⁰<http://www.ncbi.nlm.nih.gov/pubmed/12663865>

¹⁴¹<http://dx.doi.org/10.1152/physrev.00026.2002>

¹⁴²<http://www.pnas.org/content/108/23/9408>

¹⁴³<http://dx.doi.org/10.1073/pnas.1016616108>